

Architected Cementitious Cellular Materials Towards Auxetic Behavior

Xu, Y.

DOI

[10.4233/uuid:1a9e29a6-4868-4096-bc88-a1095cf568d3](https://doi.org/10.4233/uuid:1a9e29a6-4868-4096-bc88-a1095cf568d3)

Publication date

2021

Document Version

Final published version

Citation (APA)

Xu, Y. (2021). *Architected Cementitious Cellular Materials Towards Auxetic Behavior*. [Dissertation (TU Delft), Delft University of Technology]. <https://doi.org/10.4233/uuid:1a9e29a6-4868-4096-bc88-a1095cf568d3>

Important note

To cite this publication, please use the final published version (if applicable).
Please check the document version above.

Copyright

Other than for strictly personal use, it is not permitted to download, forward or distribute the text or part of it, without the consent of the author(s) and/or copyright holder(s), unless the work is under an open content license such as Creative Commons.

Takedown policy

Please contact us and provide details if you believe this document breaches copyrights.
We will remove access to the work immediately and investigate your claim.

ARCHITECTED

CEMENTITIOUS CELLULAR MATERIALS



Yading Xu

Propositions

Accompanying the dissertation

Architected Cementitious Cellular Materials Towards Auxetic Behavior

By

Yading Xu

1. PhD is a lifestyle choice, and is like a Surprise menu you never know what you're going to get.
2. Auxetic is either a material behavior or a structure behavior; this subjectively depends on the scope of view.
(This proposition pertains to this dissertation)
3. Performing measurements is technology, interpreting the measurements is art.
4. Rome wasn't built in a day, but it was started from one day.
5. Things may look bad now, but there must be something that can make it worse.
6. Trial-and-error is a fundamental methodology of materials science, and a successful thesis is mainly constructed by negative results.
(This proposition pertains to this dissertation)
7. A PhD candidate may doubt his crazy research direction at one moment, but will be relieved as soon as he remembers that it was initiated by even crazier people.
8. Strong spirit is the stuff you are supposed to live on during hard times.
9. Writing propositions should have been the easiest part of a PhD thesis, if the PhD candidate just knows/remembers that one proposition should be formulated every four months from the start of a PhD project.

These propositions are regarded as opposable and defendable, and have been approved as such by the promotor Prof.dr.ir. E. Schlangen and co-promotor Dr. B. Šavija.

**Architected Cementitious Cellular Materials
Towards Auxetic Behavior**

**Architected Cementitious Cellular Materials
Towards Auxetic Behavior**

Dissertation

for the purpose of obtaining the degree of doctor
at Delft University of Technology
by the authority of the Rector Magnificus, Prof.dr.ir. T.H.J.J. van der Hagen
chair of the Board for Doctorates
to be defended publicly on
Wednesday 15 December 2021 at 15:00 o'clock

by

Yading XU

Master of Engineering in Material Science and Engineering,
China Building Materials Academy, China,
Born in Sichuan, China

This dissertation has been approved by the promotors

Composition of the doctoral committee:

Rector Magnificus,	chairperson
Prof.dr.ir. E. Schlangen	Delft University of Technology, promotor
Dr. B. Šavija	Delft University of Technology, copromotor

Independent members:

Prof.dr.ir. L.J. Sluys	Delft University of Technology
Prof.dr. A.A. Zadpoor	Delft University of Technology
Prof. C.P. Ostertag	University of California, Berkeley, USA
Prof. G. van Zijl	Stellenbosch University, South Africa
Prof. V. Mechtcherine	Technische Universität Dresden, Germany



This research was financially supported by China Scholarship Council.

Keywords: Cementitious materials, Architected materials, Auxetic, 3D printing

Printed by: Ipskamp printing, The Netherlands

Cover design: Yading Xu

Copy right @ 2021 by Yading Xu

ISBN:978-94-6421-599-1

To my family

ACKNOWLEDGEMENTS

I would like to give my most sincere appreciation to all dear friends and colleagues. It is an amazing and joyful journey.

First of all, my special gratitude goes to the China Scholar Council (CSC) for the financial support for the work presented in this dissertation. The support ensures the accomplishment of the work done at the Microlab, department of Materials, Mechanics and Management & Design, faculty of civil engineering and geosciences, Delft University of Technology.

I would like to give my sincere gratitude to my promotor Prof. Erik Schlangen. As a professor, he always has invaluable curiosity in scientific research. This helps me to develop scientific thinking and keep me motivated to pursue novel findings. Prof. Erik Schlangen is open to questions and discussions. So many times, I could just walk into his office and have a discussion on ideas or results. These discussions often give me inspirations for my research. Apart from his professional attitude towards work, I'm grateful that he is also kind and friendly in daily life. This creates a wonderful environment and atmosphere for my PhD life.

I also would like to give my appreciation to my daily supervisor and co-promotor Dr. Branko Šavija. As a daily supervisor, he is unbelievably productive. He always responds to my questions and problems incredibly fast, with detail and constructive comments. It's amazing that he is passionate about research and has inspired me with so many great ideas for my PhD research. When I feel lost, he can always help me to find the appropriate direction and keep me motivated to achieve my goals. Of course, I'm grateful we have so many joyful coffee breaks with his interesting topics.

Besides my promotors, I would like to acknowledge the chairperson and all other committee members for my PhD defence: Prof. Klaas van Breugel, Prof. L.J. Sluys, Prof. A.A. Zadpoor, Prof. C.P. Ostertag, Prof. G. van Zijl, Prof. V. Mechtcherine.

I would like to give my gratitude to my nicest and most lovely officemates: Claudia Romero Rodriguez, Marija Nedeljković, Stefan Chaves Figueiredo and Ameya Kamat. It's my fortune and a great pleasure to share the "concrete nest" with you. It's literally the warmest office, from any perspective.

My special appreciation goes to my colleagues and friends: Dr. Guang Ye, Prof. Henk Jonkers, Dr. Oğuzhan Çopuroğlu, Dr. Mladena Luković, Renée Mors, Zhiwei Qian, Hua Dong, Tianshi Lu, Jiayi Chen, Xuliang Hou, Bei Wu, Xu Ma, Leyang Lyu, Hongzhi Zhang, Shi Xu, Wenjuan Lyu, Shizhe Zhang, Zhenming Li, Yidong Gan, Boyu Chen, Albina Kostuchenko, Bart Hendrix, Yu Chen, Yu Zhang, Yask Kulshreshtha, Anne Linde van Overmeir, Luiz Miranda de Lima Junior, Zhiyuan Xu, Fernando Mendonca Filho, Bianca Fraga Silva, Irving Alfredo Flores Beltra, Ze Chang, Lu Cheng, Emanuele Rossi, Xuhui Liang, Yun Chen, Zhi Wan, Shan He, Minfei Liang and Patrick Holthuizen. Because of you all, I have got the most beautiful and precious memories at the Microlab.

I would like to thank Maiko van Leeuwen who has the funniest jokes. As our technician, he is always willing to help me to solve problems in my research. As a friend, he always keeps us united as a team, even in the difficult corona time. Thanks for arranging all the events and gatherings.

Many thanks to Arjan Thijssen and John van den berg for their professional help in all the lab work. I also would like to acknowledge Ton Blom, Kees van Beek, Paul Vermeulen, Iris Batterham, Jacqueline Bergenhenegouwen for their support of my research.

I also would like to thank my master student: Zixia Wu. I appreciate your great work achieved even during the corona lock down period. My gratitude also goes to my bachelor students: Vincent Huigen, Karine van Bergen, Vincent Ponson, Nick Dubbeldam, Jorick Wolbert, David Ninfa, Baqir Kazmi, Niels Ruiters, Bart van't Geloof, Tahira Lee-on, Kevin Bruggeman, Ties Verhagen, Tony Theodory, Bas Berger, Jordi van Veen, Thomas Kluwer, Daan van Venrooij. Thank you all for your contribution to the work in this dissertation.

Finally, I would like to give my deepest gratitude to my parents for their understanding and support. The Netherland is not so far and four years is not so long, as we expected.

Yading Xu (徐亚丁)
November 2021
Delft

CONTENTS

CHAPTER 1 GENERAL INTRODUCTION	1
1.1 Research background	2
1.1.1 Architected cellular materials	2
1.1.2 Considerations for architected cementitious cellular materials	3
1.2 Research objectives	3
1.3 Research approach	4
1.4 Thesis outline	5
References	7
CHAPTER 2 LITERATURE REVIEW: CHALLENGES AND SCOPE OF THE STUDY	11
2.1 Introduction	12
2.2 Architecting cellular structures	13
2.2.1 Increasing porosity	13
2.2.2 Modifying damage resistance	16
2.2.3 Enhancing deformability	18
2.2.4 Turning brittleness to toughness	20
2.3 Processing methods	22
2.3.1 Indirect 3D printing	23
2.3.2 Extrusion-based 3D printing	23
2.3.3 Particle bed 3D printing	24
2.4 Architecting constituent materials	26
2.5 Final remarks	27
References	28
CHAPTER 3 FRACTURE BEHAVIOR OF CELLULAR MATERIALS: INSIGHTS FROM 3D PRINTED POLYMERIC LATTICES	33
3.1 Introduction	34
3.2 Experiments and Modellings	34
3.2.1 Lattice generation	34
3.2.2 Fabrication of polymeric lattices	36
3.2.3 Determination of lattice element properties	37
3.2.4 Uniaxial tensile tests on printed polymeric lattices	42
3.2.5 Lattice fracture modeling	42
3.3 Results and discussion	43
3.3.1 Load-displacement response	43

3.3.2 Influence of randomness on crack patterns	45
3.4 Conclusions	47
References	49

CHAPTER 4 FRACTURE BEHAVIOR OF CEMENTITIOUS TRIANGULAR LATTICES **51**

4.1 Introduction	52
4.2 Methods and materials	52
4.2.1 Multiscale approach	52
4.2.2 Specimen preparation	55
4.2.3 Mechanical tests	56
4.3 Numerical simulations	56
4.3.1 Microstructure segmentation	56
4.3.2 Lattice network generation	57
4.3.3 Lattice fracture modeling	58
4.4 Discussion	60
4.4.1 Mechanical properties of cementitious struts	60
4.4.2 Stiffness and strength of the cementitious lattices	63
4.4.3 Strength and fracture behavior of cementitious lattices	64
4.5 Conclusions	73
References	74

CHAPTER 5 CEMENTITIOUS CELLULAR COMPOSITES WITH AUXETIC BEHAVIOR **75**

5.1 Introduction	76
5.2 Methods and materials	76
5.2.1 Specimen preparation	76
5.2.2 Mechanical Experiments	78
5.3 Results and discussion	79
5.3.1 Crack bridging induced auxetic behavior	79
5.3.2 Auxetic behavior of CCCs under uniaxial compression	83
5.3.3 Behavior of CCCs under cyclic loading	88
5.4 Conclusions	91
References	93

CHAPTER 6 TUNABLE MECHANICAL BEHAVIOR OF AUXETIC CEMENTITIOUS CELLULAR COMPOSITES **95**

6.1 Introduction	96
6.2 Methods and materials	96
6.2.1 Geometry design parameters	96
6.2.2 Casting and curing	97
6.2.3 Mechanical tests	97
6.3 Numerical modelling	98

6.3.1 Model description	98
6.3.2 Model calibration	100
6.3.3 Simulation of compressive tests on CCCs	103
6.4 Results and discussion	104
6.4.1 Influence of geometrical features	104
6.5 Mechanism of auxetic behavior	112
6.6 Conclusions	116
References	117

CHAPTER 7 MECHANICAL BEHAVIOR OF THE AUXETIC CEMENTITIOUS CELLULAR COMPOSITES UNDER VARIOUS LOADING AND BOUNDARY CONDITIONS **119**

7.1 Introduction	120
7.2 Methods and materials	120
7.2.1 Specimen preparation and experimental tests	120
7.2.2 Numerical simulations	121
7.3 Results and Discussions	122
7.3.1 Influence of boundary constraint	122
7.3.2 Influence of loading rate	125
7.3.3 Impact resistance	127
7.4 Conclusions	129
References	130

CHAPTER 8 CEMENTITIOUS COMPOSITES REINFORCED BY 3D PRINTED LATTICE POLYMERIC MESHES **133**

8.1 Introduction	134
8.2 Methods and materials	134
8.2.1 Materials	134
8.2.2 Reinforcement designs	135
8.2.3 Casting and curing	139
8.2.4 Four-point bending test	140
8.2.5 Uniaxial tensile test	140
8.3 Lattice modeling	142
8.4 Results and discussion	144
8.4.1 Four-point bending tests	144
8.4.2 Uniaxial tension tests	154
8.5 Conclusions	158
References	160

CHAPTER 9 TOUGHENED CEMENTITIOUS COMPOSITES BY CUSTOMIZED THREE-DIMENSIONAL OCTET LATTICE STRUCTURES **161**

9.1 Introduction	162
9.2 Methods and materials	162

9.2.1	Designing and fabrication of polymeric lattices	162
9.2.2	Casting and curing	168
9.2.3	Mechanical tests	168
9.3	Numerical simulations	169
9.3.1	Concrete damaged plasticity model (CDPM)	169
9.3.2	Model calibration and validation	169
9.3.3	Four-point bending simulation	171
9.4	Results and discussion	172
9.4.1	Flexural stress-deflection response	172
9.4.2	Fracture behavior	181
9.5	Conclusions	187
	References	189

CHAPTER 10 AUXETIC BEHAVIOR OF CEMENTITIOUS COMPOSITES WITH THREE-DIMENSIONAL CELLULAR STRUCTURE **191**

10.1	Introduction	192
10.2	Methods and materials	192
10.2.1	Design of the cellular structure	192
10.2.2	Mixing, casting and curing	196
10.2.3	Mechanical tests	197
10.3	Compressive behavior of the 3D-ACCCs	198
10.3.1	Stress-strain response	198
10.3.2	Compressive strength	200
10.3.3	Deformability and energy absorption capacity	202
10.4	Conclusions	203
	References	205

CHAPTER 11 DISCUSSIONS, CONCLUSIONS AND OUTLOOK **207**

11.1	Discussions and conclusions	208
11.2	Recommendations for future study	209
11.2.1	Vibration-based energy harvester	209
11.2.2	Strain-energy harvester	210
	References	211

SUMMARY **213**

SAMENVATTING **215**

1

GENERAL INTRODUCTION

In this chapter, research background of architected cementitious cellular composites is introduced first. Research questions and objectives of this thesis are raised afterwards. Then research approaches of the entire work are briefly presented. In the end, the outline of the thesis is given.

1.1 RESEARCH BACKGROUND

1.1.1 Architected cellular materials

The term “architected cellular materials” refers to materials formed by specially designed, tailored or constructed cells, regardless of the size, ranging from nanoscale which includes a couple of atoms or molecules up to macroscale structures. In terms of mechanical properties of the architected cellular materials, this concept naturally requires investigations on two distinct scales: the behaviors determined by the constituent material as well as the behavior influenced by the cellular system. Therefore, the global response of the material is a result of the structural response of the constituents and the unit cells. In this sense, tailoring of the mechanical response of the global system requires architecting both the constituents and the cellular structure.

For many types of materials, architecting the cellular structures has been proven to be a very efficient method to modify material properties: examples include polymers [1-4], metals [5-7] and ceramics [8, 9]. Various cellular structures have already been studied and used in engineering practice (see Figure 1-1): Kagome structures with high relative fracture toughness [10, 11], octet lattices with high relative strength [12, 13] and auxetic structures with high deformability[14-16].

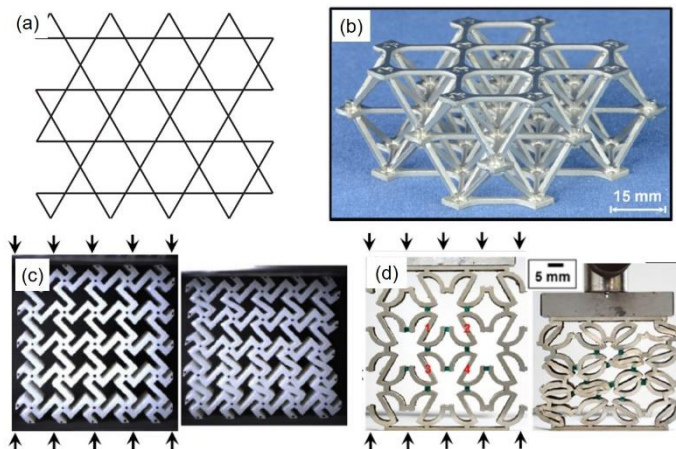


Figure 1-1 Typical Cellular structures: a) Kagome structure[10]; b) octet lattice structure[12]; c) auxetic structure[14]; d) auxetic structure[16]

However, the study of architected cementitious cellular materials has not attracted enough attention yet. To the best of author’s knowledge, at the starting stage of this PhD project in 2017, no such study has been reported. Until the finishing stage of this thesis in 2021, a few studies [17-20] have focused on architecting the cellular structure of cementitious materials and showed great potential of combining cellular structure with cementitious constituent materials to create composites with enhanced mechanical properties.

1.1.2 Considerations for architected cementitious cellular materials

It is well known the mechanical properties of cementitious materials are highly dependent not only on their constituent phases (e.g. properties of the matrix [21-23], aggregates [24, 25] and, if present, fibers [26, 27]) but also the geometrical characteristics and spatial distribution of these constituents [28, 29]. This is often referred to as “micro-” or “meso-structure” of cementitious materials. In all these approaches, the material micro/meso-structure is chemically tailored: as soon as the mixture proportion is fixed, a corresponding micro/meso-structure is already determined. Besides this traditional approach, intentionally distributing the mixture with a certain architected cellular structure enables another dimension of freedom for cementitious material design. Considering that the cellular structure and the cementitious mixture can be independently architected, this novel approach actually combines the advantage of both aspects and may thus allow creating cementitious cellular materials with unprecedented (mechanical) properties.

Compared to conventional continuum solids, cellular materials possess outstanding advantages regarding their mechanical properties. Intuitively, the cellular structure constructed by periodic unit cells affords them considerably lower weight [30-32] which may ensure the cellular materials high specific mechanical properties when normalized by their apparent density. More importantly, special cellular structures, for instance auxetic structures, introduce superior deformability and resiliency which conventional cementitious materials do not possess. These mechanical capabilities make auxetic materials rather promising in various infrastructure engineering applications such as barriers for impact resistance, offshore breakwaters, dampers for vibration mitigation caused by vehicles or, in extreme conditions, earthquakes.

Considering the possibilities of creating a novel type of cementitious materials by combing conventional cementitious mixture and tailored cellular structure, a comprehensive study on architected cementitious cellular materials is of great interest.

1.2 RESEARCH OBJECTIVES

The main objective of this thesis is to develop architected cementitious cellular materials with enhanced mechanical properties compared to the conventional cementitious materials. A specific aim was to achieve auxetic behavior, i.e. negative Poisson's ratio, in the cementitious composite. Owing to the featured negative Poisson's ratio effect, obvious improvement in mechanical properties was found by many researches [33-39] in non-cementitious auxetic materials. For instance, comparing to conventional cellular polymers, auxetic polymers exhibit approximately 2.5~16 times higher energy dissipation ability [33-35]; auxetic metallic materials were found to exhibit resiliency under cyclic loading at large amplitudes of up to 2% ~ 6% strain [40-43] which the constituent metals does not possess. These improvements in mechanical properties make the auxetic behavior rather appealing to be achieved by cementitious materials, turning the brittle and hard materials to materials with ductility.

According to previous studies, auxetic behavior is typically achieved by combining proper cellular structures with constituent materials. A commonly used method to introduce cellular structure is using 3D printing techniques. Meanwhile, all of these auxetic materials are constituted by either elastomers or metals which already possess high deformability. Therefore, for cementitious materials to achieve auxetic behaviors, the main challenges are tailoring appropriate combinations of architected cellular structures with tailored constituent materials. For this, comprehensive and in-depth understanding on the fundamental principles in mechanics and mechanical behaviors of the cementitious cellular materials is needed. In this sense, the following sub-objectives need to be accomplished:

- Using 3D printing techniques, a feasible method to prepare specimens combining tunable cellular structure and various cementitious mixtures needs to be developed, such that cementitious specimens with architected cellular structures can be prepared.
- By experimental testing and numerical modeling, a solid understanding of the mechanical behaviors, for instance stress-strain responses, fracture behaviors, deformation patterns of the cementitious cellular materials have to be obtained.
- Architected cellular structures and tailored constituent cementitious materials need to be properly combined such that negative Poisson's ratio (i.e. auxetic behavior) can be achieved.
- The obtained auxetic cementitious cellular materials need to possess improved deformability, similar to auxetic polymers and metals, at least resiliency under cyclic loading with 2% strain can be expected, meanwhile high energy absorption ability will be ensured.

1.3 RESEARCH APPROACH

In order to achieve the research objectives, the study is performed in the following three main stages:

Stage I: Preliminary understanding of the mechanical behaviors of cementitious cellular materials.

- Discover potential influential factors on the mechanical behaviors of cellular materials.
- Develop a method to fabricate cementitious cellular materials with a cellular structure. Subsequently, study peculiarities of cementitious cellular materials in terms of mechanical behavior.

Stage II: Create cementitious cellular composites (CCCs) with auxetic behavior constructed by a 2D planar cellular structure.

- Select proper two-dimensional planar cellular structures and constituent cementitious mixtures for the CCCs to achieve auxetic behavior. Perform parametric studies of their influences on the mechanical behavior.

- Evaluate the improvement of mechanical performance of the CCCs under different loading conditions. Clarify the fundamental mechanism allowing CCCs to possess auxetic behavior.

Stage III: Validate the discovered mechanism by architecting cellular structure and cementitious constituent material.

- Develop suitable cementitious constituent materials with a 3D cellular structure.
- Evaluate the mechanical behavior of ACCCs with an architected 3D spatial cellular structure.

1.4 THESIS OUTLINE

As shown in Figure 1-2, the thesis is divided in five parts. The chapters are arranged as follows:

Part I: Presents a general introduction and literature review.

Chapter 1 serves as an introduction of the research background, research objectives and the outline of the thesis.

Chapter 2 presents a literature review on the peculiarities and opportunities of architected cementitious cellular materials.

Part II: Deals with understanding the deformation and fracture behaviors of cellular materials.

Chapter 3 presents a study of polymeric cellular materials fabricated by 3D printing which gives preliminary understanding on the influential factors on mechanical properties.

Chapter 4 presents an investigation on the mechanical behavior of cementitious cellular materials in which a feasible method to prepare cementitious cellular materials is developed and the influence of heterogeneity on the constituent material scale and cellular structural scale is elaborated.

Part III: Deals with achieving auxetic behavior by cementitious materials.

Chapter 5 presents a study of achieving auxetic behavior by cementitious cellular composites through architecting the cellular structure and the cementitious constituent material.

Chapter 6 presents a comprehensive study on the compressive behavior of the auxetic cementitious cellular composites (ACCCs) based on parametric studies and clarifies the mechanism of cementitious cellular composites to achieve auxetic behavior.

Chapter 7 evaluates the mechanical behavior of ACCCs under various loading conditions and clarifies the influence of boundary conditions and strain rate.

Part IV: Develops auxetic cementitious composites with 3D cellular structure.

Chapter 8 presents a feasibility study on using 3D printed polymeric reinforcement to improve the crack bridging ability of cementitious materials which can be used as the constituent material for the ACCCs.

Chapter 9 evaluates the performance of 3D printed polymeric reinforcement to enhance the crack bridging ability of the cementitious materials under relatively low reinforcing ratio.

Chapter 10 validates the previously discovered mechanism to create ACCCs using the polymer reinforced cementitious constituent material and a spatial three-dimensional structure.

Part V: Gives the conclusions of the thesis and indicates outlook for future studies.

Chapter 11 provides the main findings of this thesis and gives recommendations for future studies.

Architected Cementitious Cellular Materials: Towards Auxetic Behavior	
Part I Introduction and literature review	
Chapter 1	General introduction
Chapter 2	Literature review: challenges and scope of the study
Part II Understanding mechanics of cellular materials	
Chapter 3	Fracture behavior of cellular materials: insights from 3D printed polymeric lattices
Chapter 4	Fracture behavior of cementitious triangular lattices
Part III Auxetic behavior achieved by cementitious materials	
Chapter 5	Cementitious Cellular Composites with Auxetic Behavior
Chapter 6	Tunable Mechanical Behavior of Auxetic Cementitious Cellular Composites (ACCCs)
Chapter 7	Mechanical behavior of the (ACCCs) under various boundary conditions
Part IV Develop auxetic cementitious composites with 3D cellular structure	
Chapter 8	Cementitious composites reinforced by 3D printed lattice polymeric meshes
Chapter 9	Toughened cementitious composites by customized 3D octet lattice structures
Chapter 10	Auxetic behavior of cementitious composites achieved with 3D cellular structure
Part V Discussions, Conclusions and outlook	
Chapter 11	Discussions, conclusions and recommendations for future study

Figure 1-2 Thesis outline

REFERENCES

- [1] M. Lei, C.M. Hamel, C. Yuan, H. Lu, H.J. Qi, 3D printed two-dimensional periodic structures with tailored in-plane dynamic responses and fracture behaviors, *Composites Science and Technology* 159 (2018) 189-198.
- [2] B.G. Compton, J.A. Lewis, 3D-printing of lightweight cellular composites, *Advanced Materials* 26(34) (2014) 5930-5.
- [3] Y. Xu, H. Zhang, B. Šavija, S. Chaves Figueiredo, E. Schlangen, Deformation and fracture of 3D printed disordered lattice materials: Experiments and modeling, *Materials & Design* 162 (2019) 143-153.
- [4] Y. Xu, B. Šavija, Development of strain hardening cementitious composite (SHCC) reinforced with 3D printed polymeric reinforcement: Mechanical properties, *Composites Part B: Engineering* 174 (2019) 107011.
- [5] H. Gu, M. Pavier, A. Shterenlikht, Experimental study of modulus, strength and toughness of 2D triangular lattices, *International Journal of Solids and Structures* (2018).
- [6] C. Bonatti, D. Mohr, Large deformation response of additively-manufactured FCC metamaterials: From octet truss lattices towards continuous shell mesostructures, *International Journal of Plasticity* 92 (2017) 122-147.
- [7] C. Qiu, S. Yue, N.J.E. Adkins, M. Ward, H. Hassanin, P.D. Lee, P.J. Withers, M.M. Attallah, Influence of processing conditions on strut structure and compressive properties of cellular lattice structures fabricated by selective laser melting, *Materials Science and Engineering: A* 628 (2015) 188-197.
- [8] Z.C. Eckel, C. Zhou, J.H. Martin, A.J. Jacobsen, W.B. Carter, T.A. Schaedler*, Additive manufacturing of polymer-derived ceramics, *Science* 351(6268) (2018) 58-62.
- [9] J. Bauer, A. Schroer, R. Schwaiger, I. Tesari, C. Lange, L. Valdevit, O. Kraft, Push-to-pull tensile testing of ultra-strong nanoscale ceramic-polymer composites made by additive manufacturing, *Extreme Mechanics Letters* 3 (2015) 105-112.
- [10] N.A. Fleck, V.S. Deshpande, M.F. Ashby, Micro-architected materials: past, present and future, *Proceedings of the Royal Society A: Mathematical, Physical and Engineering Sciences* 466(2121) (2010) 2495-2516.
- [11] N.A. Fleck, X. Qiu, The damage tolerance of elastic-brittle, two-dimensional isotropic lattices, *Journal of the Mechanics and Physics of Solids* 55(3) (2007) 562-588.
- [12] L. Dong, V. Deshpande, H. Wadley, Mechanical response of Ti-6Al-4V octet-truss lattice structures, *International Journal of Solids and Structures* 60-61 (2015) 107-124.
- [13] M.C. Messner, Optimal lattice-structured materials, *Journal of the Mechanics and Physics of Solids* 96 (2016) 162-183.
- [14] Y. Jiang, B. Rudra, J. Shim, Y. Li, Limiting strain for auxeticity under large compressive Deformation: Chiral vs. re-entrant cellular solids, *International Journal of Solids and Structures* 162 (2019) 87-95.
- [15] W. Lee, Y. Jeong, J. Yoo, H. Huh, S.-J. Park, S.H. Park, J. Yoon, Effect of auxetic structures on crash behavior of cylindrical tube, *Composite Structures* 208 (2019) 836-846.
- [16] K. Meena, S. Singamneni, A new auxetic structure with significantly reduced stress concentration effects, *Materials & Design* 173 (2019) 107779.
- [17] M. Moini, J. Olek, J.P. Youngblood, B. Magee, P.D. Zavattieri, Additive Manufacturing and Performance of Architected Cement-Based Materials, *Adv Mater* 30(43) (2018) e1802123.
- [18] D.G. Soltan, V.C. Li, Nacre-inspired composite design approaches for large-scale cementitious members and structures, *Cement and Concrete Composites* 88 (2018) 172-186.
- [19] J. Ye, C. Cui, J. Yu, K. Yu, J. Xiao, Fresh and anisotropic-mechanical properties of 3D printable ultra-high ductile concrete with crumb rubber, *Composites Part B: Engineering* 211 (2021) 108639.
- [20] J. Ye, K. Yu, J. Yu, Q. Zhang, L. Li, Designing ductile, tough, nacre-inspired concrete member in metric scale, *Cement and Concrete Composites* 118 (2021) 103987.

- [21] A. Bougara, C. Lynsdale, N.B. Milestone, The influence of slag properties, mix parameters and curing temperature on hydration and strength development of slag/cement blends, *Construction and Building Materials* 187 (2018) 339-347.
- [22] C. Herrera-Mesen, R.P. Salvador, S.H.P. Cavalaro, A. Aguado, Effect of gypsum content in sprayed cementitious matrices: Early age hydration and mechanical properties, *Cement and Concrete Composites* 95 (2019) 81-91.
- [23] F. Lavergne, R. Belhadi, J. Carriat, A. Ben Fraj, Effect of nano-silica particles on the hydration, the rheology and the strength development of a blended cement paste, *Cement and Concrete Composites* 95 (2019) 42-55.
- [24] I. Rahmouni, G. Promis, A. R'Mili, H. Beji, O. Limam, Effect of carbonated aggregates on the mechanical properties and thermal conductivity of eco-concrete, *Construction and Building Materials* 197 (2019) 241-250.
- [25] J.Y. Yoon, J.H. Kim, Mechanical properties of preplaced lightweight aggregates concrete, *Construction and Building Materials* 216 (2019) 440-449.
- [26] H. Savastano, S.F. Santos, M. Radonjic, W.O. Soboyejo, Fracture and fatigue of natural fiber-reinforced cementitious composites, *Cement and Concrete Composites* 31(4) (2009) 232-243.
- [27] D.-Y. Yoo, N. Banthia, Mechanical properties of ultra-high-performance fiber-reinforced concrete: A review, *Cement and Concrete Composites* 73 (2016) 267-280.
- [28] D.P. Bentz, C.F. Ferraris, M.A. Galler, A.S. Hansen, J.M. Guynn, Influence of particle size distributions on yield stress and viscosity of cement-fly ash pastes, *Cement and Concrete Research* 42(2) (2012) 404-409.
- [29] A. Abrishambaf, M. Pimentel, S. Nunes, Influence of fibre orientation on the tensile behaviour of ultra-high performance fibre reinforced cementitious composites, *Cement and Concrete Research* 97 (2017) 28-40.
- [30] Z.D. Sha, C.M. She, G.K. Xu, Q.X. Pei, Z.S. Liu, T.J. Wang, H.J. Gao, Metallic glass-based chiral nanolattice: Light weight, auxeticity, and superior mechanical properties, *Materials Today* 20(10) (2017) 569-576.
- [31] J. Smardzewski, Experimental and numerical analysis of wooden sandwich panels with an auxetic core and oval cells, *Materials & Design* 183 (2019) 108159.
- [32] C. Soyarslan, V. Blümer, S. Bargmann, Tunable auxeticity and elastomechanical symmetry in a class of very low density core-shell cubic crystals, *Acta Materialia* 177 (2019) 280-292.
- [33] A. Bezazi, F. Scarpa, Mechanical behaviour of conventional and negative Poisson's ratio thermoplastic polyurethane foams under compressive cyclic loading, *International Journal of Fatigue* 29(5) (2007) 922-930.
- [34] A. Bezazi, F. Scarpa, Tensile fatigue of conventional and negative Poisson's ratio open cell PU foams, *International Journal of Fatigue* 31(3) (2009) 488-494.
- [35] W.W. Clark, F. Scarpa, M. Ahmadian, J.A. Giacomini, A. Bezazi, A. Lumsdaine, W.A. Bullough, Dynamic behavior and damping capacity of auxetic foam pads, 6169 (2006) 61690T.
- [36] R. Critchley, I. Corni, J.A. Wharton, F.C. Walsh, R.J.K. Wood, K.R. Stokes, A review of the manufacture, mechanical properties and potential applications of auxetic foams, *physica status solidi (b)* (2013) 1963-1982.
- [37] X. Hou, V.V. Silberschmidt, *Metamaterials with Negative Poisson's Ratio: A Review of Mechanical Properties and Deformation Mechanisms*, (2015) 155-179.
- [38] X. Ren, *Studies on three-dimensional metamaterials and tubular structures with negative Poisson's ratio*, RMIT University, Australia, 2017.
- [39] M. Taylor, L. Francesconi, A. Baldi, X. Liang, F. Aymerich, A Novel Auxetic Structure with Enhanced Impact Performance by Means of Periodic Tessellation with Variable Poisson's Ratio, (2019) 211-218.
- [40] F. Box, C.G. Johnson, D. Pihler-Puzović, Hard auxetic metamaterials, *Extreme Mechanics Letters* 40 (2020) 100980.
- [41] V.A. Lvov, F.S. Senatov, A.A. Stepashkin, A.A. Veveris, M.D. Pavlov, A.A. Komissarov, Low-cycle fatigue behavior of 3D-printed metallic auxetic structure, *Materials Today: Proceedings* 33 (2020) 1979-1983.

- [42] D. Tomažinčič, B. Nečemer, M. Vesenjāk, J. Klemenc, Low - cycle fatigue life of thin - plate auxetic cellular structures made from aluminium alloy 7075 - T651, *Fatigue & Fracture of Engineering Materials & Structures* 42(5) (2019) 1022-1036.
- [43] H.M.A. Kolken, A.F. Garcia, A. Du Plessis, C. Rans, M.J. Mirzaali, A.A. Zadpoor, Fatigue performance of auxetic meta-biomaterials, *Acta Biomater* 126 (2021) 511-523.

2

LITERATURE REVIEW: CHALLENGES AND SCOPE OF THE STUDY

Conventionally, the properties of cementitious materials are tailored by a simple but efficient method: mixture proportion design. For a given cementitious mixture, the chemical and physical properties of cementitious materials have already been determined. Consequently, the mechanical performance of the hardened cementitious material is determined. This is attributed to the nanoscale, microscale and mesoscale structures formed during the hydration process which are also dictated by the mixture proportion. Apart from this traditional methodology, a novel approach to tailor materials mechanical performance by combining architected cellular structure with certain constituent materials is introduced. Inspired by cellular polymer materials and cellular ceramic materials which show enhanced properties comparing to conventional polymers and ceramics, creating cementitious cellular materials is also assumed to be a promising research direction. Specifically, geometrical features of promising cellular structures and their corresponding mechanical performance is reviewed. Potential processing methods for obtaining such cellular structures using cementitious materials are discussed. In addition, probable requirements on cementitious mixture for the cellular structure are analyzed.

2.1 INTRODUCTION

Cementitious materials are the most widely used construction materials in the world due to their excellent properties and relatively low cost. Since their invention, there has been a simple and efficient method to tailor the properties of cementitious materials: mixture design. It is well known that material properties are dictated by their microstructures. For cementitious materials, after a curing process in which hydration takes place, the spatial distribution of the mixture ingredients is generated. In this sense, the micro- /meso-structure of cementitious materials is determined and, therefore, mechanical properties of the cementitious materials are dictated. In the past several decades, intensive efforts have focused on configuring or modifying the micro/meso-structure of cementitious materials to improve their performance. For instance, optimizing the packing density [1-3], modifying the pore structure [4-6], modifying the air void structure [7, 8] and introducing new phases as reinforcement [9, 10].

Besides this traditional approach, owing to the rapid development of digital fabrication technology, intentionally distributing constituent cementitious materials with certain architected cellular geometry may enable combining the “material behavior” of cementitious mixtures with “structural behavior” of architected cellular structures. This novel approach has been adopted in many types of materials, such as polymers, metals and ceramics, to create metamaterials (a metamaterial is any material engineered to have a property that is not found in naturally occurring materials) with superior properties [11-15]. However, this new approach has not been applied on cementitious materials yet.

As mentioned previously, “cellular structure” normally refers to specially designed, tailored or constructed structures, regardless of the scale, ranging from nanoscale up to macroscale. In cementitious materials, as the structures below mesoscale are already determined by the mixture proportions, the definition of “structure” and “material” would be ambiguous if not clear definition is given.

In case the system is only comprising a limited number of cells or elements, the system seems to be simply a “structure” instead of “material”. Then it seems reasonable to argue that the response of this structure should not be considered as material behavior. However, considering the approach of “architecting”, even if it is a structure that consisted of, in an extreme case, only one unit cell, the global response is still a combination of the structural response of the unit cell and the constituent material. In this sense, it is valid to tailor the mechanical response of the global system by architecting the structure and the constituent, respectively. This complies well with the research topic of architected cementitious materials. For a global system consisting of a large number of cellular units, it behaves as a monolithic material, same as conventional solid materials. It is not difficult to recognize that the global response of the system should be seen as “material” behavior.

Furthermore, when discussing mechanical properties of cementitious materials, the size or the scale is of importance. The cementitious matrix is already a composite which consist of microscopic grains. In architected cementitious cellular materials, the

dimensions of each cellular unit should be at least greater than a couple of these grains. Considering the particle size of Portland cement (normally ranges within 10~100 μm), the minimum dimension of a cellular unit should be correspondingly at least 40~400 μm if cement paste is used, such that the characteristics of cementitious material can be properly presented. Actually, in most reported cases [16, 17], the dimension of the unit cells of cellular cementitious materials is not smaller than several millimeters. In the present thesis, the cellular structure only refers to structures consisting of units within a millimeter up to a couple of centimeters; In this sense, potential cementitious cellular materials can be easily processed by existing techniques such as traditional mold casting or, by more advanced methods such as 3D printing techniques.

Therefore, throughout this thesis, the term “*cellular structure*” refers to the system constructed by the cellular units at the scale not smaller than millimeters, independent from cementitious mixture propositions. On the other hand, the term “*constituent material*” refers to the substance used to form the unit cells of the cellular structure.

In this literature review, possibilities of several types of cellular structures to be adopted by cementitious materials to enhance physical or mechanical properties are introduced, as well as the processing methods related to the construction of the cellular structures. Features and requirements on architecting the constituent materials for these cellular structures are also discussed.

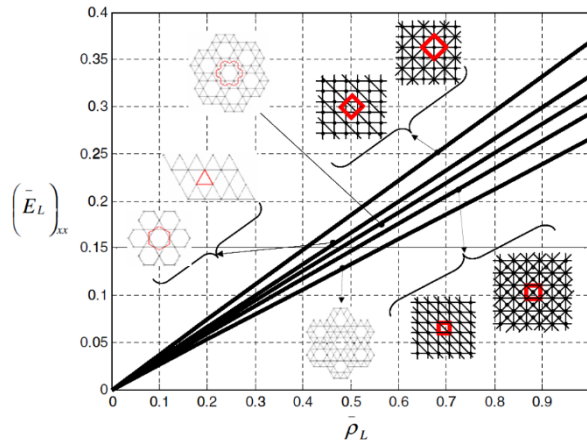
2.2 ARCHITECTING CELLULAR STRUCTURES

2.2.1 Increasing porosity

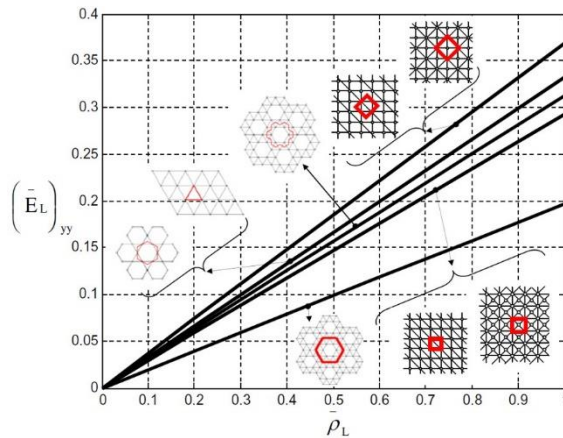
In contrast to continuum materials, the most commonly referred cellular materials are highly porous and consist of periodic or randomized cells. In the field of cementitious materials, conventional foam concrete is the most frequently studied cellular material. Containing high content of air voids, foam concrete has significantly lower thermal conductivity (approximately 0.05~0.7 W/m·K [18, 19]) than conventional concrete (approximately 1.6 W/m·K at 2200 kg/m³ [19]), making it a good choice to be used as thermal insulation construction material. However, foam stability is one of the main concerns that has to be addressed. As the foam stability is very sensitive to the ingredients in cementitious mixtures, the foam structure is highly dependent on the mixture design. Therefore, it is almost impossible to independently optimize the cellular structure and the cementitious mixture in foam concrete.

Contrary to conventional foam concrete, the ability of maintaining and architecting cellular structure makes it possible to combine an optimized *structure* and an optimized *cementitious mixture*. Among numerous types of cellular structures, lattice structures have been extensively studied. The general concept of a lattice structure is defined as “a cellular, reticulated truss or lattice structure made up of a large number of uniform lattice elements”[20]. Accompanied by high porosity (normally mentioned as low relative density in the context of lattice structures), lattice-type structures have been found to have outstanding mechanical properties. For perfect lattices without

defects, stiffness and strength are closely related to their relative density and nodal connectivity. For instance, as shown in Figure 2-1, the stiffness of the two-dimensional lattice is highly dependent on the lattice type: those with higher nodal connectivity also have higher stiffness [20, 21]. A similar trend holds for the shear modulus of lattice materials [21]. Furthermore, when joints of the lattice elements are considered, the stiffness of the lattice system would be even higher due to the nodal stiffening effect [22, 23]. The ability of achieving high relative stiffness may give cementitious lattices high deformation resistance which helps maintaining structural integrity if used in construction practice.



(a)



(b)

Figure 2-1 Relative Stiffness of 2D lattices in a) E_{xx} direction and b) E_{yy} direction, reprinted from [21]

Strength might be a critical concern in cementitious lattices. In terms of tensile response, the tensile strength of lattice materials scales with its relative density as:

$$\frac{\sigma_L}{\sigma_{TS}} = C\bar{\rho}^c \quad (2-1)$$

where σ_L is the tensile strength of the lattice material, σ_{TS} is the tensile strength of the constituent material, $\bar{\rho}$ is the relative density, C and c are structural constants which depend on the nodal connectivity [20]. Even adopting a lattice with high nodal connectivity, for instance a fully triangulated lattice, the tensile strength scales with a magnitude of $0.3\bar{\rho}\sigma_{TS}$ (C and c equal to 3 and 1/3, respectively). Considering the well-known low tensile strength of cementitious materials, the tensile strength of cementitious lattices would be a primary issue to be addressed. In most cases, σ_{TS} of non-reinforced cementitious material rarely reaches 10MPa, then σ_L of triangular cementitious lattice with 0.5 relative density would be only 1.5 MPa. In most cases, then, reinforced cementitious materials would need to be used as the constituent material. In [24], ultra-high-performance cementitious materials (UHPC) reinforced by PE fibers were used as constituent material with flexural strength of 17 MPa such that the flexural strength of the cementitious lattice reached 10 MPa.

In compression, the strength of the cementitious lattice is highly dictated by local tensile failure of the lattice elements. As reported in [25], according to numerical simulation results, tensile stress appears in the lattice elements when loaded in compression. Cracks initiate from locations with high tensile stress concentration (see Figure 2-2). Therefore, the compressive strength of cementitious lattices is relatively low (around 0.6MPa). Similar results were also found in [26-28]. The highest reported value of non-reinforced cementitious lattices is achieved by an octet structure at an approximately $\bar{\rho}=0.65$ with a compressive strength of 11MPa [28]. Even constituted by reinforced cementitious materials UHPC (see Figure 2-3) which has compressive strength of 144 MPa, the corresponding cementitious octet lattice only has compressive strength of 22 MPa ($\bar{\rho}=0.52$). which is still not sufficient for most load bearing purposes.

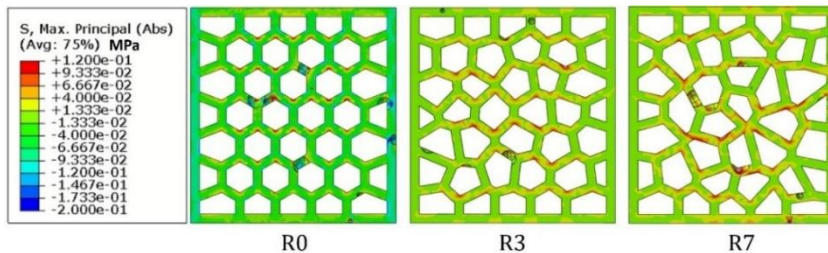


Figure 2-2 Simulated tensile stress distribution of cementitious lattice loaded in uniaxial compression, reprinted from [25]

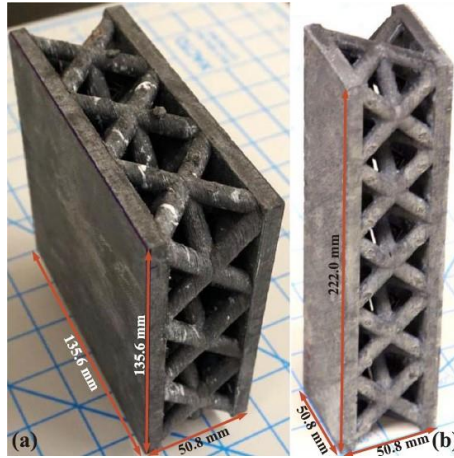


Figure 2-3 Cementitious octet lattice constituted by UHPC, reprinted from [24]

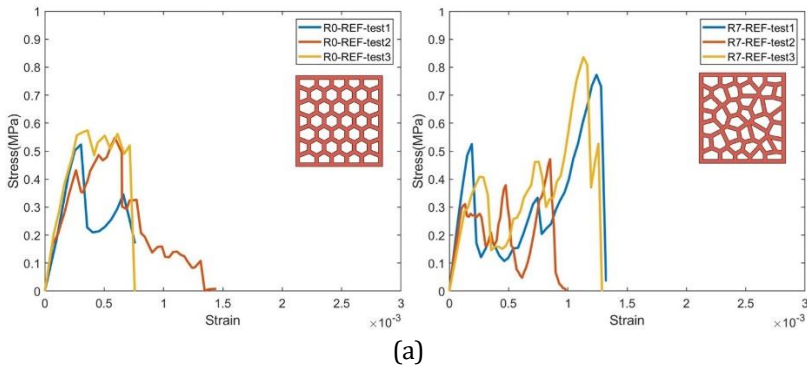
In addition, lattice systems with defects, imperfections or non-uniformities are abundant in nature [29, 30] and artificial materials [31-33]. These defects in the lattice system crucially influence mechanical performance of lattice materials, especially the strength of brittle or quasi-brittle materials. Even if the lattice structure is properly tailored, the possibility of introducing defects may be the main drawback which limits the mechanical performances of the designed lattices.

2.2.2 Modifying damage resistance

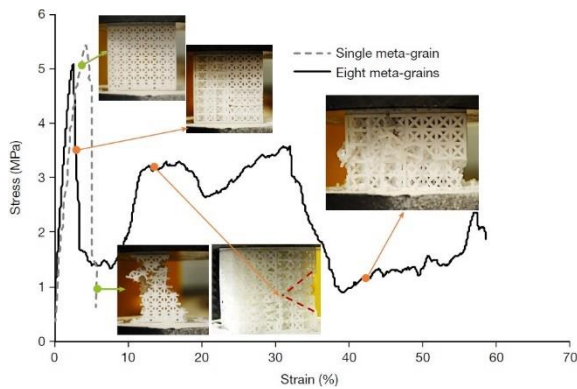
One main drawback of plain cementitious material is their brittleness, which is determined by the physical and chemical nature of the cement hydration process and cement hydrates. By properly architecting the cellular structures, it may be possible for cementitious cellular materials to have enhanced damage resistance. In theory, the damage resistance is dependent on the fracture toughness of cellular materials. In pure tension and shear, it is clear that cellular structures with higher fracture toughness which can be achieved by architecting cellular structure is more damage resistant. For instance, a randomized honeycomb exhibits higher K_{II} compared to regular hexagonal honeycomb of the same relative density [34].

Comparatively, in compression, the mechanism of damage resistance is much more complicated. On one hand, the compressive fracture process involves both tension and shear fracture. Even for continuum materials it is difficult to isolate the contribution of each fracture mode on the overall fracture resistance. On the other hand, for cellular materials, compressive fracture process often refers to a crushing process during which the interaction between the cellular units has to be considered. Then the strategy of enhancing compressive damage resistance may not be limited to increasing the fracture toughness values. This of course raises high interest for scientific research. Several studies have already shown promising results. As reported by Wu [25], cementitious cellular composites with a highly randomized Voronoi structure show higher fracture resistance than regular honeycombs made using the same cementitious

constituent material. The stress-strain response (see Figure 2-4a) exhibits multiple peaks which indicates an element-wise damage mechanism. This result implies that it is more difficult for cracks to propagate in randomized cellular structures. A similar results was also found by Pham [35], who designed a hybrid lattice structure inspired by the alloy crystals shows enhanced compressive strength and fracture resistance. Although cementitious materials were not used in this study [35], the mechanical behavior is in principle similar. As shown in Figure 2-4b, a regular lattice structure shows brittle compressive damage, which is sharply in contrast to the compressive behavior of a lattice with meta-grains (lattice structure with the same orientation). In a recent study of Nguyen-Van [36], cementitious cellular material with a fractal-like hierarchical structure was studied. According to their numerical simulations, the damage resistance of the cementitious cellular materials is dependent on the order of fractal: higher fractal order gives higher damage resistance. In these reported cases, cracking is either hindered, deflected or arrested by the architected cellular structure, which results in increased damage resistance.



(a)



(b)

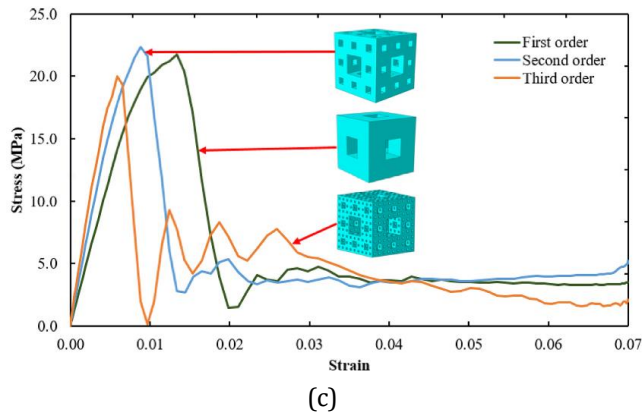


Figure 2-4 Architected cellular materials with improved damage resistance, a) cementitious Voronoi structure; b) alloy crystal inspired structure; c) fractal-like structure, reprinted from [25, 35, 36]

2.2.3 Enhancing deformability

As a construction material, high stiffness of cementitious materials allows them to resist deformation which helps to maintain structural integrity. Nevertheless, unlike the cementitious materials used for common structural elements, in some specific engineering applications such as impact resistant structures [37] and vibration mitigation structures [38, 39], materials with high deformability are required. Conventional cementitious materials are easily damaged undergoing a minor strain. By architecting the cellular structure, high deformability might be achieved by cementitious materials.

One promising structure is structures potentially exhibit auxetic behavior. The term “auxetic”, coined by Evans in 1991 [40], refers to a material possessing a negative Poisson’s ratio. This means that the material exhibits lateral contraction or expansion when compressed or stretched vertically, respectively. This unusual behavior gives auxetic materials extraordinary mechanical properties: enhanced indentation resistance [41-43], high specific energy absorption [44-46], and high shear resistance [44, 47]. In cellular materials, auxetic behavior is usually achieved by special deformation mechanisms. Bertoldi [48] created two-dimensional porous cellular structures consisting of circular holes. Under vertical uniaxial-compressive load, elastic instability was introduced to the cellular structure. In terms of stress-strain response, the stress increases as the external load continues until a critical point [49]. Pattern transformation was observed afterwards accompanied by negative Poisson ratio effect, see Figure 2-5a. This unique deformation process ensures high deformability of the cellular material with an auxetic structure. In a more recent research [50], similar auxetic behavior was observed (Figure 2-5b). As clearly shown on the corresponding stress-strain curves, a long plateau exists indicating high deformability of auxetic materials.

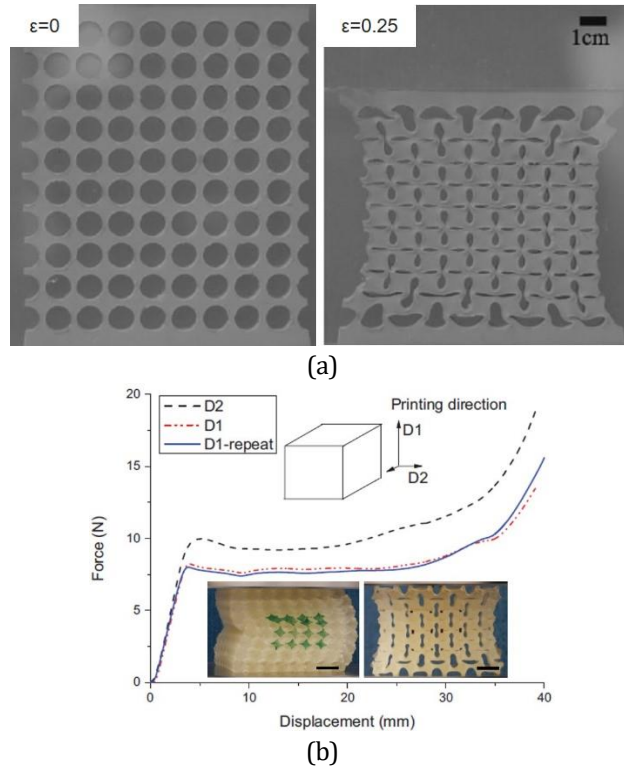
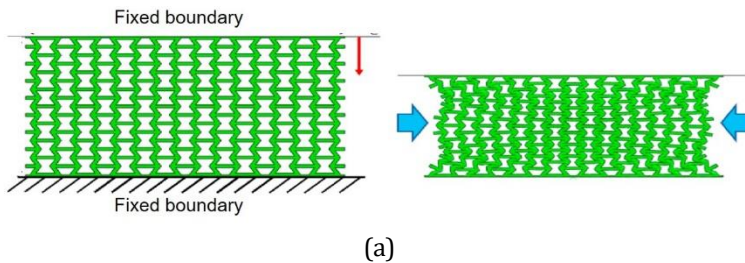


Figure 2-5 Deformation and stress-strain response of auxetic structure, a) pattern transformation observed in [48]; b) similar pattern transformation observed and corresponding stress-strain response reported in [50]

In theory, the auxetic behavior of cellular materials is mainly attributed to geometrical features of the constituent material arrangement. This can be achieved by numerous designs, such as re-entrant honeycombs [51-55], rigid body rotation structures [56-59] and chiral structures [60-64]. In practice, the mechanical response varies significantly when different constituent materials are used even for the same auxetic structure. Typically, for auxetic behavior to be achieved, the constituent material should be highly elastic and deformable. If cementitious materials are to be used as constituent materials, their brittleness and low deformability need to be addressed to achieve auxetic behavior. Therefore, the constituent cementitious materials might need to be toughened or reinforced.



(a)

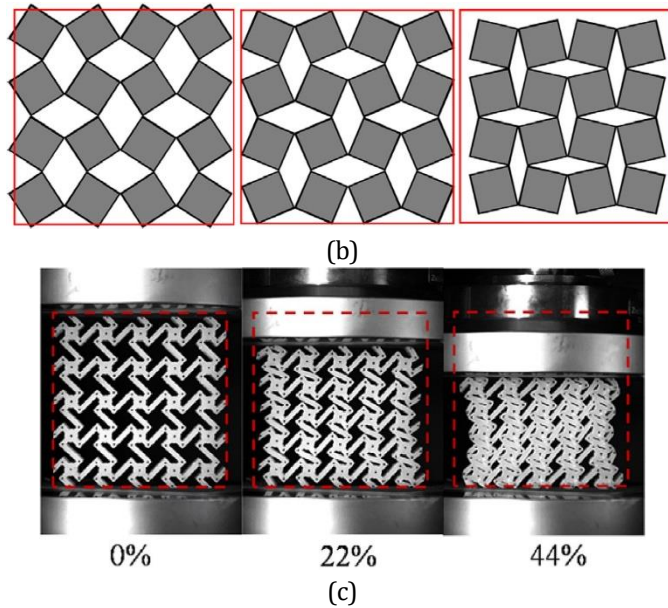


Figure 2-6 Various type of auxetic structures, a) re-entrant honeycomb; b) rotating rigid units; c) chiral structure, reprinted from [55, 59, 64]

2.2.4 Turning brittleness to toughness

More generally, the concept “cellular” not only refers to those structures constituted by dilute units with high porosity but also include the structures consisting of solid cells, tablets or blocks stacked in certain configurations.

Bouligand is a typical structure with stacked-unit configuration (shown in Figure 2-7). This structure was found in the shell of a specific beetle, *C. gloriosa* [65], which has a special layered helicoidal structure. Bouligand has studied cholesteric liquid crystals which has a similar helical structure. Therefore, Pace [66] described this structure as a Bouligand structure. One typical feature of this type of structure is the ability to enhance fracture resistance of laminated structures [67, 68]. When adopted by Moini [16] to 3D printed cementitious materials, the Bouligand structured specimens have shown deflected crack pattern and improved fracture resistance without sacrificing strength which are usually two contradicting aspects for brittle materials.

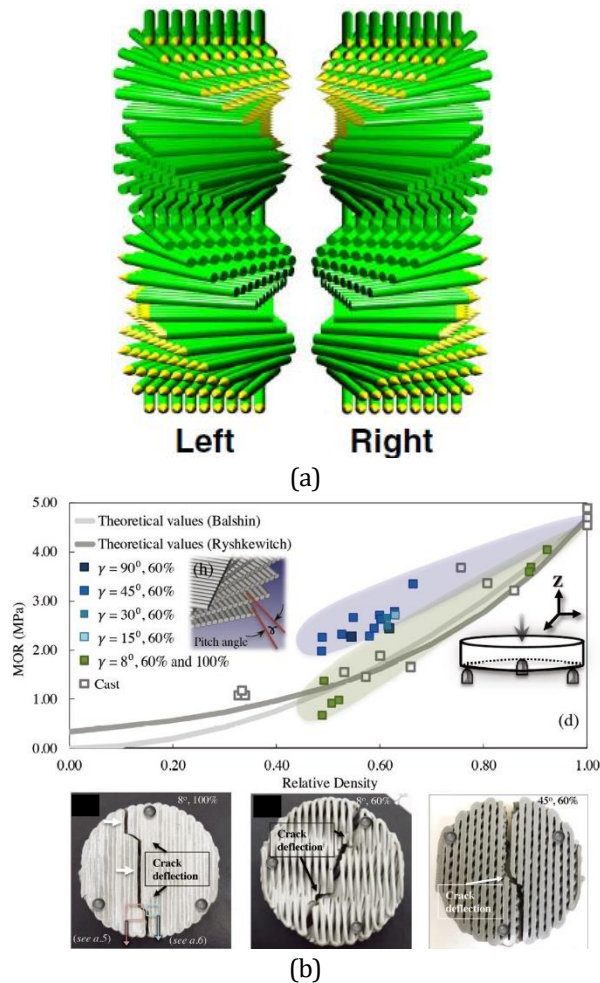


Figure 2-7 The a) Bouligand structure and b) cementitious materials with Bouligand structure, reprinted from [16, 65]

As mentioned, taking advantage of the ability to deflect cracking, fracture resistance of cementitious materials can be improved without decreasing strength. Similarly, another type of bio-inspired structure may also contribute to deflect cracks. Nacre, known as the “mother-of-pearl” [69] is naturally generated with layered cells. Although constituted by brittle ceramic material, nacre shows higher strength and fracture toughness compared to its constituent. The extraordinary mechanical properties of nacre are achieved by its special hierarchical structures (shown in Figure 2-8). The nacre structure consists of small tablets adjacently stacked in the horizontal direction and densely packed in the vertical direction with multiple layers. Because of the interlocking between the tablets [70] as well as the sliding between the layers [69], strength and toughness of the nacre structure is remarkable considering the brittleness of the ceramic tablet itself. For cementitious materials, Soltan [71, 72] combined strain

hardening cementitious composites and polymeric meshes to create nacre structured composites using 3D concrete printing. Distributed and deflected cracks were found on the flexural loaded nacre structured composites and the compressive strength, flexural strength as well as fracture toughness are found to be significantly enhanced. Similar approach and result have been reported by others recently [73, 74]. Nevertheless, looking at the structural feature of the Bouligand and nacre structure, the enhancement in mechanical properties is mainly in the direction parallel to the filaments or tablets. The improvement in interlayer mechanical properties between the stacked layers seems limited. Further studies in improving the interlayer mechanical properties are necessary.

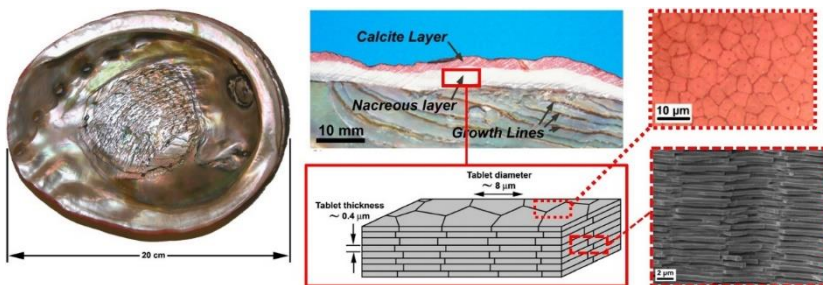


Figure 2-8 Hierarchical structure of Nacre, figures reprinted from [69]

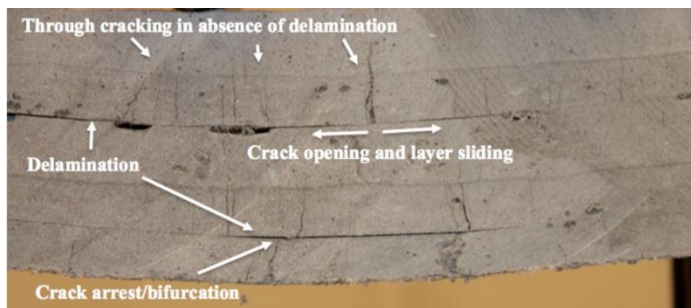


Figure 2-9 Deflected cracks by nacre-like structure reported in [72]

2.3 PROCESSING METHODS

Complex structure is a particular characteristic of cementitious cellular materials compared to conventional cementitious material. In order to prepare such complex cellular structures, special processing methods have to be applied. Owing to the rapid development of additive manufacturing (AM) technology in the past decade, 3D printing methods are becoming widely used for fabricating cellular materials with complex geometries [15, 75-77]. In most 3D printing techniques such as fused deposition modeling (FDM) [78, 79], selective laser sintering (SLS) [31] and stereolithography (SLA) [80-82], the materials are precisely deposited layer by layer to build up objects under the control of an automated system to ensure high printing

quality even with complex geometries. For cementitious materials, different types of processing methods can be adopted to fabricate cellular structures.

2.3.1 Indirect 3D printing

The so-called “indirect 3D printing” actually refers to a method that combines 3D printing technique with traditional casting. The basic principle is similar to the “investment casting” [83] usually used in metal industry.

Normally, a mold with a designed cellular structure is prepared first, using materials that are easy to be printed and demolded. Polymers are an excellent choice to be the mold material. Their simplicity in printing ensures the possibility of making complex geometries. Meanwhile, equipment for printing polymers is much more accessible than any other materials. Even a commercial desktop 3D printer can be used to prepare polymeric 3D printed objects with complex geometries. This simplicity also makes it more economical to be used for field constructions. Another aspect is the ease of demolding. Even when complex three-dimensional geometries are used, the printed polymeric mold can be dissolved in corresponding solvent. For instance, Sajadi [84] printed a cellular mold by PVA (Polyvinyl alcohol) which is dissolvable in water. Aghdasi [24] printed octet lattice molds with ABS (Acrylonitrile butadiene styrene) which is dissolvable in acetone. As the cementitious mixture needs to be casted into the mold, it naturally requires the mixture to possess high flowability otherwise air void defects easily occur [25].

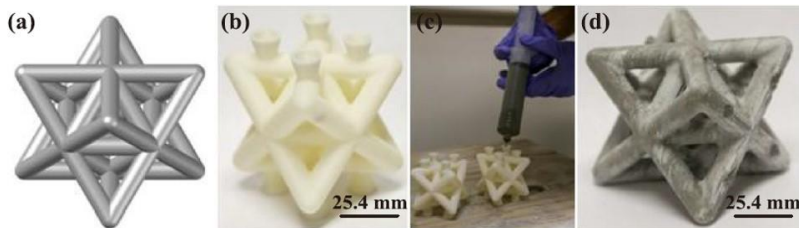


Figure 2-10 Schematics of typical procedures for indirect printing, a) designed structure, b) 3D printed polymer mold, c) casting cementitious mixture into the 3D printed molds, d) specimen after dissolving the mold [24]

2.3.2 Extrusion-based 3D printing

Cellular cementitious composites with a layered structure are of particular interest for digitally fabricated cementitious materials as the layer-wise structure is almost an intrinsic characteristic induced by the processing method. This stacked-unit structure is widely seen in nature.

In terms of the processing methods of cementitious cellular materials, the ability for fabricating complex structures at a high resolution is crucial. For the extrusion-based printing technique, the extrudability and buildability of the cementitious mixture have to be properly addressed. In order to increase printing quality, a smaller nozzle size is preferable; however, this increases the difficulty of extruding mixed cementitious

slurry. In addition, the extruded material needs to set fast such that the geometry can be properly maintained. At the moment, some authors reported cases showing good printing quality at high resolution by properly modifying the cementitious mixtures [16, 17].

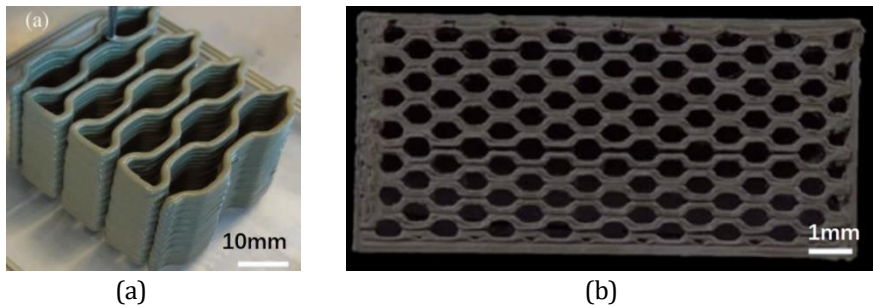


Figure 2-11 Printed cementitious cellular materials with high resolution, figures are reprinted from [16, 17]

2.3.3 Particle bed 3D printing

Particle bed printing technique is also a layer-wise building up technique. Compared to the extrusion-based 3D printing which directly deposits ready mixed material, the particle bed printing technique deposits liquid binders and dry material separately. Basically, it consists of two repeated and consecutive steps: first, a layer of dry material (for example cement particles and aggregates) is deposited on a building platform; afterwards, a liquid phase is selectively sprayed on the deposited particles according to the designed printing path. The sprayed liquid phase is used to bind the particles. These two steps are repeated such that object can be built up layer-by-layer. After the printing steps are finished, excessive non-bonded particles can be removed. As shown in Figure 2-12 [85], depending on the combination of binders and dry particles, several types of methods can be used to print cementitious materials.

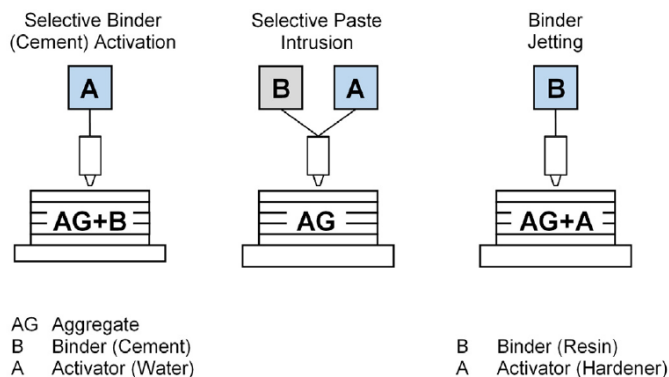


Figure 2-12 Schematics of powder, reprinted from [85]

Compared to the indirect printing and extrusion process, the particle bed printing has higher freedom of form in fabrication. This is mainly attributed to two reasons. The first is that the dry materials and liquid phase can be independently designed. This almost eliminates the negative influence of certain ingredients on the flowability or buildability as seen in the indirect printing process and the extrusion-based printing process. Therefore, there is much more freedom to design a variety of cementitious mixtures without sacrificing the printing quality. The second is that during the printing process, the non-bonded particles serve as supporting material which ensures the particle bed printing method high ability to construct complex structure, for example overhangs, undercut or cavities, which are rather difficult for extrusion-based printing. Meanwhile, the size of the printed object by this technique covers a large range, from desktop objects size with a couple of millimeters [76] up to construction size in meters [85]. However, because the liquid phase and dry particle are deposited in two steps, the equipment complexity of the particle bed printing technique is much higher than the other two techniques, which to some extent limits the application of this technique.

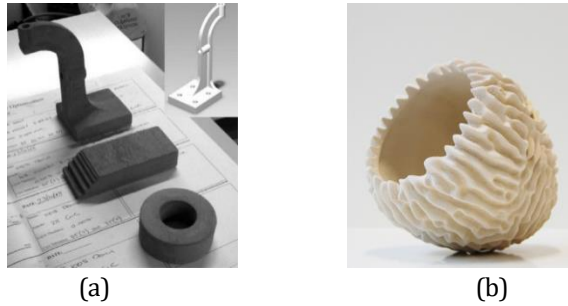


Figure 2-13 Objects with complex features fabricated by cementitious particle bed printing, reprinted from [85, 86]

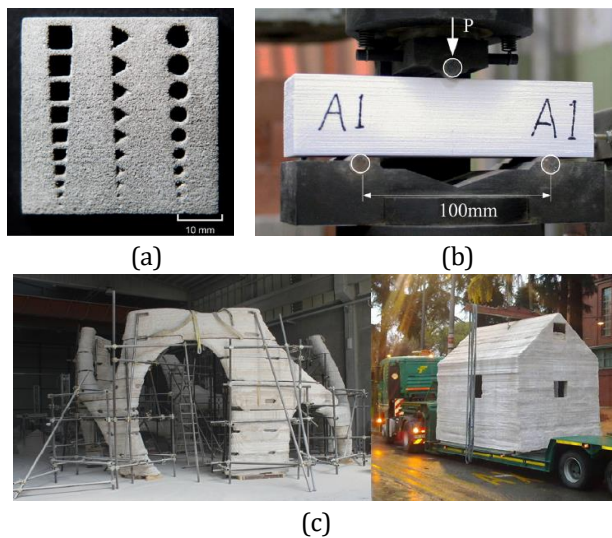


Figure 2-14 Particle bed printed objects with different sizes, reprinted from [76, 85, 87]

2.4 ARCHITECTING CONSTITUENT MATERIALS

According to previous definitions, the *constituent material* is the cementitious mixture that is designed and processed to consist the single “unit” of the cellular structure. The concept of architected cementitious cellular materials not only refers to modifying the cellular structure as indicated in Section 2.2 but combining the geometrical traits of the cellular structure with tailoring the constituent material to achieve better material performance.

Compared to other materials, the design flexibility of constituent materials is one of the major advantages of cementitious cellular materials. By simply modifying the mixture design, the properties of cementitious material can cover a large range. For example, one main drawback of cementitious materials is their lack of ductility: they have low tensile strength and are prone to cracking [88, 89]. In order to overcome the brittleness, fibers have been used as reinforcement for cementitious materials [90-93]. A typical type of fiber reinforced cementitious material is engineering cementitious composites (ECC) [90], also known as the strain hardening cementitious composites (SHCCs) [94, 95] in which PVA (Polyvinyl alcohol) fibers are often used. The main feature of this type of fiber reinforced cementitious composites is the so-called multiple cracking and pseudo strain hardening behavior in uniaxial tension: the SHCCs are able to crack multiple times before eventual failure, while the ultimate failure strength is higher than their first cracking strength. Owing to this, the SHCCs are significantly toughened compared to plain cementitious materials. Recent research [71] shows great potential by combining SHCCs with architected structure, where the architected cementitious composites exhibit obviously enhanced mechanical properties.

Before designing the mixture, the compatibility of the constituent materials with processing methods needs to be carefully addressed. Depending on the processing method, the compatibility indicates different requirements of properties of the constituent material raised by the processing technique. Taking the indirect printing method as an example, as the cementitious mixtures are casted in molds with complex structures, good flowability of the cementitious materials is a basic requirement such that the presence of defects can be minimized. In this sense, the desired mechanical performance and potential influence of mixture ingredients on flowability need to be considered. Using the same example of the SHCCs, fibers significantly increase ductility while decreasing the flowability. Meanwhile, fiber length might also be a factor that needs to be considered in case unintended fiber orientation or clogging of cellular molds during casting may occur at small geometries.

Similarly, compatibility requirements raised by the processing method can be also found in extrusion-based 3D printing, for which good extrudability and buildability of the cementitious mixture are the required properties [96, 97]. For the paste intrusion particle bed printing method, paste penetration into the packed particles has been found to be critical on the strength of printed material [98]. By properly tailoring the particle size and the rheological properties of the cement paste, cementitious mixture with good compatibility can be designed.

In general, the simplicity of tailoring cementitious mixtures facilitates achieving the desired mechanical properties independently without hindering the cellular structure of architected cementitious cellular materials. Nevertheless, potential requirements induced by the processing techniques have to be taken into consideration in the mixture designs.

2.5 FINAL REMARKS

In this chapter, several important aspects regarding cellular structures, processing techniques and constituent materials of architected cementitious cellular materials have been reviewed. Preliminary studies have shown great potential of achieving excellent mechanical properties by combining cellular structure with cementitious constituent materials. However, compared to the number of studies focusing on other types of materials such as metals and ceramics, there is still very limited knowledge on architecting cementitious cellular materials. This includes, but is not limited to, potential cellular structure to be adopted by cementitious materials, fundamental mechanics, requirements in processing methods and constituent materials, mechanical properties of architected cementitious cellular materials as well as potential applications in engineering practice. These aspects will then be the main focus of this thesis.

REFERENCES

- [1] M. Amario, C.S. Rangel, M. Pepe, R.D. Toledo Filho, Optimization of normal and high strength recycled aggregate concrete mixtures by using packing model, *Cement and Concrete Composites* 84 (2017) 83-92.
- [2] L.G. Li, C.J. Lin, G.M. Chen, A.K.H. Kwan, T. Jiang, Effects of packing on compressive behaviour of recycled aggregate concrete, *Construction and Building Materials* 157 (2017) 757-777.
- [3] Y. Sun, Z. Wang, Q. Gao, C. Liu, A new mixture design methodology based on the Packing Density Theory for high performance concrete in bridge engineering, *Construction and Building Materials* 182 (2018) 80-93.
- [4] M.-H. Zhang, J. Islam, S. Peethamparan, Use of nano-silica to increase early strength and reduce setting time of concretes with high volumes of slag, *Cement and Concrete Composites* 34(5) (2012) 650-662.
- [5] A. Keulen, Q.L. Yu, S. Zhang, S. Grünewald, Effect of admixture on the pore structure refinement and enhanced performance of alkali-activated fly ash-slag concrete, *Construction and Building Materials* 162 (2018) 27-36.
- [6] X.F. Wang, Y.J. Huang, G.Y. Wu, C. Fang, D.W. Li, N.X. Han, F. Xing, Effect of nano-SiO₂ on strength, shrinkage and cracking sensitivity of lightweight aggregate concrete, *Construction and Building Materials* 175 (2018) 115-125.
- [7] M. Qiao, J. Chen, C. Yu, S. Wu, N. Gao, Q. Ran, Gemini surfactants as novel air entraining agents for concrete, *Cement and Concrete Research* 100 (2017) 40-46.
- [8] F. Özcan, M. Emin Koç, Influence of ground pumice on compressive strength and air content of both non-air and air entrained concrete in fresh and hardened state, *Construction and Building Materials* 187 (2018) 382-393.
- [9] J. Yu, J. Lin, Z. Zhang, V.C. Li, Mechanical performance of ECC with high-volume fly ash after sub-elevated temperatures, *Construction and Building Materials* 99 (2015) 82-89.
- [10] C. Lu, V.C. Li, C.K.Y. Leung, Flaw characterization and correlation with cracking strength in Engineered Cementitious Composites (ECC), *Cement and Concrete Research* 107 (2018) 64-74.
- [11] X. Zheng, H. Lee, T.H. Weisgraber, M. Shusteff, J. DeOtte, Eric B. Duoss, J.D. Kuntz, Monika M. Biener, Ultralight, Ultrastiff Mechanical Metamaterials, *science* 344(6190) (2018) 1373-1377.
- [12] X. Ren, R. Das, P. Tran, T.D. Ngo, Y.M. Xie, Auxetic metamaterials and structures: a review, *Smart Materials and Structures* 27(2) (2018) 023001.
- [13] G.N. Greaves, A.L. Greer, R.S. Lakes, T. Rouxel, Poisson's ratio and modern materials, *Nat Mater* 10(11) (2011) 823-37.
- [14] L. Valdevit, A.J. Jacobsen, J.R. Greer, W.B. Carter, T.M. Pollock, Protocols for the Optimal Design of Multi-Functional Cellular Structures: From Hypersonics to Micro-Architected Materials, *Journal of the American Ceramic Society* 94 (2011) s15-s34.
- [15] T. Buckmann, N. Stenger, M. Kadic, J. Kaschke, A. Frolich, T. Kennerknecht, C. Eberl, M. Thiel, M. Wegener, Tailored 3D mechanical metamaterials made by dip-in direct-laser-writing optical lithography, *Advanced Materials* 24(20) (2012) 2710-4.
- [16] M. Moini, J. Olek, J.P. Youngblood, B. Magee, P.D. Zavattieri, Additive Manufacturing and Performance of Architected Cement-Based Materials, *Adv Mater* 30(43) (2018) e1802123.
- [17] S.M. Sajadi, P.J. Boul, C. Thaemlitz, A.K. Meiyazhagan, A.B. Puthirath, C.S. Tiwary, M.M. Rahman, P.M. Ajayan, Direct Ink Writing of Cement Structures Modified with Nanoscale Additive, *Advanced Engineering Materials* 21(8) (2019) 1801380.
- [18] L. Chica, A. Alzate, Cellular concrete review: New trends for application in construction, *Construction and Building Materials* 200 (2019) 637-647.
- [19] Y.H.M. Amran, N. Farzadnia, A.A. Abang Ali, Properties and applications of foamed concrete; a review, *Construction and Building Materials* 101 (2015) 990-1005.
- [20] N.A. Fleck, V.S. Deshpande, M.F. Ashby, Micro-architected materials: past, present and future, *Proceedings of the Royal Society A: Mathematical, Physical and Engineering Sciences* 466(2121) (2010) 2495-2516.

- [21] M.S.A. Elsayed, D. Pasini, Analysis of the elastostatic specific stiffness of 2D stretching-dominated lattice materials, *Mechanics of Materials* 42(7) (2010) 709-725.
- [22] G. Dong, Y.F. Zhao, Numerical and experimental investigation of the joint stiffness in lattice structures fabricated by additive manufacturing, *International Journal of Mechanical Sciences* 148 (2018) 475-485.
- [23] M.H. Luxner, J. Stampfl, H.E. Pettermann, Finite element modeling concepts and linear analyses of 3D regular open cell structures, *Journal of Materials Science* 40(22) (2005) 5859-5866.
- [24] P. Aghdasi, I.D. Williams, B. Salazar, N. Panditi, H.K. Taylor, C.P. Ostertag, An Octet-Truss Engineered Concrete (OTEC) for lightweight structures, *Composite Structures* 207 (2019) 373-384.
- [25] Z. Wu, The development of Lightweight Cementitious Cellular Composites (LCCCs), Delft University of Technology, Delft, Netherland, 2021.
- [26] V. Nguyen-Van, P. Tran, C. Peng, L. Pham, G. Zhang, H. Nguyen-Xuan, Bioinspired cellular cementitious structures for prefabricated construction: Hybrid design & performance evaluations, *Automation in Construction* 119 (2020) 103324.
- [27] J. Song, L. Li, S. Kong, B. Yu, Y. Wan, Y. Zhou, J. Chen, S. Liu, R. Xiao, W. Zhou, Y. Lu, J. Zhang, B. Zhou, C. Li, W. Long, Lightweight and low thermal conducted face-centered-cubic cementitious lattice materials (FCLMs), *Composite Structures* 263 (2021) 113536.
- [28] L. Li, J. Chen, X. Tan, Y. Zhou, Y. Zhang, W. Zhou, R. Xiao, X. Li, Y. Lu, M. Su, Z. Ding, W. Long, J. Song, 3D face-centered-cubic cement-based hybrid composites reinforced by tension-resistant polymeric truss network, *Automation in Construction* 120 (2020) 103380.
- [29] L.J. Gibson, Biomechanics of cellular solids, *Journal of biomechanics* 38(3) (2005) 377-99.
- [30] T.M. Keaveny, E.F. Morgan, G.L. Niebur, O.C. Yeh, *Biomechanics of trabecular bone*, Annual review of biomedical engineering 3 (2001) 307-333.
- [31] N. Takano, H. Takizawa, P. Wen, K. Odaka, S. Matsunaga, S. Abe, Stochastic prediction of apparent compressive stiffness of selective laser sintered lattice structure with geometrical imperfection and uncertainty in material property, *International Journal of Mechanical Sciences* 134 (2017) 347-356.
- [32] T. Mukhopadhyay, S. Adhikari, Effective in-plane elastic moduli of quasi-random spatially irregular hexagonal lattices, *International Journal of Engineering Science* 119 (2017) 142-179.
- [33] H.J. Herrmann, A. Hansen, S. Roux, Fracture of disordered, elastic lattices in two dimensions, *Physical Review B* 39(1) (1989) 637-648.
- [34] N.E.R. Romijn, N.A. Fleck, The fracture toughness of planar lattices: Imperfection sensitivity, *Journal of the Mechanics and Physics of Solids* 55(12) (2007) 2538-2564.
- [35] M.S. Pham, C. Liu, I. Todd, J. Lertthanasarn, Damage-tolerant architected materials inspired by crystal microstructure, *Nature* 565(7739) (2019) 305-311.
- [36] V. Nguyen-Van, C. Wu, F. Vogel, G. Zhang, H. Nguyen-Xuan, P. Tran, Mechanical performance of fractal-like cementitious lightweight cellular structures: Numerical investigations, *Composite Structures* 269 (2021) 114050.
- [37] R.R. Madke, R. Chowdhury, Anti-impact behavior of auxetic sandwich structure with braided face sheets and 3D re-entrant cores, *Composite Structures* 236 (2020) 111838.
- [38] N.D. Duc, K. Seung-Eock, P.H. Cong, N.T. Anh, N.D. Khoa, Dynamic response and vibration of composite double curved shallow shells with negative Poisson's ratio in auxetic honeycombs core layer on elastic foundations subjected to blast and damping loads, *International Journal of Mechanical Sciences* 133 (2017) 504-512.
- [39] Y.-L. Chen, X.-T. Wang, L. Ma, Damping mechanisms of CFRP three-dimensional double-arrow-head auxetic metamaterials, *Polymer Testing* 81 (2020) 106189.
- [40] K.E. Evans, Auxetic polymers: a new range of materials. *Endeavour*, *Endeavour* 15(4) (1991) 170-174.
- [41] V.L. Coenen, K.L. Alderson, Mechanisms of failure in the static indentation resistance of auxetic carbon fibre laminates, *physica status solidi (b)* 248(1) (2011) 66-72.

- [42] D. Photiou, N. Prastiti, E. Sarris, G. Constantinides, On the conical indentation response of elastic auxetic materials: Effects of Poisson's ratio, contact friction and cone angle, *International Journal of Solids and Structures* 81 (2016) 33-42.
- [43] L.L. Hu, M.Z. Zhou, H. Deng, Dynamic indentation of auxetic and non-auxetic honeycombs under large deformation, *Composite Structures* 207 (2019) 323-330.
- [44] H.C. Cheng, F. Scarpa, T.H. Panzera, I. Farrow, H.-X. Peng, Shear Stiffness and Energy Absorption of Auxetic Open Cell Foams as Sandwich Cores, *physica status solidi (b)* 256(1) (2019) 1800411.
- [45] C. Qi, A. Remennikov, L.-Z. Pei, S. Yang, Z.-H. Yu, T.D. Ngo, Impact and close-in blast response of auxetic honeycomb-cored sandwich panels: Experimental tests and numerical simulations, *Composite Structures* 180 (2017) 161-178.
- [46] Y. Wang, W. Zhao, G. Zhou, Q. Gao, C. Wang, Suspension mechanical performance and vehicle ride comfort applying a novel jounce bumper based on negative Poisson's ratio structure, *Advances in Engineering Software* 122 (2018) 1-12.
- [47] J. Ju, J.D. Summers, Compliant hexagonal periodic lattice structures having both high shear strength and high shear strain, *Materials & Design* 32(2) (2011) 512-524.
- [48] K. Bertoldi, P.M. Reis, S. Willshaw, T. Mullin, Negative Poisson's ratio behavior induced by an elastic instability, *Adv Mater* 22(3) (2010) 361-6.
- [49] K. Bertoldi, M.C. Boyce, S. Deschanel, S.M. Prange, T. Mullin, Mechanics of deformation-triggered pattern transformations and superelastic behavior in periodic elastomeric structures, *Journal of the Mechanics and Physics of Solids* 56(8) (2008) 2642-2668.
- [50] J. Shen, S. Zhou, X. Huang, Y.M. Xie, Simple cubic three-dimensional auxetic metamaterials, *physica status solidi (b)* 251(8) (2014) 1515-1522.
- [51] T. Mukhopadhyay, S. Adhikari, Effective in-plane elastic properties of auxetic honeycombs with spatial irregularity, *Mechanics of Materials* 95 (2016) 204-222.
- [52] K.E. Evans, A. Alderson, Auxetic Materials: Functional Materials and Structures from Lateral Thinking, *Advanced Materials* (2000).
- [53] J.X. Qiao, C.Q. Chen, Impact resistance of uniform and functionally graded auxetic double arrowhead honeycombs, *International Journal of Impact Engineering* 83 (2015) 47-58.
- [54] L. Yang, O. Harrysson, H. West, D. Cormier, Mechanical properties of 3D re-entrant honeycomb auxetic structures realized via additive manufacturing, *International Journal of Solids and Structures* 69-70 (2015) 475-490.
- [55] W. Lee, Y. Jeong, J. Yoo, H. Huh, S.-J. Park, S.H. Park, J. Yoon, Effect of auxetic structures on crash behavior of cylindrical tube, *Composite Structures* 208 (2019) 836-846.
- [56] J.N. Grima, K.E. Evans, Auxetic behavior from rotating squares, *JOURNAL OF MATERIALS SCIENCE LETTERS* (2000).
- [57] J.N. Grima, K.E. Evans, Auxetic behavior from rotating triangles, *Journal of Materials Science* 41(10) (2006) 3193-3196.
- [58] J.N. Grima, V. Zammit, R. Gatt, A. Alderson, K.E. Evans, Auxetic behaviour from rotating semi-rigid units, *physica status solidi (b)* 244(3) (2007) 866-882.
- [59] T.-C. Lim, Analogies across auxetic models based on deformation mechanism, *physica status solidi (RRL) - Rapid Research Letters* 11(6) (2017) 1600440.
- [60] A. Spadoni, M. Ruzzene, Elasto-static micropolar behavior of a chiral auxetic lattice, *Journal of the Mechanics and Physics of Solids* 60(1) (2012) 156-171.
- [61] M.-H. Fu, B.-B. Zheng, W.-H. Li, A novel chiral three-dimensional material with negative Poisson's ratio and the equivalent elastic parameters, *Composite Structures* 176 (2017) 442-448.
- [62] M. Fu, F. Liu, L. Hu, A novel category of 3D chiral material with negative Poisson's ratio, *Composites Science and Technology* 160 (2018) 111-118.
- [63] N. Novak, L. Starčević, M. Vesenjāk, Z. Ren, Blast response study of the sandwich composite panels with 3D chiral auxetic core, *Composite Structures* 210 (2019) 167-178.
- [64] Y. Jiang, Y. Li, 3D Printed Chiral Cellular Solids with Amplified Auxetic Effects Due to Elevated Internal Rotation *Advanced Engineering Materials* 19(2) (2017) 1600609.

- [65] V. Sharma, M. Crne, J.O. Park, M. Srinivasarao, Bouligand Structures Underlie Circularly Polarized Iridescence of Scarab Beetles: A Closer View, *Materials Today: Proceedings* 1 (2014) 161-171.
- [66] A.P. Jr., Cholesteric Liquid Crystal-Like Structure of the Cuticle of *Plusiotis gloriosa*, *Science* 176(4035) (1972) 678-680.
- [67] E.A. Zimmermann, B. Gludovatz, E. Schaible, N.K. Dave, W. Yang, M.A. Meyers, R.O. Ritchie, Mechanical adaptability of the Bouligand-type structure in natural dermal armour, *Nat Commun* 4 (2013) 2634.
- [68] B. Natarajan, J.W. Gilman, Bioinspired Bouligand cellulose nanocrystal composites: a review of mechanical properties, *Philos Trans A Math Phys Eng Sci* 376(2112) (2018).
- [69] F. Barthelat, H. Tang, P. Zavattieri, C. Li, H. Espinosa, On the mechanics of mother-of-pearl: A key feature in the material hierarchical structure, *Journal of the Mechanics and Physics of Solids* 55(2) (2007) 306-337.
- [70] K.S. Katti, D.R. Katti, S.M. Pradhan, A. Bhosle, Platelet interlocks are the key to toughness and strength in nacre, *Journal of Materials Research* 20(5) (2011) 1097-1100.
- [71] D.G. Soltan, V.C. Li, Nacre-inspired composite design approaches for large-scale cementitious members and structures, *Cement and Concrete Composites* 88 (2018) 172-186.
- [72] D.G. Soltan, R. Ranade, V.C. Li, A Bio-inspired Cementitious Composite for High Energy Absorption in Infrastructural Applications, *Blucher Material Science Proceedings* 1 (2014).
- [73] J. Ye, C. Cui, J. Yu, K. Yu, J. Xiao, Fresh and anisotropic-mechanical properties of 3D printable ultra-high ductile concrete with crumb rubber, *Composites Part B: Engineering* 211 (2021) 108639.
- [74] J. Ye, K. Yu, J. Yu, Q. Zhang, L. Li, Designing ductile, tough, nacre-inspired concrete member in metric scale, *Cement and Concrete Composites* 118 (2021) 103987.
- [75] M. Taheri Andani, M.R. Karamooz-Ravari, R. Mirzaeifar, J. Ni, Micromechanics modeling of metallic alloys 3D printed by selective laser melting, *Materials & Design* 137 (2018) 204-213.
- [76] M. Xia, J. Sanjayan, Method of formulating geopolymers for 3D printing for construction applications, *Materials & Design* 110 (2016) 382-390.
- [77] J. Bauer, S. Hengsbach, I. Tesari, R. Schwaiger, O. Kraft, High-strength cellular ceramic composites with 3D microarchitecture, *Proceedings of the National Academy of Sciences* 111(7) (2014) 2453-2458.
- [78] M. Kaur, T.G. Yun, S.M. Han, E.L. Thomas, W.S. Kim, 3D printed stretching-dominated micro-trusses, *Materials & Design* 134 (2017) 272-280.
- [79] M. Kucewicz, P. Baranowski, J. Małachowski, A. Popławski, P. Płatek, Modelling, and characterization of 3D printed cellular structures, *Materials & Design* 142 (2018) 177-189.
- [80] J. Hollander, R. Hakala, J. Suominen, N. Moritz, J. Yliruusi, N. Sandler, 3D printed UV light cured polydimethylsiloxane devices for drug delivery, *International journal of pharmaceutics* 544(2) (2018) 433-442.
- [81] H. Xing, B. Zou, S. Li, X. Fu, Study on surface quality, precision and mechanical properties of 3D printed ZrO₂ ceramic components by laser scanning stereolithography, *Ceramics International* 43(18) (2017) 16340-16347.
- [82] R. He, W. Liu, Z. Wu, D. An, M. Huang, H. Wu, Q. Jiang, X. Ji, S. Wu, Z. Xie, Fabrication of complex-shaped zirconia ceramic parts via a DLP- stereolithography-based 3D printing method, *Ceramics International* 44(3) (2018) 3412-3416.
- [83] S. Pattnaik, D.B. Karunakar, P.K. Jha, Developments in investment casting process—A review, *Journal of Materials Processing Technology* 212(11) (2012) 2332-2348.
- [84] S.M. Sajadi, C.S. Tiwary, A.H. Rahmati, S.L. Eichmann, C.J. Thaeamlitz, D. Salpekar, A.B. Puthirath, P.J. Boul, M.M. Rahman, A. Meiyazhagan, P.M. Ajayan, Deformation resilient cement structures using 3D-printed molds, *iScience* 24(3) (2021) 102174.
- [85] D. Lowke, E. Dini, A. Perrot, D. Weger, C. Gehlen, B. Dillenburger, Particle-bed 3D printing in concrete construction – Possibilities and challenges, *Cement and Concrete Research* 112 (2018) 50-65.
- [86] G. Gibbons, 3D Printing of cement composites, *Advances in Applied Ceramics* 109(5) (2010).

- [87] P. Feng, X. Meng, J.-F. Chen, L. Ye, Mechanical properties of structures 3D printed with cementitious powders, *Construction and Building Materials* 93 (2015) 486-497.
- [88] J.G. Van Mier, *Fracture processes of concrete*, CRC press 1997.
- [89] J.G. Van Mier, *Concrete fracture: a multiscale approach*, CRC press 2012.
- [90] V.C. Li, *On engineered cementitious composites (ECC)*, (2003).
- [91] M. Luković, H. Dong, B. Šavija, E. Schlangen, G. Ye, K.v. Breugel, Tailoring strain-hardening cementitious composite repair systems through numerical experimentation, *Cement and Concrete Composites* 53 (2014) 200-213.
- [92] P. Stähli, R. Custer, J.G. Van Mier, On flow properties, fibre distribution, fibre orientation and flexural behaviour of FRC, *Materials and Structures* 41(1) (2008) 189-196.
- [93] P. Purnell, J. Beddows, Durability and simulated ageing of new matrix glass fibre reinforced concrete, *Cement and Concrete Composites* 27(9-10) (2005) 875-884.
- [94] H.R. Pakravan, M. Latifi, M. Jamshidi, Hybrid short fiber reinforcement system in concrete: A review, *Construction and Building Materials* 142 (2017) 280-294.
- [95] V. Mechtcherine, Novel cement-based composites for the strengthening and repair of concrete structures, *Construction and Building Materials* 41 (2013) 365-373.
- [96] T.T. Le, S.A. Austin, S. Lim, R.A. Buswell, A.G.F. Gibb, T. Thorpe, Mix design and fresh properties for high-performance printing concrete, *Materials and Structures* 45(8) (2012) 1221-1232.
- [97] T.T. Le, S.A. Austin, S. Lim, R.A. Buswell, R. Law, A.G.F. Gibb, T. Thorpe, Hardened properties of high-performance printing concrete, *Cement and Concrete Research* 42(3) (2012) 558-566.
- [98] D. Lowke, D. Talke, I. Dressler, D. Weger, C. Gehlen, C. Ostertag, R. Rael, Particle bed 3D printing by selective cement activation – Applications, material and process technology, *Cement and Concrete Research* 134 (2020) 106077.

3

FRACTURE BEHAVIOR OF CELLULAR MATERIALS: INSIGHTS FROM 3D PRINTED POLYMERIC LATTICES

Heterogeneity exists at different scales of cellular materials: constituent material scale, lattice element scale and lattice structure scale. In this chapter, the influence of heterogeneity is studied based on a method to model deformation and fracture behavior of 3D printed polymeric lattices under uniaxial tensile load. Polylactic acid (PLA), which is brittle under uniaxial tension, is used as constituent material to print lattice structures with two different levels of disorder. At the lattice element scale, the impact of the typical layered structure induced by fused deposition modeling (FDM) technique on the lattice element properties is significant. The horizontally and vertically printed elements obviously differ in strengths according to tensile tests performed on the printed lattice elements. Uniaxial tensile tests were also performed on the printed lattice structures to study their crack pattern and load-displacement curves. Afterwards, the measured element strengths and bulk material strength, respectively, were used as input to model the global behavior of the lattice structures. Comparative analysis between experiments and simulations are performed and indicate that, at the lattice structure scale, the disorder also has notable influence on the global mechanical behavior of the lattice cellular materials. These experimental and numerical results emphasize the importance of understanding the influence of the heterogeneity at different scales for the overall mechanical behavior of 3D printed cellular materials.

3.1 INTRODUCTION

Defects, imperfections or non-uniformities are abundant in natural [1, 2] and artificial lattice cellular materials [3]. These heterogeneities may significantly influence the mechanical performance of cellular materials. In order to provide first insights of the influence of heterogeneity, mechanical behaviors of lattice cellular materials constituted by quasi-brittle materials are experimentally and numerically studied in this chapter.

The finite element method (FEM) has been widely used to model the mechanical response of cellular materials as complex cellular geometry can be implemented easily in the numerical models. Among all of them, the Delft lattice model might be an optimal tool for studying lattice materials. Commonly, the Delft lattice model [4-7] is used for fracture simulation of continuums, but it is still rather suitable for printed lattice materials. On one hand, the Delft lattice model has a lattice system consisting of individual elements which gives the model a corresponding geometry to lattice materials. This makes it possible to provide detailed deformation and cracking information [4, 8, 9] for each single lattice element even in complex lattice geometries. On the other hand, the variation of element properties induced by processing methods, for example 3D printing, can also be possibly taken into consideration in the simulation by varying the input properties of each lattice element [8, 10, 11]. Therefore, the Delft lattice model is used in this chapter to study the 3D printed lattice material.

For simplicity, the constituent material used in this chapter was not cement-based. The reason is that 3D printing methods for cementitious materials are still under development, and the influence of the printing method on the results would thus be unavoidable. Instead, it was decided to use a commercially-available printing filament - polylactic acid (PLA) - which also has brittle cracking behavior. PLA was thus used to 3D print lattice specimens using a commercial 3D printer, as described below.

3.2 EXPERIMENTS AND MODELLINGS

3.2.1 Lattice generation

Domain discretization and lattice generation was based on the method described in [12]: Prismatic domain with dimension of 10 cells in length and width, 20 cells in height was generated (Figure 3-1). The length of each cell was set to be $A=3\text{mm}$. Nodes were randomly placed in sub-cells within these cells. In this study, randomness (R) is defined as:

$$R = \frac{s}{A} \quad (3-1)$$

where s is the length of the sub-cell and A is the length of the cell. The disorder in the lattice material was introduced by including pseudo random numbers generated by random seeds when calculating node coordinates. The coordinates of a node in a cell located in the l^{th} row in x axis, m^{th} row in y axis and n^{th} row in z axis were determined as:

$$\begin{cases} x_l = A * \left(\frac{(1-R)}{2} + R * r + l - 1 \right) \\ y_m = A * \left(\frac{(1-R)}{2} + R * r + m - 1 \right) \\ z_n = A * \left(\frac{(1-R)}{2} + R * r + n - 1 \right) \end{cases} \quad (3-2)$$

where A is the cell length, R is the randomness of the lattice system, r is the random number (from 0~1) which differs in every single calculation, l (integers from 1~10) is the cell row number in x axis, m (integers from 1~10) is the cell row number in y axis, n (integers from 1~20) is the cell row number in z axis. $R=0$ represents a regular lattice system and $R=1$ represents a completely disordered lattice system. Note that, If $R=0$, the Delaunay tessellation of the nodes (as described below) is not possible, and if $R=1$, two nodes may overlap on the cell boundary. Herein, two different values of the randomness parameter were considered to generate two lattice systems: 0.1 ($s = 0.3\text{mm}$) and 0.5 ($s = 1.5\text{mm}$), respectively.

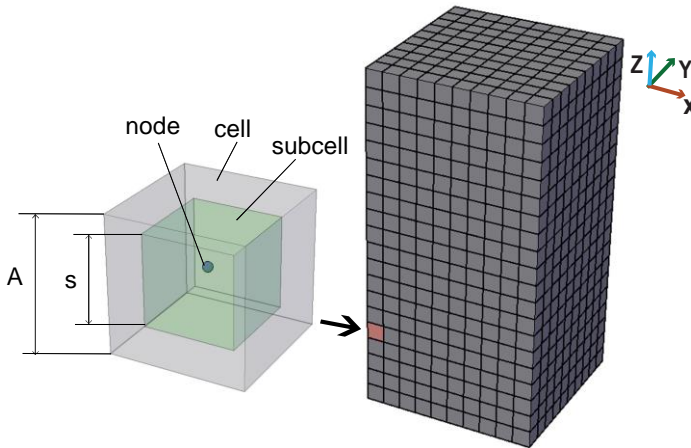


Figure 3-1 Discretization of prismatic domain

Node connectivity was determined by Delaunay tessellation (as suggested in [12]) and connected by circular beam elements with a radius of 0.375mm, forming irregular lattice systems. The nodes in the surface cells are aligned in a same plane to maintain the prismatic shape of the lattice networks. In the middle of the height direction, a notch is generated in each lattice by omitting the elements connecting nodes in the outermost two layers from the surface. Parameters of the two irregular lattice systems are given in Table 3-1.

Table 3-1 Parameters of generated lattice systems

No.	Randomness	Cells dimension (mm)	Printed lattice material size (mm)	Number of lattice elements	Element radius (mm)
L1	0.1	10 × 10 × 20	27 × 27 × 57	13103	0.375
L5	0.5	10 × 10 × 20	27 × 27 × 57	12895	0.375

3.2.2 Fabrication of polymeric lattices

In order to ensure the consistency between the printed polymeric lattices and the lattice systems in the model, the lattice systems generated in 3.2.1 were directly transformed to entities in AutoCAD and printed with PLA material using a commercial 3D printer Ultimaker 2+, which is based on FDM. Notice that the lattice elements in the model are only conceptually connected at the nodes, while for entities conceptual elements became actual cylindrical beams with a certain cross section area. When cylindrical beams connect, a sector forms in between (see Figure 3-2a). To avoid potential stress concentrations near the sector, a sphere with the same radius as the beam was generated at each node in the printed polymeric lattices (see Figure 3-2b).

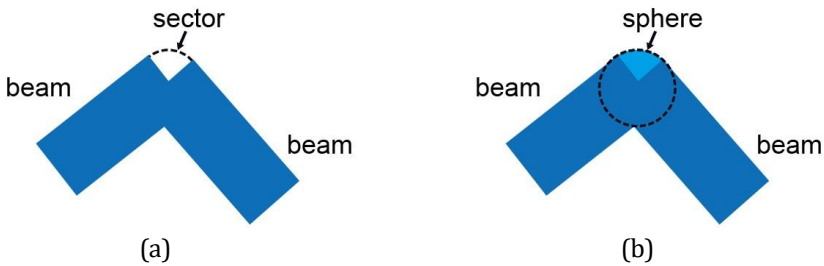


Figure 3-2 Connected beams with (a) a sector and (b) a generated sphere

Considering the principle of FDM, the polymeric lattices were printed such that the notch was positioned towards the top when printing to ensure good printing quality. Multiple lattice material samples were printed for each randomness. Printing parameters such as layer height, temperature and speed were kept constant for each print and are listed in Table 3-2. Entity models and printed lattice material samples are shown in Figure 3-3.

Table 3-2 Configurations of printing parameters

Printing parameters	Configurations
Layer height (mm)	0.15
Temperature (°C)	195
Filament diameter (mm)	2.85
Nozzle diameter (mm)	0.25
Printing speed (mm/s)	30
Travel speed (mm/s)	120

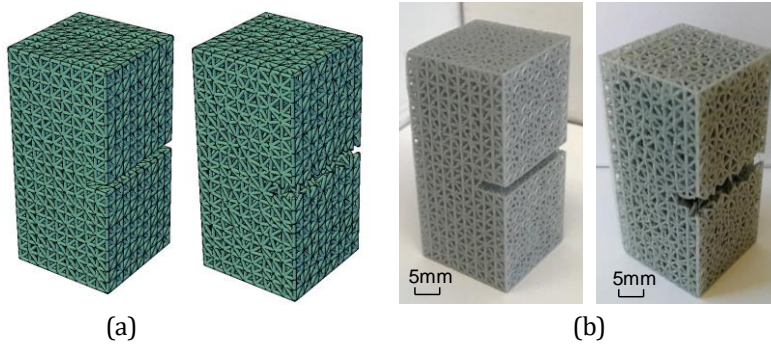


Figure 3-3. Comparison of (a) lattice systems with different randomness and (b) corresponding printed polymeric lattices

3.2.3 Determination of lattice element properties

It should be noted that elements in the printed polymeric lattices have different printing directions. Horizontally printed and vertically printed (Figure 3-4) elements may have different strength. As a simplification, in this study only two printing directions were assumed: if two nodes of an element located in cells which were in one plane parallel to the printing building plane (Figure 3-1 plane ZOY), the element was considered horizontally printed otherwise the element was considered vertically printed. So, cubic units (Figure 3-5) with the same length of the cells (3mm) were printed. These cubic units were designed to determine the mechanical properties of lattice beams in the two perpendicular printing directions: 4 horizontal beams and 4 vertical beams.

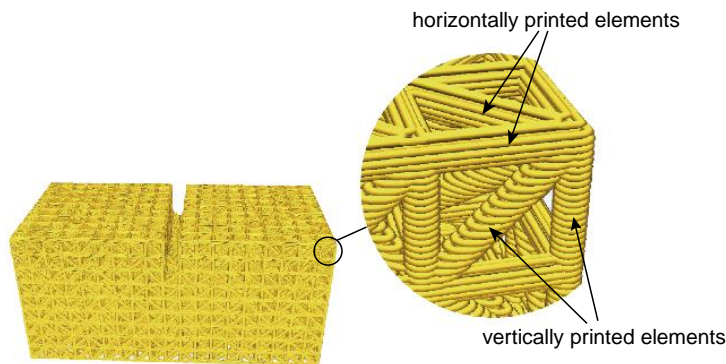


Figure 3-4 Elements of two printing directions, showing layers resulting from the FDM printing process

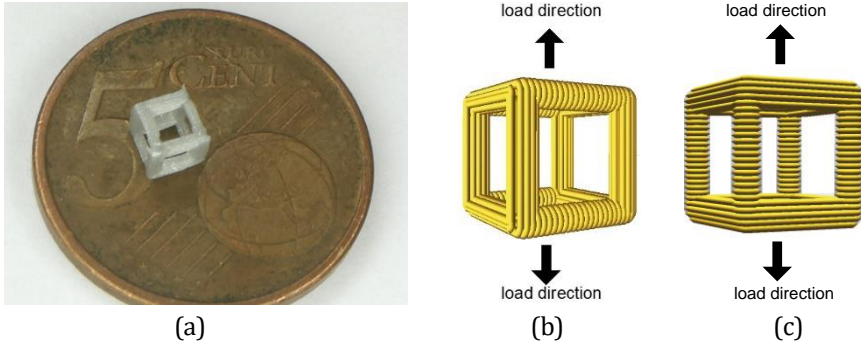


Figure 3-5 Printed cubic unit(a) and scheme of loading directions on unit cube for element property determination of (b)horizontally printed elements and (c)vertically printed elements

To obtain properties of lattice elements which were used as the input of the lattice model, printed cubic units were glued on small steel blocks (see Figure 3-6) with a mix of PLEX 7742 F and Pleximon. Uniaxial tensile tests were performed in two directions respectively with an elongating speed of 0.005mm/s using a Micro Tension-Compression Testing stage. For each printing direction, 10 tests were performed.

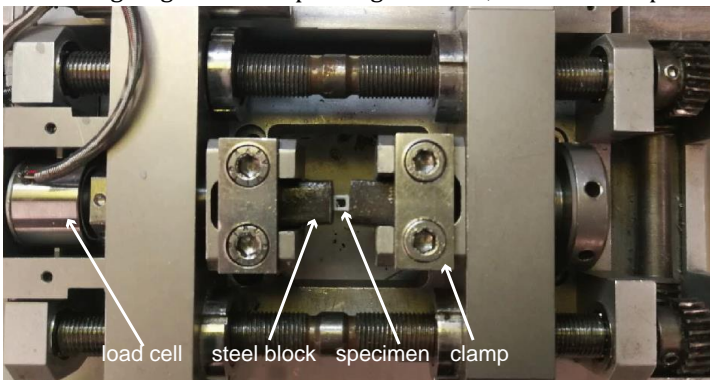


Figure 3-6 Experiment setup used for element strength determination

The strength of one beam in each cubic unit, i.e. the element strength was calculated from measurements by eq. (3-3).

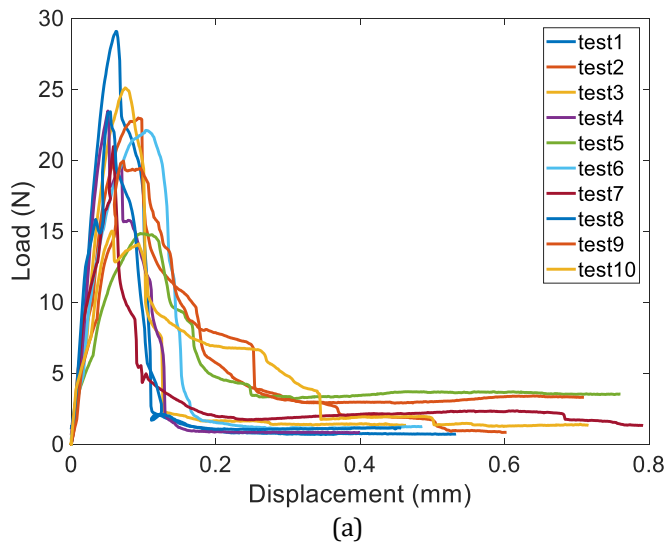
$$f_e = \frac{F}{4A} \quad (3-3)$$

where F is the measured peak load, A is the cross section of a printed small beam. Calculated element strength values of the two printing directions are listed in Table 3-3.

Table 3-3 Calculated element strength values of two printing directions (MPa)

No.	Horizontal	Vertical
Test 1	35.42	16.45
Test 2	40.71	13.00
Test 3	36.19	14.20
Test 4	38.44	13.28
Test 5	33.04	8.40
Test 6	34.53	12.51
Test 7	42.09	11.86
Test 8	40.08	13.25
Test 9	43.52	11.29
Test 10	33.98	8.50
Average	37.80	12.27
Standard deviation	3.67	2.45

From Table 3-3 and the load-displacement curves of the horizontally (Figure 3-7a) and vertically (Figure 3-7b) printed beams in the cubic units, a large difference in strength between beams in two printing directions can be observed. Vertically printed beams are much weaker than horizontally printed beams. Besides, although all beams exhibit softening behaviors after peak load, vertically printed beams are more brittle than horizontally printed beams because vertically printed beams contain layers and interfaces perpendicular to normal stress direction. Figure 3-8 shows the calculated work of fracture in the post peak branch for the two printing directions. Vertically printed beams need much less work to break than horizontally printed beams, which is another proof of higher brittleness of vertically printed beams.



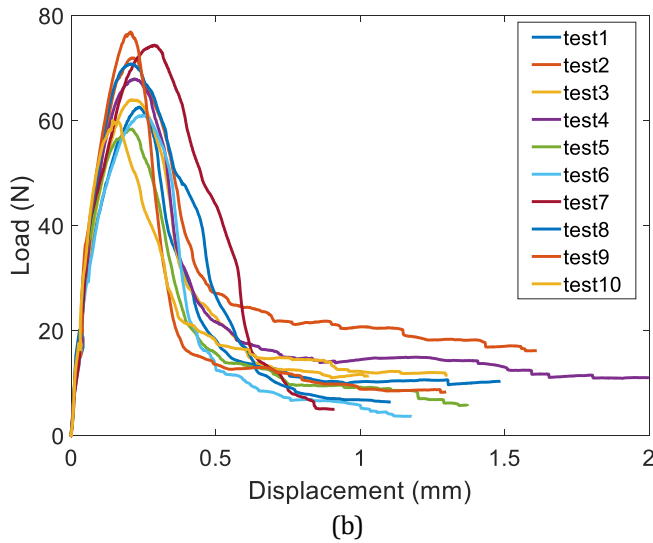


Figure 3-7 Load-displacement curves of (a) vertically printed and (b) horizontally printed elements. Note that the axes in the graphs are different and vertically printed elements are weaker than horizontally printed elements.

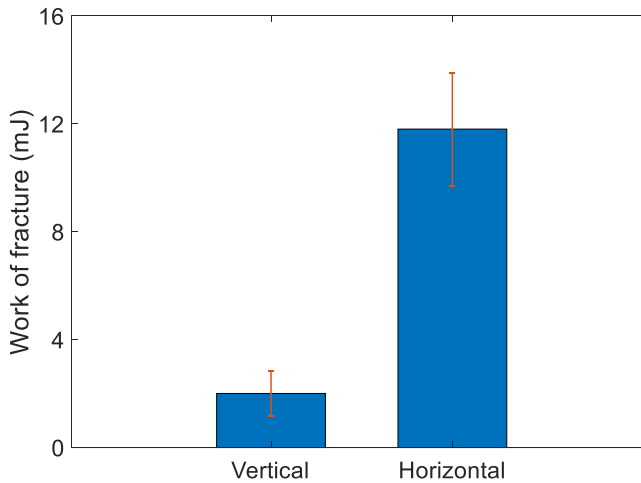
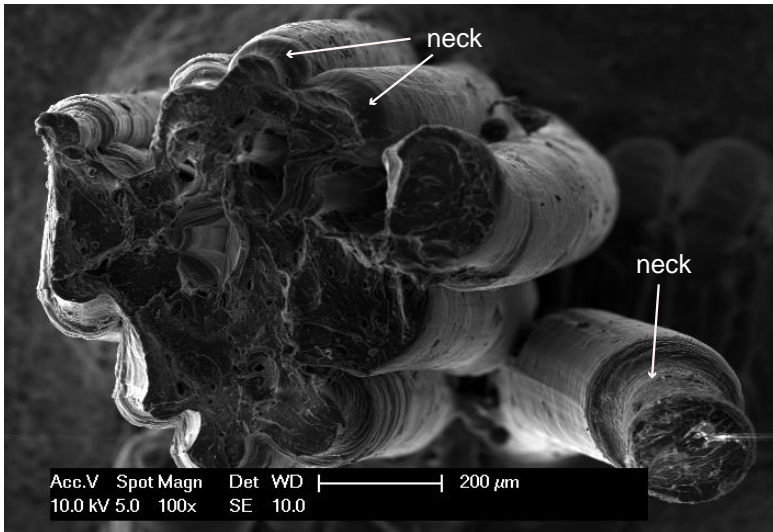


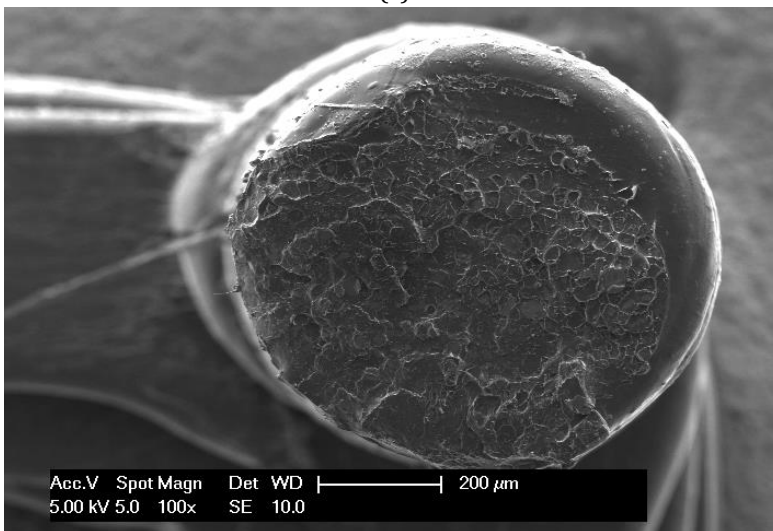
Figure 3-8 Work of fracture of elements in two printing directions (standard deviation is indicated)

Fractographs of fractured beams in the two printing directions were obtained by scanning electron microscope (SEM). Samples were coated with carbon to provide conductivity and avoid electrons accumulating on the surface. Subsequently, secondary electrons (SE) were used to obtain the images from the fractured surface of horizontally and vertically printed beams, as shown in Figure 3-9. A layered structure consisting of

individual filaments resulting from the horizontal printing process can be observed on horizontally printed beam in Figure 3-9a. Typical necking initiated fracture in polymers [13, 14], delaminated single filament and craze of ductile fracture [15] are also obvious. For a vertically printed beam, traces of brittle fracture can be found. A rough fracture surface is clear in Figure 3-9b, which is evidence of abrupt fracture under normal stress [16]. The difference of the fracture surfaces also indicates that beams printed in the two directions exhibit different mechanical properties under tensile load and horizontally printed beams are stronger and more ductile than vertically printed beams.



(a)



(b)

Figure 3-9 Fracture surface of (a)horizontally printed beam and (b)vertically printed beam

3.2.4 Uniaxial tensile tests on printed polymeric lattices

The printed polymeric lattices were glued on two parallel steel plates with a mix of PLEX 7742F and Pleximon. Two linear variable differential transformers (LVDTs) were fixed along both lateral sides for measuring displacement (Figure 3-10). Displacement controlled uniaxial tensile tests with an elongating speed of 0.003mm/s were conducted on the printed polymeric lattices by a servo hydraulic press (Instron 8872) and load displacement curves were obtained.

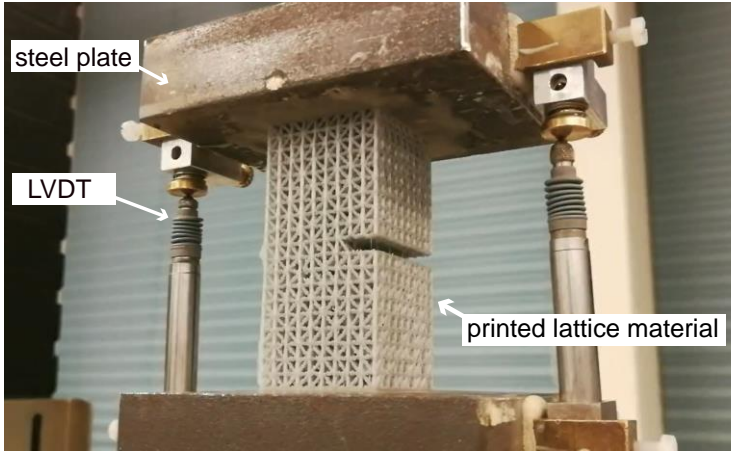


Figure 3-10 Uniaxial tensile test setup for printed polymeric lattices

3.2.5 Lattice fracture modeling

In order to simplify the simulation, linear elastic-perfectly brittle properties were assumed for the elements in the lattice model and the influence of this assumption on simulation results is discussed in detail in Section 3.3. Considering the small size of the printed cube units, it was not possible to accurately measure the displacements using an LVDT. As a result, the measured displacement was much higher than real values because the recorded data contained a considerable amount of displacement from the loading and transmission mechanisms, and not only from the tested specimen. Therefore, only the measured strength values were adopted directly as the model inputs. Elastic modulus was directly adopted from the material properties provided by the manufacturer for all elements ($E=2346.5$ MPa) and Poisson's ratio: $\nu=0.36$ was adopted as reported in [17, 18]. Shear modulus G was calculated by eq. (3-4). Normally eq. (3-4) is valid for isotropic material. According to previous studies[16, 19-24], indeed anisotropy should be considered when exceeding the elastic region (e.g. strength), while printing direction has limited influence on the isotropy of elastic properties (both shear and tensile) of printed polymer solid objects. So, shear modulus of printed PLA can be still regarded as isotropic thus eq. (3-4) is valid and adopted to calculate shear modulus of the printed elements.

$$G = \frac{E}{2(1 + \nu)} \quad (3-4)$$

For both printing directions, pseudo random numbers were used to assign the experimentally determined strength values (see Table 3-3) to elements with the same printing direction and simulation was executed three times for each lattice system (L1 and L5, respectively).

The computing process and post processing methods were similar as reported in [8]. A set of linear elastic analyses was performed under a uniform prescribed displacement boundary condition imposed on top of the lattice system while the bottom elements were clamped. Elements on the top and bottom layers were prohibited from failure in order to maintain the path of force transfer. Comparative stress of beam elements was calculated in each step according to eq. (3-5).

$$\sigma = \alpha_N * \frac{N}{A} + \alpha_M * \frac{\max(|M_i|, |M_j|)}{W} \quad (3-5)$$

where N is the normal force in the lattice element, A is the cross section of the lattice element, M_i and M_j are the bending moments in the nodes i and j . W is the section modulus, α_N is normal force influencing factor, α_M is bending influence factor, $\alpha_N=1$ and $\alpha_M=0.05$ are adopted herein.

The element with the highest stress/strength ratio was removed from the system. This constitutes one analysis step. The system was then relaxed, and the process was repeated until the entire lattice system failed. After the simulation finished, crack pattern was visualized based on the removed elements and load-displacement curve was extracted. Results are shown and analyzed in the next section.

3.3 RESULTS AND DISCUSSION

3.3.1 Load-displacement response

As a comparison for load-displacement response simulation, besides experimentally measured element strength, bulk material properties ($f_c=49.5\text{MPa}$ and $E=2346.5\text{MPa}$) provided by the manufacturer was also used and assigned to all elements. As can be seen in Figure 3-11, for (a) L1 and (b) L5, the influence of element strengths is rather obvious. When measured strengths were assigned to corresponding elements in the model, the predicted load-displacement curves (MS-Sim1, MS-Sim 2 and MS-Sim 3) including stiffness, strength, ductile part and long softening tails are in good accordance with test results (blue shadowed area). Comparatively, the simulated curve using bulk material strength (BS) deviates significantly from the test results. As the bulk materials strength is higher than the strengths of printed lattice elements (especially the strength of vertically printed elements), the simulated peak-load values are higher for both polymeric lattices which means that the element strength is a crucial influence factor in the simulation, and only when the input strength is properly assigned the simulation result would be accurate.

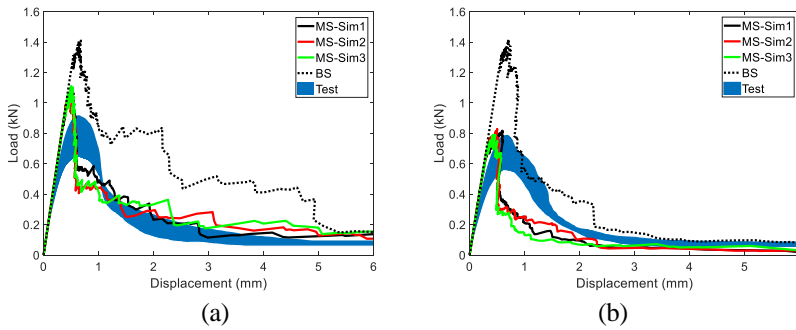


Figure 3-11 Simulated Load-displacement curves of (a) L1 and (b) L5 against experiment results

Normally, the anisotropy of 3D printed solid material mainly lies in strength and it is dominated by printing direction [22, 25, 26]. In lattice cellular materials, a unique feature exists. The lattice structure itself introduces extra anisotropy to the material. The influence of printing direction is overlapped with the orientation of local lattice elements. Because vertically and horizontally printed lattice elements are present in the lattice material simultaneously and their strengths are different (Table 3), directly using constant bulk property (i.e. PLA strength on the macroscale) will not result in correct input values for these elements. In this case, measured properties (i.e. PLA “strengths” on mesoscale in two printing directions) of local lattice elements in different printing directions must be used. The comparison of simulation results using constant bulk property (PLA strength on macroscale) and measured local element properties (PLA “strengths” on mesoscale) gives insight of the influence of printing process on the anisotropy of lattice cellular materials and it emphasizes that the anisotropy of 3D printed polymeric lattices comes from both the printing direction and the lattice element orientation.

Still, even when measured strengths were correctly assigned as model element inputs, some mismatch in the softening part can be observed from Figure 3-11 for both polymeric lattices. First, the elastic modulus of the material was taken as provided by the manufacturer, which is probably somewhat higher compared to the printed one. This resulted in a somewhat higher stiffness in the simulations compared to the experiments. Note, also, that in the simulations lattice beam elements are all considered to be perfectly brittle. In reality, the elements in the printed polymeric lattices exhibited softening after the peak load, depending on the printing direction (see Figure 3-7). The printed polymeric lattices have a less-brittle softening branch than the prediction due to the fact that, in the simulation, softening on the element level was not considered. Note that, in the model, ductility or softening behavior can be introduced by assigning a multi-linear property (as schematically shown in Figure 3-12) to the elements [27, 28]. In that case, the element loses its strength and stiffness gradually and is eventually removed from the lattice system through several analysis steps. Since the data relating to these properties could not be measured reliably in this study (see Section 3.2.3), this was not done herein.

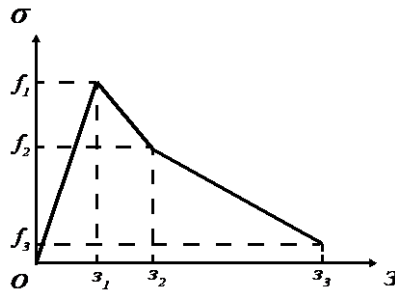


Figure 3-12 Multilinear properties of lattice element

The difference between the virtual lattice systems and actual lattice cellular materials also resulted in some mismatch in terms of strength. As described in Section 3.2.2, in the lattice model the nodes exist only conceptually and never fail, while in printed polymeric lattices, the nodes were actually generated as spheres and fractures in the spheres could be also observed in experiments. In cases when a sphere would fail first and the connected elements were unable to fail, the required external load to break the spheres was lower than breaking the connected beams and the peak load (Table 3-4) obtained from the experiment were lower than simulated value as a result. However, in the lattice model as used herein, this mechanism is not considered.

Table 3-4 Simulated strength and stiffness results against experiment data

Group	Randomness	Slope (kN/mm)	Peak load (kN)
Simulation	0.1	2.434 ± 0.007	1.093 ± 0.013
	0.5	2.293 ± 0.000	0.812 ± 0.020
Experiment	0.1	2.055 ± 0.351	0.765 ± 0.143
	0.5	1.568 ± 0.327	0.658 ± 0.112

The influence of randomness on the load-displacement response of the polymeric lattice was properly predicted by the simulation. Because more artificial disorder was introduced to the lattice system with randomness $R=0.5$ it exhibited lower stiffness and lower peak load than lattice system with $R=0.1$ and this trend can also be found in the experiment results (Table 3-4).

3.3.2 Influence of randomness on crack patterns

Figure 3-13 and Figure 3-14 show the simulated and experimentally obtained crack patterns of two lattice systems and printed polymeric lattices, respectively. The crack patterns predicted by the lattice model are in good accordance with the experimental results. In the simulated results, crack patterns before and after peak load are indicated in different colors. In L1 ($R=0.1$), a main crack plane traversed across the lattice system in the middle (Figure 3-13). Almost all failed elements localized in the main crack plane before and after the peak load, with only a few failed elements distributed outside of the main crack plane. In L5 ($R=0.5$), on the other hand, numerous

failed elements distributed in the non-notched side before the peak load, which means that L5 exhibit more ductility as more disorder was introduced. After the peak load, failed elements started to localize in the main crack plane in the middle. There are still many elements distributed outside of the main crack plane at the unnotched side and less brittleness of L5 can be expected during softening. Similarly, in the experimental results (see Figure 3-14), the crack plane is also mainly located within the elements in the middle of the sample in polymeric lattices with $R=0.1$ while concave and convex crack surface can be observed from fractured polymeric lattices with $R=0.5$.

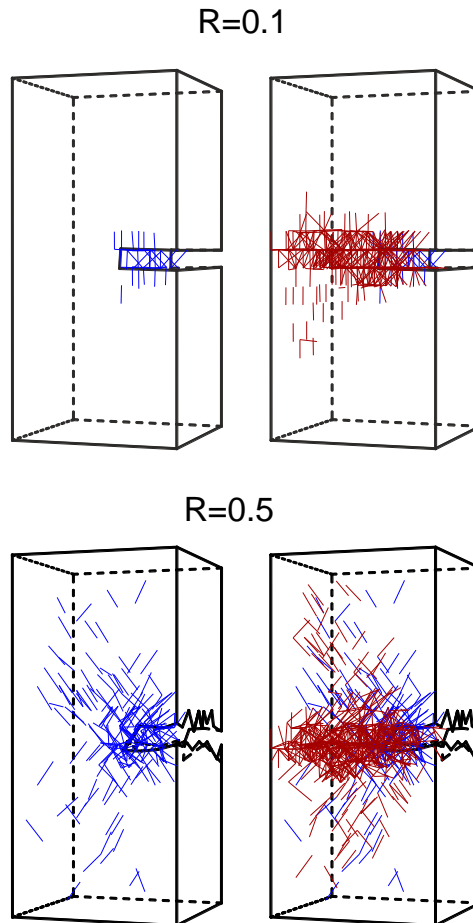


Figure 3-13 Simulated crack patterns before peak load (blue elements) and after peak load (red elements). Figures on the left show cracks at maximum load, while on the right they show cracks at failure.

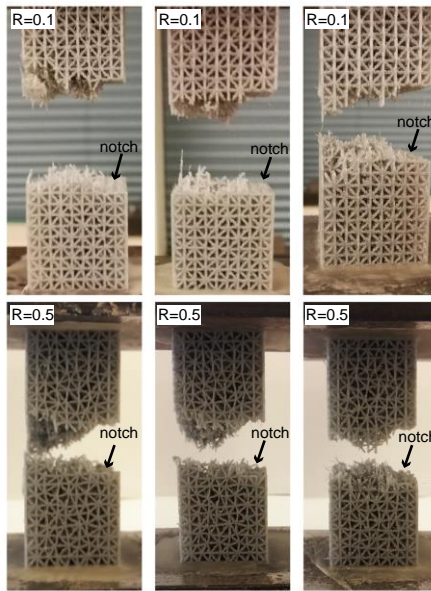


Figure 3-14 Fractured polymeric lattices, three tested specimens for each randomness are shown

The influence of randomness on the crack pattern can be explained by the fact that the strain non-uniformity appeared in the lattice system as heterogeneities were introduced and stress concentration appeared near the notch when external load was imposed. For L1, elements near the notch and further away from the notch are elastically similar owing to the relatively regular node distribution. When the external load was applied, a stress concentration appeared near the notch and the elements close to the notch had higher stress/strength ratio compared to other elements so that the crack initiated in these elements and propagated across the lattice material from the notch forming a main crack plane. Because the randomness was 0.1 and not 0, some disorder was present, and there are still a few failed elements outside of the main crack plane. For beam lattice systems, increasing randomness introduces more disorder into the system. Therefore, in L5 the stiffness differs in regions within the irregular lattice system. Note that the cross section of all beams is equal. In regions with closer node spacing a denser material is created, which results in a higher local stiffness. Elements in lower stiffness regions were forced to exhibit more strain and the stress in the elements were higher than other elements which made them easier to fail than other elements. As a result, a concave main crack plane and numerous failed elements outside of the main crack plane can be observed.

3.4 CONCLUSIONS

In this chapter, lattice structures with different randomness were 3D printed from PLA using FDM. A numerical lattice model with the same geometries was used to analyze their deformation and fracture behavior under uniaxial tensile load. By

comparing and analyzing the simulated and experimental results, some conclusions can be drawn:

- Heterogeneity exists both on the lattice structure scale (the lattice networks with different randomness) as well as the lattice element scale (different mechanical properties for different printing directions).
- At the lattice structure scale, according to experiments and simulations, lattice cellular materials with higher randomness exhibit less stiffness, lower strength and less brittleness since higher randomness introduces more scattered distribution of failed lattice elements.
- At the lattice element scale, according to the simulation results, simply adopting the bulk material strength does not allow obtaining accurate simulation results. Only when the heterogeneity induced by processing method (extrusion-based printing) was taken into consideration could the strength of the lattice cellular materials be properly simulated.
- As a result of the assumption of perfectly brittle lattice elements, a mismatch can be found in the post peak part of the global tensile response: the actual lattice cellular materials exhibit wider softening part than the simulations. This indicates that the properties of the constituent material itself must be investigated at an even lower scale to obtain more realistic tensile behavior, which is in fact not ideally brittle. This may be especially important for cementitious lattice materials because of the well-known quasi-brittle behavior of the cementitious constituent.

In the next chapter, further research will focus on the mechanical behavior of cementitious lattice cellular material. The study includes an investigation at the constituent material scale to provide more in-depth knowledge of the influence of heterogeneity on the mechanical behavior of cementitious lattices.

REFERENCES

- [1] L.J. Gibson, Biomechanics of cellular solids, *Journal of biomechanics* 38(3) (2005) 377-99.
- [2] T.M. Keaveny, E.F. Morgan, G.L. Niebur, O.C. Yeh, Biomechanics of trabecular bone, *Annual review of biomedical engineering* 3 (2001) 307-333.
- [3] N. Takano, H. Takizawa, P. Wen, K. Odaka, S. Matsunaga, S. Abe, Stochastic prediction of apparent compressive stiffness of selective laser sintered lattice structure with geometrical imperfection and uncertainty in material property, *International Journal of Mechanical Sciences* 134 (2017) 347-356.
- [4] E.Schlangen, J.G.M.v. Mier, Simple lattice model for numerical simulation of fracture of concrete materials and structures, *Materials and Structures* 25 (1992) 534-542.
- [5] E. Schlangen, Crack Development in Concrete, Part 2: Modelling of Fracture Process, *Key Engineering Materials* 385-387 (2008) 73-76.
- [6] E. Schlangen, Crack Development in Concrete, Part 1: Fracture Experiments and CT-Scan Observations, *Key Engineering Materials* 385-387 (2008) 69-72.
- [7] Z. Qian, E. Schlangen, G. Ye, K. van Breugel, 3D Lattice Fracture Model: Theory and Computer Implementation, *Key Engineering Materials* 452-453 (2010) 69-72.
- [8] Z. Qian, Multiscale Modeling of Fracture Processes in Cementitious Materials, *Civil Engineering and Geoscience*, TU Delft, Delft, 2012.
- [9] M. Nikolić, E. Karavelić, A. Ibrahimbegovic, P. Mišević, Lattice Element Models and Their Peculiarities, *Archives of Computational Methods in Engineering* (2017).
- [10] J.G.M.v. Mier, M.R.A.v. Vliet, T.K. Wang, Fracture mechanisms in particle composites statistical aspects in lattice type analysis, *Mechanics of Materials* 34 (2002) 705-724.
- [11] Z. Qian, G. Ye, E.Schlangen, K. van Breugel, 3D Lattice Fracture Model: Application to Cement Paste at Microscale, *Key Engineering Materials* 452-453 (2010) 65-68.
- [12] M. Yip, J. Mohle, J.E. Bolander, Automated Modeling of Three-Dimensional Structural Components Using Irregular Lattices, *Computer-Aided Civil and Infrastructure Engineering* 20 (2005) 393-407.
- [13] A.R. Torrado Perez, D.A. Roberson, R.B. Wicker, Fracture Surface Analysis of 3D-Printed Tensile Specimens of Novel ABS-Based Materials, *Journal of Failure Analysis and Prevention* 14(3) (2014) 343-353.
- [14] A.R. Torrado, C.M. Shemelya, J.D. English, Y. Lin, R.B. Wicker, D.A. Roberson, Characterizing the effect of additives to ABS on the mechanical property anisotropy of specimens fabricated by material extrusion 3D printing, *Additive Manufacturing* 6 (2015) 16-29.
- [15] E.S. Greenhalgh, Delamination-dominated failures in polymer composites, CRC press 2009.
- [16] Y. Song, Y. Li, W. Song, K. Yee, K.Y. Lee, V.L. Tagarielli, Measurements of the mechanical response of unidirectional 3D-printed PLA, *Materials & Design* 123 (2017) 154-164.
- [17] J. Torres, J. Cotelo, J. Karl, A.P. Gordon, Mechanical Property Optimization of FDM PLA in Shear with Multiple Objectives, *Jom* 67(5) (2015) 1183-1193.
- [18] G.W. Melenka, D. Euijin Pei, J.S. Schofield, M.R. Dawson, J.P. Carey, Evaluation of dimensional accuracy and material properties of the MakerBot 3D desktop printer, *Rapid Prototyping Journal* 21(5) (2015) 618-627.
- [19] J.M. Chacón, M.A. Caminero, E. García-Plaza, P.J. Núñez, Additive manufacturing of PLA structures using fused deposition modelling: Effect of process parameters on mechanical properties and their optimal selection, *Materials & Design* 124 (2017) 143-157.
- [20] M. Domingo-Espin, J.M. Puigoriol-Forcada, A.-A. Garcia-Granada, J. Llumà, S. Borros, G. Reyes, Mechanical property characterization and simulation of fused deposition modeling Polycarbonate parts, *Materials & Design* 83 (2015) 670-677.
- [21] S. Bhandari, R. Lopez-Anido, Finite element analysis of thermoplastic polymer extrusion 3D printed material for mechanical property prediction, *Additive Manufacturing* 22 (2018) 187-196.
- [22] R. Zou, Y. Xia, S. Liu, P. Hu, W. Hou, Q. Hu, C. Shan, Isotropic and anisotropic elasticity and yielding of 3D printed material, *Composites Part B: Engineering* 99 (2016) 506-513.

- [23] W.C. Smith, R.W. Dean, Structural characteristics of fused deposition modeling polycarbonate material, *Polymer Testing* 32(8) (2013) 1306-1312.
- [24] O.S. Es-Said, J. Foyos, R. Noorani, M. Mendelson, R. Marloth, B.A. Pregger, Effect of Layer Orientation on Mechanical Properties of Rapid Prototyped Samples, *Materials and Manufacturing Processes* 15(1) (2000) 107-122.
- [25] A. Lanzotti, D. Eujin Pei, M. Grasso, G. Staiano, M. Martorelli, The impact of process parameters on mechanical properties of parts fabricated in PLA with an open-source 3-D printer, *Rapid Prototyping Journal* 21(5) (2015) 604-617.
- [26] A.R. Torrado, D.A. Roberson, Failure Analysis and Anisotropy Evaluation of 3D-Printed Tensile Test Specimens of Different Geometries and Print Raster Patterns, *Journal of Failure Analysis and Prevention* 16(1) (2016) 154-164.
- [27] B.L. Karihaloo, P.F. Shao, Q.Z. Xiao, Lattice modelling of the failure of particle composites, *Engineering Fracture Mechanics* 70(17) (2003) 2385-2406.
- [28] D. Liu, B. Šavija, G.E. Smith, P.E.J. Flewitt, T. Lowe, E. Schlangen, Towards understanding the influence of porosity on mechanical and fracture behaviour of quasi-brittle materials: experiments and modelling, *International Journal of Fracture* 205(1) (2017) 57-72.

4

FRACTURE BEHAVIOR OF CEMENTITIOUS TRIANGULAR LATTICES

As clarified in the previous chapter, the fracture behavior of lattice cellular materials is influenced by the heterogeneity introduced on different scales. In order to understand the fracture behavior of cementitious cellular materials, in this chapter, multi-scale-based experimental tests were performed. Afterwards, simulations were carried out to help interpreting the experiments. With the aid of 3D printing technology, macroscopic cementitious lattice specimens are prepared and experimentally tested. On the microscale, the quasi-brittle fracture behavior of the cementitious lattice struts is numerically simulated using a microstructure-informed model. On the macroscale, using the obtained results, fracture behaviors of cementitious lattices with different triangular lattice structures are also simulated. By a comparative study between experimental and numerical simulation results, the critical influence of the heterogeneity on the mechanical properties of cementitious lattices is clarified.

4.1 INTRODUCTION

In order to investigate the fracture behavior of the cementitious lattices, as the constituent material, the mechanical properties of cementitious materials need to be elaborated first. Mechanical properties of the cementitious materials are known to be dependent on the heterogeneity. On the microscale, multiple phases exist such as hydrates, anhydrous particles, pores, and air voids. Due to the difference in chemical and physical properties of these phases, cementitious materials show quasi-brittle fracture behavior. According to previous studies [1-4], a microstructure-informed Delft lattice model is able to accurately simulate the fracture behavior of cementitious materials. Therefore, in this chapter, this lattice model is adopted to study the stress-strain response of the cementitious struts. In addition, based on the findings from the previous chapter, the Delft lattice model precisely simulated the fracture behavior of the lattice material. Therefore, this model is also used to study the fracture behavior of macroscopic cementitious lattices with a regular and a randomized triangular structure. Then, specifically, the influence of heterogeneity of the cementitious lattices on the constituent material scale as well as on the lattice structure scale is studied in this chapter.

4.2 METHODS AND MATERIALS

4.2.1 Multiscale approach

In order to provide in-depth knowledge of the fracture behavior of cementitious lattices, a combined experimental and numerical multiscale approach [2] (from microscale to macroscale) based on the Delft lattice model is adopted (see Figure 4-1).

On the microscale, the heterogeneity introduced by the multiple phases present in hardened cement paste, which influence the mechanical response of the hardened cementitious paste, is investigated. A micro-structure informed numerical model is used to simulate the tensile stress-strain response of the cementitious struts that form the macroscale cementitious lattices.

On the mesoscale, the simulated tensile strength of cementitious struts is experimentally validated. Dog bone shape specimens are used to determine the tensile strength of the cementitious struts by the Micro Tension-Compression Testing stage (Figure 4-2). The middle part of the dog bone shape specimens is designed to have the same dimension as a single lattice strut used in the microscale simulation. It is worth mentioning that precisely measuring the strain on this scale of a specimen loaded in tension is extremely difficult, so the experimental validation of the simulated E-modulus is not possible under this condition. Alternatively, the simulated E-modulus is validated through comparing with values reported in the literature for hardened cement pastes with the same w/c (water-to-cement ratio) and curing age. In addition, as strain is not precisely measured, the simulated post peak behavior of individual cementitious struts can also not be validated on the mesoscale. However, the

experimentally measured macroscale fracture behavior of the cementitious lattices may validate the simulated post peak behavior of the cementitious struts.

On the macroscale, as indicated by the previous chapter, the role of heterogeneity is investigated by adopting different lattice structures and the tensile response of the cementitious lattice is specifically studied. Triangular cementitious lattices with two different levels of disorder (i.e. different randomness) are generated, prepared, and then tested under uniaxial tension. Schematics of generating two designed cementitious lattices is shown in Figure 4-3. Layer-wisely staggered prismatic grids are used to discretize the two-dimensional domain. The vertices of each grid are aligned on the midpoint of the edge on the previous and the next layer of grids. The length (l) of each grid is 6.0 mm and the height (h) of each grid equals to $\frac{\sqrt{3}}{2} * l$. Then, a sub-cell is generated in each grid. The length ($R*l$) and height ($R*h$) of the sub-cell is proportional to the grid. The length ratio R of the sub-cell to the grid is defined as the randomness of the cementitious lattices. A node is placed in each sub-cell and the struts are generated by connecting nodes in adjacent cells forming a triangular lattice network.

Prior to preparing the specimens, several pre-conditions must be clarified. Restricted by inevitable features of cementitious material (to be specific, the shrinkage induced by cement hydration or drying and low tensile/bending strength) dimensions of the real specimen are limited. For a uniaxial tension test set-up, on one hand the characteristic height of the specimen should be much larger compared to the notch length, while, on the other hand making a large plate may result in considerable warping of specimens due to the shrinkage. In addition, the thickness of the plate also needs to be small in order to use a plane stress discrete numerical model based on beam theory. Meanwhile, due to the low tensile strength of cementitious materials, the lattice specimen needs to be thick enough in order to remain intact after casting. Considering these restrictions, the dimensions of the cementitious lattices are designed as follows (see Figure 4-3): The struts of the formed lattice networks are rectangular section beams with a dimension of 1 mm × 5 mm (height × depth). The total length and height of the cementitious lattices are 115 mm × 53 mm, respectively. A notch is made by removing 3 × 2 (x axis × y axis) layers of grids on one side of the lattices. Two types of lattices are designed, regular (R0) and randomized (R5). For $R=0$, namely the length and height ratio of the sub-cell to the grid equals to 0 and the node is placed at the very center of the sub-cell and the generated lattice network (denoted as R0) is constituted by equilateral triangles; for $R=5$, the node is placed at a random location within the sub-cell and the generated lattice network (denoted as R5) is constituted by stochastic triangles. The numerical lattice models which have an identical structure to the cementitious lattices are used to simulate the macroscopic fracture behavior. The stress-strain curves obtained from the microscale simulations are used as input parameters for the cementitious struts in the numerical macroscopic lattice structures (R0 and R5).

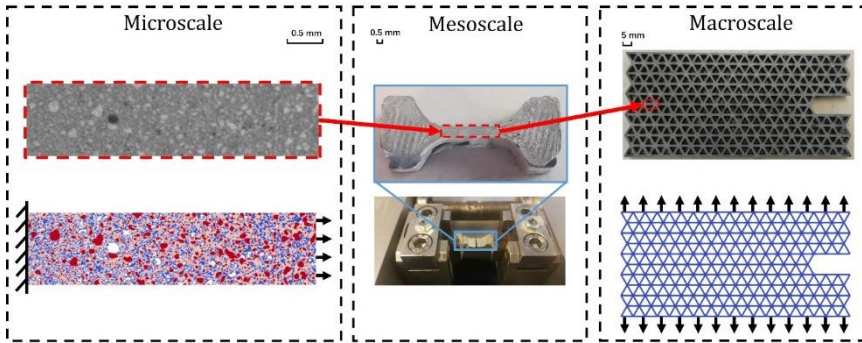


Figure 4-1 Schematics of the multiscale approach for studying fracture behavior of cementitious lattices

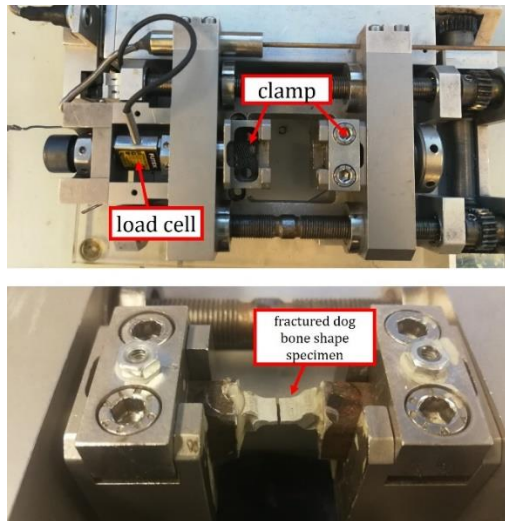


Figure 4-2 Micro Tension-Compression Testing stage

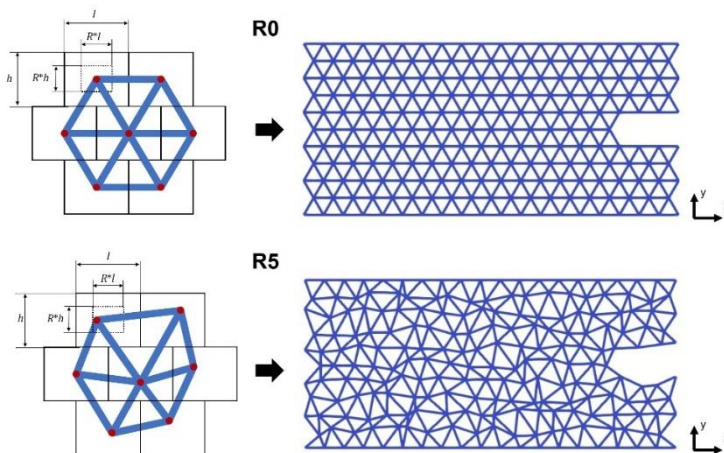


Figure 4-3 Schematics of generating macroscale cementitious lattice

4.2.2 Specimen preparation

Two series of specimens were prepared: cementitious lattice specimens with two different lattice structures for studying the global fracture behavior; and dog bone shape specimens to obtain tensile strength of the cementitious struts on the mesoscale and the micro-structure of the hardened cement paste by CT scan.

The specimen preparation procedure was as follows, see Figure 4-4:

- A commercial 3D printer (Ultimaker 2+) was used to print the geometries of the specimens using acrylonitrile butadiene styrene (ABS) as the printing material.
- The printed structures were glued in a cardboard box. A two-component silicone rubber (Poly-Sil PS 8510) (1:1 by weight) was then vacuum impregnated into the cardboard box (vacuum was kept for 1 minute to remove air bubbles). The silicone rubber was left to harden for 2 hours at room temperature.
- The hardened silicone rubber was detached from the printed ABS structure, resulting in a mold for creating specimens. These silicone rubber molds are easy to demold and durable enough for reuse.
- Cement pastes with 0.3 w/c (CEM I 42.5 N) were used for casting all specimens. The mix proportion is listed in Table 4-1. During the mixing process, a Hobart machine was used. All gradients (cement, water and superplasticizer) were weighted and added to the mixing bowl then mixed for 4 minutes. Afterwards, the freshly mixed cement paste was casted into the prepared molds.
- After 2 days, the specimens were demolded and then cured in water until the age of 14 days.

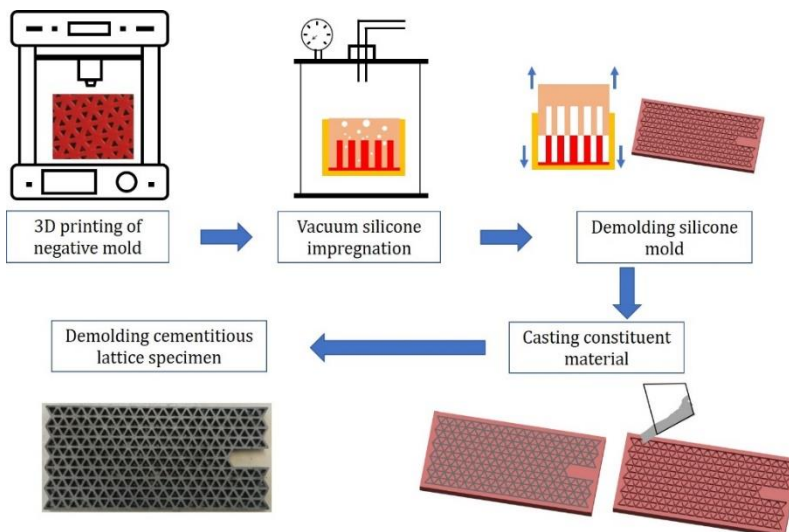


Figure 4-4 Specimen preparation procedures

Table 4-1 Mix proportion of cement paste (g/L)

CEMI 42.5 N	Water	w/c	Superplasticizer (Glenium 51)
1616.0	484.8	0.30	2.4

4.2.3 Mechanical tests

One hour before testing, the cementitious lattice specimens were surface dried by wiping off water on the specimen surface, painted with white acrylic paint and then sprayed with red dots on the surface in order to perform a digital image correlation (DIC) analysis. Uniaxial tensile tests on the cementitious lattices were performed by a hydraulic press INSTRON 8872 by a displacement-controlled loading method. The displacement is measured and controlled by the linear variable differential transducers (LVDTs) at a loading rate of $0.010 \mu\text{m/s}$. Considering that the cementitious lattice might be much more brittle than normal cementitious materials, an extremely low loading rate is used here to ensure post-peak behavior of the cement lattice can be captured. Uniaxial tensile tests on the dog bone shape specimens were performed using the Micro Tension-Compression testing stage (shown in Figure 4-2) by a displacement-controlled loading rate of $0.10 \mu\text{m/s}$ to obtain the tensile strength of the cement paste on the lattice strut scale. The loading rate of the dog bone shape specimens is faster than the cement lattices, but still within the quasi-static regime. Then it is assumed that the influence of the loading rate is negligible.

4.3 NUMERICAL SIMULATIONS

A lattice model (introduced in the previous chapter) was used to perform numerical simulations based on the multiscale simulation framework proposed in [2]. The simulations were performed on two different scales: the microscale and the macroscale. As two-dimensional triangular lattice patterns were used to make the cementitious lattice, on both investigated scales, the simulations were also performed using two-dimensional lattice model.

4.3.1 Microstructure segmentation

On the microscale, for a given type of cementitious material, the micro-structure is a determinative factor for the mechanical properties. It has been shown by recent studies [5, 6] that including the micro-structure of cementitious materials in the simulations results in realistic simulated stress-strain response of hardened cementitious materials. In this chapter, X-ray computational tomography (xCT) was used to obtain the microstructure of hardened cement paste. Grey scale value (GSV) images were obtained from the CT scan at a resolution of $5 \mu\text{m}$ per voxel. Four phases were segmented according to the GSV by the method proposed in [4, 7, 8]: pores (P), high-density hydrates (H), low-density hydrates (L) and anhydrous cement particles (A). The pore phase was first segmented by a threshold (T_1) using the inflection point

of the cumulative distribution curve (Figure 4-5). Afterwards, anhydrites were segmented using a threshold (T_3) where a sudden change in the slope of the pixel count curve occurs (Figure 4-5). After T_3 was determined, the degree of hydration (α) was calculated and an average of 0.61 was obtained. The degree of hydration can be calculated by [5]:

$$\alpha = \frac{V_{HP}}{\delta_V V_{AH} + V_{HP}} \quad (4-1)$$

where, V_{HP} is the volume of hydrates; δ_V is a constant determined by cement composites which is typically 2.2; V_{AH} is the volume of anhydrites.

At last, the volumetric ratio of low-density hydrates (V_L) to high-density hydrates (V_H) was determined. According to the results reported in [9], the ratio of V_L to V_H is directly related to the degree of hydration. For cement paste with a $w/c=0.3$, the volumetric ratio V_L/V_H is within a relatively narrow range between 0.65 and 0.81, as long as the degree of hydration α exceeds 0.4[9]. Then, 0.75 is assumed as the overall V_L/V_H value within all tested images thus a fixed T_2 was obtained. In total, four phases were segmented, details are given in Section 4.4.

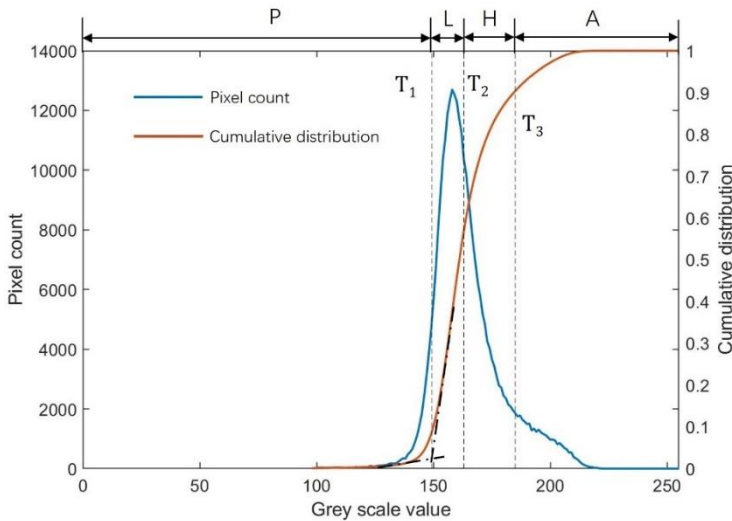


Figure 4-5 Phase segmentation based on grey scale value histogram

4.3.2 Lattice network generation

On the microscale, lattice networks were generated based on the segmented GSV images from CT scans. for numerical simulations. A domain covering 200×800 pixels on the GSV picture was first generated. A node was placed in the center of each pixel (except the pore phase) and lattice elements were generated by connecting adjacent nodes forming a triangular lattice network. The heterogeneity of the hardened cement paste was introduced to the generated lattice network by mapping local mechanical properties of these segmented phases according to their GSV value. Therefore, in total of six types of elements were generated. Elements with both nodes locating in the pixels of the same phase were assigned with mechanical properties of the corresponding

phase. Elements with nodes located in the pixels of two different phases were identified as interface elements between the two phases and they were assigned with arithmetic averaged mechanical properties of the two corresponding phases. On the macroscale, the lattice networks were consistent with the lattice structure of the experimental specimens (R0 and R5, respectively).

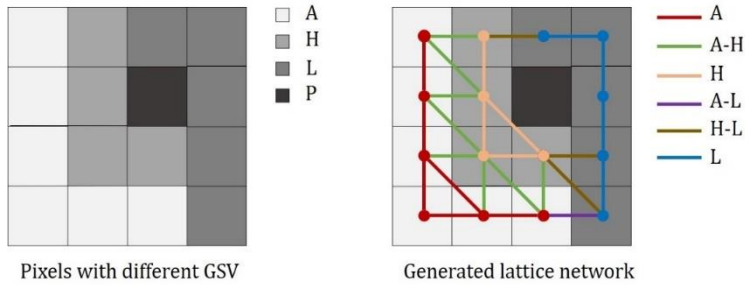


Figure 4-6 Schematics of generating lattice network based on the phases segmented from GSV picture, anhydrous cement particles (A), high-density hydrates (H), low-density hydrates (L), pores (P) and their interface phases are indicated.

4.3.3 Lattice fracture modeling

After the lattice network was generated, mechanical properties of each segmented phase were assigned to the corresponding phase. Then a set of linear elastic analyses was performed under a uniform prescribed displacement imposed on the right-side boundary of the generated lattice system while the left-side boundary was clamped (Figure 4-1 left). Elements on the boundary layers were prohibited from failure in order to maintain the path of force transferring. Comparative stress of beam elements was calculated in each step according to eq. (3-5) (Chapter 3). For microscale simulations, $\alpha_N=1$ and $\alpha_M=0.5$ was assumed. On this scale, as each element represents a relatively small region of material ($5\mu\text{m}$), it was not possible to experimentally detect the softening behavior of the phases in hardened cement paste. In most studies, the mechanical behavior of these phases on this scale is regarded as linear-elastic perfectly brittle, namely the stress linearly increases with strain before tensile strength meanwhile no softening branch after fracture. Similarly, for the microscale simulations, ideally-brittle behavior is assumed for the segmented phases in this chapter. Mechanical properties of the segmented phases are listed in Table 4-2. The E-modulus and tensile strength of the low-density hydrates (L), high-density hydrates (H) and anhydrates (A) were adopted according to the curing time, referring to literatures [4, 10] in which the mechanical properties of these phases were tested on a scale similar to this study. The simulation algorithm is identical as the procedures introduced in Chapter 3. In each step, the element with the highest comparative stress-to-strength ratio was removed from the lattice system and a scaling factor was obtained which is the inverse of this ratio. Then displacement of the lattice system is obtained by this scaling factor.

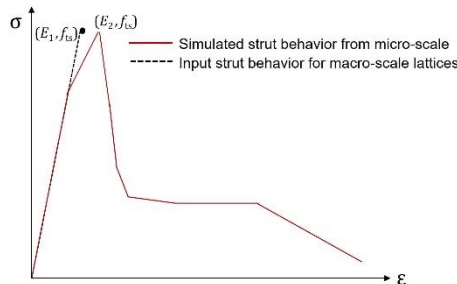
Table 4-2 Input parameters of the segmented phase on the microscale, partially from [4, 10]

Phases	E (GPa)	G (GPa)	f_t (MPa)	f_c (MPa)
L	21.6	9.0	55.0	$-f_t * 8$
L-H	26.4	11.0	65.0	$-f_t * 8$
H	31.2	13.0	75.0	$-f_t * 8$
L-A	58.4	24.3	35.3	$-f_t * 8$
H-A	63.2	26.3	36.3	$-f_t * 8$
A	95.2	39.6	650.0	$-f_t * 8$

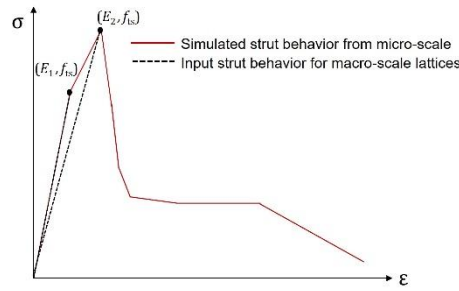
The results from microscale simulations were used as input for the struts of the macroscale cementitious lattices. As shown in Chapter 3, on the macroscale, without considering local hardening and softening behavior the simulated fracture resistance of the polymeric lattice was obviously lower than experimental results. A similar trend would also be expected in the fracture behavior of cementitious lattices. Therefore, based on the stress-strain response of the struts, three types of constitutive behaviors were used to simulate the fracture process of the cementitious lattices as shown in Figure 4-7:

- Single linear (SL) behavior, which corresponds to an ideally-brittle response, namely only the elastic branch is used: E-modulus corresponds to the elastic branch and strength equals to the tensile strength.
- Bi-linear (BL) behavior, in which two linear pre-peak segments were used (Figure 4-7b).
- Multi-linear behavior (ML), in which five linear segments were used: the elastic branch; the peak stress; and 70%, 40% and 20% of the peak stress in the post-peak regime (Figure 4-7c).

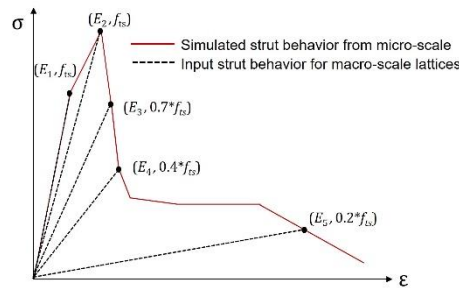
For macroscale simulations, $\alpha_N=1$ and $\alpha_M=0.05$ was assumed. A strut with SL behavior is immediately removed from the lattice system when peak stress is reached, while struts with BL and SL behavior lose their strength and stiffness gradually (in steps) until eventually being removed from the lattice system through several analysis steps.



(a)



(b)



(c)

Figure 4-7 Schematics of stress-strain curve obtained from microscale simulation and corresponding strut behavior input for macroscale cementitious lattice, a) single linear, b) bi-linear and c) multi-linear behavior

4.4 DISCUSSION

4.4.1 Mechanical properties of cementitious struts

Quasi-brittle tensile behavior is commonly seen in hardened cement paste, i.e. a softening branch can be observed. As described in Section 4.3.3, to model the fracture behavior of the macroscopic cementitious lattices, a proper stress-strain response of the cementitious struts is needed. Nevertheless, it was not possible to experimentally determine the entire stress-strain response (especially the softening branch) of the cementitious struts due to the limitations of the experimental setup. Therefore, it was necessary to numerically simulate the stress-strain response of the cementitious struts on a lower scale. On the microscale, hardened cement paste is typically seen as mechanically heterogenous due to the complex chemical composition of different phases and their spatial distribution. In this sense, it is important to properly segment the microstructure of hardened cement paste. Using the GSV based method, different phases were segmented. For the studied cases, in total 20 GSV images were used, and a volumetric ratio of the segmented phases in these specimens is shown in Figure 4-8. On average, the degree of hydration of these specimens is 0.61 ± 0.04 and the ratio of the low-density hydrates to high-density hydrates V_L/V_H is 0.75 ± 0.16 . These values are

consistent with the results in the literature [5, 9, 11, 12]. Comparison of a GSV picture and the segmented phases is shown in Figure 4-1.

Spatial resolution is a determinative factor of the segmentation accuracy. In general, a more accurate phase segmentation would be obtained under a higher resolution consequently the simulated mechanical properties would also be more precise. As described previously, $5\mu\text{m}$ is used as the resolution of the GSV images in this chapter, therefore, pores below $5\mu\text{m}$ are undetectable. The measured mechanical properties of other phases would also be higher as they contain less pores. Meanwhile, the segmented porosity should be higher as well. Therefore, using the experimentally measured values of the mechanical properties at the similar resolution is a tradeoff of the resolution limit while performing segmentation.

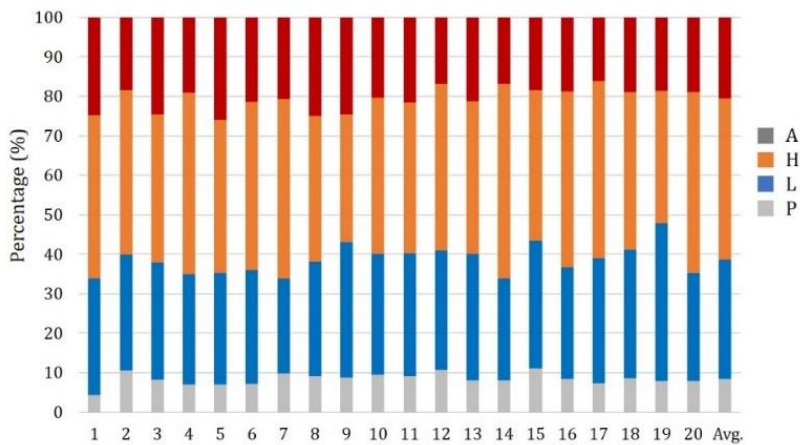


Figure 4-8 Volumetric ratio of four segmented phase in all obtained GSV images, horizontal axis indicates image number.

A typical simulated stress-strain response of a lattice strut is shown in Figure 4-9. After the elastic stage, the strut does not fracture immediately but a small precritical crack branch [13] can be found before the tensile strength. Therefore, for simulating the cementitious lattices, if a pure brittle (SL) behavior of the strut is assumed, the E-modulus input should be equal to the slope of the curve calculated at the end of the elastic stage (point No.1 in Figure 4-9), however, the stress input equals to the ultimate fracture strength (point No.2 in Figure 4-9) of the strut instead of the stress value at the same point (see Figure 4-7a).

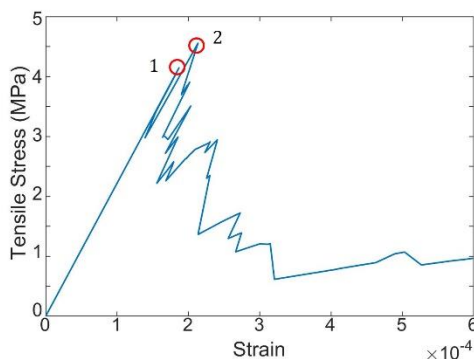


Figure 4-9 Typical stress-strain response of the cementitious strut, point No.1 indicates the elastic stage; point No.2 indicates the fracture strength.

A comparison between the simulated and experimentally measured tensile strength of cementitious struts is shown in Figure 4-10. The simulation results match the experiments very well, not only in terms of the average strength, but also in terms of the standard deviation induced by the heterogeneity of cement paste. The large deviation indicates that the size of the cementitious struts is small and that their heterogeneity should not be neglected when studying the macroscale cementitious lattices. Therefore, to properly simulate the mechanical response of the macroscale cementitious lattices, using the average value as the input for the struts in the macroscale lattices is not the best choice. Instead, using randomly selected values from the simulated results allows including the heterogeneity of the struts.

After reaching the tensile strength, as expected, the struts show an obvious tensile softening. Correspondingly, a tortuous crack pattern can be observed during the fracture process of the cement paste. From the crack pattern (indicated in black in Figure 4-11), it is clear that the pores play a critical role: cracking initiated at locations with high local porosity. During the further cracking process, the cracks propagate through the weaker phase (L) and a tortuous main cracking plane was generated. In addition, distributed cracks form outside the main cracking plane, which contributes to the overall softening behavior. Tortuous cracking plane and distributed cracks indicate more failed elements compared to a straight cracking plane, as a result, a softening branch is witnessed on the stress-strain curve in Figure 4-9.

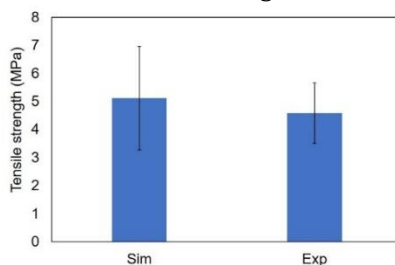


Figure 4-10 Tensile strength of the cementitious strut obtained from experiment (obtained from dog bone shape specimens) and simulations; standard deviation is indicated

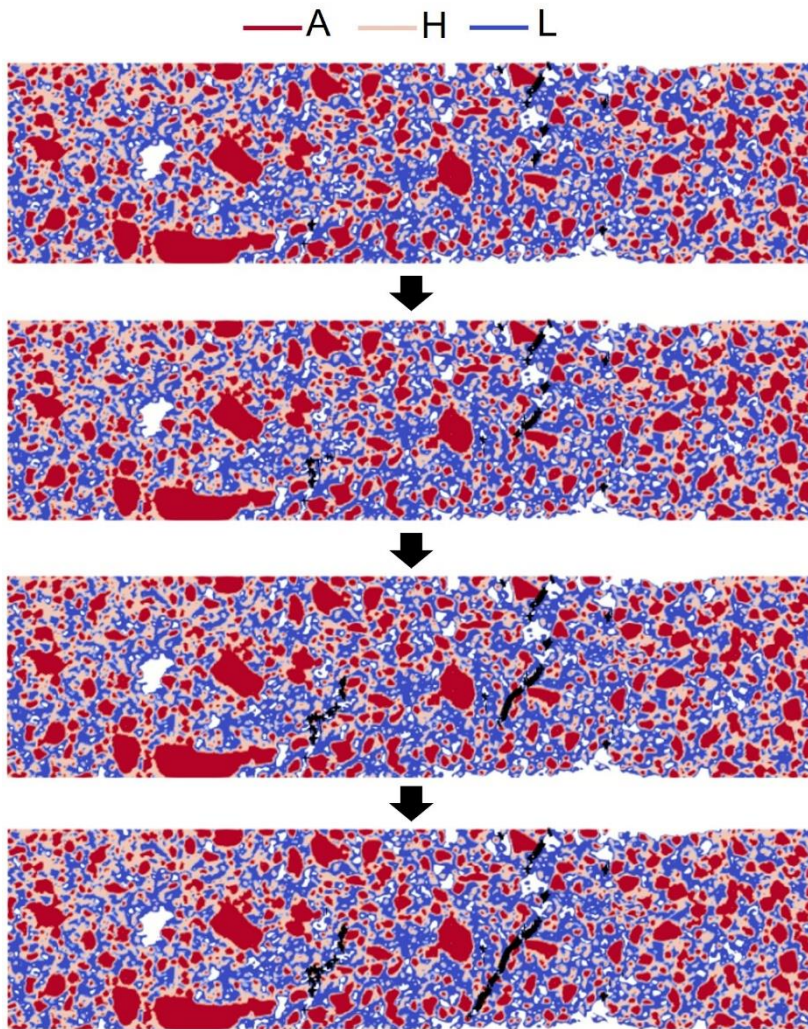


Figure 4-11 Simulated crack pattern of the cementitious struts, failed elements are indicated in black; other phase are indicated, respectively; the quantities of the interface elements are too small to be visible

4.4.2 Stiffness and strength of the cementitious lattices

In this chapter, two types of cementitious lattices were prepared: a regular triangular lattice (R0) and a randomized triangular lattice structure (R5). By randomly placing nodes in the sub-cells (see Figure 4-3), heterogeneity was introduced to the lattice structure. Previously, it was found that the triangular lattice is relatively insensitive to the random nodes heterogeneity in terms of the elastic behavior [14]. Of course, the stiffness of lattice cellular materials is dependent on their relative density. For lattice with extremely low relative density (<0.1), the stiffness is very dependent on the nodal randomness [10]. For the studied cementitious lattices (R0 and R5, with

relative density around 0.5), it can be seen from Figure 4-12 that no significant difference between R0 and R5 can be found in both the experiments and the numerical simulations. Meanwhile, since in the elastic stage there is no difference in the E-modulus of the adopted three types of struts behavior (SL, BL and ML) the simulated global stiffness is almost the same (a slight difference does exist because the E-moduli of individual struts were randomly assigned using the results from microscale simulations).

For both R0 and R5, the simulated stiffness values are lower than the experimental values, which is possibly caused by the so-called “joint stiffening” [15, 16] effect. In the experimental specimens, the joints between the lattice struts also account for a certain amount of material, which contributes to the global stiffness of the cementitious lattice. However, in the simulation the joints were not included because beam elements instead of solid elements were used. For further studies, this “joint stiffening” effect can be compensated by equivalently increasing the size of elemental cross section.

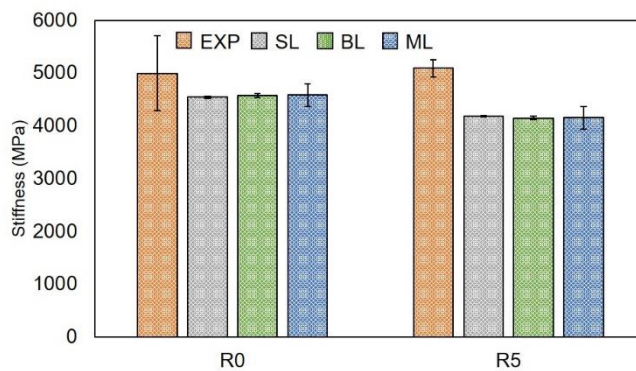


Figure 4-12 Comparison of the experimentally tested and numerically simulated stiffness of the cementitious lattices, standard deviation is indicated

4.4.3 Strength and fracture behavior of cementitious lattices

The tensile strength of the cementitious lattices is more sensitive to heterogeneity compared to the elastic response. Figure 4-13 clearly shows that the tensile strength of a regular cementitious lattice (R0) is 21.6% higher than the randomized cementitious lattice (R5). Similarly, using the three types of struts, the simulated strength is consistent with the experiment: the simulated tensile strength of R0 is higher than R5 by 26.4% (SL), 22.4% (BL) and 22.0% (ML), respectively.

Still, the simulated tensile strength values are all slightly higher than those obtained from experiments (ML has the largest difference of 15.6%). On the one hand, as the simulated strut strength is in itself higher than those obtained from experiments (Figure 4-10), so that the simulated global strength of the cementitious lattice is consequently higher. An additional reason could be related to the local defects of the macroscale lattices, which generate additional stress on the lattice struts in the experiments. This, however, was not accounted in the simulations. Because beam elements were used in the numerical simulation, only axial stress and bending moment

generated by the nodal movements was considered. In the experiments, sharp corners in the vicinity of the joints may introduce additional stress concentrations and the joints may break before the simulated critical stress was reached. A similar effect introduced by the joint of the lattice struts was reported in Chapter 3.

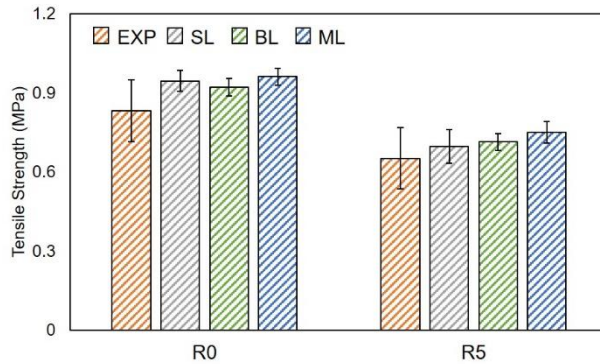
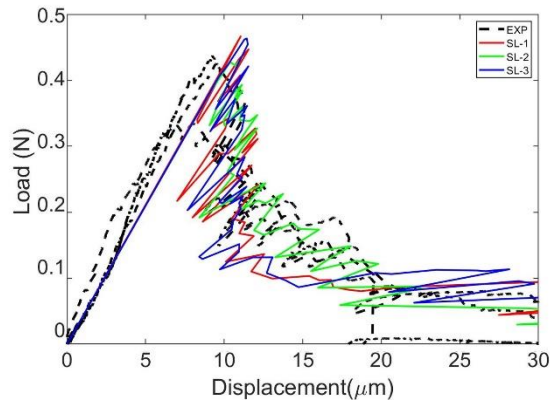


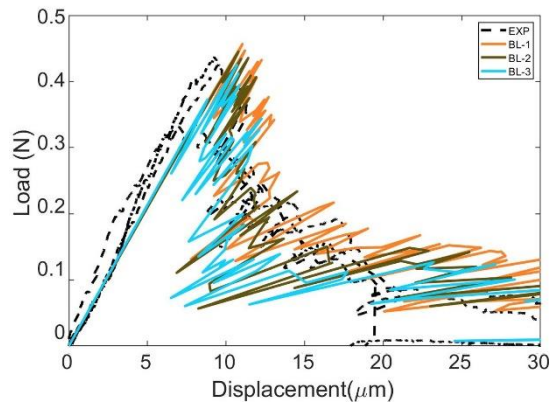
Figure 4-13 Comparison of the experimentally tested and numerically simulated tensile strength of the cementitious lattices, standard deviation is indicated

One important conclusion from Chapter 3 is that the fracture behavior of lattice cellular materials depends not only on the lattice structure, but also highly on the properties of the constituent material. Although it is shown in the previous section that the lattice strut exhibits quasi-brittle behavior, cementitious materials are more brittle than polymers (cracking). Therefore, the influence of lattice strut local precritical cracking or softening on the global fracture process is less significant. This can be observed from the load-displacement curves of the cementitious lattices (shown in Figure 4-14 and Figure 4-15). In general, the simulated curves agree well with the experiments for R0 (see Figure 4-14) and R5 (see Figure 4-15).

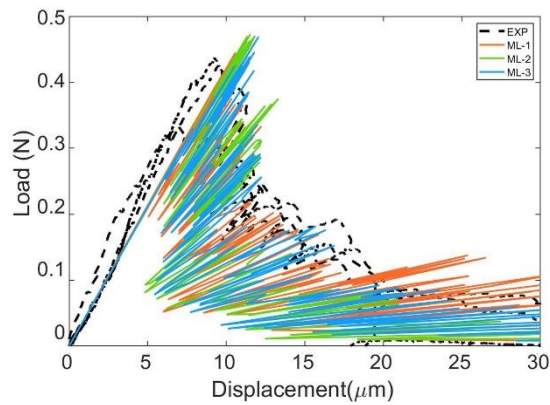
It seems that using any of the three types of struts in the simulations can properly capture the load-displacement response of the cementitious lattices. Nevertheless, the main difference lies in the precritical cracking branch (the branch after elastic stage and before the peak stress). From the experimental curves, this precritical cracking branch can be found both in R0 and R5 curves. Comparatively, from the simulations, an obvious precritical cracking branch can only be found on the simulated curves using the quasi-brittle strut behavior (BL and ML). In the curve simulated by assuming pure brittle behavior (single linear input, denoted as SL), the precritical branch is almost invisible.



(a)

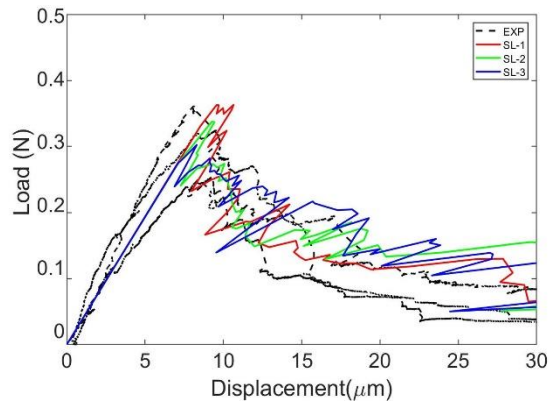


(b)

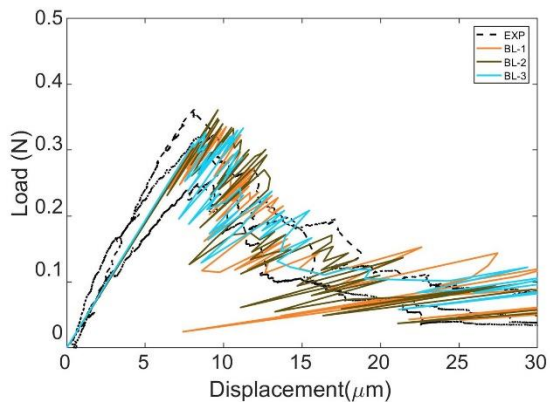


(c)

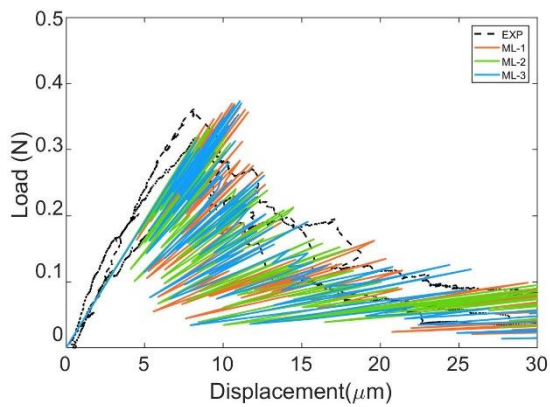
Figure 4-14 Comparison of load-displacement curves of R0 obtained from experiment and simulation with different strut properties, a) struts with ideally-brittle behavior, b) struts with bi-linear behavior c) struts with multiple linear behavior



(a)



(b)



(c)

Figure 4-15 Comparison of load-displacement curves of R5 obtained from experiment and simulation with different strut properties, a) struts with single linear property, b) struts with bi-linear property c) struts with multiple linear property

The precritical cracking stage is an important indicator of the real fracture process of the cementitious lattices. It means that before the main crack propagated, the cementitious lattice before crack started to propagate from the crack tip (notch). This should be the result of local struts weakening. Due to the heterogeneity of cementitious material, these struts may be positioned far from the crack tip, which leads to stiffness degradation of the lattice system instead of immediate fracture and load drop. It can be found on the load-displacement curve that the tangential slope suddenly decreased (shown in Figure 4-16). Simultaneously, the weakened struts can be observed from the locations with high local strains DIC images. Furthermore, similar to [17], the snapbacks which can be witnessed on the experimental load-displacement curves indicates the gradually fracturing process of the lattice cellular materials. This process can be observed from the DIC results (Figure 4-17). The snapbacks were also captured by the simulated load-displacement curves and the fracture process of the cementitious lattices is even more clearly depicted by a step-wisely strut removal process. The simulated crack patterns at the corresponding points are shown in Figure 4-18. For the purely brittle struts (SL), the fracture pattern is directly indicated by the failed struts. For the quasi-brittle struts (BL and ML), a large number of weakened (stiffness decreased but not failed) struts are also visible. It is rather obvious that the crack plane of R5 is more tortuous than R0 as the main crack plane has to follow the lattice element orientation. Therefore, it is determined by the lattice structure.

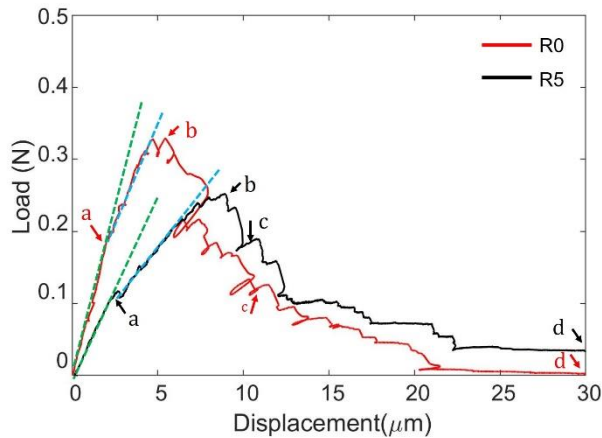


Figure 4-16 Comparison of the load-displacement curve between R0 and R5, stiffness degradation of the cementitious lattice due to struts weakening and several points for explaining fracture pattern is indicated

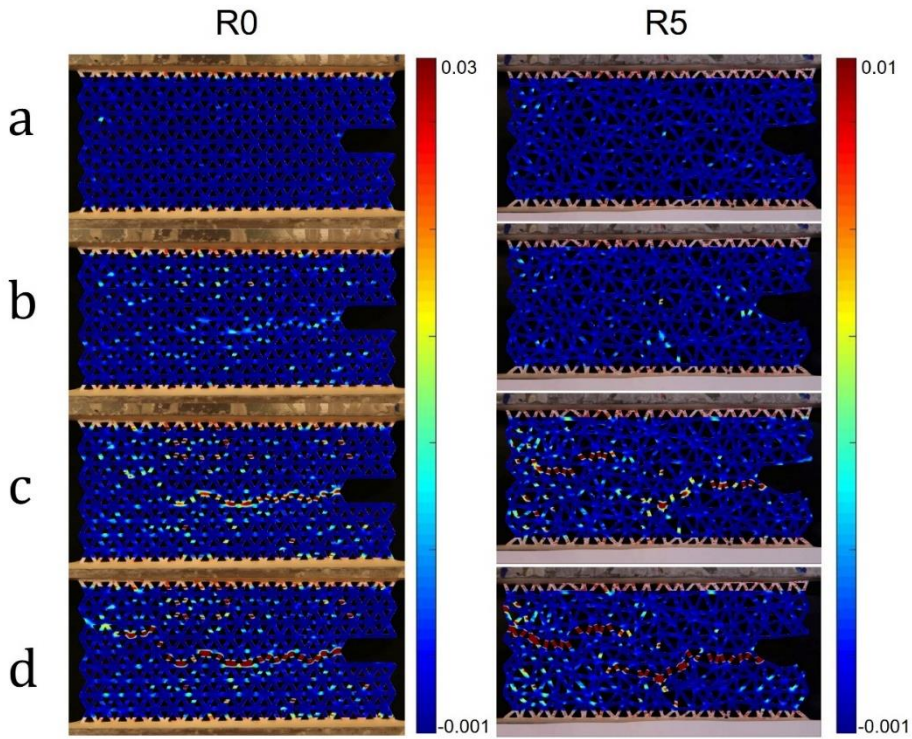
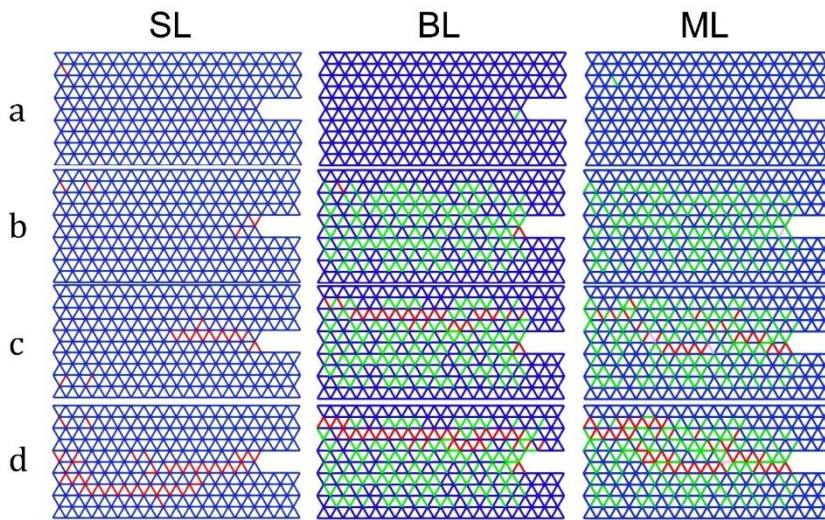


Figure 4-17 Crack pattern obtained from experiments by DIC, strain is indicated by the legend; the “a, b, c, d” corresponds to the points in Figure 4-16.



(a)

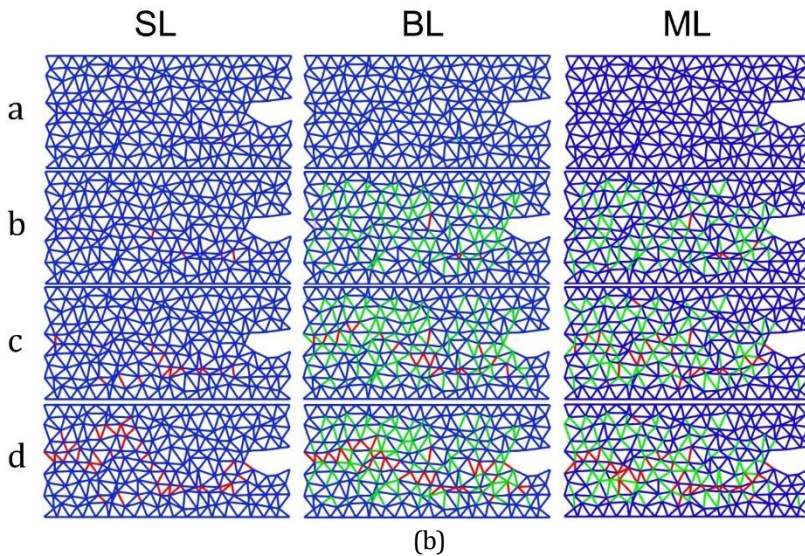


Figure 4-18 Fracture pattern simulated by three different types of struts input of the cementitious lattice a) R0 and b) R5, weakened struts are indicated in green, failed struts are indicated in red, the “a, b, c, d” corresponds to the points in Figure 4-16.

For a quasi-brittle fracture process, it can be assumed that the total work applied on the cementitious lattice comprises of three parts as shown in Figure 4-19: defined as elastic energy (E_e), precritical cracking energy (E_p) and the post-peak cracking energy (E_c). Among the precritical cracking energy and the post-peak cracking energy, there was also some energy dissipated by sound or generated heat. These are all included in the fracture energy. The fracture energy (E_g) is the sum of the precritical cracking energy and post-peak cracking energy. As described in Chapter 3, during the computing process the Delft lattice model gives load-displacement curves with true snapbacks (see Figure 4-14 and Figure 4-15). But this was not captured by the experiment method used in this chapter as the upper and lower boundary of the cementitious lattices were loaded under a constantly increasing displacement. Therefore, the simulated load-displacement curves were smoothed (see Figure 4-20) such that the displacement of the simulated curves monotonically increases to ensure more precise energy calculation. For the studied cementitious lattices, it can be seen from Figure 4-21 that the total work required to rupture the R0 is slightly higher than R5 specimens. The simulations show similar results: using the same type of BL and ML struts input behavior, the total work of R0 is higher than R5. While the SL as input, the simulation did not show obvious difference.

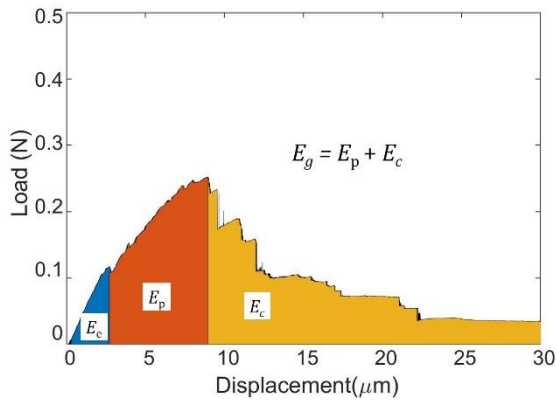


Figure 4-19 Energy components during fracture process of cementitious lattices

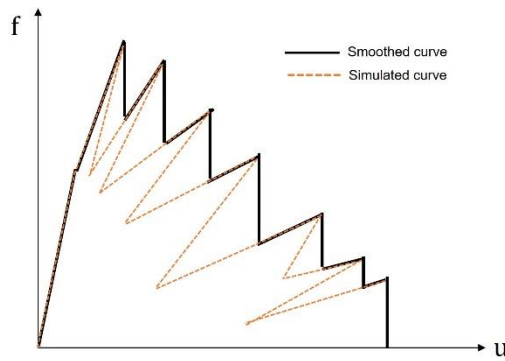


Figure 4-20 Schematics of smoothing the simulated load-displacement curve to compensate the influence of snapbacks from the Delft lattice model, smoothed curve ensures monotonic displacement increase

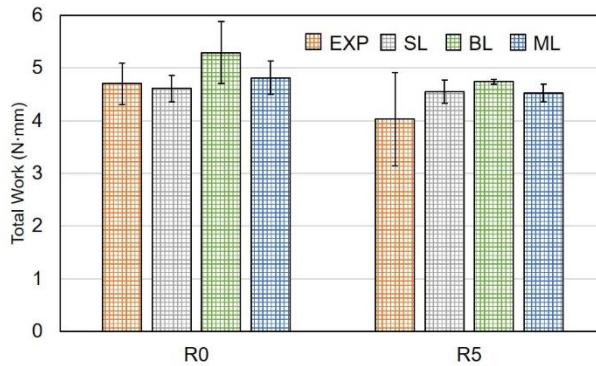


Figure 4-21 Total work required to rupture the cementitious lattice

On the contrary, when it comes to fracture energy, the heterogeneity of the struts on the microscale has significant impact. As the precritical cracking stage of the load-displacement curves simulated by the quasi-brittle struts (BL and ML) is longer than the pure brittle (SL) struts, the fracture energy simulated by the quasi-brittle struts is obviously higher than SL struts, see Figure 4-22. Among the three types of struts the bi-linear (BL) and multiple linear (ML) struts input behavior gives higher fracture energy as it included the precritical cracking and softening of the struts, which should be closer to the real material behavior. In these cases, the simulated fracture energy values are higher than experiment. This was mainly caused by the lower simulated stiffness (see Figure 4-12) of the lattices which leaves higher remained energy when elastic energy was excluded from the total work.

For the macroscopic heterogeneity, only considering the brittle behavior (note that the microscopic heterogeneity still exists because of the E-modulus and strength of the struts varied), the randomized cementitious lattice shows a higher fracture energy (R5-SL) compared to the regular triangular lattice (R0). While, if quasi-brittleness is taken into consideration, the obvious difference in fracture energy between regular and randomized lattices disappears, the randomized lattice has even slightly lower fracture energy (approximately 10%). In this sense, the BL and ML show better agreement with experiment. These results indicate that the quasi-brittleness of the constituent cementitious material instead of the structural heterogeneity dominates the fracture energy of the studied cementitious lattices.

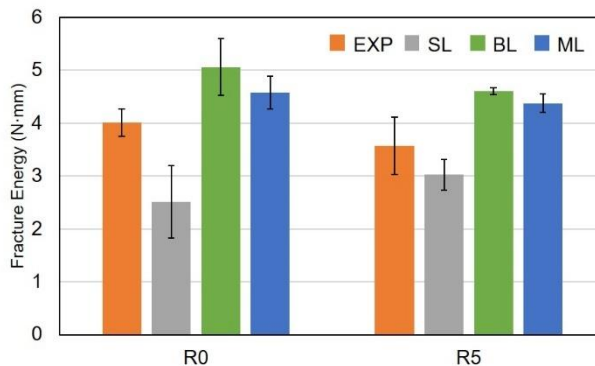


Figure 4-22 Comparison of the experimentally tested and numerically simulated fracture energy of the cementitious lattices, standard deviation is indicated

Reviewing all simulated results, for stiffness and strength, all three types of strut behavior can provide accurate simulation results: namely, the heterogeneity induced on the microscale by cementitious constituent material has limited influence on the stiffness and strength of triangular cementitious lattices. Comparatively, the heterogeneity introduced on the macroscale by the randomness obviously decreases the stiffness and strength of the triangular cementitious lattices.

In terms of fracture energy, the heterogeneity on the microscale has significant impact: comparing to brittle lattices, the quasi-brittle cementitious lattices have much higher fracture energy expense. On the macroscale, although macroscopic

heterogeneity introduced by the randomized lattice structure also increases the fracture energy, the heterogeneity of the constituent cementitious material is rather dominant.

4.5 CONCLUSIONS

In this chapter, mechanical properties of cementitious lattices were investigated. By a comparative study between experimental and numerical simulations, mechanical properties of the cementitious lattices are investigated. Distinct from other lattice materials, heterogeneity of cementitious lattice materials exists on different scales which substantially influences the mechanical properties. Therefore, the role of heterogeneity is specifically studied in this chapter on different scales: microscale, on which the influence of the heterogeneity is introduced by the microstructure of hardened cement paste on the fracture behavior of lattice struts is studied; and macroscale, on which heterogeneity induced by the nodal distribution of the lattice structure is studied. According to the obtained results, several conclusions can be drawn as follows:

- In terms of the elastic response, the cementitious lattices are insensitive to heterogenous nodal distribution at relative density around 0.5. From experiment and simulation results, the studied randomized lattice R5 and the regular lattice R0 have a similar stiffness of approximately 5000 MPa.
- Tensile strength of the cementitious lattice is dependent on the macroscopic heterogeneity introduced by lattice nodal distribution. According to the experiment and simulation, the tensile strength of randomized cementitious lattice (R5) is lower than regular cementitious lattice (R0) by 21.6%.
- Heterogeneity of the cementitious lattices on both microscopic (the cementitious constituent material) and macroscopic (the lattice structure) has significant influence on fracture behavior. The main crack pattern has to follow the lattice element orientation, therefore heterogenous lattice structure has more tortuous crack pattern. Meanwhile, comparing to macroscopic nodal randomness, microscopic heterogeneity of the cementitious constituent material is dominant in terms of the fracture energy.

REFERENCES

- [1] Z. Qian, E. Schlangen, G. Ye, K. van Breugel, Modeling Framework for Fracture in Multiscale Cement-Based Material Structures, *Materials (Basel)* 10(6) (2017).
- [2] Z. Qian, Multiscale Modeling of Fracture Processes in Cementitious Materials, *Civil Engineering and Geoscience*, TU Delft, Delft, 2012.
- [3] H. Zhang, B. Šavija, S.C. Figueiredo, E. Schlangen, Experimentally validated multi-scale modelling scheme of deformation and fracture of cement paste, *Cement and Concrete Research* 102 (2017) 175-186.
- [4] H. Zhang, B. Saviija, S. Chaves Figueiredo, M. Lukovic, E. Schlangen, Microscale Testing and Modelling of Cement Paste as Basis for Multi-Scale Modelling, *Materials (Basel)* 9(11) (2016).
- [5] H.S. Wong, N.R. Buenfeld, Determining the water-cement ratio, cement content, water content and degree of hydration of hardened cement paste: Method development and validation on paste samples, *Cement and Concrete Research* 39(10) (2009) 957-965.
- [6] E. Schlangen, Crack Development in Concrete, Part 2: Modelling of Fracture Process, *Key Engineering Materials* 385-387 (2008) 73-76.
- [7] H.S. Wong, M.K. Head, N.R. Buenfeld, Pore segmentation of cement-based materials from backscattered electron images, *Cement and Concrete Research* 36(6) (2006) 1083-1090.
- [8] M. Zhang, Y. He, G. Ye, D.A. Lange, K.v. Breugel, Computational investigation on mass diffusivity in Portland cement paste based on X-ray computed microtomography (μ CT) image, *Construction and Building Materials* 27(1) (2012) 472-481.
- [9] P.D. Tennis, H.M. Jennings, A model for two types of calcium silicate hydrate in the microstructure of Portland cement pastes, *Cement and Concrete Research* (2000) 855-863.
- [10] C. Hu, Z. Li, Micromechanical investigation of Portland cement paste, *Construction and Building Materials* 71 (2014) 44-52.
- [11] S. Igarashi, M. Kawamura, A. Watanabe, Analysis of cement pastes and mortars by a combination of backscatter-based SEM image analysis and calculations based on the Powers model, *Cement and Concrete Composites* 26(8) (2004) 977-985.
- [12] K. Kurumisawa, T. Nawa, Electrical Conductivity and Chloride Ingress in Hardened Cement Paste, *Journal of Advanced Concrete Technology* 14(3) (2016) 87-94.
- [13] J.G. Van Mier, *Concrete fracture: a multiscale approach*, CRC press 2012.
- [14] N.E.R. Romijn, N.A. Fleck, The fracture toughness of planar lattices: Imperfection sensitivity, *Journal of the Mechanics and Physics of Solids* 55(12) (2007) 2538-2564.
- [15] G. Dong, Y.F. Zhao, Numerical and experimental investigation of the joint stiffness in lattice structures fabricated by additive manufacturing, *International Journal of Mechanical Sciences* 148 (2018) 475-485.
- [16] M.H. Luxner, J. Stampfl, H.E. Pettermann, Finite element modeling concepts and linear analyses of 3D regular open cell structures, *Journal of Materials Science* 40(22) (2005) 5859-5866.
- [17] A. Glacet, J. Réthoré, A. Tanguy, F. Morestin, On the failure resistance of quasi-periodic lattices, *Scripta Materialia* 156 (2018) 23-26.

5

CEMENTITIOUS CELLULAR COMPOSITES WITH AUXETIC BEHAVIOR

In Chapter 4, it was shown that the cracking behavior of cementitious lattice cellular materials is influenced by the cellular structure together with the constituent cementitious material. In this chapter, by a specially designed cellular structure and cementitious constituent material, it is shown that cracking could be tailored so that unprecedented auxetic behavior is achieved by a cementitious composite material. Auxetic behavior, which is normally seen in elastomers, refers to the phenomenon of a negative Poisson's ratio. In contrast to the local buckling mechanism commonly employed to trigger auxetic behavior, a novel crack bridging auxetic mechanism was discovered in the auxetic cementitious cellular composites (CCCs). Taking advantage of 3D printing techniques, cementitious cellular composite specimens with specific cellular structures were prepared. Through a specially tailored cellular structure, crack initiation was induced at desired locations, and, by the designed constituent material mixture, these cracks could be bridged. As a result, auxetic behavior could be achieved.

5.1 INTRODUCTION

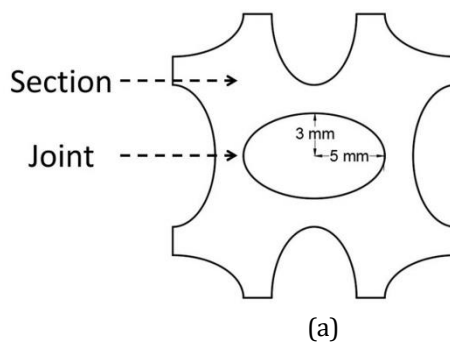
The term “auxetic”, coined by Evans in 1991 [1], refers to a material with a negative Poisson’s ratio. This means that the material exhibits lateral contraction or expansion when compressed or stretched vertically, respectively. This unusual behavior gives auxetic materials extraordinary mechanical properties: enhanced indentation resistance [2-4], high specific energy absorption [5-7], and high shear resistance [5, 8]. Unlike the high strength concrete used for common structural elements, the unusual feature of the auxetic materials indicates that they could be promising alternatives for specific engineering applications such as impact resistant structures [9] and vibration mitigating structures [10, 11]. In this chapter, auxetic behavior is achieved by cementitious cellular composites (CCCs). The principles of designing such auxetic CCCs are discussed in terms of the cellular structure and the cementitious constituents.

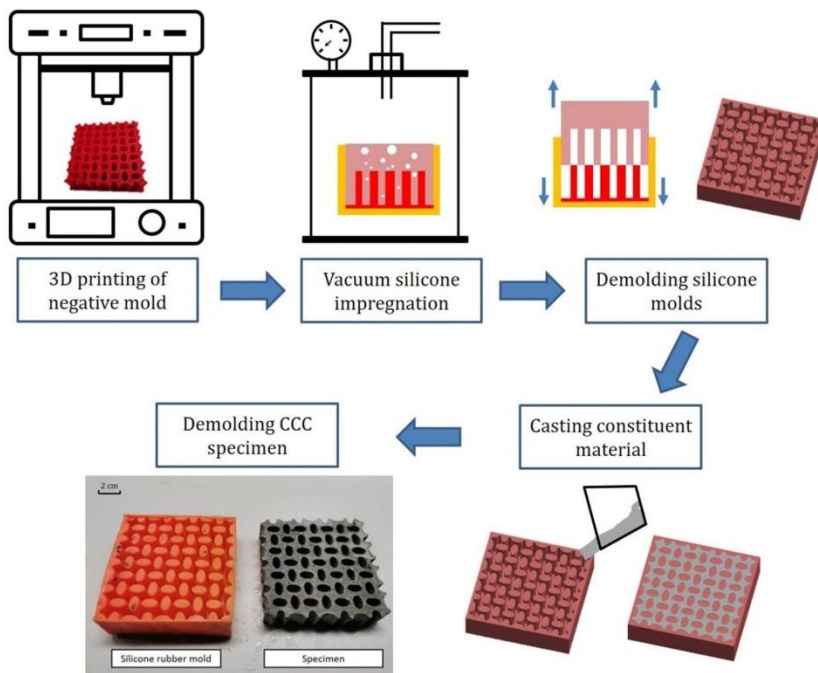
5.2 METHODS AND MATERIALS

5.2.1 Specimen preparation

Two types of specimens were fabricated for two types of tests. First, for characterizing the properties of the cementitious constituent materials, four-point bending tests were performed. For these tests, thin bar specimens with dimensions of $160 \times 30 \times 10$ were prepared. Then, for evaluating the compressive behavior of the cementitious cellular composites, uniaxial and cyclic compressive tests were performed.

Cellular structures with repeating unit cells were designed. The total volume of the cellular structure is 67.6 cm^3 at a relative density of 52.8%. Each unit cell consists of four sections connected by four joints (shown in Figure 5-1a). The same “indirect” 3D printing technique used in the previous chapter was used. The specimen preparation procedure is the same as that described in Chapter 4. Of course, a different cellular structure was used in this chapter. The procedure is shown in Figure 5-1b.





(b)

Figure 5-1 (a) a unit cell of the cellular structure with $a=5$ mm and $b=3$ mm (b) Schematics of “indirect 3D printing” process

In this chapter, three mixes were used as constituent materials and their mixture proportions are given in

Table 5-2. Polyvinyl Alcohol (PVA) fibers, produced by Changzhou TianYi Engineering Fiber, were used as reinforcement by 0%, 1% and 2% in volume and denoted as F_0 , F_1 and F_2 , respectively. Physical and mechanical properties of the PVA fibers are listed in Table 5-1. Methylcellulose produced by Shanghai Ying Jia Industrial Development Co. Ltd. was used as viscosity modifying agent (VA) to optimize the fiber distribution. Glenium 51 (Cugla B.V.) was used as superplasticizer (SP) to adjust mixture fluidity. The cement matrix material was a fine-grained cementitious mortar containing Portland cement (CEM I 42.5 N) and fly ash (FA) as binder materials. Tap water was used as mixing water. Water to binder ratio was set to 0.42 for all mixtures. During the casting process of the constituent materials, dry materials (without fibers) were first mixed for 4 minutes using a Hobart machine; then, water and superplasticizer were added and mixed for 2 minutes; then fibers were added in and mixed for another 2 minutes. The total mixing time for each mixture was 8 minutes. The fresh mixture was cast into molds, vibrated for 40 seconds and covered by a plastic sheet to prevent water loss. One day after casting, the specimens were demolded and cured under water until 28 days of age.

Table 5-1 Properties of PVA fibers used in the cementitious matrix

Diameter	Length	Tensile Strength	Young's modulus	Density
15 μm	6 mm	1.6 GPa	34 GPa	1.28 g/cm ³

Table 5-2 Proportions of different constituent materials (kg/m³)

Mix.	Cement	Fly ash	Sand (125 μm ~250 μm)	Water	SP	VA	Fiber
F ₀							0
F ₁	471	556	385	428	0.86	0.3	12.8
F ₂							25.6

5.2.2 Mechanical Experiments

The four-point bending tests were performed on the specimens at 28 days of age. A servo hydraulic press (INSTRON 8872) was used for testing. Displacement control with a constant rate of 0.01mm/s was used. The load was measured by the load cell and the deflection was measured by two linear variable differential transducers (LVDTs) placed at the mid-span. Five specimens were tested for each batch. The loading schematics and experimental setup are shown in Figure 5-2a and Figure 5-2b, respectively.

The uniaxial compressive test was done by a servo hydraulic press (INSTRON 8872) under displacement control, with a constant rate of 0.01mm/s. The load and displacement were measured by the INSTRON 8872. To minimize lateral restraint at the boundaries caused by friction, a plastic film was placed between the specimen and the steel loading plates at the top and the bottom. The specimens were covered with white paint and a speckle pattern to facilitate digital image correlation (DIC) analyses. The experimental setup is shown in Figure 5-2c. For each test, stress-strain curve was calculated from the obtained load and displacement data, using the sample cross section 1600 mm² (80 mm × 20 mm) and the sample length 80 mm. The cyclic loading tests were performed in the same loading setup of uniaxial compression at a constant amplitude of 1 mm and frequency of 1Hz by a sine wave. For each cyclic loading test, 2.5×10^4 cycles were performed. Three replicates were tested for uniaxial compression and cyclic loading test, respectively.

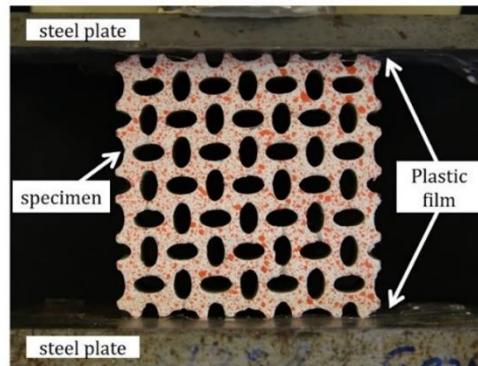
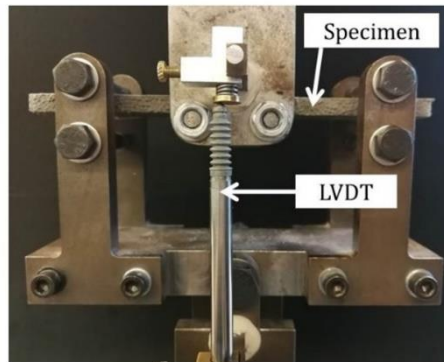
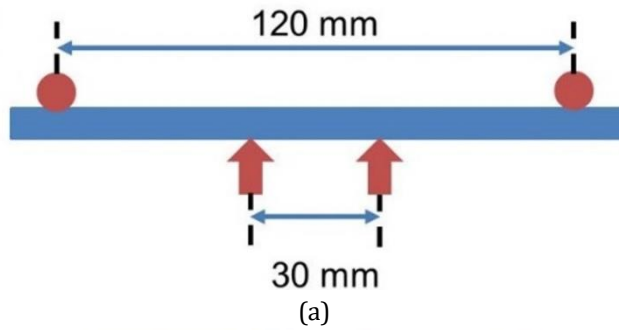


Figure 5-2 (a) Schematics of the four-point bending test; (b) four-point bending test setup on INSTRON 8872; (c) uniaxial compression and cyclic loading test setup on INSTRON 8872

5.3 RESULTS AND DISCUSSION

5.3.1 Crack bridging induced auxetic behavior

Global mechanical properties of cellular composites depend on the cellular structural configuration as well as the properties of the constituent materials. Although a similar structure was used before [12-14] in which local buckling is the mechanism of

the auxetic behavior, for cellular structures made of cementitious materials the mechanism has not been studied before and is potentially different. Therefore, prior to examining the experimental results, a theoretical analysis on the possible mechanism of CCCs exhibiting auxetic behavior will help understanding the phenomena involved.

The studied auxetic mechanism on the level of a unit cell is shown schematically in Figure 5-3. For the cellular structure used in this chapter, because of the chirality of the sections of the single cell, locally the joints of each single cell are misaligned. As a result, when uniaxial compressive loading is applied on the specimen, the joints are subjected to bending moment which is similar to a four-point bending condition (Figure 5-3a). Consequently, tensile and compressive stresses are generated at the joints near the ends of the semi-minor axis and the semi-major axis of the ellipse, respectively (Figure 5-3b). Since cementitious materials are much weaker in tension than in compression (compressive strength is typically 8~10 times higher than the tensile strength [15]), cracks will initiate at the tension side of the joint (Figure 5-3c). Depending on the crack bridging ability of the cementitious constituent material, the crack-initiated specimen will behave differently afterwards.

If the constituent material does not have any crack bridging ability (e.g. plain mortar F_0), the crack will propagate through the joints, leading to immediate fracture of the entire cellular structure; consequently, auxetic behavior will not be observed (Figure 5-3d). On the other hand, if the constituent material possesses crack bridging ability, the sections will be able to rotate and auxetic behavior may be obtained because the joints of each cell will locally be subjected to bending. However, as shown in Figure 5-3e, if the constituent material has limited crack bridging ability (e.g. mix F_1 with lower fiber content), the sections will only be able to rotate at the beginning of the compression. As compression continues, fiber pullout will be observed. For the 6mm PVA fiber used in this studied, embedded fiber length varies from 0 mm to 3mm. When the crack opening increase is higher than 3 mm, the fibers will be completely pulled out. Meanwhile, some fibers still bridge the crack at places where the crack opening is still lower than 3 mm. Eventually, some sections separate at the joints where fibers will be completely pulled out. Only when the crack bridging ability is high enough (e.g. mix F_2 with the higher fiber content), the joints will not fracture because of the crack bridging and the sections will rotate during the entire compression until the joints are compressed together; eventually, the elliptical cellular structure will disappear (Figure 5-3f). Because the length in the lateral direction of a fully rotated section (L_r) is shorter than the length before rotation (L_0 , see Figure 5-3g), globally the specimen will exhibit lateral contraction when compressed and auxetic behavior will be obtained in this case.

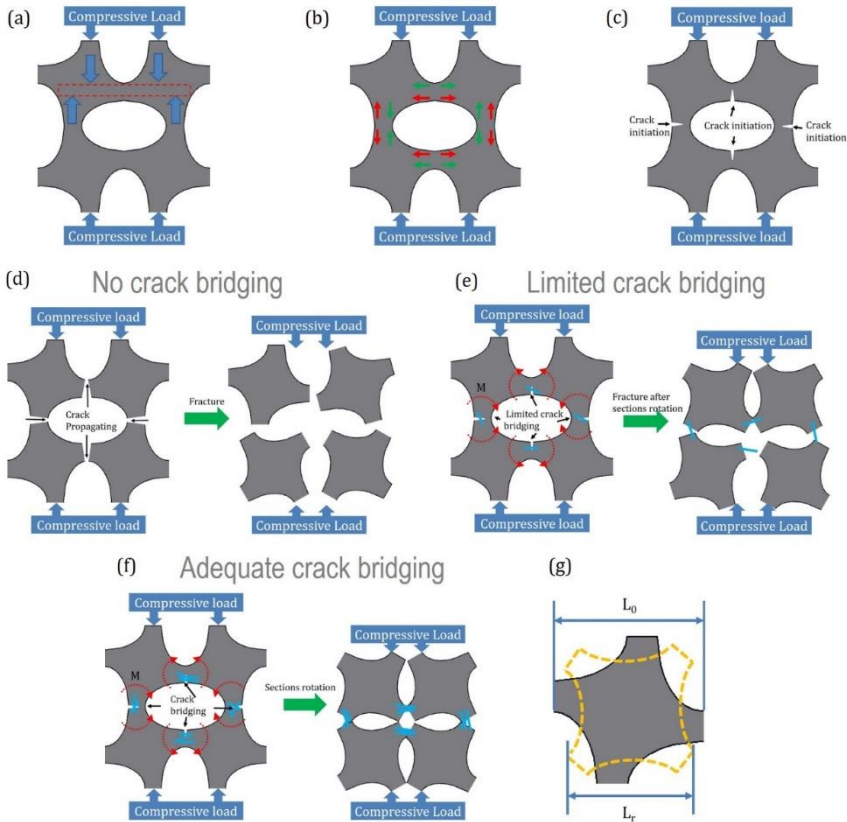


Figure 5-3 Schematics of auxetic mechanism of CCCs. (a) the joints subjected to a condition similar to four-point bending when compressive load is applied because of the chirality of each section in the single cell; (b) stress distribution at the joints after compressive load is applied, red arrow indicates the tensile stress and green arrow indicates the compressive stress; (c) a crack initiates at the tension side of the joints, marked by black arrows; (d) if the constituent material has no crack bridging ability, crack propagation leads to joints fracture, black arrows show the crack propagation direction; (e) if the constituent material has limited crack bridging ability, joints separate after rotation; (f) if the constituent material has adequate crack bridging ability, joints rotate without separating; (d) dimension comparison of the section in a single cell before and after rotation, $L_0 > L_r$

According to the proposed mechanism, for the structures used in this chapter, the crack bridging ability of the constituent material (which was evaluated by four-point bending tests) is crucial for achieving auxetic behavior. A flexural-deflection curve is shown in Figure 5-4a, first cracking strength (first peak load), fiber slipping strength (second peak load) and enhanced deflection (deflection at the second peak) are defined in this chapter (marked on the curve). The flexural-deflection curves of F_0 , F_1 and F_2 are shown in Figure 5-4b~Figure 5-4d. As expected, the F_0 specimens (Figure 5-4b) show brittle fracture under flexural load: all specimens failed as soon as the first crack

appeared, signified by the sudden drop after the peak load. Therefore, low deflection capacity was achieved during the test. While F_1 (Figure 5-4c) and F_2 (Figure 5-4d) show relatively higher ductility comparing to F_0 : after the first crack instead of immediate rupture the load increased again and a second peak load was achieved afterwards as a result of fibers presence. As shown in Figure 5-4e, because F_0 , F_1 and F_2 used the same cementitious matrix, no significant difference in the first cracking strength (4.8 MPa, 4.4 MPa and 4.5 MPa for F_0 , F_1 and F_2 respectively) was found. For F_1 (Figure 5-4c) and F_2 (Figure 5-4d), after the first crack instead of immediate rupture the load increased again and a second peak load was achieved afterwards. This secondary rise can be explained by the bonding characteristics between PVA fibers and the cementitious matrix [16-18]: when the applied load is high enough to violate the chemical bond between the PVA fibers and the cementitious matrix, fibers started to de-bond and generally be pulled out from the matrix. During the pulling out process, a so called “fibrillation” [16, 18, 19] process of the fiber surface appears, which means that small fiber branches occurred on the fiber surface because of the damage of the PVA fibers. The presence of the branches on the fiber surface creates a jamming effect at the fiber-matrix interface, resulting in frictional bond that effectively increases during the pulling out process. Usually, this process is defined as slip-hardening behavior. For F_2 , a higher fiber volume provided a higher friction load from fiber slipping during the bending tests, resulting in a fiber slipping strength (Figure 5-4f) of 2.6 MPa, compared to 1.6 MPa of F_1 . However, the enhanced deflection capacity (Figure 5-4g) of these two mixes is similar (about 2.9 mm). The difference in fiber slipping strength is an important indicator of the compressive behavior of CCCs made with different constituent materials. This will be discussed in detail in Section 5.3.2.

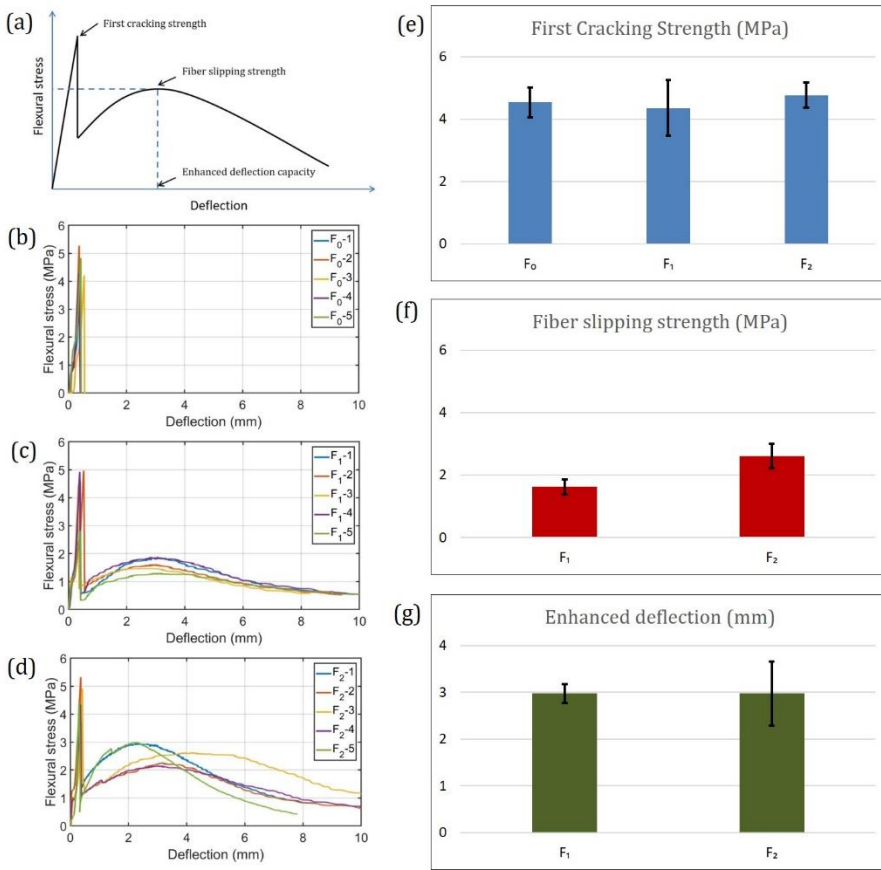
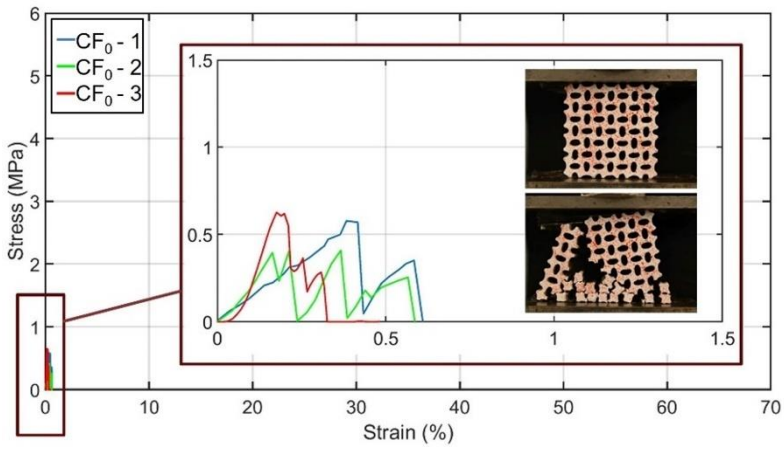


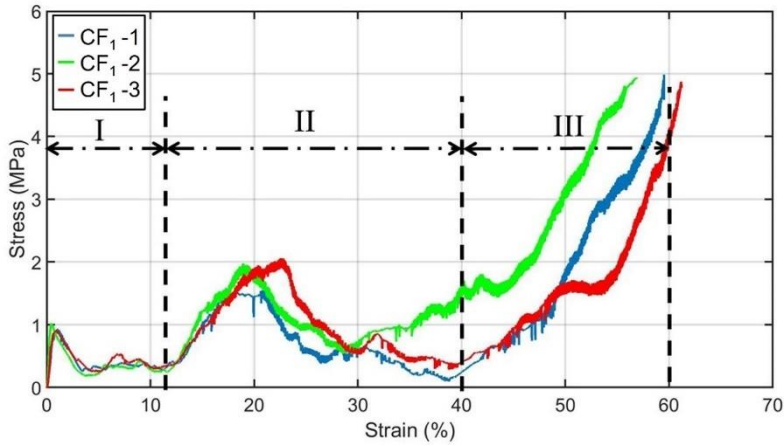
Figure 5-4 (a) Several defined parameters are for the obtained flexural-deflection curves of constituent materials; (b) flexural-deflection curves of plain mortar F₀; (c) flexural-deflection curves of fiber reinforced mortar F₁ with 1% fiber; (d) flexural-deflection curves of fiber reinforced mortar F₂ with 2% fiber; (e) comparison of first cracking strength of three constituent materials; (f) comparison of fiber slipping strength of two fiber reinforced constituent materials F₁ and F₂; (g) comparison of enhanced deflection of two fiber reinforced constituent materials F₁ and F₂

5.3.2 Auxetic behavior of CCCs under uniaxial compression

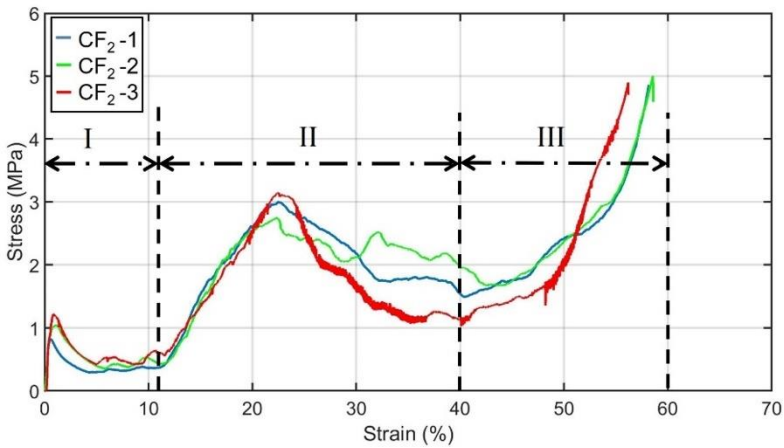
Figure 5-5 shows the stress-strain curves and the compression process of the CCCs. CCCs with F₀, F₁ and F₂ as constituent materials are denoted as CF₀, CF₁ and CF₂ respectively. As can be seen from Figure 5-5a, CF₀ specimens showed brittle fracture during the compression tests: after the peak load was reached, micro cracks rapidly localized which eventually led to the failure of the compressed specimen, witnessed by a sharp drop in the stress-strain curve. Owing to the cellular structure, in some cases cracks developed through the cellular structure layer by layer and multiple sharp drops can be observed in the stress-strain curves.



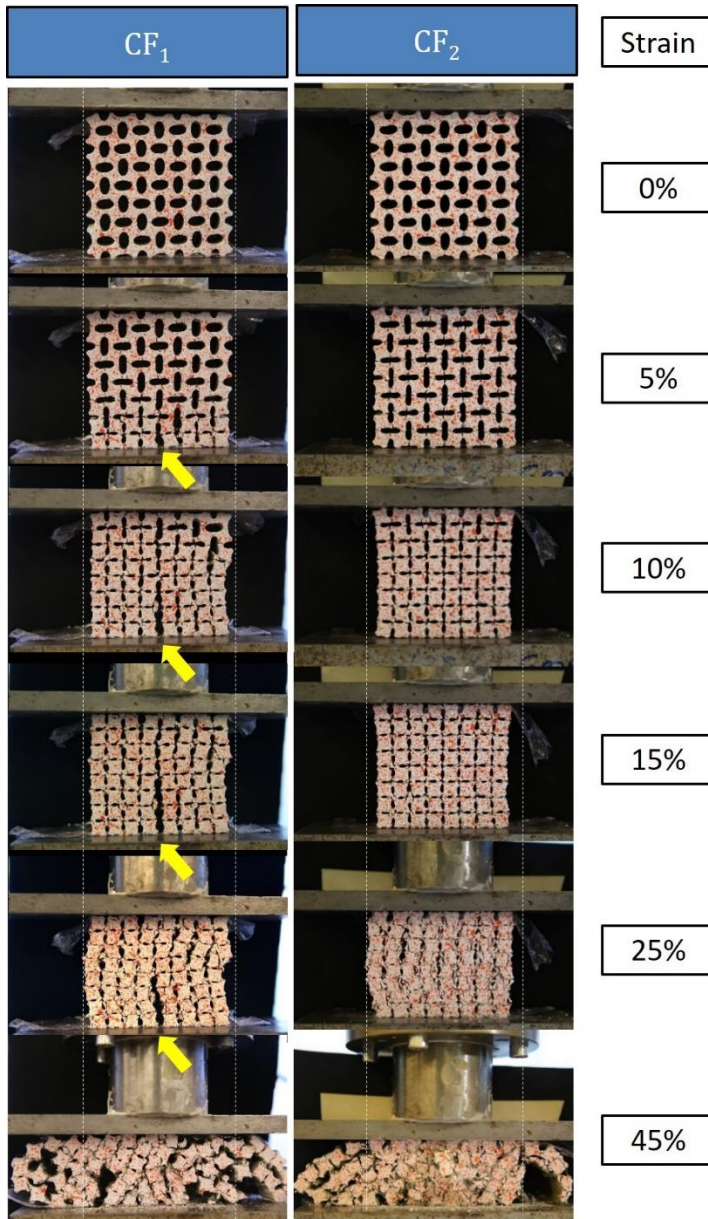
(a)



(b)



(c)



(d)

Figure 5-5 (a) stress-strain curves of CCCs with F_0 as constituent material; (b) stress-strain curves of CCCs with F_1 as constituent material, three stages are marked by dashed lines; (c) stress-strain curves of CCCs with F_2 as constituent material, three stages are marked by black dashed lines; (d) comparison of the compression process at different strain level of CCCs with F_1 and F_2 as constituent materials, separated joints can be found on CF_1 specimen and marked by yellow arrows

The compression behavior of specimens with fiber reinforced cementitious constituent materials (F_1 and F_2) at 28 days can be also roughly divided into three stages, marked as “I”, “II” and “III” on the stress-strain curves in Figure 5-5.

In stage “I”(from 0% strain to roughly 11% strain), the mechanical response under compression is similar to conventional cementitious materials [15]: an ascending branch can be found as compressive load is applied on the specimen, after the elastic regime micro cracks started to initiate; as soon as peak load was reached (around 1 MPa), micro cracks started to localize at the joints of individual cells. For the CF_2 specimens, localized small cracks at the joints opened slowly as compression went on, owing to the fiber bridging effect. As a result, the sections of individual cells started to rotate. Meanwhile, lateral contraction could be observed during the test (see Figure 5-5d): auxetic behavior was achieved in this stage. As can be seen from the DIC results of CF_2 at 5% strain in Figure 5-6a, the areas with high local strain indicate that the crack initiation locations are at the joints near the ends of minor axis in each ellipse structure. Because the external load was applied vertically, it also can be seen from the DIC results that the local strain in the horizontal direction (ϵ_{xx}) is higher than that of vertical direction (ϵ_{yy}) at the same global strain level. As explained in Figure 5-3, the joint rotation contributed to the auxetic behavior of CCCs under uniaxial compression. As assumed in the previous section, after cracks appeared, the fiber bridging ability of the constituent material started to dictate and contributed to prevent the joints from separating. Comparatively, although auxetic behavior was observed during the tests for CF_1 , separated joints can be found (separated joints in the middle bottom of the specimen are clearly shown in Figure 5-5d, marked by yellow arrows).

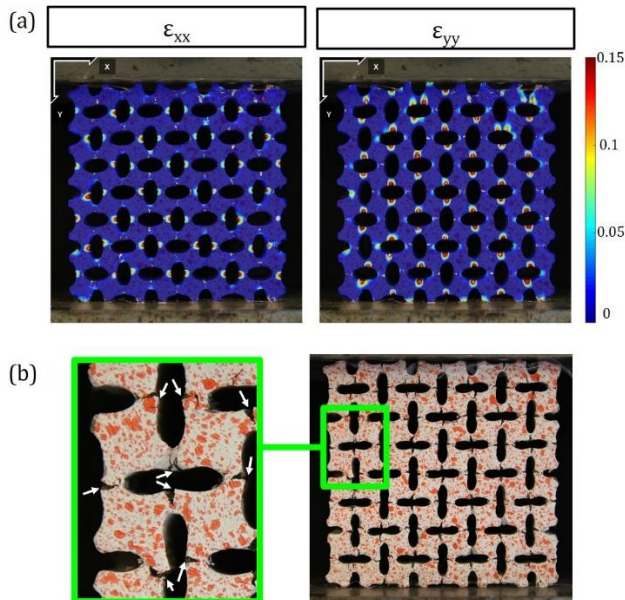


Figure 5-6 (a) shows high local strain area of the CF_2 specimen at 5 % strain on both ϵ_{xx} and ϵ_{yy} direction; (b) magnification of a single cell at 5% compressive strain, white arrows indicate the location of initiated cracks

Stage “II” (from 11% strain to 40% strain) can be recognized as compacting process of the cellular structure and subsequently failure process of the compacted “solid” material. It can be seen from Figure 5-5d that the hollow ellipse structure was generally compacted as a consequence of the rotation of the individual cell sections. More contraction in the lateral direction could be observed when the vertical compression continued. In other words, the cellular structure was destroyed during this process. Correspondingly, in the stress-strain curves (Figure 5-5b and Figure 5-5c) strain hardening behaviors witnessed by a load increase can be observed for both CF₁ and CF₂. This is because the cellular structure was compressed and the sections eventually touched each other. As a result, the compacted “solid” material started to bear an increasing load. Similar strain hardening process can be also found in other auxetic materials [20-22]. After the secondary peak was reached (around 2MPa for CF₁ and 3 MPa for CF₂; because of the joints separating, the secondary peak load of CF₁ is lower) cracks started to initiate and localize in the sections of individual cells and then eventually developed to be crack planes, represented in the stress-strain curves by a descending branch after the secondary peak. In this sense, it is quite similar to the typical compression process of a conventional solid fiber reinforced cementitious material.

One feature of the curve in stage “II” is very interesting: normally for solid cementitious materials, the elastic behavior regime is within one third of the peak load. As the curve of CCC in stage “II” resembles solid cementitious materials, it is also reasonable to assume that CCC also behaves elastically during this regime in stage “II”. This was verified by cyclic loading tests which discussed in detail in the next section.

Stage “III” (after 40% strain) is a pure compacting process of the crushed constituent material which leads to rapid stress rise because the materials were compacted denser. A similar phenomenon is mentioned in a thought experiment by van Mier [15].

From the results presented above, only CF₂ shows auxetic behavior within all tested specimens. The Poisson’s ratio of CF₂ was calculated using the displacement at the middle height of the specimen as lateral contraction (measured from photos). Figure 5-7 shows the Poisson’s ratio of CF₂ at different strain levels (only data up to stage “II” is taken into consideration as stage “III” is the compression process of crushed debris). Negative Poisson’s ratio from the beginning of the compression is found. As compressive load increased, the lowest Poisson’s ratio was reached at 10% strain in stage “I”. In stage “II” the Poisson’s ratio started to increase indicating that several sections of individual cells started to touch each other and cracks began developing in the sections as a result. Considering the geometry of the designed structure, there is an auxetic strain limit (20%) for the CCCs to show negative Poisson’s ratio which usually exists in open cell auxetic foams [23].

As a consequence of the section’s rotation accompanied by fiber pulling out, negative Poisson’s ratio is achieved for the CCCs. One probable advantage for these CCCs with auxetic behavior is their potential for high energy absorption efficiency as found in many other auxetic cellular materials. Figure 5-7 shows the accumulative

specific energy absorption of CF_2 at different strain. The specific energy absorption is calculated using the area under the stress-strain curves of CF_2 divided by the specimen volume (67.6 cm^3). For the same reason as Poisson's ratio, stage "III" is not included in the calculation. During stage "I", the specific energy absorption increases slowly. While, after the first peak owing to the rotation of the sections, the elliptical shape generally disappeared and sections came into contact. In this case, the energy absorption started to increase rapidly roughly at 10% strain which also corresponds to the strain level with the lowest Poisson's ratio. The reason is that the cellular structure of CF_2 is compacted and the sections in each individual cell started to bear load, leading to a secondary rise in the stress-strain curve as described before.

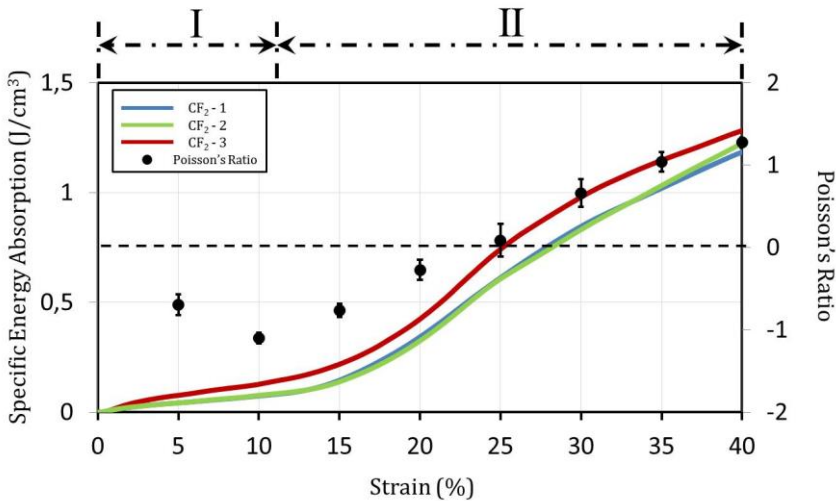


Figure 5-7 Accumulative specific energy absorption of CF_2 (left y axis) and Poisson's Ratio (right axis) at different strain level for both stages are indicated by dashed lines, standard deviation are indicated for Poisson's ratio value

5.3.3 Behavior of CCCs under cyclic loading

As mentioned previously, CF_2 specimens may have an "elastic" regime in stage "II" from the beginning until one third of the peak load in this stage. Therefore, CF_2 specimens were also submitted to cyclic loading within the presumable elastic range in stage "II" from 11.25% strain to 13.75% strain (one third displacement of the peak load, see Figure 5-8a). In order to reach this range, the specimens were first pre-compressed from 0 % strain to 12.5% strain by 0.01mm/s which is the same as the uniaxial compression tests and then subjected to cyclic loading with a constant amplitude of 1.25% strain (1 mm) and frequency of 1Hz by a sine wave. The curve of stress versus time and strain versus time at the beginning several cycles is also shown in Figure 5-8b.

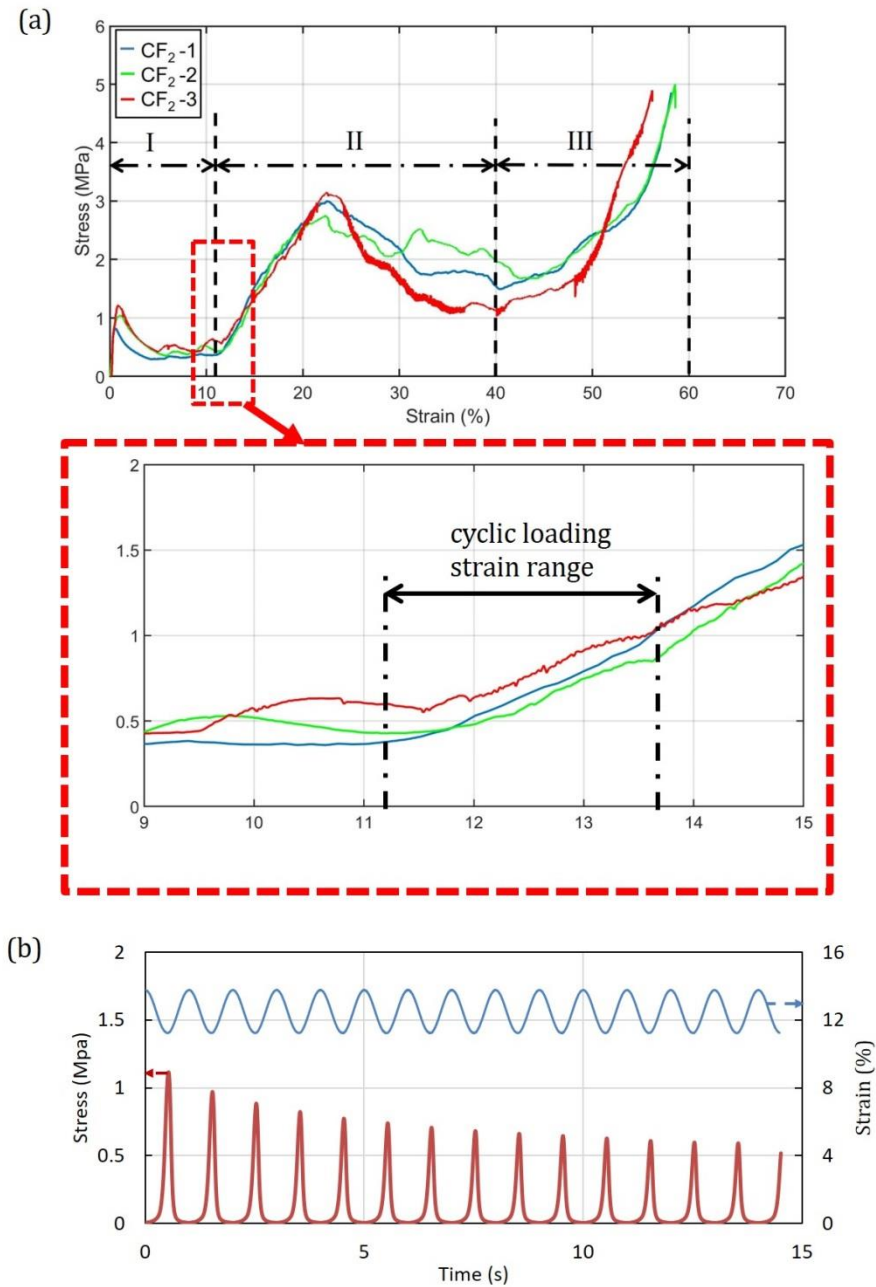


Figure 5-8 (a) Cyclic loading range in the secondary rise, magnified on the stress-strain curves of CF₂ within the red window; (b) stress-time curve in red and strain-time curve in blue at the beginning several cycles.

According to the previous discussion, the tested CCCs exhibit auxetic behavior and they are efficient in energy absorption under quasi-static uniaxial compression. However, more importantly, much energy can be dissipated if CCCs behave flexibly under cyclic loading. The stress-strain curve of CF₂ under cyclic loading at the first cycle is shown in Figure 5-9a ~ Figure 5-9c. As can be seen from the curve, the cyclic loading curve shows a typical hysteresis behavior: the loading branch A-B-C and unloading branch C-D-A do not overlap in one cycle. From Figure 5-9b and Figure 5-9d, it can be seen that the maximum load of each cycle dropped rapidly at the first 3000 cycles (from around 1.3 MPa to 0.18 MPa), which indicates the fatigue damage of the constituent material in those contacted sections and more small cracks may appear in those sections. However, after 3000 cycles the maximum load increased again slowly with the increasing number of cycles (from 0.18 MPa to 0.22 MPa, see Figure 5-9c and Figure 5-9d). A similar trend can be also observed from the specific dissipated energy in one cycle (calculated by the area of shaded region surrounded by the loading and unloading branch in each cycle and divided by the specimen volume, see Figure 5-9e). The energy dissipation decreased rapidly in the beginning followed by a gradual increase after 3000 cycles. This phenomenon is rather interesting: as explained before, fibrillation of PVA fibers causes slip-hardening behavior when fibers are pulled out from cementitious matrix. Similarly, fibrillation of PVA fibers under cyclic loading may generate more small fiber branches [24] and more jamming effects at the fiber-matrix interface can be present, which may be the reason of increased load and energy dissipation after 3000 cycles. The energy dissipation in each cycle is around 4.0×10^{-4} J/cm³ from 3000 cycles to 2.5×10^4 cycles which is rather high compared to other auxetic materials [25-27]. In general, the developed CCCs possessed pseudo-elasticity of 2.5% reversible strain even after 2.5×10^4 cycles, which means that the CCCs is a promising energy dissipating material.

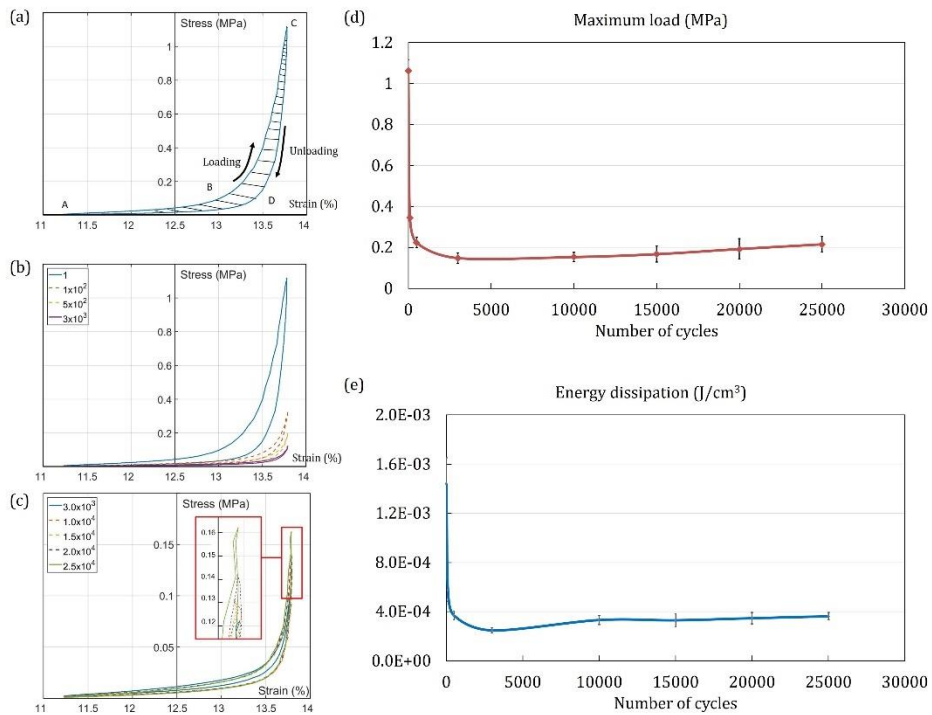


Figure 5-9 (a) stress-strain curve of the first cycle, loading and unloading direction is indicated by black arrow; (b) stress-strain curves of the 1~3000 cycles; (c) stress-strain curves of the 3000~25000 cycles, the maximum load area is magnified within the red window; (d) maximum load versus cycle numbers, standard deviation is indicated; (e) energy dissipation versus cycle numbers, standard deviation is indicated.

5.4 CONCLUSIONS

In this chapter, cementitious cellular composites (CCCs) with auxetic behavior are developed and fabricated with the aid of 3D printing. Mechanical properties of CCCs are evaluated under uniaxial compression and cyclic loading. The influence of crack bridging ability of constituent material on the mechanical behavior of CCCs is studied. Based on the obtained experimental results, several conclusions can be drawn:

- During the compression process of the fiber reinforced CCCs, section rotation is observed accompanied by fiber pulling out at the joints of each individual cell. As a consequence, auxetic behavior is achieved for the fiber reinforced CCCs.
- The auxetic behavior of CCCs is induced by crack bridging effect of the constituent fiber reinforced cementitious material. Only when fiber slipping strength is high enough auxetic behavior can be obtained while no separated cells will be found. For the studied constituent materials in this work, 2% PVA fibers (which gives 2.6MPa of fiber slipping strength) is enough while 0% (no fiber slipping strength) and 1% of PVA fibers (with fiber slipping strength of 1.6MPa) is inadequate.
- Under uniaxial compression, a strain limit of auxetic behavior is found for the tested specimens in this work. CF_2 has a strain limit of 20% up to which the CCCs

exhibit negative Poisson's ratio. Owing to the rotation of the sections in each single cell, sections contact increases as the compression continues, making CF₂ show strain hardening behavior under compression.

- For the developed CCCs (CF₂), a pseudo-elastic regime is found between 11.25%~13.75% strain (in total 2.5% compressive deformation). In 2.5×10^4 cycles, within this regime, CF₂ shows flexible behavior and excellent energy dissipation.
- Comparing to traditional cementitious materials, the fatigue damage of CF₂ is unique during the cyclic loading process: in the first 3000 cycles, fatigue damage in the cementitious matrix is significant which is indicated by the rapid drop of the maximum load. Afterwards, the maximum load starts to increase again. A corresponding trend is also found on the energy dissipation in each cycle. The regain in maximum load and energy dissipation implies that CCCs can recover fatigue damage under cyclic loading. A possible reason of this phenomenon could be the fibrillation of PVA fibers under numerous cyclic loads.

To the best of the authors' knowledge, this is the first time that auxetic behavior has been observed in cementitious materials. The properties such as of the developed CCCs can be improved by modifying the cellular structure and the constituent material. This is studied further in the next chapter.

REFERENCES

- [1] K.E. Evans, Auxetic polymers: a new range of materials. *Endeavour*, *Endeavour* 15(4) (1991) 170-174.
- [2] V.L. Coenen, K.L. Alderson, Mechanisms of failure in the static indentation resistance of auxetic carbon fibre laminates, *physica status solidi (b)* 248(1) (2011) 66-72.
- [3] D. Photiou, N. Prastiti, E. Sarris, G. Constantinides, On the conical indentation response of elastic auxetic materials: Effects of Poisson's ratio, contact friction and cone angle, *International Journal of Solids and Structures* 81 (2016) 33-42.
- [4] L.L. Hu, M.Z. Zhou, H. Deng, Dynamic indentation of auxetic and non-auxetic honeycombs under large deformation, *Composite Structures* 207 (2019) 323-330.
- [5] H.C. Cheng, F. Scarpa, T.H. Panzera, I. Farrow, H.-X. Peng, Shear Stiffness and Energy Absorption of Auxetic Open Cell Foams as Sandwich Cores, *physica status solidi (b)* 256(1) (2019) 1800411.
- [6] C. Qi, A. Remennikov, L.-Z. Pei, S. Yang, Z.-H. Yu, T.D. Ngo, Impact and close-in blast response of auxetic honeycomb-cored sandwich panels: Experimental tests and numerical simulations, *Composite Structures* 180 (2017) 161-178.
- [7] Y. Wang, W. Zhao, G. Zhou, Q. Gao, C. Wang, Suspension mechanical performance and vehicle ride comfort applying a novel jounce bumper based on negative Poisson's ratio structure, *Advances in Engineering Software* 122 (2018) 1-12.
- [8] J. Ju, J.D. Summers, Compliant hexagonal periodic lattice structures having both high shear strength and high shear strain, *Materials & Design* 32(2) (2011) 512-524.
- [9] R.R. Madke, R. Chowdhury, Anti-impact behavior of auxetic sandwich structure with braided face sheets and 3D re-entrant cores, *Composite Structures* 236 (2020) 111838.
- [10] N.D. Duc, K. Seung-Eock, P.H. Cong, N.T. Anh, N.D. Khoa, Dynamic response and vibration of composite double curved shallow shells with negative Poisson's ratio in auxetic honeycombs core layer on elastic foundations subjected to blast and damping loads, *International Journal of Mechanical Sciences* 133 (2017) 504-512.
- [11] Y.-L. Chen, X.-T. Wang, L. Ma, Damping mechanisms of CFRP three-dimensional double-arrow-head auxetic metamaterials, *Polymer Testing* 81 (2020) 106189.
- [12] X. Ren, Studies on three-dimensional metamaterials and tubular structures with negative Poisson's ratio, RMIT University, Australia, 2017.
- [13] M. Taylor, L. Francesconi, A. Baldi, X. Liang, F. Aymerich, A Novel Auxetic Structure with Enhanced Impact Performance by Means of Periodic Tessellation with Variable Poisson's Ratio, (2019) 211-218.
- [14] C. Coulais, J.T. Overvelde, L.A. Lubbers, K. Bertoldi, M. van Hecke, Discontinuous Buckling of Wide Beams and Metabeams, *Phys Rev Lett* 115(4) (2015) 044301.
- [15] J.G. Van Mier, Fracture processes of concrete, CRC press 1997.
- [16] V.C. Li, C. Wu, S. Wang, A. Ogawa, T. Saito, Interface tailoring for strain-hardening polyvinyl alcohol-engineered cementitious composite (PVA-ECC), (2002).
- [17] V.C. Li, From micromechanics to structural engineering-the design of cementitious composites for civil engineering applications, (1993).
- [18] Z. Lin, T. Kanda, V.C. Li, On interface property characterization and performance of fiber-reinforced cementitious composites, *Concrete Science and Engineering* (1999).
- [19] A.J. Uddin, J. Araki, Y. Gotoh, M. Takatera, A novel approach to reduce fibrillation of PVA fibres using cellulose whiskers, *Textile Research Journal* 81(5) (2011) 447-458.
- [20] Z. Dong, Y. Li, T. Zhao, W. Wu, D. Xiao, J. Liang, Experimental and numerical studies on the compressive mechanical properties of the metallic auxetic reentrant honeycomb, *Materials & Design* (2019) 108036.
- [21] K. Meena, S. Singamneni, A new auxetic structure with significantly reduced stress concentration effects, *Materials & Design* 173 (2019) 107779.
- [22] H. Yang, B. Wang, L. Ma, Mechanical properties of 3D double-U auxetic structures, *International Journal of Solids and Structures* (2019).

- [23] Y. Jiang, B. Rudra, J. Shim, Y. Li, Limiting strain for auxeticity under large compressive Deformation: Chiral vs. re-entrant cellular solids, *International Journal of Solids and Structures* 162 (2019) 87-95.
- [24] W. SeokLyoo, W. ShikHa, In situ fibrillation of poly(vinyl alcohol) during saponification of poly(vinyl ester) (1). Chemorheological and morphological investigations of in situ fibrillation, *Polymer* 40(2) (1999).
- [25] J. Ju, J.D. Summers, J. Ziegert, G. Fadel, Cyclic energy loss of honeycombs under in-plane shear loading, (2009) 283-289.
- [26] R. Critchley, I. Corni, J.A. Wharton, F.C. Walsh, R.J.K. Wood, K.R. Stokes, A review of the manufacture, mechanical properties and potential applications of auxetic foams, *physica status solidi (b)* (2013) 1963-1982.
- [27] M. Bianchi, F.L. Scarpa, C.W. Smith, Stiffness and energy dissipation in polyurethane auxetic foams, *Journal of Materials Science* 43(17) (2008) 5851-5860.

6

TUNABLE MECHANICAL BEHAVIOR OF AUXETIC CEMENTITIOUS CELLULAR COMPOSITES

This chapter presents an investigation of the compressive behavior of auxetic cementitious cellular composites (CCCs) using a combination of experiments and finite element (FE) simulations. Similar to the previous chapter, centrosymmetric geometry and fiber reinforced cementitious mortar were used as the cellular structure and constituent material, respectively. By varying the cellular geometry, three CCCs (P0, P25 and P50) were experimentally and numerically tested under uniaxial compression to investigate the influence of structural parameters on the compressive behavior of the CCCs. Good agreement is found between experimental and FE simulated results: only CCCs with chiral sections (P25 and P50) exhibited auxetic behavior and the typical compressive stress-strain response with two peaks is found. More importantly, a cracking-initiated section rotation mechanism behind the CCCs' auxetic behavior (mentioned in Chapter 5) is clarified.

6.1 INTRODUCTION

Auxetic behavior is usually achieved by introducing special cellular structures [1, 2]. By programming the cellular structure [2, 3] or modifying the constituent materials [4], mechanical properties of the auxetic materials can be rationally designed. The centrosymmetric chiral structures adopted in the previous chapter are usually identified as “elastic-instability” structures in which the auxetic mechanism is attributed to elastic buckling. In this sense, materials with high deformability, such as polymeric materials, are often used for this type of structures to achieve auxetic behavior. However, the basic NPR (negative Poisson’s ratio) mechanism in the auxetic cementitious cellular composites (CCCs) has not yet been fully understood.

Programming cellular structures of the auxetic cementitious materials makes a new material developing strategy which, however, requires a rational understanding on the NPR mechanism and the impact of geometrical features on the mechanical behavior of auxetic materials. In this chapter, an in-depth investigation of the mechanical behavior of auxetic CCCs with tuned structural features is presented. In addition to experiments, finite element numerical models are adopted, calibrated and used to simulate the compression process of the CCCs as a supplementary tool for understanding the deformation and fracture mechanism of the CCCs.

6.2 METHODS AND MATERIALS

6.2.1 Geometry design parameters

The same types of cellular structure as in the previous chapter were used in this chapter however, structural parameters were varied. A single unit cell of the CCCs is shown in Figure 6-10. Geometry parameters are listed in Table 6-3. The designed CCCs consist of duplicate unit cells: an example of the designed CCCs is shown in Figure 6-11. The pattern deformation factor of each group is defined as the increased length percentage of the major axis comparing to P0.

Table 6-3 Specimen groups with different design parameters and boundary conditions

Specimen groups	Major axis (mm)	Minor axis (mm)	Ellipse Area (mm ²)	Pattern deformation factor	Specimen Volume (cm ³)	Relative density
P0	8	8	50.24	0	63.66	49.7%
P25*	10	6	47.10	25	67.68	52.8%
P50	12	4	37.68	50	79.75	62.3%

*P25 used identical structure as the previous chapter

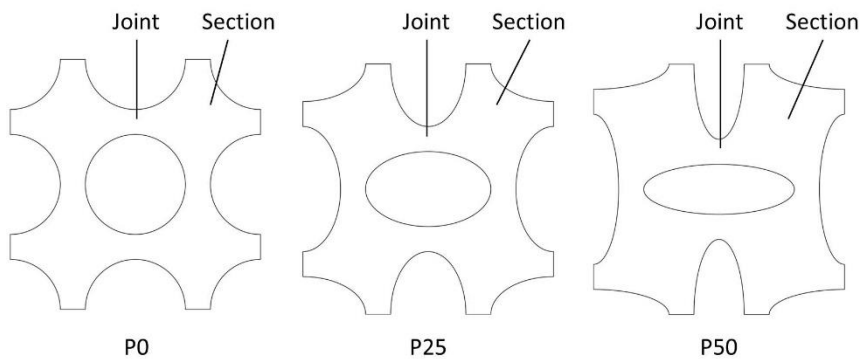


Figure 6-10 Design parameters of cementitious cellular composites

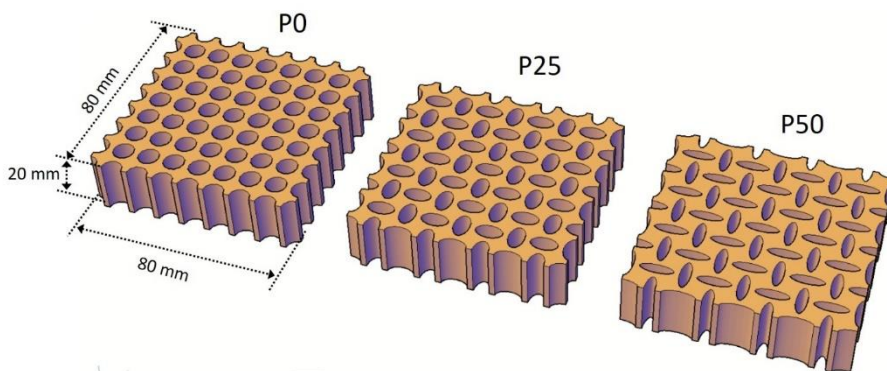


Figure 6-11 Designed CCCs specimens

6.2.2 Casting and curing

The same fiber reinforced material mixture (F_2 in Chapter 5) and method described in the previous chapter was also adopted to prepare the CCCs specimens. The difference was that the specimens varied in design parameters. Note that, depending on the printing quality, the actual dimension of the molds may vary within 0.8 mm from the design parameters because the 0.8mm nozzle was used and the actual geometry of the prepared specimen by 3D printer may fluctuate a bit within this range. In order to calibrate the numerical model (ABAQUS/Explicit), bar specimens ($100 \times 30 \times 8$ mm) and cubic specimens ($20 \times 20 \times 20$ mm) were cast using the same mixture.

6.2.3 Mechanical tests

At the age of 28 days, all specimens were taken out of the curing chamber an hour before testing. The bar specimens were tested under uniaxial tension, and cubic specimens were tested under uniaxial compression. For tension tests, the bar specimens were glued (clamped) on steel loading plates; for compression tests, a plastic film was placed between the cube specimens and loading plates. All tests were performed by displacement control at a constant rate of 0.01 mm/s. The results of these tests are presented in the next section where the numerical modelling is discussed.

6.3 NUMERICAL MODELLING

6.3.1 Model description

In order to provide further understanding of the compressive behavior and NPR mechanism of the CCCs, numerical models were adopted to simulate the compression process of the CCCs. From Chapter 3 and Chapter 4, the Delft lattice model which used beam elements was proven to be suitable to simulate the deformation and fracture behavior of lattice materials. Good agreement was found between experimental and numerical results. However, principal stress distribution in the cellular material was not able to be precisely indicated by the beam elements used in the Delft lattice model. In addition, the deformation of the CCCs involved complex contact problems which is extremely difficult to be implemented in the Delft lattice model. Therefore, in this chapter, the numerical simulations were performed by a commercial numerical package (ABAQUS/Explicit) using two dimensional solid elements. Geometric nonlinearity (Nlgeom) was used and concrete damage plasticity model (CDPM) which is commonly used for simulating fiber reinforced cementitious materials [5-7] in ABAQUS, was used as material model for the constituent material in this chapter. According to ABAQUS documentation[8], the constitutive equation of CDPM can be described as follows:

$$\sigma = (1 - d)E_0(\varepsilon - \varepsilon^{pl}) \quad (6-1)$$

where σ is Cauchy stress; ε and ε^{pl} are total strain and equivalent plastic strain, respectively; E_0 is initial elastic modulus. In the presence of modulus degradation, d is damage variable and can be defined from 0 to 1 and it requires that the d increases monotonically with strain. Here, as fiber reinforced cementitious material was used, the stress doesn't decrease monotonically with strain when the material was loaded in tension. Hence, stiffness degradation was not able to be considered in this chapter.

The yield criterion beyond which the plastic strain initiates of CDPM is given as:

$$F = \frac{1}{1 - \alpha} (\bar{q} - 3\alpha\bar{p} + \beta(\bar{\varepsilon}^{pl})\langle \hat{\sigma}_{max} \rangle - \gamma\langle -\hat{\sigma}_{max} \rangle) - \hat{\sigma}_c(\bar{\varepsilon}_c^{pl}) = 0 \quad (6-2)$$

With

$$\alpha = \frac{(\sigma_{b0}/\sigma_{c0}) - 1}{2(\sigma_{b0}/\sigma_{c0}) - 1} \quad (6-3)$$

$$\beta = \frac{\bar{\sigma}_c(\bar{\varepsilon}_c^{pl})}{\bar{\sigma}_t(\bar{\varepsilon}_t^{pl}) - 1} (1 - \alpha) - (1 + \alpha) \quad (6-4)$$

$$\gamma = \frac{3(1 - K_c)}{2K_c - 1} \quad (6-5)$$

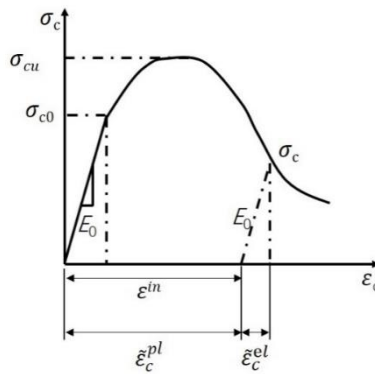
where, $\hat{\sigma}_{max}$ is the maximum principal effective stress; σ_{b0}/σ_{c0} is the ratio of initial equi-biaxial compressive yield stress to initial uniaxial compressive yield stress for which the default value from ABAQUS 1.16 is adopted. K_c describes the tensile meridian second stress invariant to that on the compressive meridian for a given invariant p , $0.5 < K_c \leq 1$ must be satisfied and as an ABAQUS default value $K_c = 0.667$ is also adopted by different researches[7, 9].

Non-associated potential plastic flow is assumed for CDPM, and the flow potential G is described as:

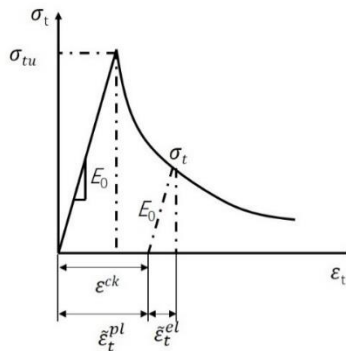
$$G = \sqrt{(\epsilon \sigma_{t0} \tan \psi)^2 + \bar{q}^2} - \bar{p} \tan \psi \tag{6-6}$$

where ψ is the dilation angle, σ_{t0} is the uniaxial tensile failure strength, ϵ is the eccentricity which determines the rate at which the function approaches the asymptote. $\epsilon = 0.1$ is adopted as a default value.

According to CDPM, uniaxial compression and tension response are characterized by plasticity, the evolution of the failure is controlled by compressive plastic strain $\tilde{\epsilon}_c^{pl}$ and tensile plastic strain $\tilde{\epsilon}_t^{pl}$, respectively. These two variables can be determined by material uniaxial loading behavior, as shown in Figure 6-12. Under compression, the failure stress (σ_{c0}) corresponds to the onset of micro-cracking of the cementitious material after elastic stage. Under tension, the failure stress (σ_{tu}) corresponds to the ultimate tensile strength. The compressive inelastic strain (ϵ^{in}) and tensile crack strain (ϵ^{ck}) is defined as the total strain minus the elastic strain corresponding to the undamaged material, respectively. In this chapter, E-modulus degradation is not defined, in this sense compressive plastic strain $\tilde{\epsilon}_c^{pl} = \epsilon^{in}$ and tensile plastic strain $\tilde{\epsilon}_t^{pl} = \epsilon^{in}$.



(a)



(b)

Figure 6-12 The definition of uniaxial a) compressive and b) tensile behavior for CDPM

6.3.2 Model calibration

Prior to simulating the uniaxial compression behavior of the CCCs, the models were calibrated to obtain proper input parameters. By fitting the uniaxial compression tests on the cubic specimens and the uniaxial tension tests on the bar specimens, compressive behavior parameters and tensile behavior parameters of the constituent material can be obtained as model inputs. In terms of the element type and size, of course using three dimensional and very fine elements would be more precise; however, this requires high computational efforts. As the studied specimens all have two-dimensional cellular structures and the minimum joint of the cellular structure is 2mm, two-dimensional plane stress elements with a mesh size of 0.5mm (a quarter of the minimum joint size) were chosen and kept constant for all numerical simulations in this chapter. As described previously, in the CDPM inelastic and cracking strains are used to model the material damage in compression and tension, respectively. Therefore, besides the elastic modulus, density (shown in Table 6-4) and plasticity parameters (adopted from literature where a similar mix was used [7]), inelastic regime (compression) and post peak cracking regime (tension) of the stress-strain response need to be specified to simulate the damage process. Figure 6-13a shows the stress-strain curves (blue dashed lines) of the cubic specimens obtained from uniaxial compression experiments. As the constituent material is fiber reinforced, a ductile compressive damage behavior can be identified from the experimental results: stress increased as compression initiated and kept increasing until compressive strength was reached. Afterwards, the stress started to drop slowly which is normally described as a softening branch [10, 11]. Comparing to the typical quasi-brittle damage of an unreinforced cementitious material [10, 11], the softening branch of fiber reinforced cementitious material is considerably longer as the fibers significantly increase the material ductility. In the stress-strain curves (see Figure 6-13a), a long plateau stage was observed from experiments. Several points were chosen by averaging strain and stress values based on the experiment curves (plotted as black dots connected by green line in Figure 6-13a) and then used as material inputs for simulation (listed in Table 6-5 and Table 6-6, note that in ABAQUS, tension input strain need to be converted to displacement accordingly), the material compressive curve is plotted as green line in Figure 6-13a). A numerical compression test was performed using the constitutive curve. The simulated result is also plotted in Figure 6-13a, marked as “Calibration” (red line). The simulated compression curve shows good agreement with experiment curves, meanwhile the crack pattern shows reasonable indicating that the material compressive parameters are calibrated.

A similar calibration approach was also applied for tension model input parameters. The comparison of the model input curves and the experimental curves are shown in Figure 6-13b. After the first crack (witnessed by a sharp drop of the stress-inelastic strain curve), the specimen did not fail completely, owing to the so called “slip hardening” behavior described in the previous chapter. Due to this slip hardening behavior, the load still increased again until a second peak was reached. As a result, the slip-hardening behavior cannot easily be captured by the simulation; therefore, the

simulated second peak is slightly lower than the experiment (Figure 6-13b red line). In any case, the simulated curve still shows good agreement with the experimental result, in this case the tension model input parameters are also well calibrated regarding the good agreement between simulation and experiment. In this chapter, the damage parameters were not assigned. Therefore, according to the CDPM constitutive law, compressive inelastic strain and tensile cracking strain are assumed to be equal to plastic strain which indicates damage, as described previously. The damage pattern of the compression and tension calibration is shown in Figure 6-14, localized damage (plastic strain) can be observed.

Table 6-4 Material input parameters

Material input parameters	Value
Density (kg/m ³)	1870
Elastic Modulus (MPa)	8230
Poisson's Ratio	0.2
Dilation Angle (ψ , °)	35
Eccentricity (ϵ)	0.1
σ_{b0}/σ_{c0}	1.16
K_c	0.667
Viscosity Parameter	0.001

Table 6-5 Compressive behavior parameters

Yield Stress (MPa)	Inelastic Strain (%)
12.16	0
20.53	1.49
15.06	6.39
14.08	13.13
14.46	18.21
14.47	24.56

Table 6-6 Tensile behavior parameters

Yield Stress (MPa)	Cracking Strain (%)
1.74	0
0.50	0.05
1.08	0.26
1.08	0.48
0.85	0.73
0.49	1.17
0.10	2.00

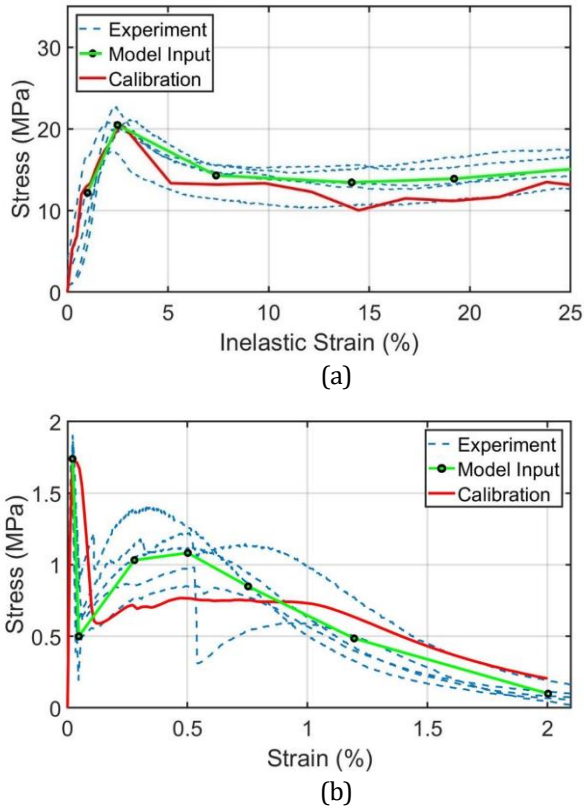
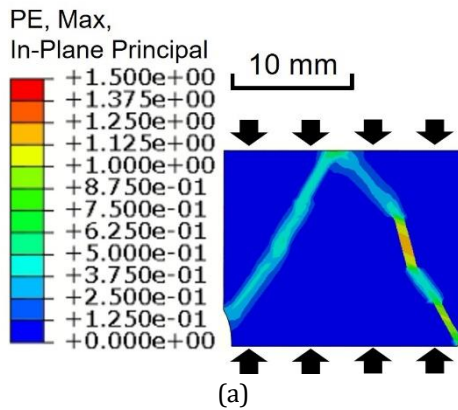


Figure 6-13 Comparison of experimental, model input and calibration curves in (a) uniaxial compression and (b) uniaxial tension



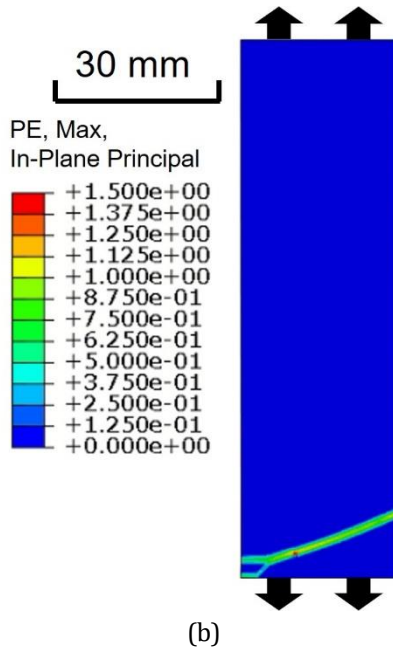


Figure 6-14 Damage pattern of a) compression calibration specimen and b) tensile calibration specimen, plastic strain is indicated

6.3.3 Simulation of compressive tests on CCCs

Abaqus/Explicit was used to simulate the compression process of the CCCs. As shown in Figure 6-15, in order to simulate the real experimental condition of the compression tests, in the numerical model external load was not directly applied on the specimen; instead, two loading plates were added as rigid body parts and placed at the top and the bottom of the specimen. Vertical displacement was applied downwards on the top plate while the bottom plate was fixed.

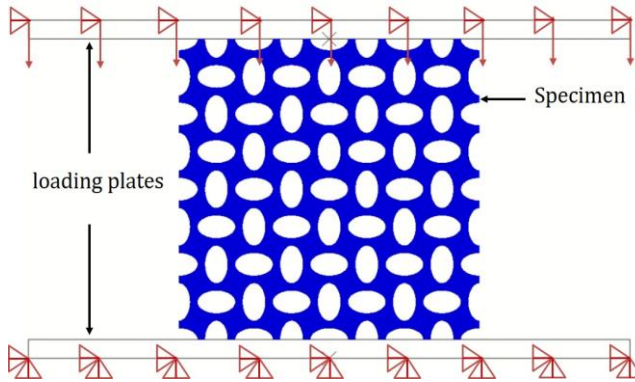


Figure 6-15 Simulation set-up for compression of the CCCs

Although plastic films were applied between the specimen and loading plates, slight friction still occurred during experimental testing. Therefore, a low friction

coefficient 0.105 was assumed and used to simulate the slight friction between the specimen and loading plates. Note that the friction coefficient may affect the post peak behavior of cementitious materials, in this case this parameter is determined based on a trial-and-error method: the friction coefficient is increased from 0 until the specimen does not show unrealistic slide along the loading plates. A similar process is also used to determine the friction coefficient between the constituent material elements. Linear normal contact was used and 8000 MPa (same level to the constituent material E-modulus) contact stiffness. Penalty friction coefficient of 0.95 was used for the tangential contact and the 0.2 MPa was assumed for the shear stress limit as well as 2000 MPa was assumed for the elastic slip stiffness. As the Explicit package was used, not static but real quasi-static loading condition was applied. In case the simulation was performed using the real loading strain rate, the computational cost was extremely large. Therefore, for this type of simulations mass scaling technique is commonly used as long as the kinetic energy is obviously lower than the internal energy of the entire system.

6.4 RESULTS AND DISCUSSION

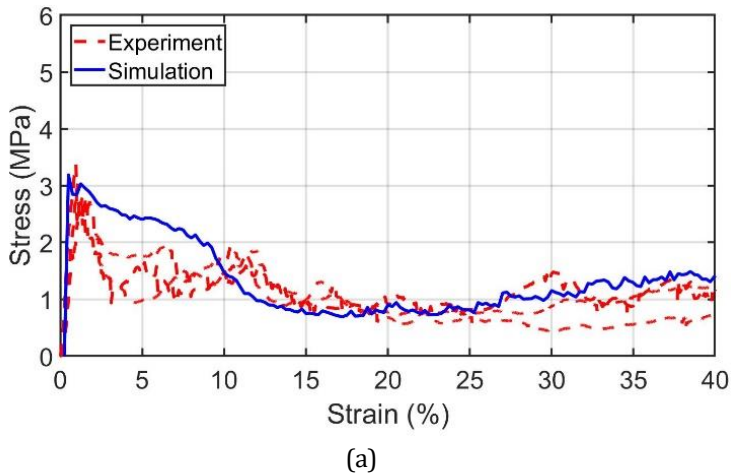
6.4.1 Influence of geometrical features

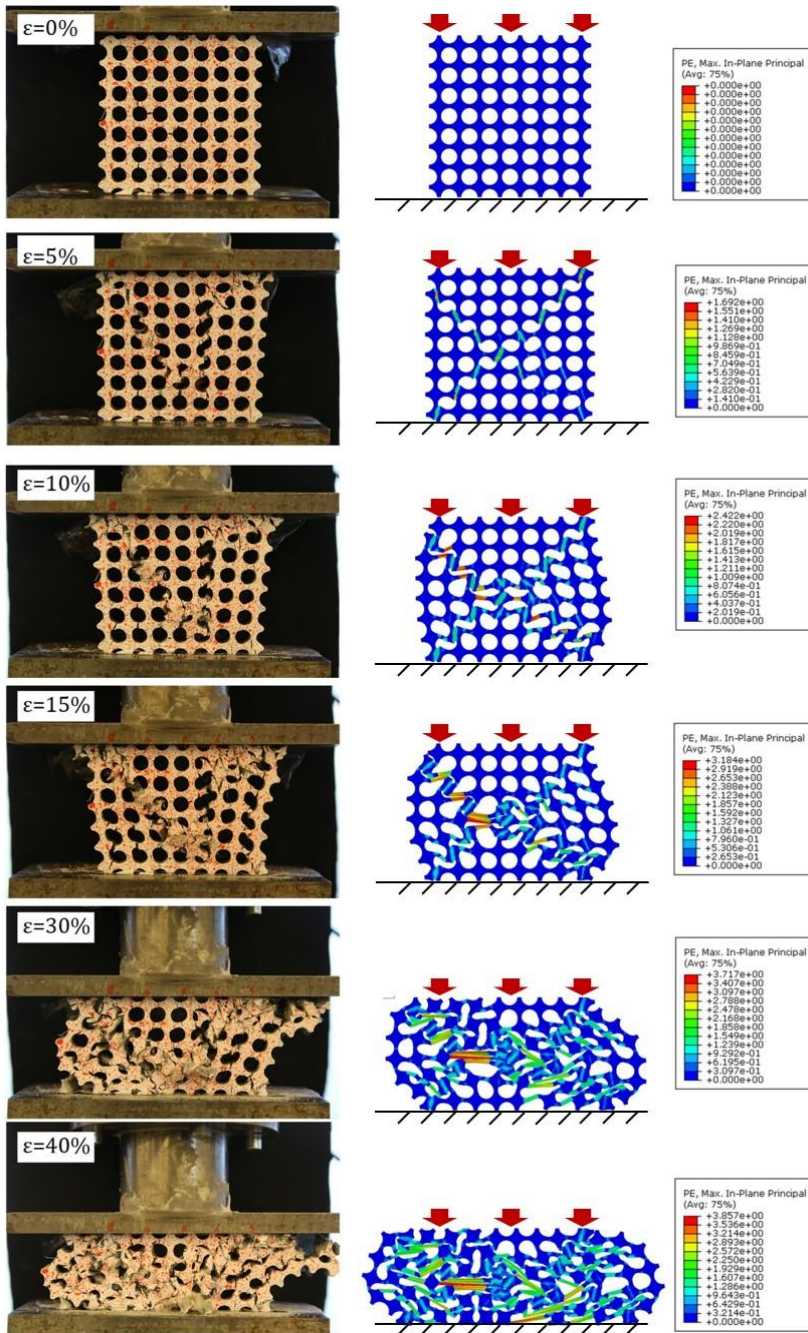
Figure 6-16 to Figure 6-18 show the stress-strain curves and compression process (until 40% strain) obtained from experiments and numerical simulations of the CCC specimens. Note that as the CDPM is used in the simulation, cracks are simulated by plastic deformation. Therefore, highly deformed locations in Figure 6-16 to Figure 6-18 show high plastic strain which correspond to the cracked regions observed in the experiments. In general, owing to the difference in geometrical features, P0, P25 and P50 behave significantly different during the compression process. With regard to the entire compressive behavior, for all three different geometries tested, a very good agreement was found between experimental results and numerical simulations.

The compressive behavior of P0 resembles the compressive damage process of conventional fiber reinforced cementitious materials [6, 12]: a single peak can be found during the entire compression process. In the pre-peak regime, an ascending branch can be observed (Figure 6-16a), the specimen deformed elastically as soon as external load was applied. When the peak load was reached, cracks started to appear and propagate through the cellular structure. It can be seen from both experiment and simulation in Figure 6-16b that cracks (high strain area) propagated through the cellular structure by connecting the hollow parts of the specimen forming shear crack planes which is commonly found in the compressive failure process of conventional cementitious materials [10]. Cementitious materials are very heterogenous, and their compressive failure is a process of tensile microcracking (Mode I fracture at microscale) inclined to the shear direction [13]. Depending on the boundary conditions, the inclination angle of the shear fracture plane varies: under frictionless condition, an inclination around 21 degrees has been observed [10]. For cellular materials, the fracture plane must follow the configuration of the cellular structure/elements, as voids

cannot transfer stresses. In this chapter, the shear fracture plane must follow the “section” part in each single unit which has the highest stress as the “section” are the load bearing part of the cellular structure. The diagonal shear fracture plane can be also witnessed from the experimental result. A symmetric diagonal plane from top left to bottom right direction can be observed in the experiment. However, since the top and the bottom surface of the experimental sample are not perfectly flat, the shear plane is not exactly diagonal but somewhat deflected. Eventually, cracks propagated through the entire structure leading to the failure of the compressed specimen. Correspondingly, from stress-strain curves (Figure 6-16a), a long descending branch can be witnessed in the post peak regime.

Within the entire compression process P0 did not show auxetic behavior, which is different from the behavior of similar P0 structure made using highly elastic polymers [14]. The Poisson's ratio development with strain of P0 can be seen in Figure 6-19.





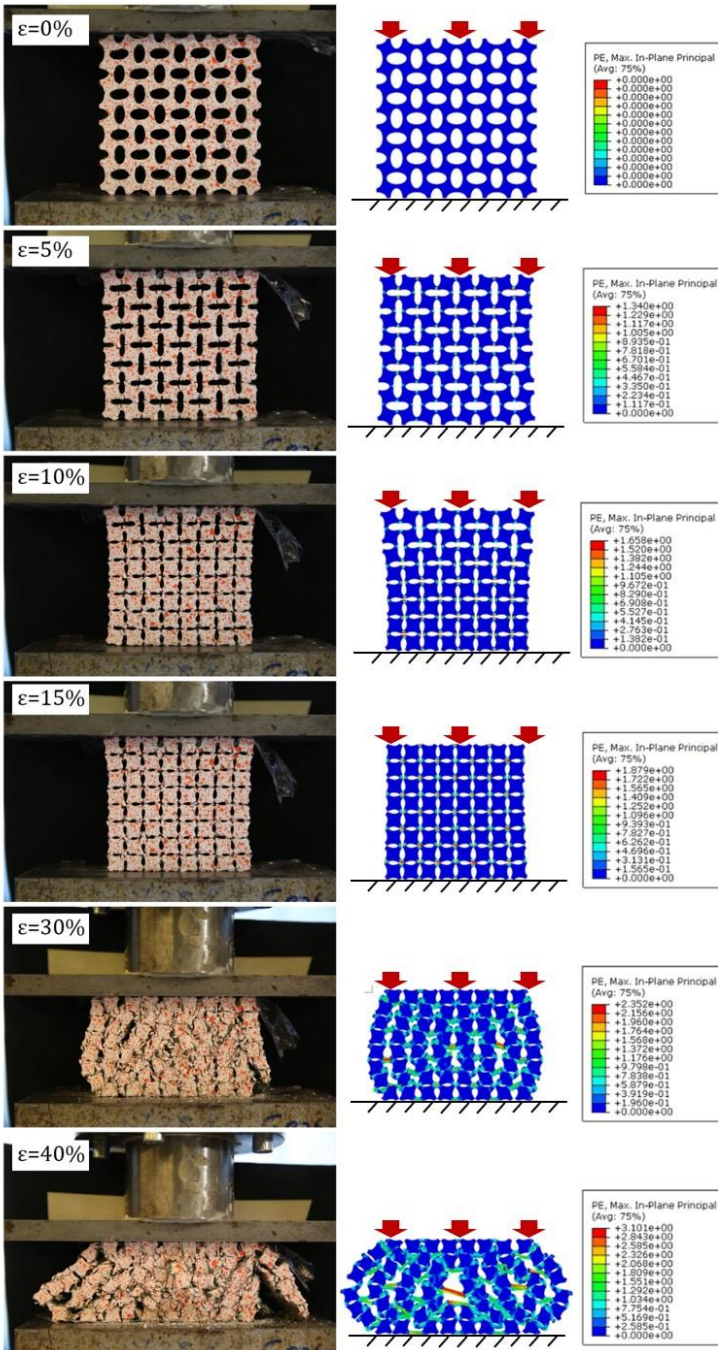
(b)

Figure 6-16 Experiment and numerical simulation of P0, a) stress-strain curves, b) compression process, cracks are indicated by plastic strain

The compressive behavior of P25 and P50 is substantially different: an obvious lateral contraction can be witnessed when P25 (see Figure 6-17a) and P50 (see Figure 6-17b) were compressed. Namely, the NPR or the so-called auxetic behavior was achieved within this process. P25 and P50 are therefore categorized as ACCCs (auxetic CCCs) in the context below. As defined in the previous chapter, the experimental compression process of these ACCCs is divided into two stages until 40% of strain (marked in Figure 6-18). In the first stage, both from the experiment and the simulated curves, the stress-strain response of the ACCCs looks quite similar to that of P0: a peak load can be found which consisted of an ascending branch and a long descending branch. The compression process of the ACCCs, however, is rather different. As can be seen from (Figure 6-17) the ACCCs exhibit obvious lateral contraction during the entire first stage, the cellular structure of the ACCCs was generally damaged and eventually disappeared until the ACCCs were compacted to resemble a “continuum material”. More detailed information can be found from the Poisson’s ratio curves in Figure 6-19. For all three cellular structures, the experimental measured Poisson’s ratio shows good agreement with the simulated results: during the entire compression process P0 shows lateral expansion, a positive Poisson’s ratio was obtained as a result. Comparatively, P25 and P50 show lateral contraction as soon as the compression initiated. For the ACCCs, the division of compression stages is based on their stress-strain response as well as the corresponding development of the Poisson’s ratio. Throughout the first stage, the Poisson’s ratio kept decreasing until a minimum Poisson’s was reached at a certain strain indicating that the cellular structure was completely compacted. The first stage ended at this strain, afterwards the ACCCs started to expand under compression although the calculated Poisson’s ratio is still negative.

In the first stage, the differences found between P0, P25 and P50 are attributed to their geometrical features. The peak load values of P0, P25 and P50 is normalized by their relative density, both in the experiments and the simulations the first peak (see Figure 6-20a) of P0 is always the highest and P25 is lower while the P50 is the lowest because of the stress concentration induced by the cellular structure under compression. A more in-depth discussion related to the stress concentration induced by geometrical features is presented later. On the other hand, as the sections start to get in contact near the minor axis end of the ellipse and the ellipse minor axis of P25 (6 mm) was higher than P50 (4 mm), P25 had more space in each unit cell to be compressed during the first stage. Therefore, the first stage of P25 ended at 13.5% of strain while P50 ended at 10%.

Normalized E-modulus of the CCCs is shown in Figure 6-20c, obviously the cellular structure drastically decreased the E-modulus of all the CCCs compared to the used constituent material (8.23 GPa). However, for the CCCs as the relative density increases from P0 to P50, the elastic modulus, on the contrary, decreases. This indicates that the deformation pattern or the shape of the cellular structure, and not the density, dominates the elastic response of the CCCs.



(a)

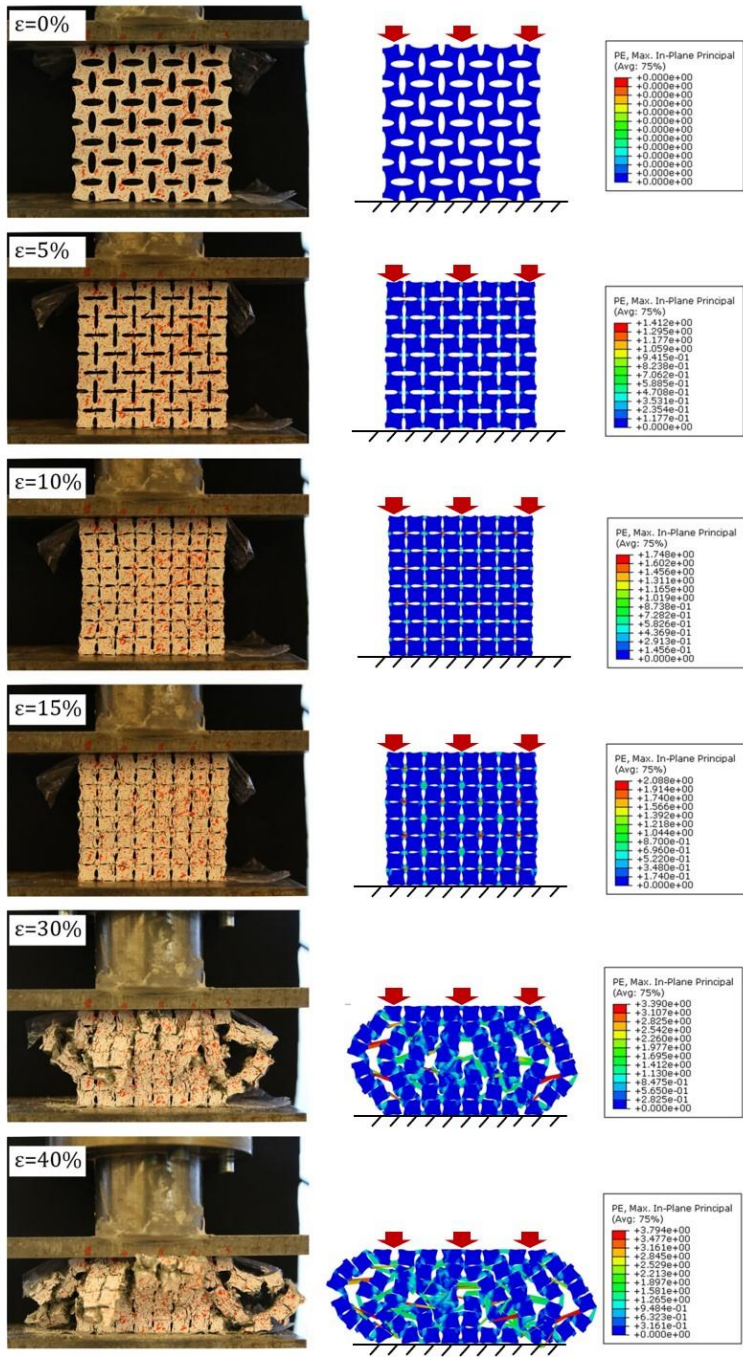
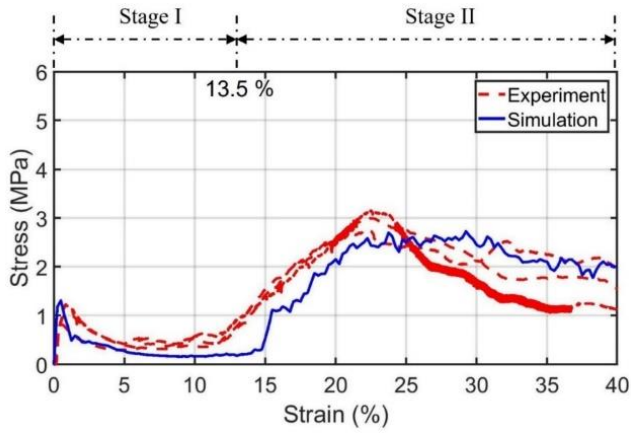
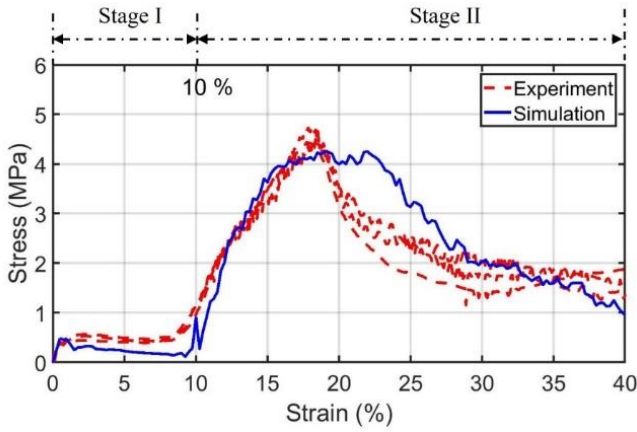


Figure 6-17 Experiment and numerical simulated compression process of a) P25 and b) P50



(a)*



(b)

Figure 6-18 Comparison of stress-strain curves obtained from experiment and simulation of a) P25 and b) P50,

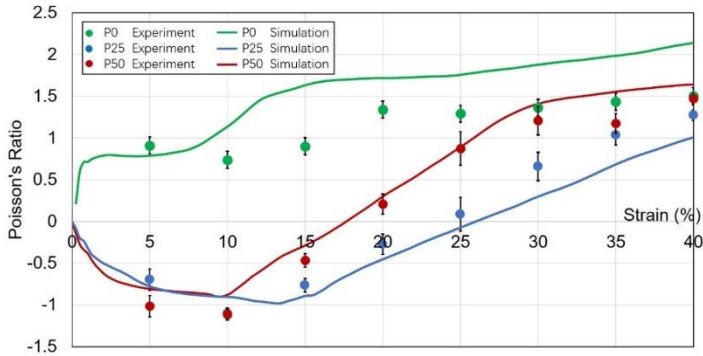


Figure 6-19 Poisson's ratio of P0, P25 and P50 obtained from experiment and simulation, standard deviation is indicated;

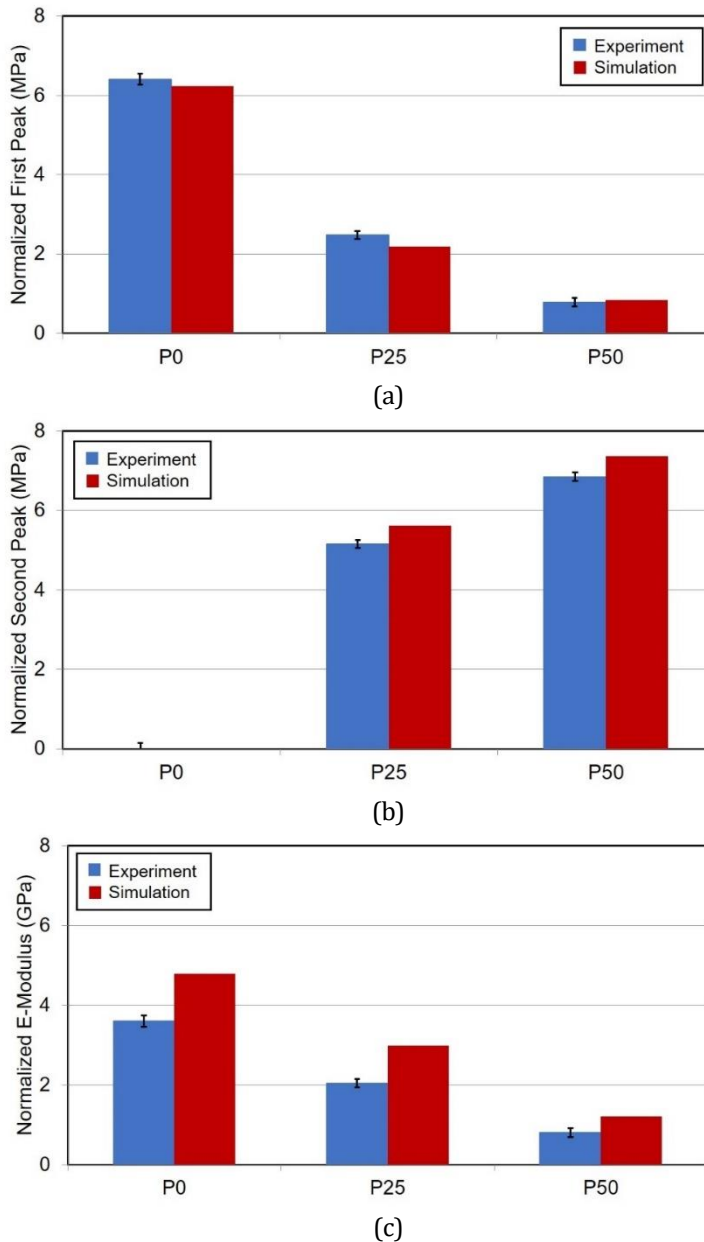


Figure 6-20 Comparison of the a) the normalized first peak load, b) the normalized second peak load and c) normalized E-modulus between experiment and simulation, experiment standard deviation is indicated

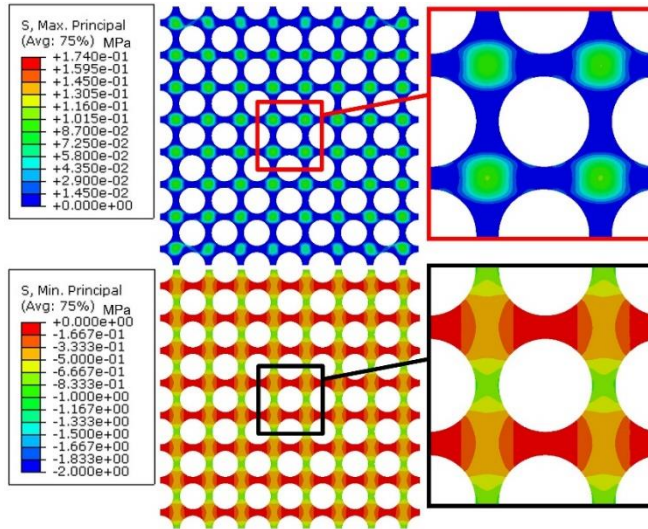
While the first stage indicates the damage and compacting process of the cellular structure, the second stage indicates the damage process of the constituent material. In the second stage, the “sections” of each unit cell started to contact and cracks started to propagate in the sections generally leading to the failure of the compacted “continuum”

constituent material. Accordingly, in the stress-strain curves, a second peak which consisted of another ascending and descending branch can be identified. In this sense, this process is also rather similar to that of conventional fiber reinforced materials. It can be seen from Figure 6-20b, because of higher specimen volume, P50 (79.75 cm^3) has a higher second peak than P25 (67.68 cm^3). The simulated second peak load is slightly lower than the experiment which may be caused by the slight inconsistency in cellular geometry and the boundary friction between the numerical models and the real experimental conditions.

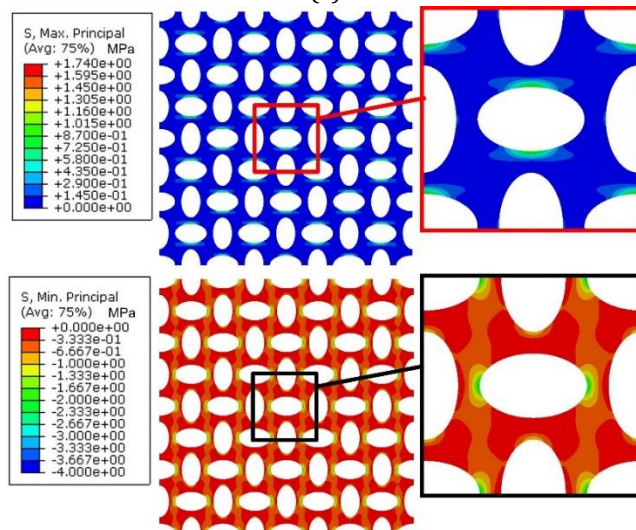
6.5 MECHANISM OF AUXETIC BEHAVIOR

With regard to the auxetic mechanism, a rod-spring model was proposed in [16] for a similar centrosymmetric chiral structure made using the elastomers in which elastic buckling is a crucial factor for the auxetic behavior. For cementitious materials, because of their low deformability, the auxetic behavior is more related to cracking rather than elastic deformation only. Regarding to the auxetic mechanism of the ACCCs in this chapter, more specifically, a hypothesis was proposed in the previous chapter. The origin of this behavior was assumed to be both the crack bridging ability due to the fibers in the constituent material and the chirality of the cellular structure. With the aid of numerical simulations, this hypothesis may be supported.

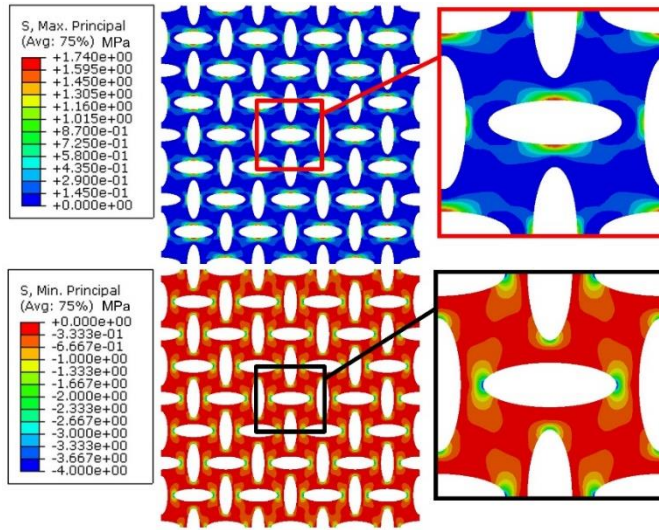
According to the previous chapter, the chirality of the “sections” in each unit cell introduces stress concentration when external compressive load is applied. Figure 6-21 shows the distribution of maximum principal stress (tensile stress) and minimum principal stress (compressive stress) on three cellular structures in the elastic regime subjected to the same load (250 N). It can be seen from Figure 6-21a, for P0 the highest principle tensile stress distributes in the “section” region of the cellular structure which will eventually result in cracking when the principal tensile stress reaches the tensile strength of the constituent material. However, for P25 and P50, the tensile principal stress concentrates in the “joint” region of each unit cell. More importantly, as assumed by [15], when this cellular structure is loaded, because of the section chirality, the “joint” of each unit cell is submitted to a condition similar to a four point bending scheme (shown in Figure 6-22), under which the minor and major axis side of the ellipse are in tension and compression, respectively. The simulation results are in good agreement with this assumption: it can be seen from Figure 6-21b and Figure 6-21c that, for both P25 and P50, the tensile principal stress mainly concentrates at the “joint” near the minor axis side, while the compressive stress mainly concentrates near the major axis side. Owing to the stress concentration, a crack initiates at the tension stress concentrated area as soon as the tensile stress reaches the material tensile strength. Comparing to P25, higher concentrated tensile stress can be found in P50 under the same external load (250 N): the highest tensile stress of P50 at the “joint” is almost exceeding the tensile strength (1.74 MPa) of the constituent material, while the highest tensile stress of P25 is lower than 1MPa. This explains the phenomenon that the first peak load of P50 is lower than P25 (see Figure 6-20a).



(a)



(b)



(c)

Figure 6-21 Maximum and minimum principal stress distribution of a) P0, b) P25 and c) P50, note that the scale of P0 is different from P25 and P50

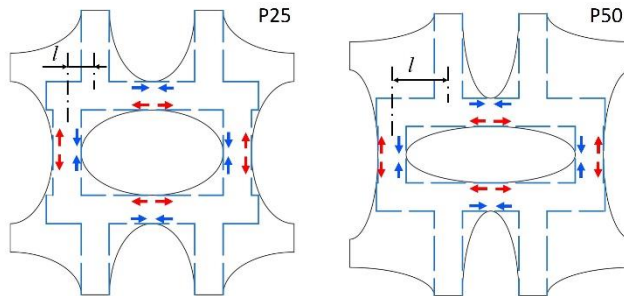


Figure 6-22 Simplified loading scheme of the auxetic CCCs (P25 and P50), blue arrow and red arrow represent compressive and tensile stress respectively

As described in Section 6.4.1, the cellular structure of the ACCCs was destroyed in the first stage. This process was initiated by cracking which subsequently led to compacting of the unit cell until the cellular structure generally disappeared. Auxetic behavior was observed during this process. According to the simulation results, for P25 (Figure 6-23a) and P50 (Figure 6-23b), cracks first appear at the tensile stress concentrated area. The simulation results and the DIC results (see Figure 6-24) show good agreement with regard to the cracking location. After cracking, similar to the rod-spring model described by [15], in each unit cell the joints act as hinges which allows the sections to rotate and eventually the sections get in contact with each other. As the horizontal length of the unit cell decreases with rotation, globally the CCCs exhibit auxetic behavior. In this sense, the behavior can be seen as similar to the rotating square geometries [16-18] where the joints act as nodes and the sections acts as rotating bodies. In addition, because the ellipse minor axis length of P25 (6 mm, see Table 6-3)

is 30% longer than P50 (4 mm, see Table 6-3), a larger strain (3.5% higher than P50) is needed for P25 to be compacted. In summary, the mechanism of the auxetic behavior of ACCCs can be described as cracking initiated section rotation.

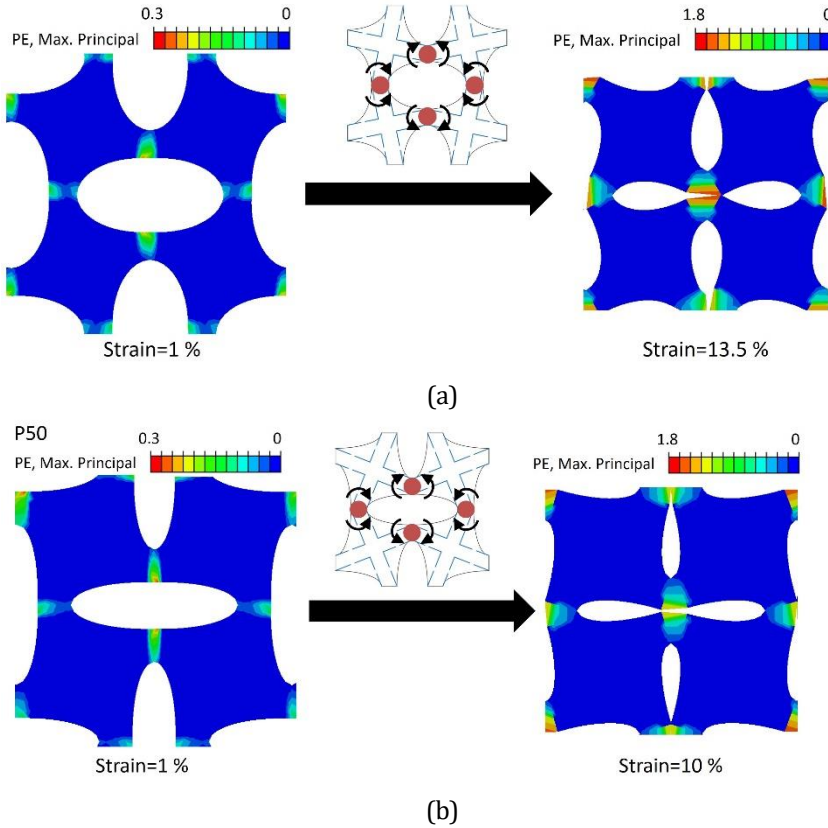


Figure 6-23 Simulated compacting process of a) P25 and b) P50 unit cell by section rotation after cracking, crack is indicated by plastic deformation, plastic strain is indicated

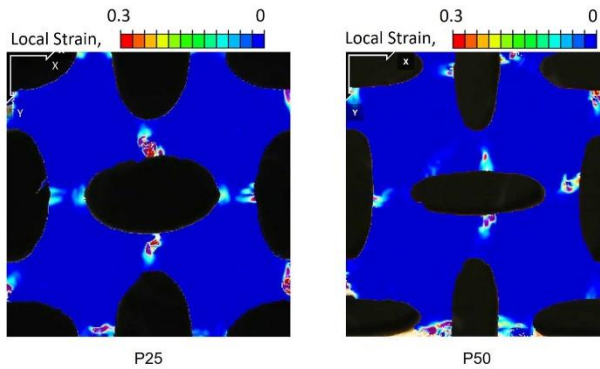


Figure 6-24 DIC results on a unit cell of P25 and P50 at 1% of total strain, high local strain location indicates cracking

6.6 CONCLUSIONS

In this chapter, a study combining experiments and numerical simulations was performed to investigate the compressive behavior of the cementitious cellular composites (CCCs). Based on the obtained experimental and numerical results and the corresponding analysis, main conclusions can be drawn as follows:

- Physical and mechanical properties of the ACCCs can be tuned and modified by varying the pattern deformation factor. Increasing the pattern deformation factor increases the relative density compressive strength while decreasing the E-modulus.
- Compressive deformation patterns of the CCCs are crucially influenced by the geometrical features. Only CCCs with chiral sections (P25 and P50) show negative Poisson's ratio and can be defined as auxetic CCCs (ACCCs).
- A cracking initiated section rotation mechanism is identified as a source of the ACCCs auxetic behavior, in contrast to the elastic buckling mechanism of the elastomers with similar cellular structures.

As discussed in the previous chapter, for a given cellular structure, the ability of section rotation is determined by the crack bridging ability of the constituent material. Only when the constituent material itself has sufficient crack bridging ability the CCCs are able to exhibit auxetic behavior. Reinforcement or toughening phase is able to ensure this crack bridging ability for cementitious materials. Normally fibers are a good choice while in the context of additive manufacturing, 3D printed polymeric structures may be a promising alternative. This will be discussed in detail later in Chapter 8 and Chapter 9.

REFERENCES

- [1] M. Mir, M.N. Ali, J. Sami, U. Ansari, Review of Mechanics and Applications of Auxetic Structures, *Advances in Materials Science and Engineering* 2014 (2014) 1-17.
- [2] M.J. Mirzaali, R. Hedayati, P. Vena, L. Vergani, M. Strano, A.A. Zadpoor, Rational design of soft mechanical metamaterials: Independent tailoring of elastic properties with randomness, *Applied Physics Letters* 111(5) (2017) 051903.
- [3] H.L. Tan, Z.C. He, K.X. Li, E. Li, A.G. Cheng, B. Xu, In-plane crashworthiness of re-entrant hierarchical honeycombs with negative Poisson's ratio, *Composite Structures* 229 (2019) 111415.
- [4] M.J. Mirzaali, A. Caracciolo, H. Pahlavani, S. Janbaz, L. Vergani, A.A. Zadpoor, Multi-material 3D printed mechanical metamaterials: Rational design of elastic properties through spatial distribution of hard and soft phases, *Applied Physics Letters* 113(24) (2018) 241903.
- [5] Y. Tao, J.F. Chen, Concrete Damage Plasticity Model for Modeling FRP-to-Concrete Bond Behavior, *Journal of Composites for Construction* 19(1) (2015).
- [6] Y. Chi, M. Yu, L. Huang, L. Xu, Finite element modeling of steel-polypropylene hybrid fiber reinforced concrete using modified concrete damaged plasticity, *Engineering Structures* 148 (2017) 23-35.
- [7] D. Meng, T. Huang, Y.X. Zhang, C.K. Lee, Mechanical behaviour of a polyvinyl alcohol fibre reinforced engineered cementitious composite (PVA-ECC) using local ingredients, *Construction and Building Materials* 141 (2017) 259-270.
- [8] Dassault, Abaqus documentation, Concrete damaged plasticity(<https://abaqus-docs.mit.edu/2017/English/SIMACAEMATRefMap/simamat-c-concretedamaged.htm>) (2017).
- [9] T. Jankowiak, T. Lodygowski, Identification of parameters of concrete damage plasticity constitutive model., *Foundations of civil and environmental engineering* (2005).
- [10] J.G. Van Mier, *Fracture processes of concrete*, CRC press 1997.
- [11] J.G. Van Mier, *Concrete fracture: a multiscale approach*, CRC press 2012.
- [12] D.-Y. Yoo, N. Banthia, Mechanical properties of ultra-high-performance fiber-reinforced concrete: A review, *Cement and Concrete Composites* 73 (2016) 267-280.
- [13] Z.P. Bažant, Y. Xiang, Size effect in compression fracture: splitting crack band propagation, *Journal of engineering mechanics* 123(2) (1997) 162-172.
- [14] K. Bertoldi, P.M. Reis, S. Willshaw, T. Mullin, Negative Poisson's ratio behavior induced by an elastic instability, *Adv Mater* 22(3) (2010) 361-6.
- [15] Y. Zhang, Y. Wang, C.Q. Chen, Ordered deformation localization in cellular mechanical metamaterials, *Journal of the Mechanics and Physics of Solids* 123 (2019) 28-40.
- [16] X. Hou, V.V. Silberschmidt, *Metamaterials with Negative Poisson's Ratio: A Review of Mechanical Properties and Deformation Mechanisms*, (2015) 155-179.
- [17] J.N. Grima, R. Caruana-Gauci, M.R. Dudek, K.W. Wojciechowski, R. Gatt, Smart metamaterials with tunable auxetic and other properties, *Smart Materials and Structures* 22(8) (2013) 084016.
- [18] W. Wu, W. Hu, G. Qian, H. Liao, X. Xu, F. Berto, Mechanical design and multifunctional applications of chiral mechanical metamaterials: A review, *Materials & Design* 180 (2019) 107950.

7

MECHANICAL BEHAVIOR OF THE AUXETIC CEMENTITIOUS CELLULAR COMPOSITES UNDER VARIOUS LOADING AND BOUNDARY CONDITIONS

In previous chapters, it was elaborated that the mechanical behavior of the CCCs depends on intrinsic characteristics: the structural design parameters as well as the properties of the cementitious constituent material. It should be noticed that the observed behavior is also influenced by the experimental set-up, or, in other words, loading and boundary conditions. Considering the potential to be used in engineering practice, the CCCs may be submitted to various loading and boundary conditions. In this chapter, the compressive behavior of the CCCs under constrained boundary conditions is studied by experiments and numerical simulations. It is found that the fracture pattern of the CCCs is substantially determined by the constraints. As a consequence, the overall stress-strain response differs from that observed under low friction condition which was clarified in previous chapters. In addition, the influence of strain rate dependence of the compressive stress-strain response is experimentally elaborated from $10^{-4}/s$ to $10^{-2}/s$. Furthermore, the energy absorption of the CCCs under impact is evaluated using Schmidt hammer. The dominant role of structural parameters on the energy absorption performance is clarified.

7.1 INTRODUCTION

Experimentally measured mechanical response of cementitious materials is highly dependent on the loading and boundary conditions [1, 2]. In terms of boundary constraints, for bulk cementitious materials, the lateral expansion is restrained when vertically compressed by the friction between the specimen and the loading plates because of their positive Poisson's ratio (0.15 to 0.22 [3-6]). As a result, the compressive behavior such as (measured) strength and cracking pattern deviates from that observed in unrestrained conditions. For the ACCCs, lateral contraction instead of expansion is restrained by the loading plates and the direction of the frictional restraining force is inverted. In this sense, the influence of boundary restraint on the compressive behavior of the auxetic cementitious materials may be rather different. Moreover, it is well known that the compressive and tensile behavior of cementitious materials is dependent on the loading rate (strain rate) [7-10]. As the ACCCs can potentially be used as an energy absorption material in engineering applications, their compressive behavior under different loading and boundary conditions is of interest and is investigated in this chapter.

7.2 METHODS AND MATERIALS

7.2.1 Specimen preparation and experimental tests

To provide a proper comparison, the geometrical parameters, the mixture design of the cementitious constituent material, and the sample preparation procedures the same as those of "P25" and "P50" series described in Chapter 6. The test setup for uniaxial compression tests on the CCCs specimens was the same as in Chapter 6, but the strain rate or boundary conditions vary. For the strain rate, besides the 0.01mm/s (1.25×10^{-4} by strain) used in Chapter 5 and Chapter 6, two other strain rates (see Table 7-1) were used while maintaining the same low friction boundary condition by apply plastic films between the specimen and the load plates. In terms of boundary constraints, apart from the unconfined condition used in Chapter 6, the CCCs were also tested under single side glued (P25SG) and double sides glued (P25DG) conditions.

Table 7-1 Test groups of the CCCs under uniaxial compression

Test groups	Strain rate (/s)	Boundary Constraints
P25SG	1.25×10^{-4}	Single side glued
P25DG		Double sides glued
P25	1.25×10^{-4}	Low friction
	1.25×10^{-3}	Low friction
	1.25×10^{-2}	Low friction

Moreover, low speed impact tests were also performed using a Schmidt hammer OS-120PM, which is normally used for evaluating compressive strength [11, 12]. The

basic principle of the Schmidt hammer is the energy balance between the elastic energy stored in the springs of the Schmidt hammer and the energy absorbed or dissipated by impact on tested specimens. Depending on the type, the Schmidt hammer has different impact kinetic energy. For the used OS-120PM [13], each single impact delivers 0.833 J of kinetic energy to the surface of the tested specimen by the impact tip. Before impact, the spring is loaded to a fixed original position $x_0=75$. After impacting on the specimen surface, the impact tip rebounds back to another position R which is recorded as the rebound value of this impact. Neglecting the energy dissipated by heat and sound, the energy absorbed by the specimen E is then written as:

$$E = \frac{x_0 - R}{x_0} * E_0 \quad (3-6)$$

where, E_0 is the initial kinetic impact energy which varies for different devices. For the Schmidt hammer used herein, $E_0=0.833$ J.

In order to comply with the Schmidt hammer set-up, a quarter of a P25 and a P50 specimen (defined in Chapter 6) was tested, respectively. Considering that the auxetic feature may dominate the impact resistance of P25 and P50, two series of specimens were prepared: the pre-compressed and the non-deformed specimens. The pre-compressed specimens were prepared by performing uniaxial compression on a unit cell of P25 and P50, respectively, to a certain strain threshold such that the auxetic deformation of the CCCs is triggered prior to the impact. For P25, the threshold is 13.5%, and for P50, it is 10%, after which the auxetic behavior of the CCCs disappears, as elaborated in Chapter 6. Test groups of the CCCs subjected to impact loading are listed in Table 7-2.

Table 7-2 Test groups of the CCCs under impact loading

Test groups	Specimen type
P25	Non-deformed unit cell
P50	Non-deformed unit cell
P25C	Pre-compressed unit cell
P50C	Pre-compressed unit cell

7.2.2 Numerical simulations

To investigate the role of boundary constraints on the compressive behavior of the CCCs, uniaxial compression tests were simulated using ABAQOUS/Explicit (as introduced in Chapter 6). The only difference is that the boundary conditions are adjusted according to the single side fixed and both sides fixed condition. Under single side fixed conditions, the bottom side of the specimen is tied with the bottom loading plate. Under the double-sided fixed condition, both the top and the bottom of the specimen are tied with corresponding loading plates, respectively.

7.3 RESULTS AND DISCUSSIONS

7.3.1 Influence of boundary constraint

Similar to bulk cementitious materials (Figure 7-1), for the ACCCs, influence of the confined zone can be also observed: however, unlike bulk cementitious materials, the compressed specimen tries to contract laterally under compressive vertical load, owing to the negative Poisson's ratio (NPR). Therefore, the direction of confinement is inverted, which leads to re-entrant angle shape of the confined zone instead of a cone. As can be seen from Figure 7-2a, for P25SG (the P25 specimen with top side glued on the loading plate) at 5% strain obvious difference can be seen between the glued side (top) and low friction side (bottom). The undeformed cells show confined zone of a re-entrant shape. At the low friction side (bottom), the cellular structure is compacted by a previously described cracking initiated rotation mechanism, while at the glued side (top), the cells are barely deformed because of the lateral confinement from the upper loading plate. Similarly, for P25DG (the P25 specimen with both top and bottom side glued on the loading plates) at 5% strain, both sides show re-entrant confined zones consisting of undeformed cells near the two loading plates (see Figure 7-2b). A similar deformation pattern can be also seen in elastomers, but it is caused by elastic instability in the elastic stage.

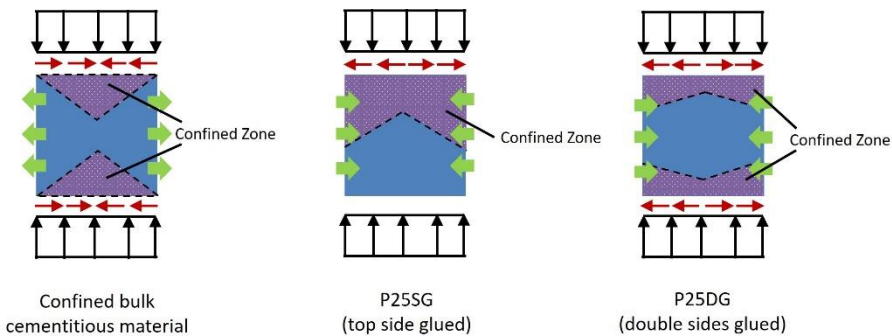


Figure 7-1 Schematics of the confined zone of confined bulk cementitious material and ACCCs with top side confined (P25SG) and double side confined (P25DG)

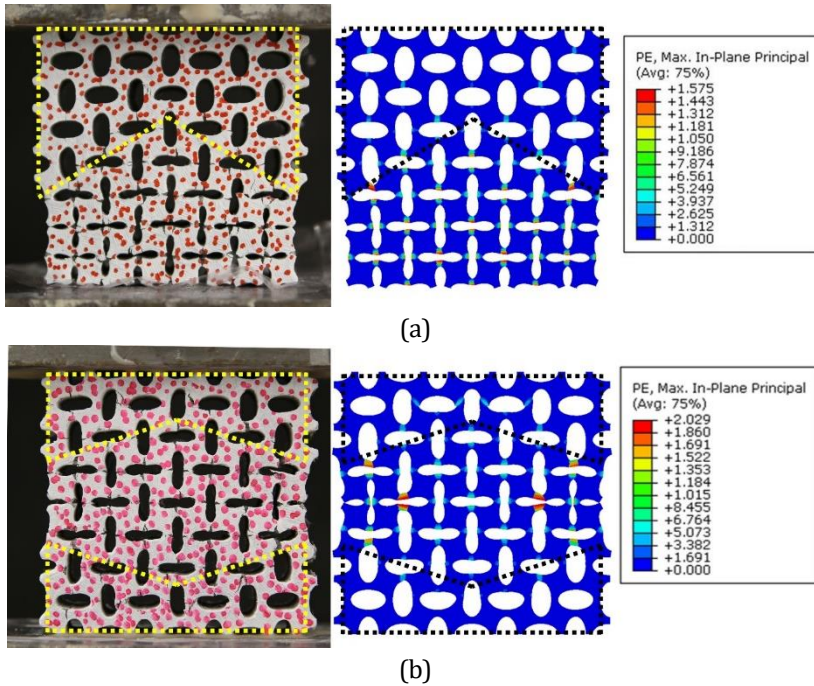


Figure 7-2 Deformed specimen of a) P25SG and b) P25DG at 5% strain from the experiment and the simulation, confined zones are marked by dashed lines

The stress-strain response of P25DG and P25SG is also affected by the boundary restraint. As already discussed in the previous chapter, the void closure causes a typical two-stage stress-strain response of P25. Under low friction condition, the cells are not confined and are free to deform and crack. Consequently, the first peak of the P25 stress-strain curve signifies cracking of the cellular structure, while subsequently the second load increase after section rotation signifies compacting of the constituent material. Under glued boundary conditions, the typical second load increase still can be found both from the experiment and simulated stress-strain curves (see Figure 7-3). However, the crack initiation and the section rotation were restrained. As shown in Figure 7-4, due to the highest applied restraint, the normalized first peak stress of P25DG (3.48 MPa from the experiment and 3.18 MPa from the simulation) is also the highest. The first peak stress of P25SG is lower (2.75 MPa from the experiment and 2.56 MPa from the simulation) because of lower restraint. Finally, the first peak stress of P25 is the lowest (2.18 MPa from experiment and 2.47 MPa from simulation) because of the low friction boundary condition. This phenomenon can be attributed to the confined fracture localization, similar to the fact that bulk cementitious materials show higher compressive strength under restrained boundary condition [1]. As mentioned previously, cementitious materials are very heterogenous, and their compressive failure comprises a process of tensile microcracking (Mode I fracture at microscale) and crack localization (crack shearing) [2]. For bulk cementitious materials, compressive strength is reached around the onset of crack localization. When a macroscopic

compressive load is imposed, tensile stresses are generated at the micro heterogeneities. Under the condition that the specimen is laterally confined, the generated tensile stresses would be reduced by the confinement. As a result, higher compressive load is required to initiate microcracks. Also, lateral confinement may slow down the shearing on the crack surface of the microcracks which potentially increases the compressive strength. For P25, the first peak strength is mainly determined by the tensile cracking at the joints. Higher compressive load is required to generate microcracks at the joints due to lateral confinement, as a result first peak strength of confined P25 is higher. After the first peak, the second load increase of P25DG and P25SG is observed both in experiment and simulated curves. However, as the cell sections rotation near the loading plates was restrained, less cells could deform and be compacted which led to a slower load increase and is seen in the stress-strain curves by a much longer and milder ascending branch under glued boundary conditions.

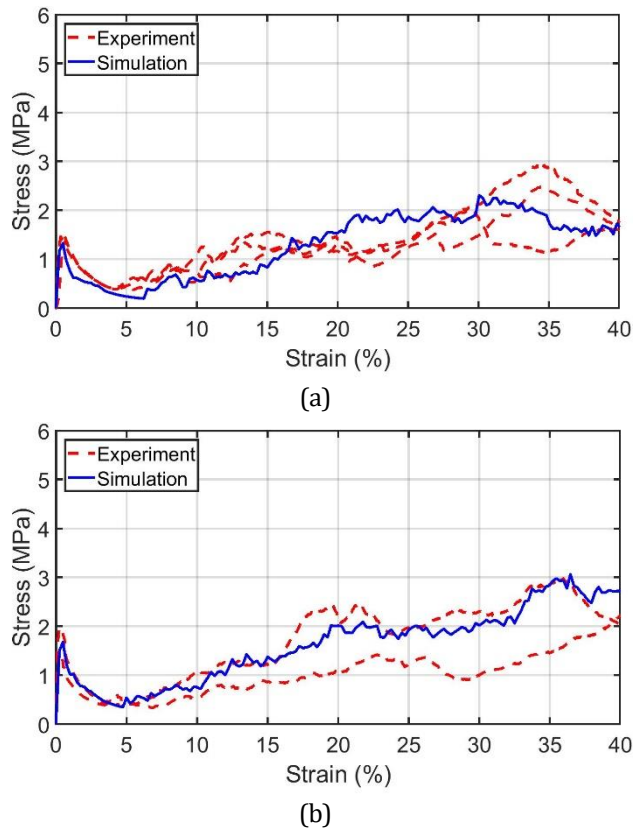


Figure 7-3 Stress-strain curves of a) P25SG and b) P25DG obtained from experiment and simulation

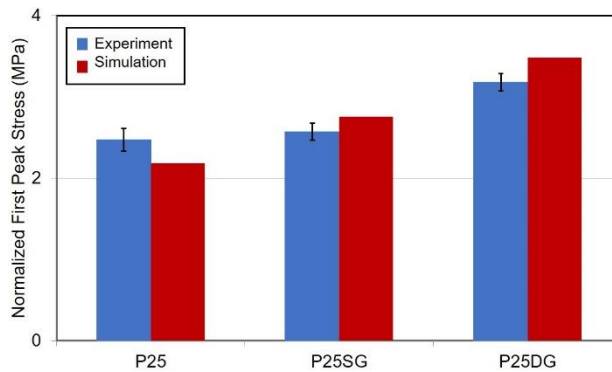


Figure 7-4 Comparison of the normalized first peak load of the ACCCs under different boundary conditions

7.3.2 Influence of loading rate

As mentioned before, the compressive and tensile behavior of cementitious materials are dependent on the loading rate (strain rate) [7-10]. The strength measured by uniaxial tension, uniaxial compression, and bending increases with respect to the strain rate under a rather wide range (referred results range from $10^{-6}/s$ up to $10/s$) [14-17]. The increased strength is usually quantitatively evaluated by the dynamic increase factor (DIF), which is defined as the strength ratio between the dynamic and the static response. Specifically, in this chapter, such strain rate effect on the constituent material also influences the compressive behaviors of the ACCCs under different strain rate.

It was already clarified in Chapter 5 and Chapter 6 that the stress-strain curve of the ACCCs consists of two stages until 40% of strain. Each of these two stages has a peak stress, which is dominated by the tensile (flexural) and compressive strength of the constituent material itself, respectively. As shown in Figure 7-5, under different strain rate, the compressive stress-strain curves of the ACCCs shows a similar trend, however, the peak stress varies. Within the “Stage I” (from 0% to 10% strain), the peak stress increased by 23 % (DIF=1.23) as strain rate increased from a magnitude of $10^{-4}/s$ to $10^{-3}/s$ as shown in Figure 7-6. It was elaborated by [9] that, under higher strain rate, lower stress intensity occurs at the crack tip of pre-existing microcracks in cementitious materials. For the ACCCs, as explained in Chapter 6, cracks occur in the first stage at the joints of the cellular structure due to the tensile stress concentrations. Lower stress intensity should be present at the joints under higher strain rate. As a consequence, a higher external load is required to for the cracks to propagate and the recorded strength would be higher. Nevertheless, the first peak strength seems not significantly increased by increasing strain rate from $10^{-3}/s$ to $10^{-2}/s$. Similarly, in previous studies [8, 18] it was found that within the strain rate ranges from $10^{-3}/s$ to $10^{-2}/s$, tensile cracking strength of the PVA FRCs increased 5%~8% which is also not significant.

After the first stage, a second stress peak exists (from 10% to 40% strain). This peak stress is mainly dependent on the compressive strength of the constituent

material. Compared to the first stage, the strength increase of the second peak is much more obvious. From $10^{-4}/s$ to $10^{-2}/s$, the second peak stress increased from 5.6MPa to 7.6MPa (DIF=1.36) at the strain rate of $10^{-3}/s$ and 8.8MPa (DIF=1.57) at $10^{-2}/s$, respectively. It is worth of noticing that due to the ultimate compressive strength (normalized to the same density) of the ACCCs being much lower than ordinary plain concrete and FRCs, the DIF of the ACCCs in the “Stage II” is significantly higher than ordinary plain concrete or FRCs. In ordinary FRCs the DIF will not reach 1.5 until the strain rate reaches a magnitude of $10/s$ [19, 20]. The physical origin of the strain rate dependency of the cementitious materials has been intensively studied. However, it is still not fully understood. For plain concrete, possible reasons were attributed to the free water viscosity [21, 22]: when free water is present, cohesive force between crack surface increases with load rate[23]. For fiber reinforced cementitious materials, such strain rate dependency also exists. It was proved that the tensile cracking strength which is mainly determined by the cementitious matrix increases with respect to strain rate[7, 18]. This agrees with the trend of the first peak found in Figure 7-5 which is also attributed to tensile cracking. As for the compression fracture process, besides the cracking of cementitious matrix, the interaction between fibers and cementitious matrix may also accounts for a reason of the load rate dependency. The fiber pullout resistance was found to increase with respect to strain rate[24-26], which can substantially increase the compressive strength of FRCs.

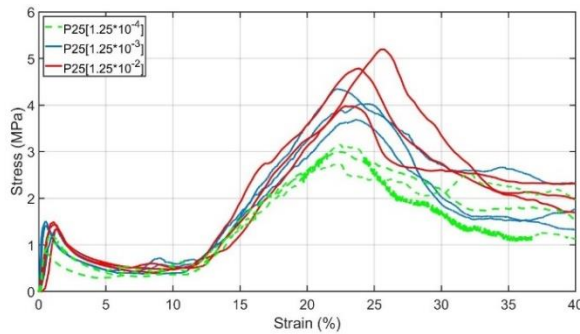


Figure 7-5 Stress-strain curves of P25 under various loading rate

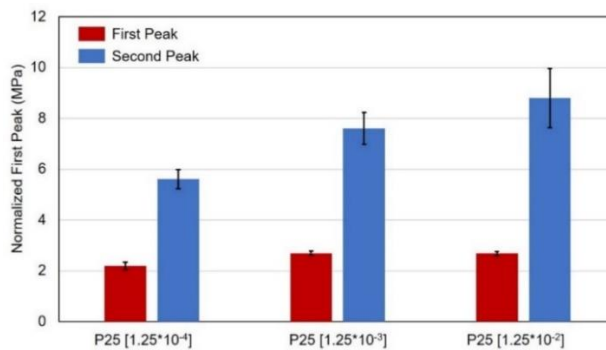


Figure 7-6 Peak stress against different strain rates

7.3.3 Impact resistance

As described in 7.2.1, the impact resistance of the ACCCs can be evaluated using the Schmidt hammer. For solid materials, after impact the total energy only consists of elastic energy stored in the spring after the rebound, the surface plastic deformation energy of the specimen and the energy dissipated by heat or sound. For the ACCCs, due to the high deformability, apart from the plastic deformation energy dissipated by the specimen surface, a large fraction of energy is absorbed by the structural damage of the ACCCs, for instance the cracking at the joints. So, the rebound value indicates the impact resistance of the ACCCs in every single impact. A higher rebound value means less damage caused by the impactor on the specimen and therefore, the impact resistance is better.

It is visible from Figure 7-7 that some impact energy was absorbed by the ACCCs specimens with each impact. As the number of impacts increases, damage done on the specimen became more severe, thus the amount of absorbed energy also increases. Consequently, it can be observed from Figure 7-8 that in general the rebound value of the ACCCs decreases as the number of impacts increases. As explained previously, the ACCCs shows “strain hardening” response under compression, and after the initial cracking they can still withstand increasing load as strain increases. When the ACCCs were damaged by the first several impacts, the auxetic behavior was triggered and the impact resistance increased due to the “strain hardening” effect.

In addition, a very interesting phenomenon is found: the influence of pre-compression on the rebound of the two series of ACCCs exhibits an opposite trend. This phenomenon is also caused by the auxetic behavior of the ACCCs. The pre-compression influences the impact resistance of the ACCCs from two competing aspects. The auxetic deformation behavior which potentially ensures the ACCCs higher impact resistance was triggered by the pre-compression, but a certain degree of damage was also introduced. For the P25 series, the pre-compressed specimens show better impact resistance owing to the auxetic behavior as the rebound value decreases sharper with the number of impacts. However, for the P50 series, the pre-compressed specimens exhibit worse impact resistance because of the damage introduced by pre-compression. This is also visible from the damaged ACCCs specimens (see Figure 7-9): without pre-compression, the auxetic behavior of the P50 was still triggered after impacts (the cellular structure was compacted and disappeared which resembles the deformed specimens under uniaxial compression), in contrast the P25 does not. The difference comes from the structural designs of the ACCCs. In principle, it is easier to trigger the auxetic behavior in the P50 series than in the P25 series. On one hand, under the same boundary condition, a lower external load is required to trigger the auxetic deformation behavior in the P50; most importantly, on the other hand P50 has less compressible space available before the constituent material comes into contact which may provide the “strain hardening” response under impact. Therefore, after impacts the impact resistance of P50 was improved due to the triggered auxetic behavior.

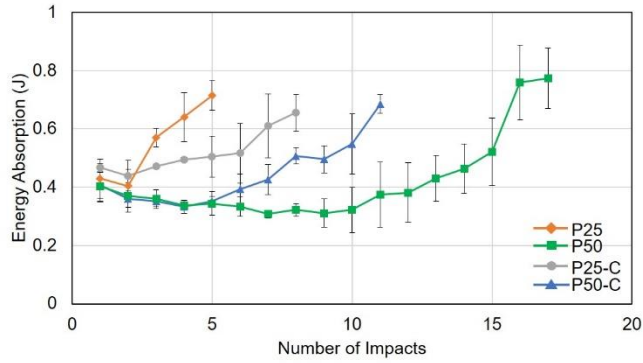


Figure 7-7 Energy absorption in each impact by the ACCCs against number of impacts, “C” indicates pre-compressed specimens

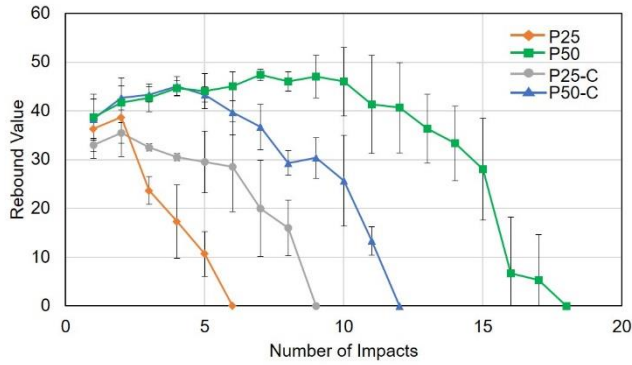


Figure 7-8 Rebound values in each impact against number of impacts, “C” indicates pre-compressed specimens

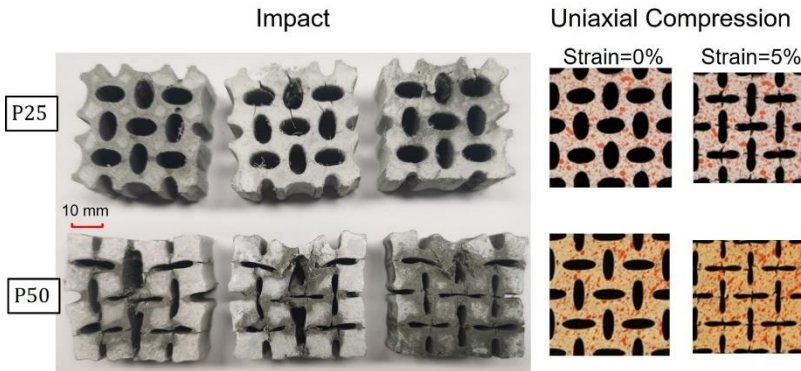


Figure 7-9 Damage pattern of the ACCCs (without pre-compression) under impact after rebound value decreased to zero, and damage pattern under uniaxial compression

7.4 CONCLUSIONS

In this chapter, the influence of loading and boundary conditions on the compressive behavior of the ACCCs is investigated. Based on the obtained experimental and numerical results and corresponding analysis, the main conclusions can be drawn as follows:

- Under boundary confinement, compressed ACCCs undergo lateral restraint. Different from the commonly found cone shape fracture zone of bulk cementitious materials, a re-entrant shape fracture zone was found on the confined ACCCs under uniaxial compression.
- The compressive response of the ACCCs is strain rate sensitive. Increasing the strain rate from $10^{-4}/s$ to $10^{-2}/s$, the dynamic increase factor (DIF) of tensile strength dominated peak and compression strength dominated peak (i.e. first and second peak) reaches 1.23 and 1.57, respectively.
- The impact resistance of the ACCCs is influenced by the auxetic behavior, which is determined by the structural design parameters. Between the tested ACCCs, the P50 exhibits significantly higher impact resistance than P25 owing to the auxetic behavior triggered by impact.

In Chapter 5 - Chapter 7, the mechanical behavior of the ACCCs is discussed in detail. It is obvious that the low strength of the ACCCs limits their application as structural members because they do not satisfy the strength requirements for many structural applications. However, in some specific applications, for example impact absorption, at which the impacting object need to be protected, the ACCCs would be an ideal choice due to the ability to absorb large amount of energy meanwhile conduct minor reaction force to the object.

In Chapter 5 and Chapter 6, in terms of creating the auxetic cementitious cellular composites, it is emphasized that besides proper structural design, the properties of the constituent material also need to be carefully tailored. A conclusion is that crack-bridging ability is necessary, for the previously used cellular structure 2.6 MPa of crack-bridging stress is already enough. The addition of fibers would be an obvious first choice to enhance the crack bridging ability of cementitious material. However, their negative effect on flowability may limit the application, especially in creating composites with a complex three-dimensional structure. At the moment, molds are still used for creating ACCCs specimens, and preparing ACCCs with three-dimensional geometries would be a more difficult and a laborious task. Therefore, taking advantage of the free-form fabrication ability of 3D printing, directly making a built-in reinforcing or toughening phase for cementitious cellular composites would be possible. This will be the focus of the coming Chapters 8 - Chapter 10.

REFERENCES

- [1] M.R.A. Van Vliet, J.G. Van Mier, Experimental investigation of concrete fracture under uniaxial compression, *Mechanics of Cohesive-frictional Materials* 1 (1996) 115-127.
- [2] J.G. Van Mier, *Fracture processes of concrete*, CRC press 1997.
- [3] B. Persson, Poisson's ratio of high-performance concrete, *cement and Concrete Research* (1999).
- [4] J. Carrillo, J. Ramirez, J. Lizarazo-Marriaga, Modulus of elasticity and Poisson's ratio of fiber-reinforced concrete in Colombia from ultrasonic pulse velocities, *Journal of Building Engineering* 23 (2019) 18-26.
- [5] Y. Li, Y. Li, Evaluation of elastic properties of fiber reinforced concrete with homogenization theory and finite element simulation, *Construction and Building Materials* 200 (2019) 301-309.
- [6] G.P.A.G. van Zijl, D.J.A. de Jager, Improved ductility of SHCC retrofitted unreinforced load bearing masonry via a strip-debonded approach, *Journal of Building Engineering* 24 (2019) 100722.
- [7] E.-H. Yang, V.C. Li, Tailoring engineered cementitious composites for impact resistance, *Cement and Concrete Research* 42(8) (2012) 1066-1071.
- [8] V. Mechtcherine, F.d.A. Silva, S. Müller, P. Jun, R.D.T. Filho, Coupled strain rate and temperature effects on the tensile behavior of strain-hardening cement-based composites (SHCC) with PVA fibers, *Cement and Concrete Research* 42(11) (2012) 1417-1427.
- [9] J.Eibl, M.Curbach, An attempt to explain strength increase due to high loading rates, *Nuclear Engineering and Design* 112 (1989) 45-50.
- [10] Y. Gan, C.R. Rodriguez, E. Schlangen, K. van Breugel, B. Šavija, Assessing strain rate sensitivity of cement paste at the micro-scale through micro-cantilever testing, *Cement and Concrete Composites* 121 (2021) 104084.
- [11] S. Teixeira, A. Santilli, I. Puente, Demoulding vertical elements: Recommendations for apply maturity functions, *Construction and Building Materials* 145 (2017) 392-401.
- [12] A. Aydin, A. Basu, The Schmidt hammer in rock material characterization, *Engineering Geology* 81(1) (2005) 1-14.
- [13] ProceqSA, Schmidt OS-120_Operating Instructions., https://www.proceq.com/uploads/tx_proceqproductcms/import_data/files/Schmidt%20OS-120_Operating%20Instructions_English_high.pdf (2017).
- [14] S. Pyo, K. Wille, S. El-Tawil, A.E. Naaman, Strain rate dependent properties of ultra high performance fiber reinforced concrete (UHP-FRC) under tension, *Cement and Concrete Composites* 56 (2015) 15-24.
- [15] K. Habel, P. Gauvreau, Response of ultra-high performance fiber reinforced concrete (UHPFRC) to impact and static loading, *Cement and Concrete Composites* 30(10) (2008) 938-946.
- [16] D.j. Kim, S. El-Tawil, A.E. Naaman, Rate-dependent tensile behavior of high performance fiber reinforced cementitious composites, *Materials and Structures* 42(3) (2008) 399-414.
- [17] T.K. Tran, D.J. Kim, Investigating direct tensile behavior of high performance fiber reinforced cementitious composites at high strain rates, *Cement and Concrete Research* 50 (2013) 62-73.
- [18] W.P. Boshoff, G.P.A.G. van Zijl, Time-dependent response of ECC: Characterisation of creep and rate dependence, *Cement and Concrete Research* 37(5) (2007) 725-734.
- [19] S. Wang, M.-H. Zhang, S.T. Quek, Effect of high strain rate loading on compressive behaviour of fibre-reinforced high-strength concrete, *Magazine of Concrete Research* 63(11) (2011) 813-827.
- [20] S. Wang, H.T.N. Le, L.H. Poh, S.T. Quek, M.-H. Zhang, Effect of high strain rate on compressive behavior of strain-hardening cement composite in comparison to that of ordinary fiber-reinforced concrete, *Construction and Building Materials* 136 (2017) 31-43.
- [21] R. Pierre, J.G. Van Mier, T. François, L.M. Fabrice, B. Claude, Effect of loading rate on the strength of concrete subjected to uniaxial tension, *Materials and structures* 27(5) (1994) 260-4.

- [22] R. Pierre, J.G. Van Mier, B. Claude, L.M. Fabrice, The dynamic behaviour of concrete: influence of free water, *Materials and Structures* 25(9) (1992) 509-14.
- [23] D. Zheng, Q. Li, An explanation for rate effect of concrete strength based on fracture toughness including free water viscosity, *Engineering Fracture Mechanics* 71(16-17) (2004) 2319-2327.
- [24] W.P. Boshoff, V. Mechtcherine, G.P.A.G. van Zijl, Characterising the time-dependant behaviour on the single fibre level of SHCC: Part 2: The rate effects on fibre pull-out tests, *Cement and Concrete Research* 39(9) (2009) 787-797.
- [25] K.-Q. Yu, J.-G. Dai, Z.-D. Lu, C.-S. Poon, Rate-dependent tensile properties of ultra-high performance engineered cementitious composites (UHP-ECC), *Cement and Concrete Composites* 93 (2018) 218-234.
- [26] V. Mechtcherine, F.d.A. Silva, M. Butler, D. Zhu, B. Mobasher, S.-L. Gao, E. Mäder, Behaviour of strain-hardening cement-based composites under high strain rates, 9(1) (2011) 51-62.

8

CEMENTITIOUS COMPOSITES REINFORCED BY 3D PRINTED LATTICE POLYMERIC MESHES

As indicated previously, the crack bridging ability of the constituent material is crucial for cementitious cellular composites to exhibit auxetic behavior. Reinforcement is commonly used to enhance fracture resistance of cementitious materials. With certain fiber types and micromechanical design, it is even possible to create cement-based materials with steel-like (i.e. quasi-plastic) properties – so called strain hardening cementitious composites (SHCCs). In this chapter, an alternative approach for creating SHCC – through use of additive manufacturing to create polymeric reinforcement meshes – is investigated. Different designs are manufactured, casted in the cementitious mortar, and tested in four-point bending and uniaxial tension. It is found that, with proper design, it is possible to create cementitious composites with deflection hardening or strain hardening properties. Furthermore, with proper design, multiple cracking behavior of conventional SHCC can be replicated. In addition, numerical simulations were performed using the Delft lattice model. Four-point-bending tests of mortar bars reinforced by two different mesh designs were simulated and the results show good agreement with the experiments. In this chapter, a great potential of using additive manufacturing for enhancing the crack bridging ability of cementitious materials is shown.

8.1 INTRODUCTION

In this chapter, 3D printed polymeric meshes with two dimensional triangular patterns are used as reinforcement for the purpose of enhancing fracture resistance of cementitious mortar. Different reinforcement geometries are manufactured and tested in four-point bending and uniaxial tension. Furthermore, in order to simulate the cracking patterns as well as the load-displacement response of the reinforced composites, numerical simulations of the experiments are performed using the Delft lattice model, which is already introduced in Chapter 3 and Chapter 4.

8.2 METHODS AND MATERIALS

8.2.1 Materials

The cementitious matrix material used was a fine-grained cementitious mortar containing CEM I 42.5 N and fly ash as binder materials, with a water-to-binder ratio of 0.33. The same mixture was used to develop SHCC in [1], and has a relatively high fluidity which makes it easy to fill the hollow cells of the printed reinforcement in this study. The mixture is listed in Table 8-1.

Table 8-1 Mixture design of the matrix material (g/l), adapted from [1]

CEM I 42.5 N	Fly ash	Sand (0.125~0.250 mm)	Superplasticizer (Glenium 51)	Water
550	650	550	2	395

Polymeric reinforcement meshes were manufactured using a commercially available FDM 3D printer Ultimaker 2+ (Figure 8-1). In FDM, the model is printed layer by layer, from the bottom up. As a result, overhangs are difficult to print and may be of poor quality. Therefore, relatively simple mesh patterns were selected in this study, as described below. Acrylonitrile Butadiene Styrene (ABS) was used as the printing material (i.e. filament). ABS has excellent mechanical properties, interlayer adhesion, minimal warping, reliable bed adhesion and high alkaline resistance [2], which is important for use in cement-based materials.

Printing parameters may affect the mechanical properties of the resulting structure. Therefore, they are kept constant throughout this chapter. Printing parameters used are given in Table 8-2. Printing direction has a significant effect on the mechanical properties as discussed in Chapter 3. Therefore, printing was performed in the direction parallel to the normal stress, resulting in maximum strength.

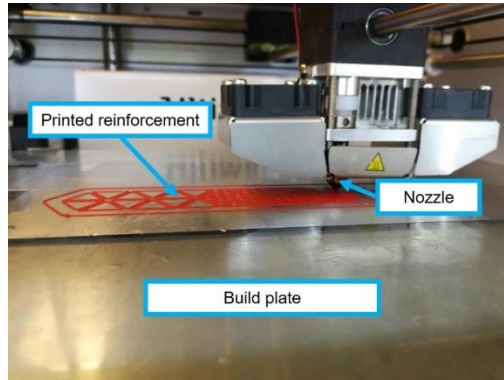


Figure 8-1 Schematics of reinforcement printing setup in the Ultimaker 2+.

Table 8-2 Printing parameters for reinforcement meshes used

Printing parameter	Configuration
Nozzle diameter (mm)	0.8
Temperature (°C)	260
Layer height (mm)	0.2
Line width (mm)	0.7
Infill density (%)	100
Infill pattern	Lines
Printing speed (mm/s)	40

8.2.2 Reinforcement designs

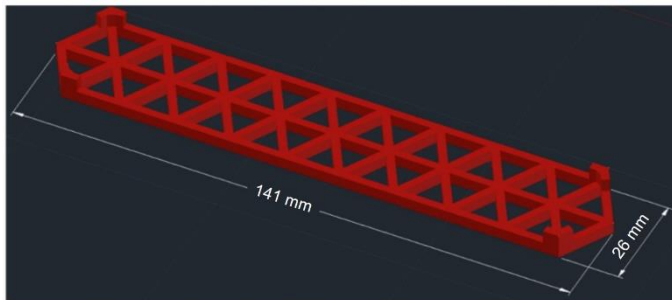
Reinforcements with three different patterns were manufactured and tested. All patterns are based on triangular lattices, as shown in Figure 8-2 and Figure 8-3. As can be seen, different sizes of triangles are used, and the cross section of the reinforcement along the printed mesh is not constant. For small triangles, large triangles and mixed triangles, the cross-sectional reinforcing ratio of different patterns is listed in Table 8-3 and the triangle pattern size parameters are shown in Figure 8-2d and Figure 8-2e. The small triangle pattern has a higher overall cross-sectional reinforcing ratio, therefore, it was expected that smaller triangle size (Figure 8-2b) will provide a better reinforcement effect compared to larger triangles (Figure 8-2a) and, as a result, better global behavior. The pattern in Figure 8-2c is a mix of the two previous patterns: large triangles are used in the outer parts of the mesh, while a denser mesh is created in the middle. This pattern was used only in four-point bending tests. In four-point bending, the middle portion of the specimen is subjected to a constant bending moment, which is higher than in the outer regions, and thus requires more reinforcement. In that case, additive manufacturing may enable optimization of the reinforcement compared to traditional textile or fiber reinforcement. Therefore, the pattern shown in Figure 8-2c was developed to test that it is possible to create a simple functionally graded material,

in which the material structure (in this case, printed “fiber” reinforcement) is adjusted to the actual stress state, through use of additive manufacturing.

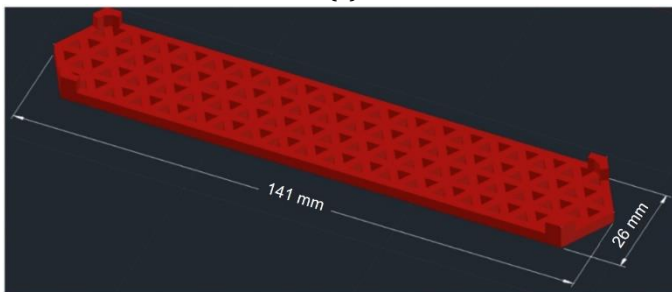
Table 8-3 Cross sectional reinforcing ratio of different reinforcement patterns

Reinforcement pattern	Cross sectional reinforcing ratio (%)
Large triangles	12.5 ~ 17.5
Small triangles	17.5 ~ 32.5
Mixed triangles	12.5 ~ 32.5

In addition to different patterns, roughness of the printed reinforcement mesh may have an effect on the bond and, consequently, the mechanical properties of the composite material. Therefore, for each of the loading conditions tested (i.e. four-point bending and uniaxial tension, respectively), one of the patterns was additionally roughened by introducing a rough profile on one side of the printed mesh as shown in Figure 8-3d (in order to avoid large overhangs during 3D printing which may result in poor printing quality, only the upper side of the mesh was printed with rough profile). These were mixed triangles pattern and the large triangles pattern for four-point bending and uniaxial tension experiments, respectively. A summary of all patterns and tests is given in Table 8-4. Note also that all reinforcement meshes were produced with “studs” that enabled the meshes to be easily positioned in the middle of the specimen during casting.



(a)



(b)

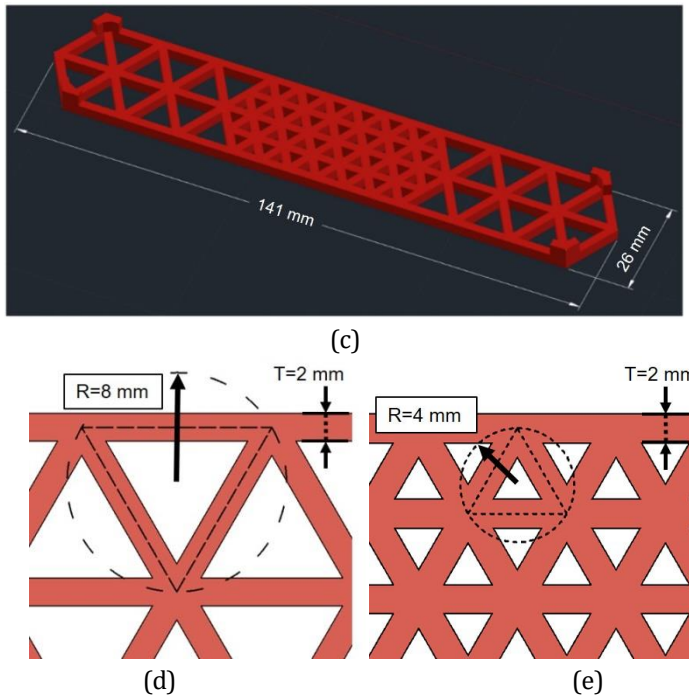
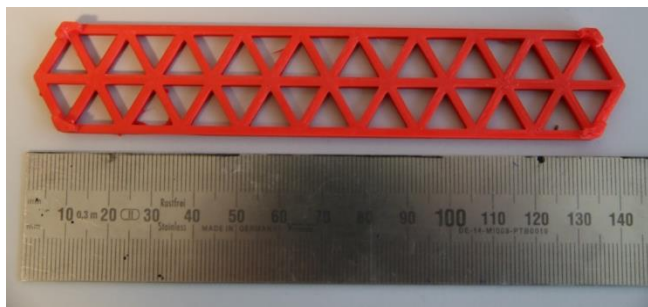
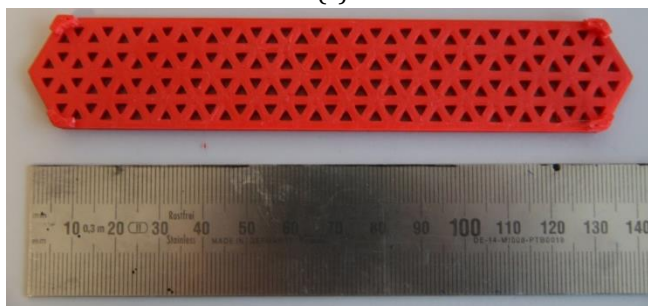


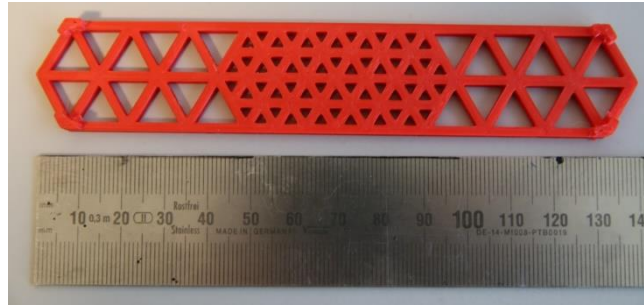
Figure 8-2. Design of polymeric reinforcement meshes and printed reinforcement. (a) large triangles; (b) small triangles; (c) mixed triangles (dimensions are in mm); (d) design parameters of large triangles; (e) design parameters of small triangles.



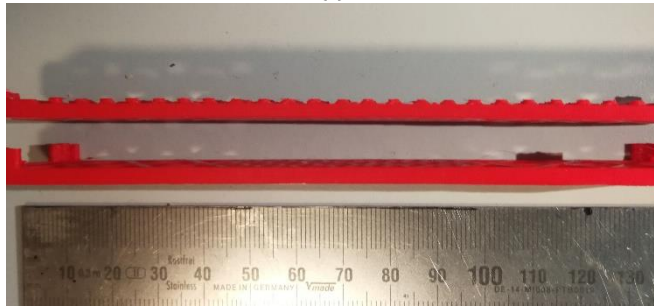
(a)



(b)



(c)



(d)

Figure 8-3. Printed reinforcement with (a) large triangle pattern; (b) small triangle pattern; (c) mixed triangle pattern; (d) smooth surface and rough surface

Table 8-4 A summary of all designs and tests

Triangle mesh type	Surface profile	Series ID	Diameter of cell circumscribed circle (mm)	Four-point bending	Uniaxial tension	Age
None	/	Ref, Ref28	/	Yes	Yes	7d, 28d
Large	Smooth	LT	8	Yes	Yes	7d
Large	Rough	LTR	8	No	Yes	7d
Small	Smooth	ST, ST28	4	Yes	Yes	7d, 28d
Mixed	Smooth	MT, MT28	4,8	Yes	No	7d, 28d
Mixed	Rough	MTR	4,8	Yes	No	7d

8.2.3 Casting and curing

The bottom surfaces of printed meshes were sanded for 30 seconds with 125 μ m sand paper before casting to remove the glue layer in contact with 3D printer build plate. The positions of reinforcement were marked on Styrofoam molds. Then they were placed in Styrofoam molds (190 \times 180 \times 8 mm) with their studs pressed into the molds for 1mm (shown in Figure 8-4) and glued with silicone rubber to make sure that the reinforcement stays in the middle and does not move during vibration.

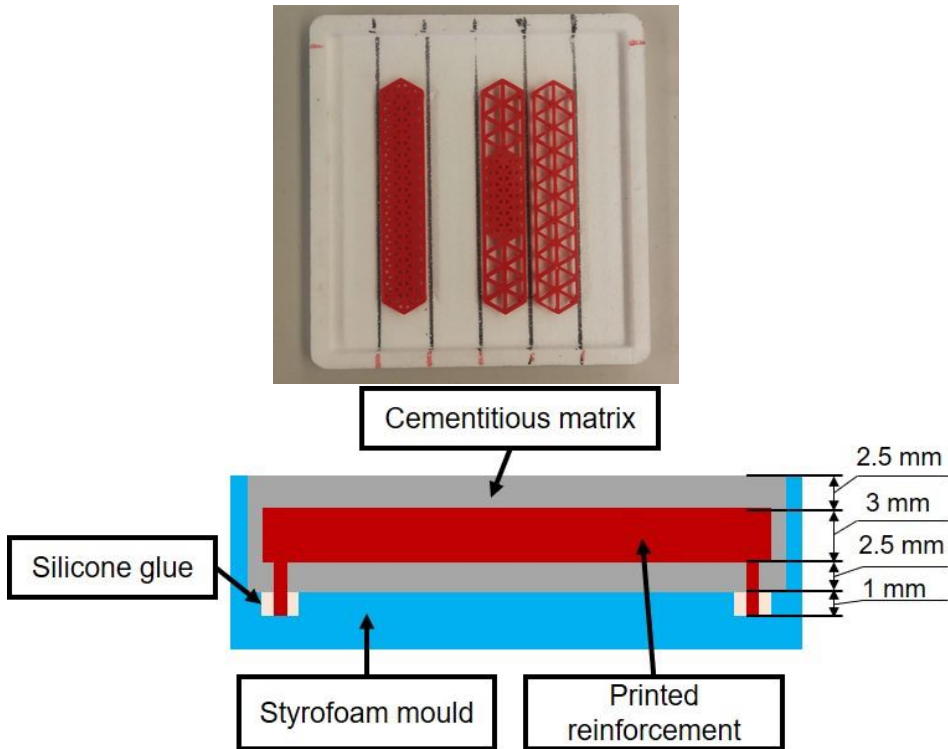


Figure 8-4 Position of printed reinforcement in Styrofoam mold.

The cementitious matrix materials were weighted according to the mix proportion given in Table 8-1. First, solid ingredients were dry-mixed for four minutes in a Hobart laboratory mixer. After four minutes, water and superplasticizer were added to the mixture and mixed for additional four minutes. Subsequently, the materials were cast in the prepared molds (with reinforcement already positioned) and vibrated for 30 seconds. Fresh specimens were covered with plastic sheets for one day (uniaxial tension) and two days (four-point bending), and then demolded. After demolding, they were placed in a curing room ($20 \pm 2^\circ\text{C}$, $96 \pm 2\% \text{RH}$). Samples were cut to appropriate size for testing (described below) one day before testing.

8.2.4 Four-point bending test

Based on the auxetic mechanism demonstrated in Chapter 5 and Chapter 6, under compression the stress distribution at the “joint” in a unit cell can be equivalently compared to a four-point bended beam. Therefore, the same set ups described in Chapter 5 were also adopted in this chapter to perform four-point bending tests using the same loading condition. Specimen size used was 180 x 30 x 8 mm. Note that the pattern given in Figure 8-2c was optimized for this loading setup: if a different loading setup were used, the middle region (i.e. the region with the maximum bending moment where a denser lattice mesh was printed) would have been different. For each specimen, flexural strength and flexural deflection capacity were determined as shown in Figure 8-5, and the area below the load-displacement/load-deflection curve was defined as the total work needed to fracture the specimen. For each configuration, at 7d four replicate specimens were tested and at 28d three replicate specimens were tested.

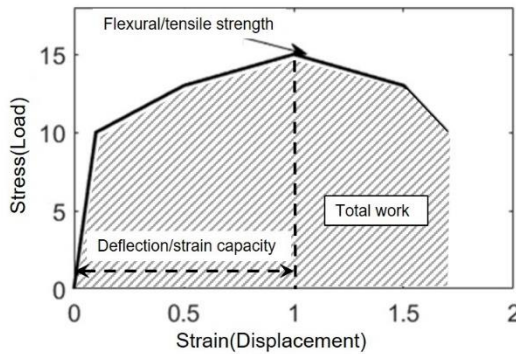


Figure 8-5. Definition of flexural/tensile strength and flexural deflection capacity/strain capacity as determined by four-point bending/uniaxial tensile tests (adapted from [3])

8.2.5 Uniaxial tensile test

Similar to the four-point bending tests, uniaxial tensile tests were performed on cured samples using a servo-hydraulic press (INSTRON 8872) under displacement control with a constant rate of 0.005 mm/s. The load was measured by a load cell and the displacements were measured by two linear variable differential transducers (LVDTs) placed on both sides of the specimen. Prior to testing, specimens were glued with a mix of PLEX 7742F and Pleximon on two parallel (non-rotating) steel plates. Note that both the cementitious matrix and also the reinforcement (which is visible in the cross section after cutting) were glued to the steel plates. Specimen size used was 120 × 30 × 8 mm after cutting. The test is shown schematically in Figure 8-6. For each configuration, three replicate specimens were tested for reference (Ref) and large triangle patterns (LT and LT_R), and four replicate specimens were tested for small triangle patterns (ST and ST₂₈). During the uniaxial tensile test, a camera was placed in front of the specimen to capture photos of the cracking process. Afterwards, digital image correlation (DIC) analyses were performed to determine the strain field on the specimen surface during testing.

In order to obtain input parameters for ABS reinforcement needed for the lattice model, uniaxial tensile tests on printed ABS bars were also performed. The height and the width of printed ABS bars was kept constant with the wall of a single cell of printed reinforcement meshes, namely 2 mm in width and 3 mm in height. The length of ABS bars was 100 mm. The same test setup as shown Figure 8-6 is used. Specimens for four-point bending and uniaxial tension are shown in Figure 8-7.

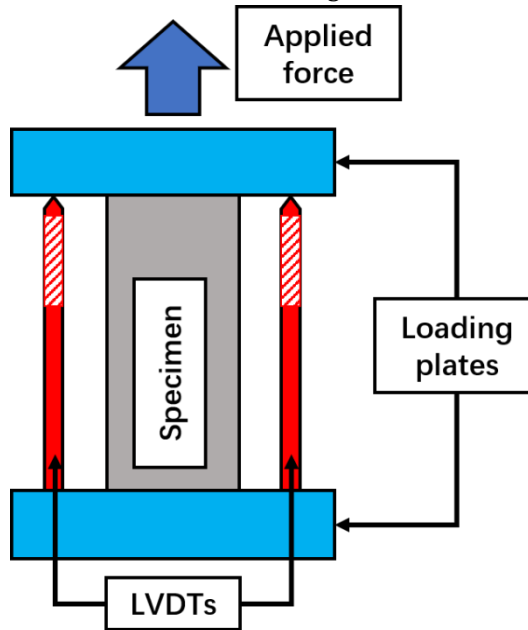


Figure 8-6. Schematic representation of the uniaxial tensile test on reinforced specimen.

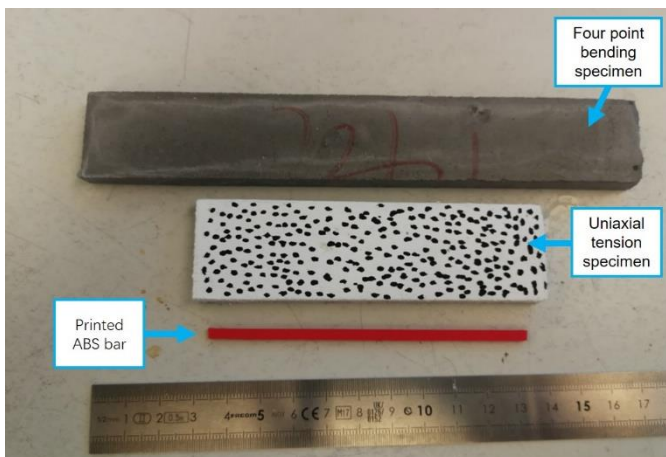


Figure 8-7 Specimens for four-point bending, uniaxial tension.

8.3 LATTICE MODELING

Numerical simulations of the deformation and fracture process during four-point bending were carried out using the Delft lattice model. Detail description of the modeling procedures was already given in Chapter 3 and Chapter 4, specific procedures used in this chapter is as follows:

- A three-dimensional lattice network is generated with the same method described in the Chapter 3. In this study $R=0.99$ is used for all grids (as cementitious material is rather heterogenous, a high randomness is necessary for simulating realistic cracking patterns [4], for all simulated specimen the randomness is kept the same), only the randomness of specimen surface was set to be $R=0$ in order to apply load and supports evenly.
- As shown in Figure 8-8, when an element has two nodes located in the matrix region, it was defined as a matrix element and similar criterion applies for defining reinforcement elements. When an element has two nodes located in different regions, it was defined as an interface element. The generated lattice networks for the three simulated cases are shown in Figure 8-9.

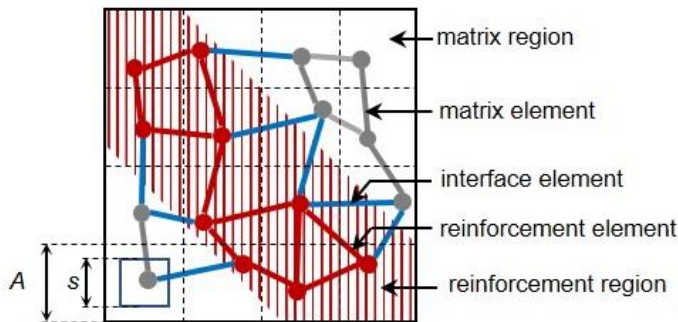


Figure 8-8. Schematics of domain discretization and element definition (shown in 2D for simplicity)

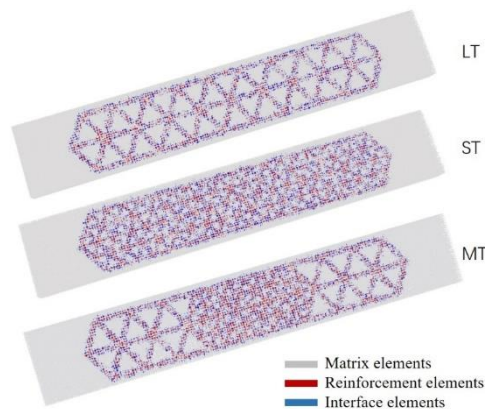


Figure 8-9 Lattice network of mortar bar reinforced by large triangles and small triangles.

Linear elastic properties were assigned to the elements according to their categories. A prescribed displacement boundary condition was imposed on the lattice network corresponding to the loading boundary condition and a set of linear elastic analyses were performed. In each step, the stress in every element was calculated and one critical element of which the stress exceeded the strength was removed from the lattice. Then, another linear analysis is performed, and this procedure is repeated until the entire lattice system fails. After the computing process, crack pattern and stress-deflection curve were extracted.

In order to obtain input mechanical properties for the lattice elements, several simulations were carried out first to fit reinforcement element properties and matrix element properties using the experimental results on ABS bars and the matrix. The interface element strength was assumed and the elastic modulus was assumed to be the mean value of the Voigt upper bound [40] (calculated by eq. 8-1) and Reuss lower bound (calculated by eq.8-2) [40] for composites.

$$E_i = V_m E_m + V_r E_r \quad (8-1)$$

$$\frac{1}{E_i} = \frac{V_m}{E_m} + \frac{V_r}{E_r} \quad (8-2)$$

where E_i , E_m and E_r are the elastic moduli of interface elements, matrix elements and reinforcement elements, respectively. V_m and V_r are the volume fraction of matrix and reinforcement in an interface element. As the lattice network has a rather high randomness ($R=0.99$), $V_m = V_r = 0.5$ were assumed here for all interface elements.

During the fitting process, input parameters were varied in the simulation of four-point bending tests on the matrix and uniaxial tensile tests on ABS bars until the simulated results was close to the experimental results. The last input parameters were then adopted as inputs for the simulations of reinforced specimens. A comparison of fitting simulation results and experiments are shown in Figure 8-10, the simulated results are similar to experiment results. The input properties of the simulation are listed in Table 8-5 . In this work, only four-point bending tests on LT, ST and MT at 7 days were simulated, as in the case of roughened surface much finer grids are required and in tension simulations multiple linear properties, as described in [35], are required. As those simulations require too much computational resources, these tests were not simulated here.

Table 8-5 Input values for lattice model

Element	E-modulus (GPa)	f_t (MPa)	f_c (MPa)
Matrix	14.95	6.00	-8* f_t
Reinforcement	1.59	35.00	-2* f_t
Interface	5.57	0.10	-8* f_t

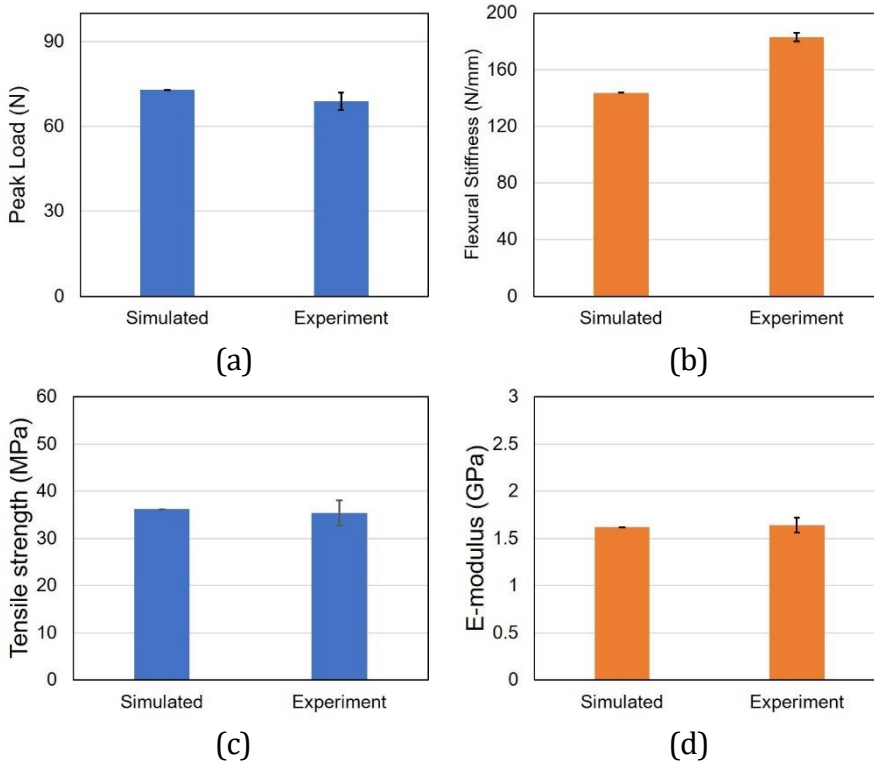


Figure 8-10 Comparison of simulated values and experiment values of (a) flexural peak load of the matrix, (b) flexural stiffness of the matrix in four-point bending tests, (c) Tensile strength of printed ABS bars, (d) E-modulus of printed ABS bars.

8.4 RESULTS AND DISCUSSION

8.4.1 Four-point bending tests

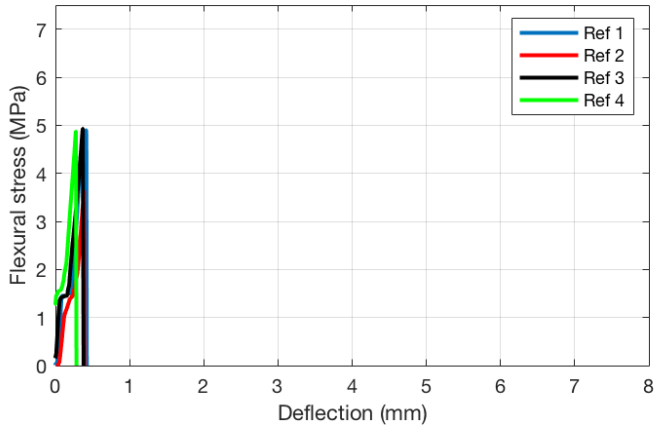
Flexural stress/deflection curves (average deflection measured by the two LVDTs) for all tested specimens with different 3D printed polymeric reinforcement designs are given in Figure 8-11 and Figure 8-12. A summary of the results is given in Table 8-6.

As expected, at 7d the reference specimens show a brittle response with relatively low deflection at failure (Figure 8-11a). On the other hand, all specimens reinforced with 3D printed polymeric meshes can undertake appreciably higher deformation. Nevertheless, there are significant differences between various reinforcement designs. Not all designs are able to achieve the so-called deflection-hardening behavior, wherein the flexural strength is higher than the first cracking strength. In that sense, looking at the average values given in Table 8-6 may be misleading in some cases. For the LT pattern, the average flexural strength is higher than the average of the first cracking strength. However, from Figure 8-11b it is clear that not all LT specimens show deflection hardening behavior. In fact, only specimen LT 1 (shown in blue) shows deflection hardening behavior. In other specimens, although they do not fail after the

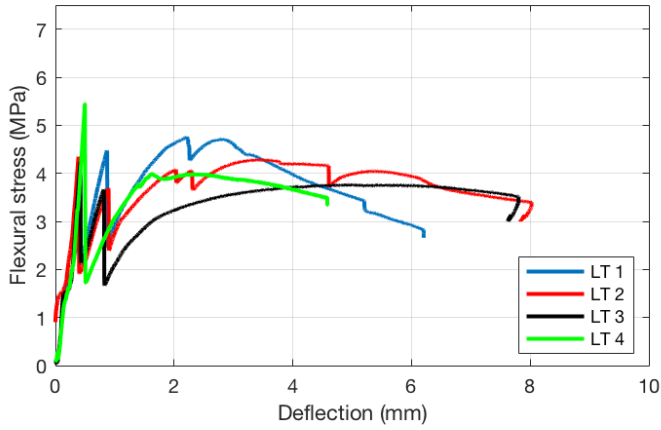
first crack occurs, the stress does not exceed the first cracking strength. In essence, although large triangular reinforcement does provide these specimens with some ductility, it cannot be used for obtaining (reliable) deflection hardening. In cementitious materials such as e.g. SHCC, deflection hardening is typically achieved through multiple cracking. Multiple cracking (witnessed by large drops in the stress/deflection diagrams) was not observed in LT series, which mostly had only two cracks, typically close to the loading points (as shown in Figure 8-13). The ductility in this case was provided by the pullout of the polymeric reinforcement from the cementitious matrix. Note that a different matrix design could possibly result in deflection hardening even in this case, e.g. if a weaker matrix would have been used.

All specimens from other series showed a characteristic deflection hardening behavior. First, the 7d ST series (Figure 8-11c) showed deflection hardening achieved through multiple micro-cracking. Compared with the LT series, this is clearly an improvement. This was expected, however: similar to conventional fiber reinforced cementitious composites, more ductility is achieved with a higher percentage of fiber reinforcement. It is very interesting to note, however, as shown in Figure 8-11d that the MT (i.e. “functionally graded”) series showed deflection hardening behavior as well, achieved through multiple micro-cracking (multiple cracks can be found in Figure 8-13). Again, in this series, the designed polymeric mesh was denser in the middle (constant moment region) than at the sides. This simple modification shows great potential of additive manufacturing: it is possible to achieve significant savings in the material if the reinforcement design is such that it is used only where needed (i.e. regions of high stress). This is something that cannot be achieved by conventional fiber reinforcement. The design with additively manufactured surface roughness (MT_R) did not show markedly different behavior (Figure 8-11e) – deflection hardening was achieved in this case as well. It is possible that, if the cementitious matrix would have been weaker, surface roughness would have had a higher impact on the post-peak behavior.

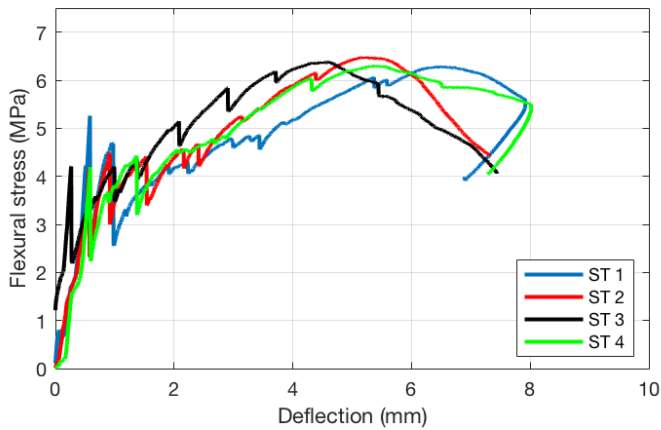
The two series at 28d of small triangles (ST_{28}) and mixed triangles (MT_{28}) were also tested, flexural stress-deflection curves are shown in Figure 8-12. Normally, mortar bars with longer curing age are stronger and more brittle. This can also be found in Table 8-6, the flexural strength of 28d specimen is higher and the strain capacity is lower. It could be even more difficult to have deflection hardening behavior for the reinforced mortar bars. However, as can be seen in Figure 8-12b and Figure 8-12c, both ST_{28} series and MT_{28} series still showed obvious deflection hardening behavior.



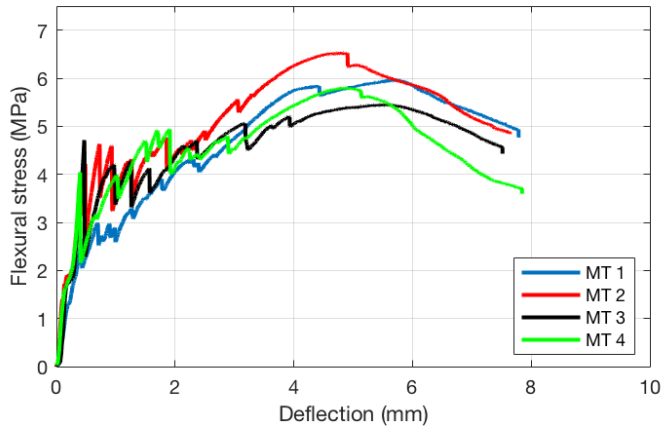
(a)



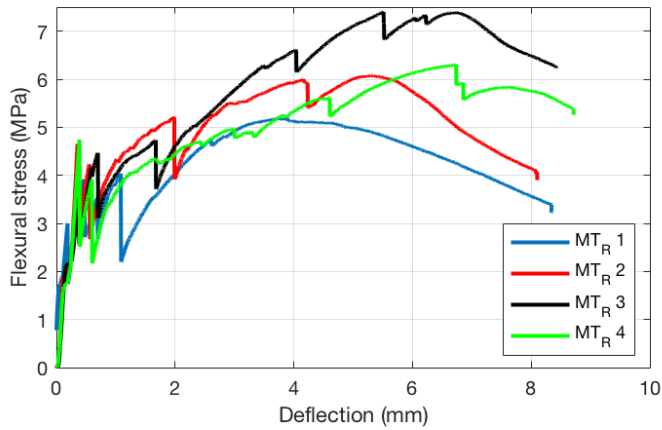
(b)



(c)

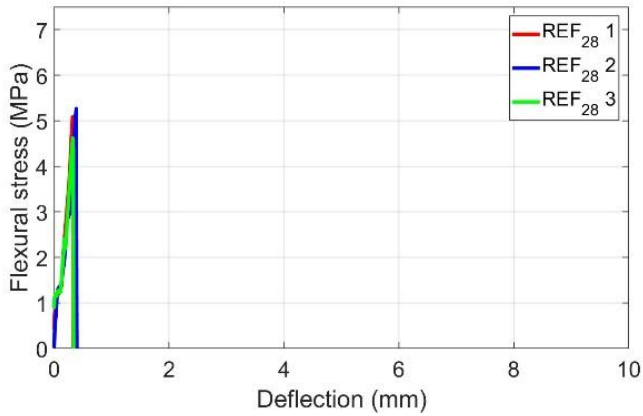


(d)

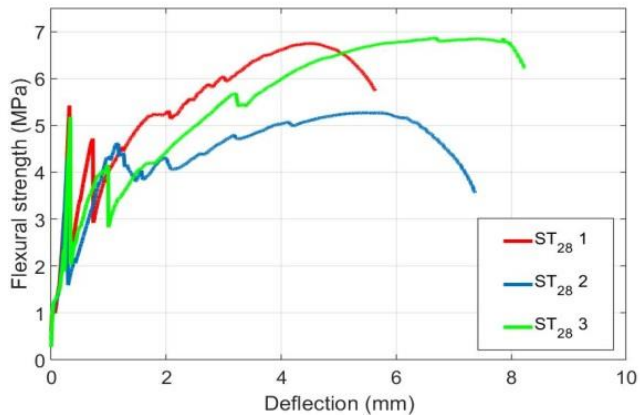


(e)

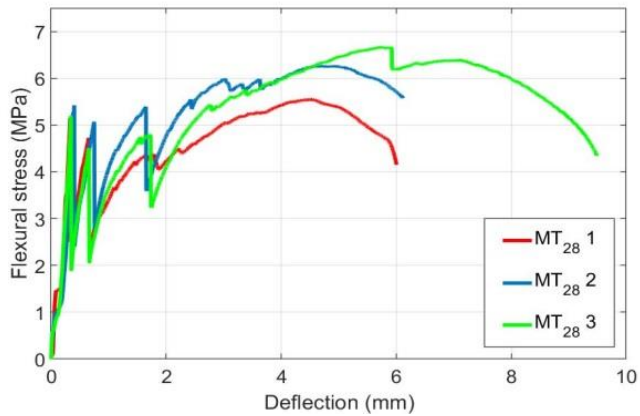
Figure 8-11. Flexural stress-deflection curves for 7d specimens tested in bending. (a) reference (no reinforcement); (b) large triangles (LT); (c) small triangles (ST); (d) mixed triangles (MT); (e) mixed triangles with a rough surface (MT_R).



(a)



(b)



(c)

Figure 8-12 Flexural stress-deflection curves for 28d specimens tested in 4-point bending. (a) reference (no reinforcement); (b) small triangles (ST₂₈); (c) mixed triangles (MT₂₈).

Table 8-6. A summary of four-point bending test results

Series	First cracking strength (Standard deviation) [MPa]	Flexural strength (Standard deviation) [MPa]	Deflection capacity (Standard deviation) [mm]	Total work (Standard deviation) [J]
Ref	4.584 (0.549)	4.584 (0.549)	0.361 (0.052)	0.010 (0.004)
LT	4.514 (0.546)	4.693 (0.472)	0.944 (0.881)	0.236 (0.043)
ST	4.308 (0.606)	6.127 (0.337)	5.429 (0.675)	0.440 (0.048)
MT	4.321 (0.666)	6.002 (0.541)	5.312 (0.605)	0.419 (0.019)
MT _R	4.255 (0.712)	6.243 (0.784)	5.369 (1.010)	0.418 (0.043)
Ref ₂₈	4.992 (0.337)	4.992 (0.337)	0.343 (0.036)	0.011 (0.002)
ST ₂₈	4.973 (0.583)	6.298 (0.890)	5.545 (1.012)	0.575 (0.073)
MT ₂₈	5.255 (0.147)	6.162 (0.569)	4.985 (0.661)	0.545 (0.141)

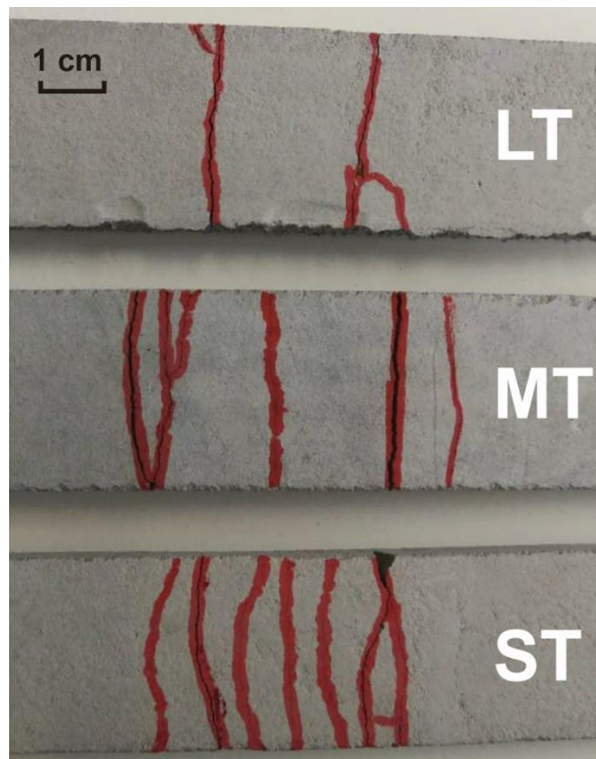


Figure 8-13 Highlighted cracks in the middle region of specimens with larger triangles (LT), mixed triangles (MT) and small triangles (ST), respectively, after the four-point bending test.

In Figure 8-14, Figure 8-15 and Figure 8-16 the reinforced specimens and reference specimens are compared in terms of the first cracking strength, flexural strength, deflection capacity, and total work for different specimen series. From Figure 8-14, it can be seen that the first cracking strength is not obviously affected when

printed mesh is used in all experimental series of the same age. The highest difference between the reinforced specimens and reference is 7.2% (between Ref and MT_R) at 7d and 5.3% (between Ref₂₈ and MT₂₈) at 28d. However, while the LT series doesn't show an obvious increase in average flexural strength compared to the reference (increase is less than 2.5%), other series show a significantly increased flexural strength (33.7%, 30.9% and 36.2% for the ST, MT, and MT_R series, respectively). Similar increase in flexural strength at 28d can also be found: 26.2% and 23.4% for ST₂₈ and MT₂₈ respectively. The increase in the flexural strength is a result of deflection hardening in these series. The most important difference between different series is the flexural deflection capacity (Figure 8-15). While the LT specimen series shows only a slightly higher average flexural deflection capacity compared to the reference (and only due to the one specimen which did exhibit deflection hardening), other tested series ST, MT, MT_R, ST₂₈ and MT₂₈ all show significantly improved flexural deflection capacity. Due to the improvement in deflection capacity, comparing to the reference specimens the reinforced specimens also require significantly higher total work to be fractured. Meanwhile, as the flexural strength is higher at 28d, the reinforced specimens at 28d also requires highest total work to be fractured.

It is rather interesting that at 7d and 28d, small triangle series (ST and ST₂₈) and mixed series (MT, MT_R and MT₂₈) show quite similar increased flexural deflection capacity and compared to reference: at 7d, 1403% (ST), 1345% (MT) and 1387% (MT_R). At 28d, they are 1516% (ST₂₈) and 1353% (MT₂₈). Similar improvement can be found in total work: at 4215% (ST), 4015% (MT) and 4003% (MT_R). At 28d, they are 5542% (ST₂₈) and 5251% (MT₂₈). This is an additional proof that, with additive manufacturing of reinforcement, there is potential for creating functionally graded cementitious composites and thereby optimizing material usage. Additionally, MT_R and MT have quite similar flexural strength and deflection capacity. Comparing to flat surface designs, the rough surface design did not provide the reinforced mortar bars with any additional ductility in the performed tests.

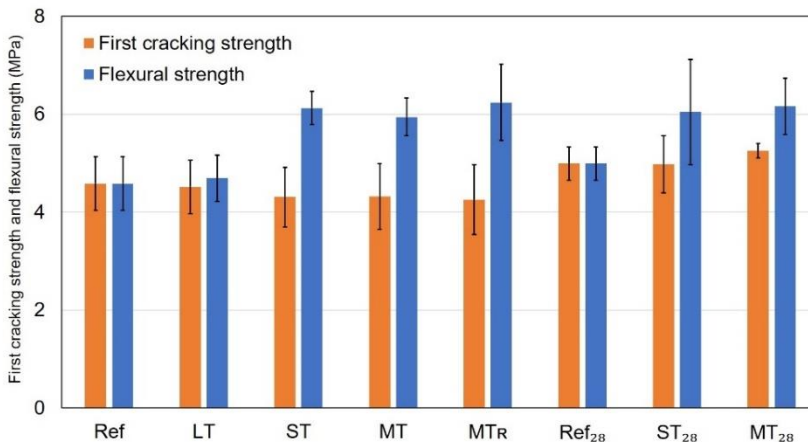


Figure 8-14. Comparison of first cracking strength and flexural strength of specimens tested in four-point bending (standard deviation is indicated).

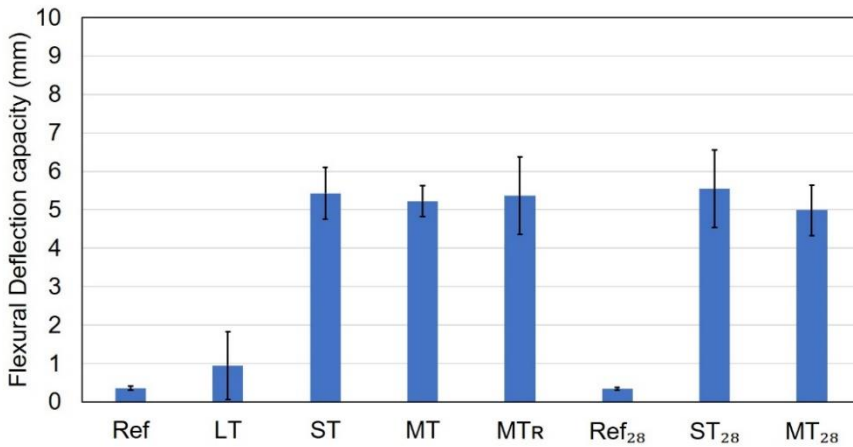


Figure 8-15. Flexural deflection capacity of specimens tested in four-point bending (standard deviation is indicated).

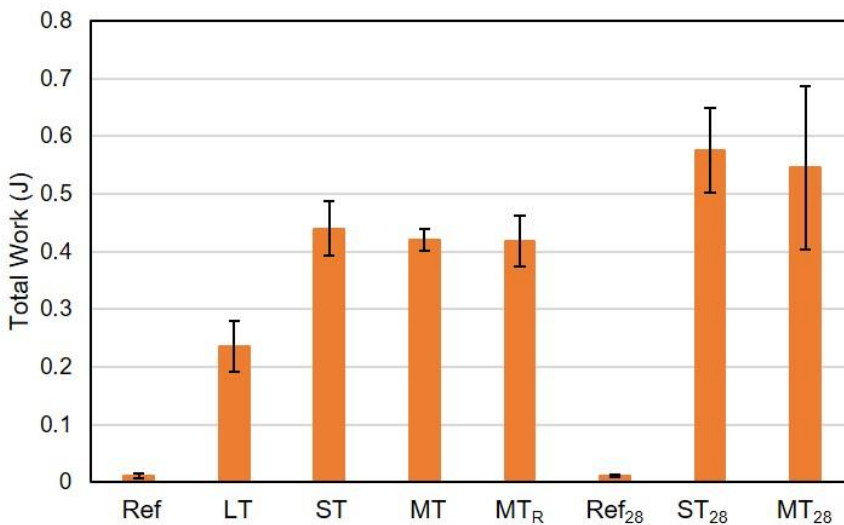


Figure 8-16 Total work of specimens tested in four-point bending (standard deviation is indicated)

Correspondingly, as can be seen in Figure 8-17, the simulated curves of LT and ST both show good agreement with experiments. For LT (shown in Figure 8-17a), after the first peak the reinforcement took over the load and stress increased again, while, deflection hardening behavior was not observed. Although ductility of the specimen was increased from the simulated flexural stress-deflection curve, only two main cracks can be seen from the fractured specimen (shown in Figure 8-18a), which resembles the cracking pattern obtained from the experiment (Figure 8-13). For ST and MT, the simulated stress-deflection also corresponds to the experiment (shown in Figure 8-17b and Figure 8-17c). After the first crack, the stress increased and was higher than the

first peak until failure. Multiple cracking behavior can be observed from the cracking history (shown in Figure 8-18b and Figure 8-18c).

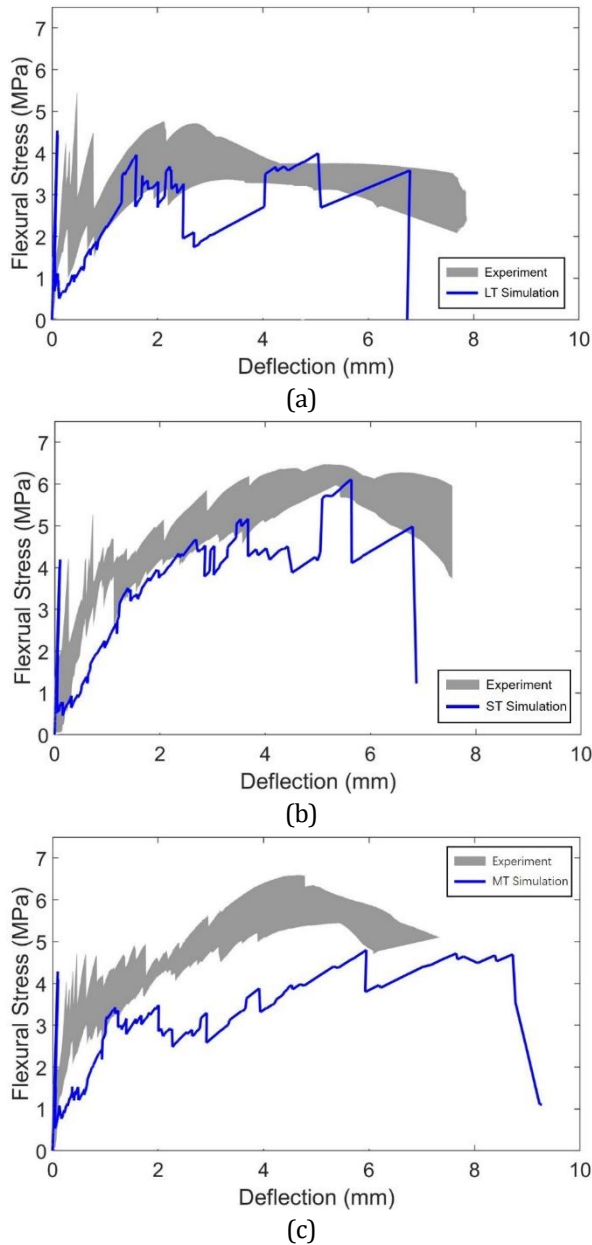


Figure 8-17 Comparison of experiment results and simulation results of four-point bending tests on mortar bars reinforced by (a) large triangles, (b) small triangles and (c) mixed triangles.

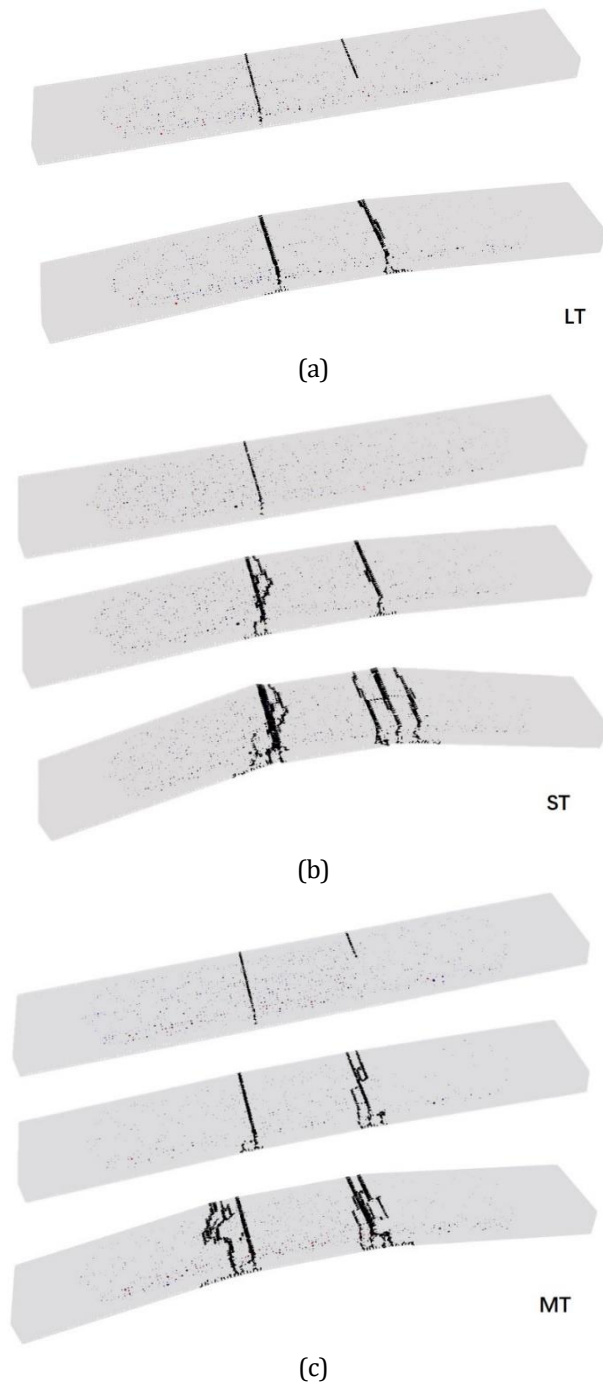


Figure 8-18 Simulated cracking history of (a) 7d large triangles, (b) 7d small triangles (ST) and (c) 7d mixed triangles (MT), black elements are failed elements.

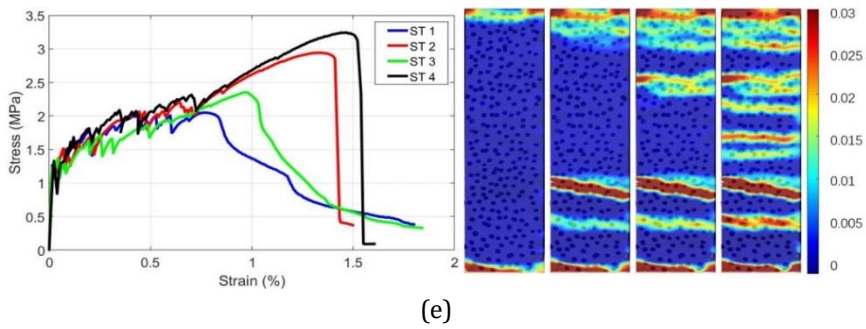
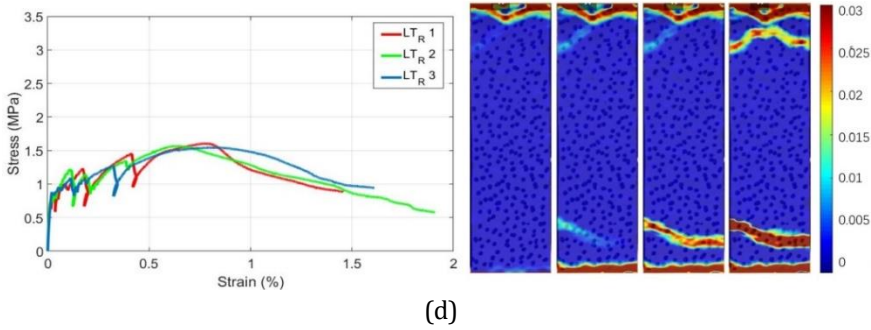
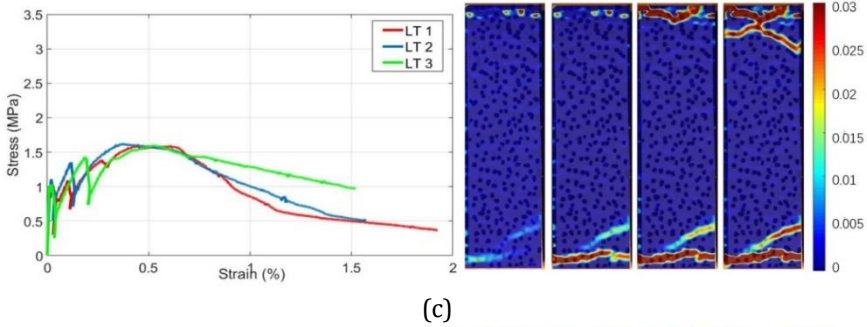
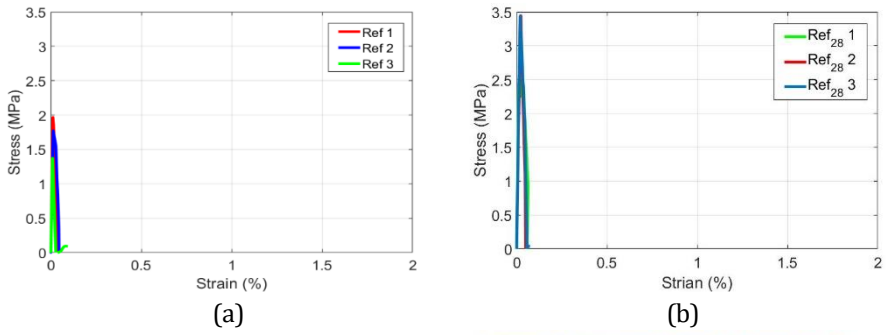
8.4.2 Uniaxial tension tests

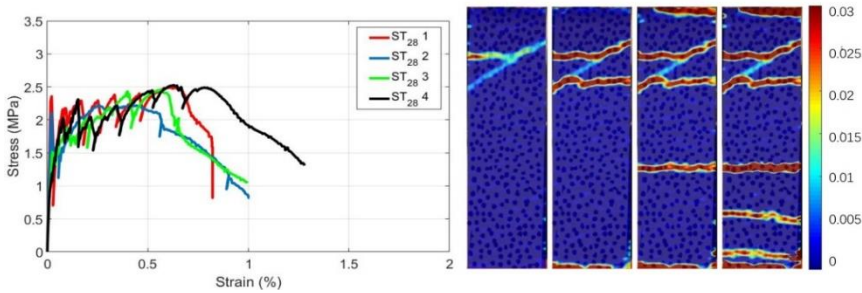
Uniaxial stress/strain curves (average strain measured by the two LVDTs) for all tested specimens reinforced by 3D printed polymeric meshes with different patterns are given in Figure 8-19. A summary of the results is given in Table 8-7. It is clear that the reference specimen (i.e. the one without polymeric reinforcement) exhibits brittle behavior in tension (Figure 8-19a), which is typical of cementitious materials [5]. It has a low strain capacity and only a single crack formed. On the other hand, all specimens reinforced with 3D printed polymeric meshes are capable of undertaking larger strains. Furthermore, as can be seen from Figure 8-19, in tension all tested reinforced specimens of various configurations did show strain hardening behavior: after the first cracking, all reinforced specimens were able to carry increasing amounts of stress until the maximum stress was reached. Still, different behaviors of reinforced specimens are obvious within varied reinforcement patterns.

The large triangle patterns (LT and LT_R) exhibit quite similar strain hardening behavior: after cracking, only a few cracks formed before the ultimate strain was reached. The strain hardening behavior occurred mainly not from multiple cracking mechanism but the so-called slip hardening behavior [6], namely the friction between the reinforcement and the matrix which resists the slippage. In the observed case, the friction is sufficient to result in slip hardening behavior, providing the LT_R and LT with overall higher strain capacity. As the roughed surface provides higher friction (rough surface has more contacting area between matrix and reinforcement), the strain capacity of LT_R series (0.741%) is slightly higher than LT series (0.503%).

Comparing to the large triangle patterns, the multiple cracking behavior of specimens reinforced with small triangles (ST and ST₂₈ series) is much more obvious which is similar to the typical strain hardening behavior of e.g. SHCC [7, 8] or TRC [9, 10]. In most specimens in ST and ST₂₈ series, numerous drops in the stress-strain curve indicate multiple cracks forming in the loading process. Finally, after the maximum stress is reached, the specimen fails in a manner similar to LT specimens, i.e. through pullout of the polymeric reinforcement and localization of a single wide crack. It is interesting to observe that in ST series (Figure 8-19), results of all specimens are quite constant, only in the final pulling out stage, two specimens (ST 2 and ST 4) behave differently than other specimens in the final pull out stage: instead of being pulled out at the final drop, the printed meshes suddenly ruptured in tension (sudden drop of the last peak) which resulted in relatively higher strain capacity and flexural strength.

In the previous section, it was shown that the flexural strength of 28d reference specimens is slightly stronger than 7d reference specimens. However, in tension the influence of curing age on the tensile strength of the matrix is considerable. From Table 8-7, tensile strength of the reference series at 28d (3.444 MPa) is much higher than that of reference series at 7d (1.705 MPa) and consequently, the strain capacity of ST₂₈ series (0.579%) is much lower than ST series (1.135%).





(f)

Figure 8-19. Tensile stress-strain curves and corresponding DIC results for specimens reinforced with different 3D printed polymeric meshes. (a) reference (no reinforcement) at 7d; (b) reference (no reinforcement) at 28d; (c) large triangles at 7d (LT); (d) large triangles with a rough surface at 7d (LT_R); (e) small triangles at 7d (ST); (f) small triangles at 28d (ST₂₈).

Table 8-7. A summary of uniaxial tension results

Series	First cracking strength (Standard deviation) [MPa]	Tensile strength (Standard deviation) [MPa]	Strain capacity (standard deviation) [%]	Total work (Standard deviation) [J]
Ref	1.705 (0.302)	1.705 (0.302)	0.012 (0.002)	0.005 (0.002)
LT	0.944 (0.051)	1.604 (0.017)	0.503 (0.120)	0.399 (0.047)
LT _R	0.784 (0.087)	1.572 (0.030)	0.741 (0.111)	0.412 (0.022)
ST	1.223 (0.070)	2.647 (0.543)	1.135 (0.323)	0.617 (0.144)
Ref ₂₈	3.136 (0.533)	3.136 (0.533)	0.021 (0.002)	0.009 (0.004)
ST ₂₈	1.093 (0.181)	2.424 (0.140)	0.579 (0.095)	0.539 (0.112)

Figure 8-20 provides a comparison between correlated first cracking strength (first cracking strength divided by cross sectional reinforcing ratio) and tensile strength of different series. As can be seen in Figure 8-20, all reinforced specimens show significant improvement compared to the first cracking strength which is a result of strain hardening in these materials. In uniaxial tension tests, because part of the cross section is replaced by the printed mesh in reinforced specimen, the real cross-sectional area of the matrix is smaller than that of the reference specimen, which resulted in lower first cracking strength in reinforced series. In this sense, the matrix cracking strength is correlated according to the first cracking strength and the highest cross-sectional reinforcing ratio from Table 8-3 of each pattern. As shown in Figure 8-21, considering the deviation, there is no significant difference between the reinforced test series and reference specimens in correlated cracking strength of the matrix. Still, in LT series the correlated first cracking strength is relatively lower. This could be the fact that printed reinforcement might introduce many interfacial zones between the matrix and the reinforcement making the crack easier to initiate in the reinforced specimens. Furthermore, matrix compaction is somewhat more difficult in the reinforced series

due to the spacing regions of the printed reinforcement, possibly causing more imperfections to form in some of the specimens compared to the reference series.

Even more significant improvements can be seen in terms of tensile strain capacity (Figure 8-22): the tensile strain capacity of the LT, LT_R, ST and ST₂₈ series is increased by 4092%, 6075%, and 9358%, and 2657% compared to the reference series at the same age, respectively. Similar to the cases under bending, the total work to fracture the specimens has also been improved by 7450% (LT), 7682% (LT_R), 11567% (ST), and 6013% (ST₂₈), respectively. Even with a simple reinforcement mesh design used herein, these are significant improvements. Clearly, there is still room for improvement. This indicates a huge potential that additive manufacturing has in creating strain hardening cementitious composites.

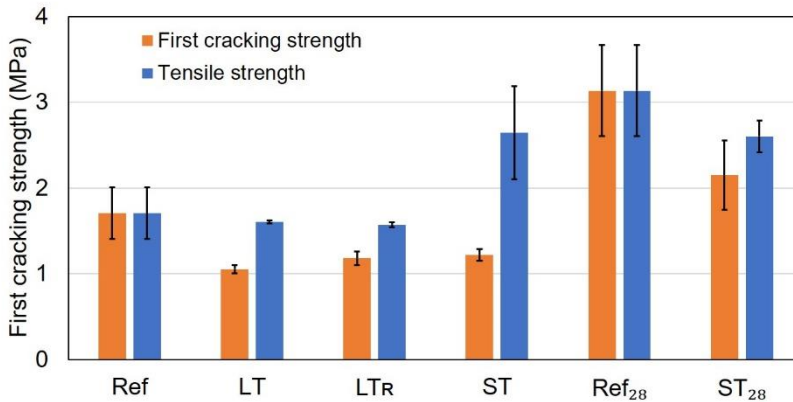


Figure 8-20. First cracking strength and Tensile strength of specimens tested in tension (standard deviation is indicated)

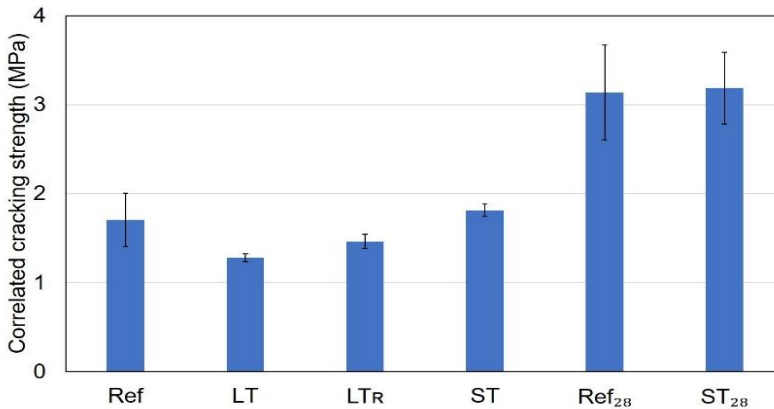


Figure 8-21 Correlated cracking strength of the matrix (standard deviation is indicated)

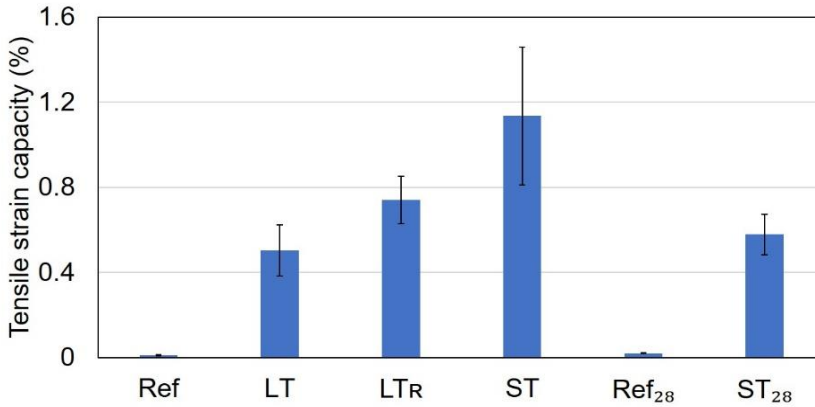


Figure 8-22. Tensile strain capacity of specimens tested in tension (standard deviation is indicated).

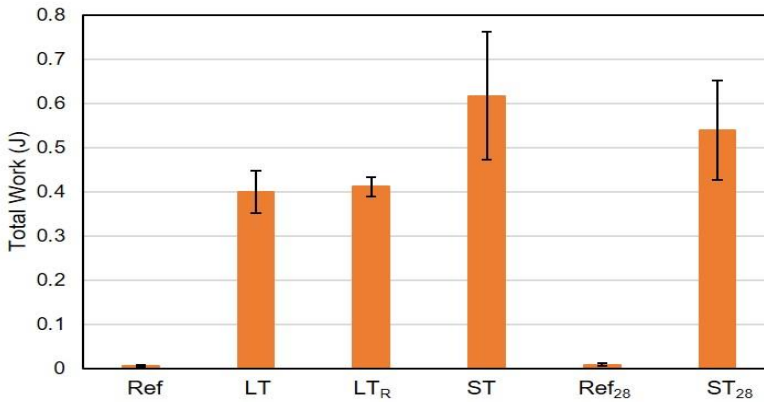


Figure 8-23 Total work of specimens tested in tension (standard deviation is indicated).

8.5 CONCLUSIONS

In this chapter, additively manufactured polymeric meshes with 2D patterns were used as reinforcement for enhancing fracture resistance of cementitious materials. Simple reinforcement meshes were designed, manufactured, and tested in four-point bending and uniaxial tension. In addition, four-point bending tests were simulated using the lattice model. Based on the performed experiments and simulations, the following conclusions can be drawn:

- Use of 3D printed polymeric reinforcement enables significantly increasing the deflection and tensile strain capacity of cementitious composites compared to the reference material; the fracture resistance of cementitious materials is able to be substantially enhanced by 3D printed polymeric meshes.
- Strain hardening and deflection hardening behavior is achieved by the reinforced cementitious composites which mainly depends on the mesh design in terms of a same matrix.

- According to experimental results, deflection hardening was observed only in specimens which showed multiple cracking. Other specimens (in which pull-out of the reinforcement was the only mechanism) did show increased ductility compared to the reference, but no significant hardening was observed.
- Numerical simulation results show good agreement with the experiment, specimen reinforced by finer mesh (ST) and mixed mesh (MT) show multiple cracking behavior and deflection hardening was obtained while specimen reinforced by coarser mesh (LT) didn't show multiple cracking and deflection hardening.
- In four-point bending, a simple mesh pattern (MT) showed great potential of using additive manufacturing for creating functionally graded cementitious composites.

The proposed reinforcing approach shows high capability to enhance the crack bridging ability of the constituent material which can be used to create auxetic cementitious cellular composites (ACCCs). However, the two-dimensional patterns used in this chapter to some extent may limit the design of auxetic structures, especially three-dimensional cellular structures. 3D printed three-dimensional reinforcement structures might be required when more complex cellular structures are designed for the ACCCs. Therefore, the possibility of using 3D printed reinforcement with three-dimensional patterns to increase cracking resistance of cementitious composites will be discussed in the next chapter.

REFERENCES

- [1] J. Shang, F.H. Wittmann, T. Zhao, Properties of SHCC produced with natural fibres, 3rd International RILEM Conference on Strain Hardening Cementitious Composites, 2014, p. 179.
- [2] R. Zou, Y. Xia, S. Liu, P. Hu, W. Hou, Q. Hu, C. Shan, Isotropic and anisotropic elasticity and yielding of 3D printed material, *Composites Part B: Engineering* 99 (2016) 506-513.
- [3] B. Šavija, M. Luković, G.M. Kotteaman, S.C. Figuieredo, F.F. de Mendonça Filho, E. Schlangen, Development of ductile cementitious composites incorporating microencapsulated phase change materials, *International Journal of Advances in Engineering Sciences and Applied Mathematics* 9(3) (2017) 169-180.
- [4] E. Schlangen, E.J. Garboczi, Fracture simulations of concrete using lattice models: computational aspects, *Engineering Fracture Mechanics* 57 (1997) 319-332.
- [5] J.G. Van Mier, *Concrete fracture: a multiscale approach*, CRC press 2012.
- [6] M. Luković, H. Dong, B. Šavija, E. Schlangen, G. Ye, K. van Breugel, Tailoring strain-hardening cementitious composite repair systems through numerical experimentation, *Cement and Concrete Composites* 53 (2014) 200-213.
- [7] V.C. Li, *From micromechanics to structural engineering-the design of cementitious composites for civil engineering applications*, (1993).
- [8] V.C. Li, On engineered cementitious composites (ECC), *Journal of advanced concrete technology* 1(3) (2003) 215-230.
- [9] J. Hegger, N. Will, O. Bruckermann, S. Voss, Load-bearing behaviour and simulation of textile reinforced concrete, *Materials and structures* 39(8) (2006) 765-776.
- [10] J. Hartig, U. Häußler-Combe, K. Schicktanz, Influence of bond properties on the tensile behaviour of Textile Reinforced Concrete, *Cement and Concrete Composites* 30(10) (2008) 898-906.

9

TOUGHENED CEMENTITIOUS COMPOSITES BY CUSTOMIZED THREE-DIMENSIONAL OCTET LATTICE STRUCTURES

In this chapter, three-dimensional octet polymeric lattice structures are used to improve the crack-bridging ability of cementitious materials. Experimental and numerical four-point bending tests are performed to evaluate the mechanical properties of the toughened cementitious mortar. A good agreement between experiments and simulations is found: the toughened specimens have significantly increased cracking resistance compared to the reference plain mortar. In addition, the fracture behavior of the toughened cementitious composites was evaluated using a fracture energy based analytical model. The analysis shows that, from the perspective of fracture energy release, the steady state cracking criterion is not satisfied by the developed cementitious composites so that multiple cracking and strain hardening behavior is not obtained. However, according to numerical predictions, increasing the strength of the printed polymeric material by 40 % would allow such behaviors to be potentially achieved. The geometrical customizability and the ability of toughening cementitious materials indicates that the three-dimensional lattice structure possesses the potential to create auxetic cementitious composites with various complex cellular structures.

9.1 INTRODUCTION

It was demonstrated in the previous chapter that the fracture resistance of cementitious materials can be significantly enhanced by the 3D printed polymeric meshes by forming a cementitious composite in which the polymeric meshes serve as the toughening phase. However, in order to be used as an alternative of the fiber reinforced cementitious materials F_2 (see mixture F_2 in Chapter 5) to create auxetic cementitious materials constructed with more complex cellular structures, a three-dimensional reinforcement or toughening structure should be used.

Considering the four-point bending loading condition (shown in Figure 9-1), under the flexural Mode I fracture state, stretch dominated lattice structures have significantly higher fracture resistance comparing to the bending dominated lattices counterparts [1, 2]. Octet structure is one of the most commonly studied and used stretch dominated lattice structures. A previous study [3] has shown that the 3D octet lattice structure is an optimal structure among other lattice structures to create a composite material with high fracture resistance. Therefore, in this chapter, three-dimensional polymeric octet lattice structures are adopted, 3D printed and used to toughen cementitious mortar. The octet lattice structures are functionally graded to optimize the flexural ductility of the cementitious composites meanwhile minimizing the toughening phase material use. Flexural behavior of the toughened cementitious composites is experimentally and numerically studied and then critically discussed. Adopting the experimental and numerical results, crack bridging ability of the toughened cementitious composites is further analytically investigated. Based on these analyses, suggestions for potential methods to enhance the performance of the cementitious composites are given. In terms of the numerical simulation, as introduced in Chapter 6, a commercial modeling package ABAQUS/Explicit is required to indicate the principal stress distribution. Hence, the same modeling tool is also used in this chapter.

9.2 METHODS AND MATERIALS

9.2.1 Designing and fabrication of polymeric lattices

Similar to the previous chapter, four-point bending which is preferable to evaluate the crack bridging ability of the constituent material for auxetic cementitious materials is used. A unit cell of the octet structure to create the toughening phase for cementitious mortar is shown in Figure 9-2. The toughening octet lattice structures are designed by combining the unit cells with different sizes. Four different functionally graded lattice structures are designed, printed and used to toughen cementitious mortar.

Different from the two-dimensional patterns used in the previous chapter, not only in the longitudinal direction along the specimen, in the vertical direction the lattice structures are also functionally graded. This is determined according to the bending moment as well as the tensile stress distribution of a bended specimen. As can be seen in Figure 9-1, in the longitudinal direction, in order to maintain the structural integrity

of the octet cells while varying the relative density (defined as the density of the octet structure divided by the ABS material), four types of octet cells (shown in Figure 9-3) are designed. The length “x” varies with the four types of octet cells. The dimensional design parameters and the relative density of these cells are listed in Table 9-1. Subsequently, the toughening lattice structures for cementitious mortar were configured by combining these octet cells. At the mid span region, as it has a constant and the highest bending moment, octet cells with smaller relative density (C10 and C15) are used. Identical to the length of the midspan (30mm), three C10 (10 mm) or two C15 (15 mm) cells are used at this region for two lattices L10 and L15, respectively (shown in Figure 9-4). At the regions outside the midspan, as the bending moment decreases along the longitudinal direction from both sides of the midspan, octet cells with larger relative density are used (one C25 and one C40 used at both sides respectively) such that the relative density of the lattice structure also decreases along the same direction. In this sense, in the longitudinal direction, the designed lattice structures have functionally graded relative density meanwhile integrity of the octet structures is still maintained.

In the vertical direction, because the tensile stress is linearly distributed across the specimen cross section (see Figure 9-1), the diameter of the lattice struts is also functionally graded ensuring that more material is used at the bottom which is subjected to higher tensile stress. This is done by linearly decreasing the strut diameter from 3 mm to 2 mm bottom up. Dimensional parameters of all used unit cells are listed in Table 9-1. The configuration of these unit cells in the designed lattice structures are shown in Figure 9-4. Note that four “studs” are also designed for each lattice structure to make sure they can be easily positioned in the molds during casting. The “studs” are designed outside the midspan region so that they would have limited influence on the mechanical behavior of the bended specimen. All designed lattice structures are printed and then used as toughening phase for cementitious mortar under four-point bending tests, description of experimental test groups is listed in Table 9-2.

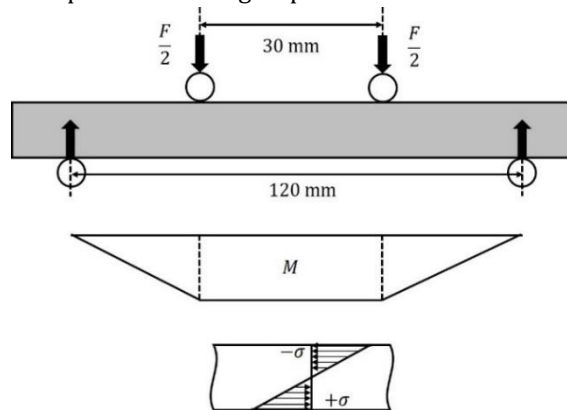


Figure 9-1 Schematics of four-point bending, distribution of bending moment and stress on the loaded specimen is shown, maximum bending moment exists at the mid span of the specimen and highest tensile stress exists at the bottom of the specimen mid span

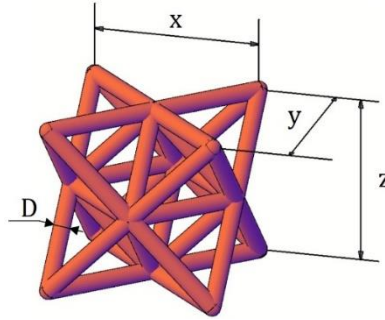


Figure 9-2 Unit cell of the lattice structure, x, y and z are the dimensions of a unit cell in three directions, D is the diameter of the lattice strut, detail information of used unit cells can be found in Table 9-1

C10		RC10	
C15		RC15	
C25		RC25	
C40		RC40	

Figure 9-3 Octet unit cells C10~C40 are the cells with varying length x , RC10~RC40 are the cells with varying length x and varying struts diameter D , dimensional parameters of these cells can be found in Table 1

Table 9-1 Dimensional parameters of the used unit cells

Unit Cell	x (mm)	y (mm)	z (mm)	D (mm)	Relative density (%)
C10	10	20	20	3	37.4
C15	15	20	20	3	28.0
C25	25	20	20	3	20.8
C40	40	20	20	3	17.1
RC10	10	20	20	2 (top) ~ 3 (bottom)	27.8
RC15	15	20	20	2 (top) ~ 3 (bottom)	20.1
RC25	25	20	20	2 (top) ~ 3 (bottom)	15.2
RC40	40	20	20	2 (top) ~ 3 (bottom)	12.4

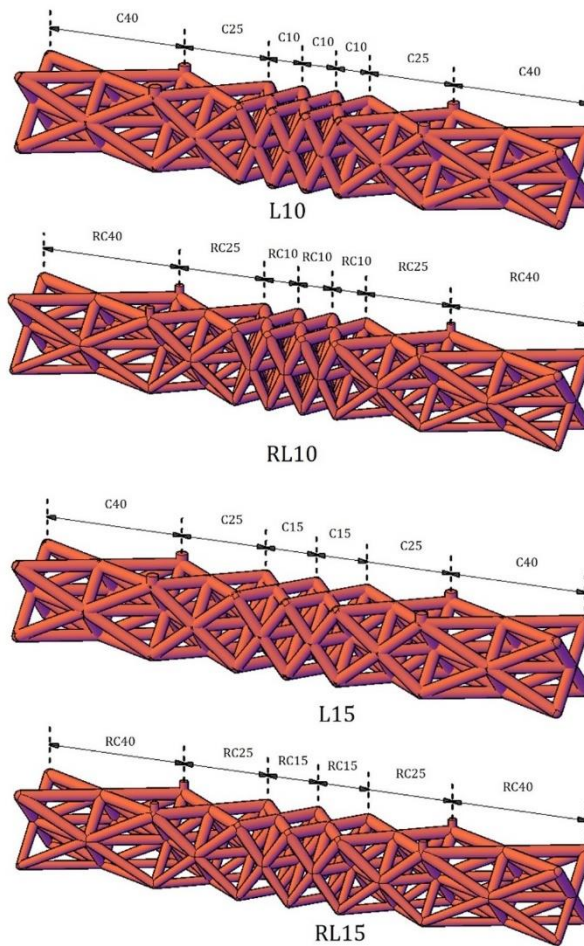


Figure 9-4 Designed functionally graded octet lattice structures, unit cells are indicated, “C” and “RC” indicate the type of used unit cells, dimensions of these unit cells can be found in Table 9-1.

Table 9-2 Testing groups

No.	Toughening phase ratio by volume	Description
REF	0%	Reference
L10	11.22%	Unit cell size graded in longitudinal direction with C10 cell in the middle
L15	10.13%	Unit cell size graded in longitudinal direction with C15 cell in the middle
RL10	5.78%	L10 with strut diameter functionally graded in height direction
RL15	5.32%	L15 with strut diameter functionally graded in height direction

The designed lattice structures are printed using the 3D printer Ultimaker 2+ and ABS (Acrylonitrile Butadiene Styrene) is used as printing material. Printing parameters for all four designs are kept the same as in the previous chapter, except that the layer height is slightly increased to 0.25 mm to decrease the printing time. All parameters are listed in Table 9-3. In order to ensure the printed lattice structure with maximum tensile resistance [4], the printing direction of the lattice structures was arranged such that the printed layers were parallel to the tensile stress direction (shown in Figure 9-5c). The orientation of the lattice structure printed on the build plate is shown in Figure 9-6. Owing to the geometry of octet structures, overhangs existed between two lattice struts. During the printing of the overhangs, the nozzle directly moved from one strut to another at a constant velocity of 40 mm/s. The extruded ABS material is immediately cooled down by a fan above the printing nozzle to ensure fast hardening (see Figure 9-7). After printing the first layer of an overhang region, the nozzle moves backwards and deposits the next layer on top. For all designed lattice structures, the longest overhang is around 22.4 mm, and it only took about half a second for the nozzle to print one layer so that good printing quality is obtained. After printing, no significant defects at the overhangs are found and the integrity of the designed lattices structures is maintained.

The printed lattice structures are placed inside the Styrofoam molds and the “studs” are glued on the molds by silicone rubber making sure the lattice structure unable to detach from the molds during vibration (see Figure 9-5c). The casted specimens have dimensions of 40 × 40 × 160 mm. In addition, in order to obtain input parameters for numerical simulations, dog bone shaped ABS bars with a cross section of 3 × 3 mm are printed and tested in uniaxial tension (shown in Figure 9-5b).

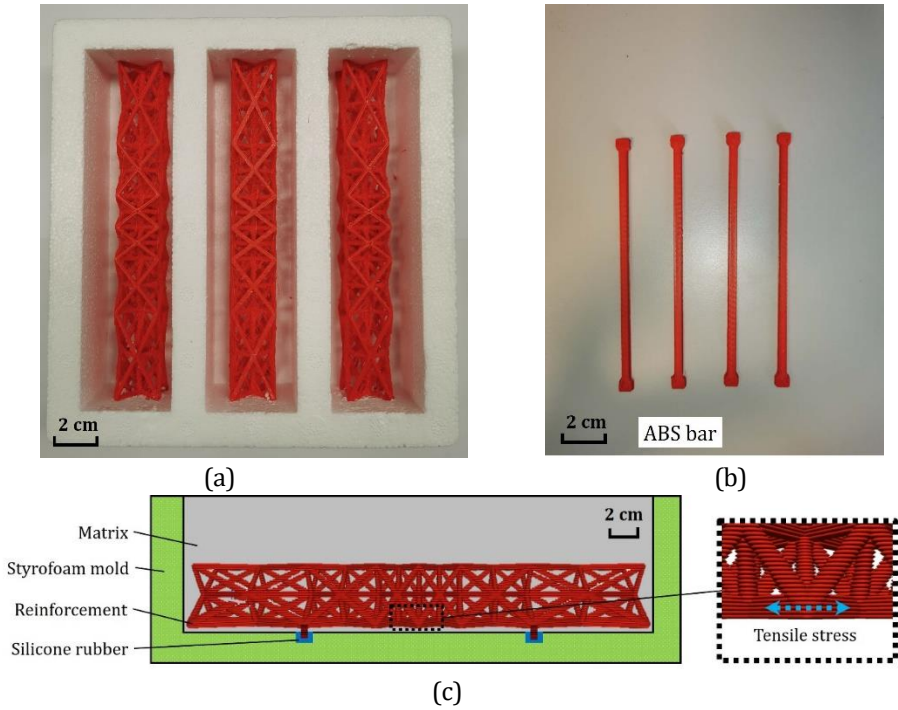


Figure 9-5 Schematics of a) printed specimens and Styrofoam mold; b) the printed ABS bars; c) positioning of specimen in Styrofoam mold during casting

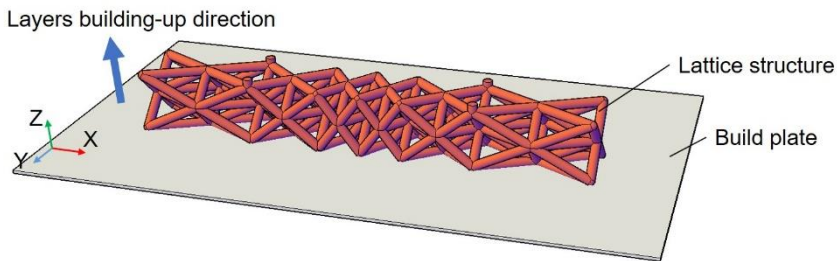


Figure 9-6 Lattice structure orientation on the building plate and layers building-up direction

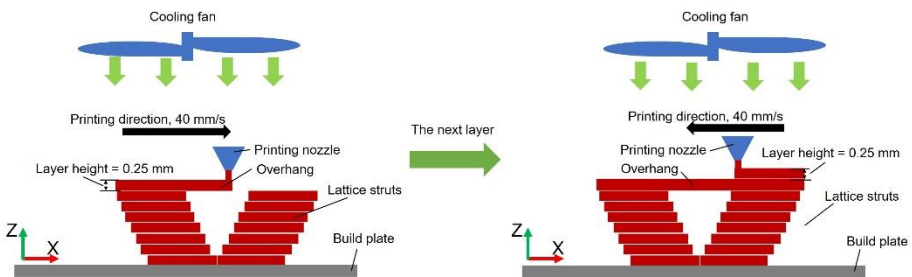


Figure 9-7 Printing process of the overhangs on the lattice structure

Table 9-3 Printing parameters for reinforcement meshes used*

Printing parameter	Configuration
Nozzle diameter (mm)	0.8
Temperature (°C)	260
Layer height (mm)	0.25
Line width (mm)	0.7
Infill density (%)	100
Infill pattern	Lines
Printing speed (mm/s)	40

*Printing parameters differ from Chapter 8

9.2.2 Casting and curing

The same cementitious material and mixing and curing procedures as Chapter 8 are used. One hour before the test, the specimens were taken out of the curing chamber and painted on one surface by white background and black dots for DIC analysis used for measuring crack mouth opening displacement (CMOD). In order to obtain compressive and tensile parameters needed for the numerical model, cementitious mortar cubes ($15 \times 15 \times 15$ mm) and cementitious mortar bars ($30 \times 10 \times 100$ mm) were also cast and cured under the same conditions until 28 days of age. These specimens were then tested under uniaxial compression and tension, respectively.

9.2.3 Mechanical tests

Four-point bending tests were performed on all the prepared specimens by a servo hydraulic press (INSTRON 8872). Loading was applied on the top of the specimens under displacement control with a constant rate 0.01mm/s. The loading scheme and the experimental setup of the four-point bending test are shown in Figure 9-8. A digital camera was placed in front of the specimen to take pictures for DIC. During the test, load and deflection (vertical displacement at the middle of the specimens) was measured by Instron 8872 and DIC, respectively. After the first main crack appeared, crack mouth opening displacement (CMOD) was measured by DIC. Uniaxial compression and tension tests were performed on cementitious mortar cubes, mortar bars and ABS bars respectively to obtain compressive and tensile stress-strain curves for calibration the numerical models.

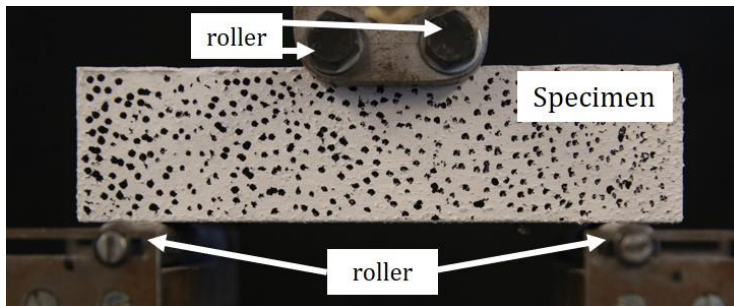


Figure 9-8 Four-point bending experimental setup

9.3 NUMERICAL SIMULATIONS

9.3.1 Concrete damaged plasticity model (CDPM)

Similar to Chapter 6, a commercial FEA software Abaqus/Explicit is used to simulate the four-point bending tests. Detailed description of the CDPM can be found in Chapter 6.

9.3.2 Model calibration and validation

Prior to simulating the four-point bending tests, calibration and validation procedures are performed to obtain proper material compressive and tensile input parameters. Considering the accuracy and computational cost, 2 mm hexahedron elements are used for cementitious matrix and 2 mm tetrahedron elements are used for ABS lattice structure. The mesh size is kept constant for all numerical simulations in this chapter. In order to model the interaction between the cementitious matrix and the lattice structure, the “embedded region” constraint is assigned for the toughened composites using the cementitious matrix as the host region and the printed lattice structure as the embedded region. Table 9-4 shows the physical properties of cementitious mortar and input parameters for CDPM. Elastic modulus, density and Poisson’s ratio are measured from experiments, while other parameters are adopted using ABAQUS default values. By trial and error, the compressive and tensile input parameters are calibrated through varying the input parameters so that the simulated compressive and tensile stress-strain curves fit the experimental results. In order to simulate the damage process of the cementitious matrix and the ABS lattice structure, respectively, CDPM material model is used for cementitious mortar while brittle cracking material model is used for ABS lattice structure. Numerical uniaxial compression tests are performed on the cubic mortar specimens to calibrate the cementitious matrix compressive parameters. Input parameters of the cementitious mortar and the ABS lattice structure are listed in Table 9-5 to Table 9-7. The comparison of calibrated compression curve and experimental curves are shown in Figure 9-9a. Similarly, numerical uniaxial tension tests are performed on the mortar and ABS bars to validate tensile input parameters of the cementitious matrix and the ABS lattice structure. The comparison of calibrated compression curve and experimental curves are shown in Figure 9-9b and Figure 9-9c.

Table 9-4 Input parameters for CDPM

Material input parameters	Value
Density (kg/m ³)	1870
Elastic Modulus (MPa)	15500
Poisson's Ratio	0.2
Dilation Angle (°)	35
Eccentricity	0.1
fb0/fc0	1.16
K	0.667
Viscosity Parameter	0.001

Table 9-5 Compressive parameters of cementitious mortar

Yield Stress (MPa)	Inelastic Strain
38	0
42	0.00149
3	0.0018
1	0.002

Table 9-6 Tensile parameters of cementitious mortar

Yield Stress (MPa)	Cracking strain
5.8	0
0.1	0.0005

Table 9-7 Tensile parameters of ABS lattice structure

Direct Stress after cracking (MPa)	Direct cracking strain
25	0
20	0.2
0.1	0.25

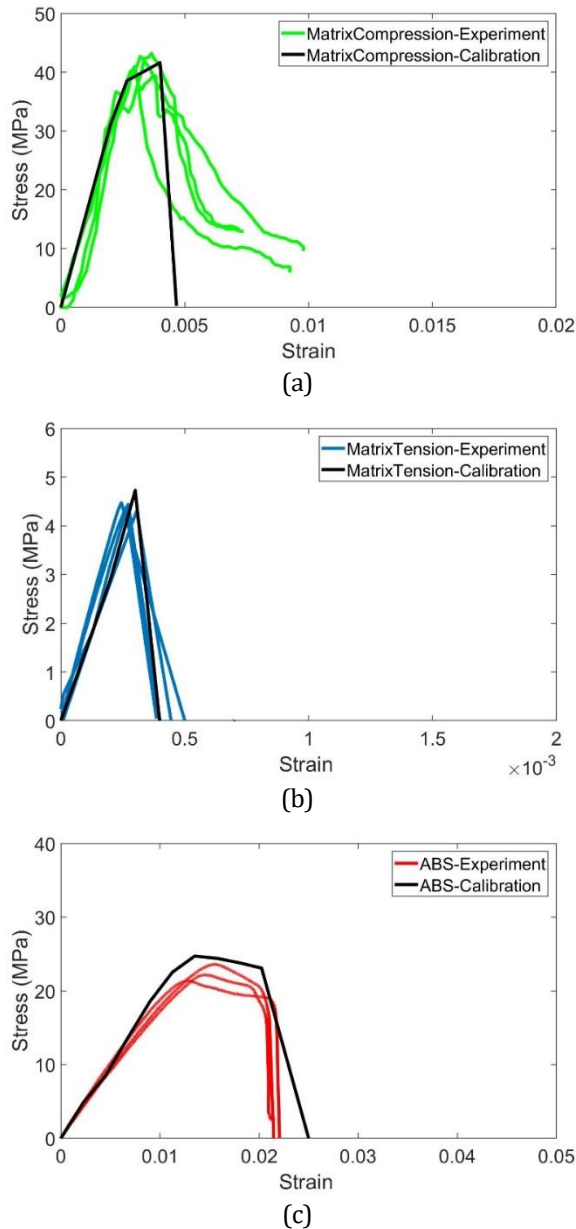


Figure 9-9 Calibrated stress-strain curve of cementitious mortar in a) compression, b) tension and c) ABS bars in tension

9.3.3 Four-point bending simulation

Corresponding to experiment set-up, numerical four-point bending tests are performed. In order to decrease the computational cost, symmetrical boundary

conditions are used and half of the actual specimen (shown in Figure 9-10) is numerically simulated. Four rigid rollers are generated as loading and supporting devices on top and bottom of the specimen. A minor friction coefficient (0.15) is assigned between the loading rollers and the specimen to prevent unrealistically large lateral movement of the specimen in the case of an ideal frictionless contact. Downwards displacement is applied on the two upper loading rollers while all degrees of freedom of the bottom loading rollers are completely fixed (Figure 9-10). Plain mortar specimen and the four toughened specimens are numerically tested. In terms of the loading process, similar to Chapter 6, the simulations were performed under a mass scaled condition such that the stable time increment remained below $1e^{-5}$. The results of numerical simulations are discussed in detail in the next section.

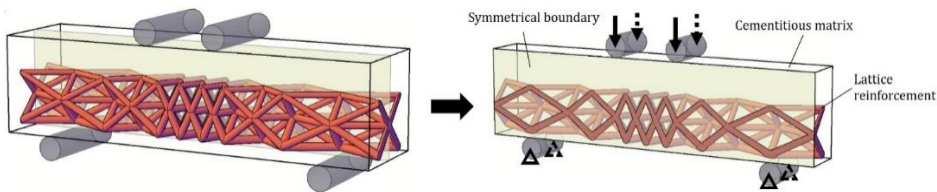


Figure 9-10 Schematics of flexural loading condition in numerical simulation, half of the specimen was simulated under a symmetrical boundary condition

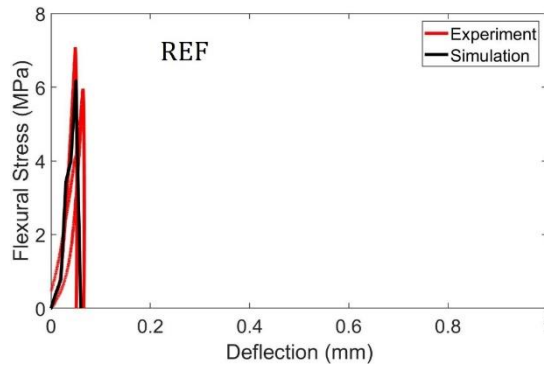
9.4 RESULTS AND DISCUSSION

9.4.1 Flexural stress-deflection response

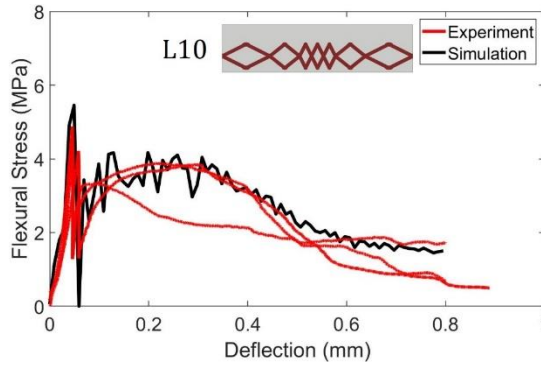
The comparison of experiments and simulated stress-deflection curve of the four-point bending test results are shown in Figure 9-11. A good agreement can be found between experiment (red curves) and numerical simulation (black curve) results. For the plain specimen (see Figure 9-11a REF), as no toughening phase was used, brittle cracking behavior (witnessed by a sudden load drop as deflection increases) can be observed on the stress-deflection curves. The flexural strength of plain mortar reached around 5.8 MPa at 28 days which is somewhat higher than the flexural strength (5.0 MPa) reported in the previous chapter for the same mix. This difference can be attributed to the fact that in [5] a much thinner specimen was used which could be more sensitive to the influence of small defects such as air voids on flexural strength.

On the other hand, it can be seen from Figure 9-11b to Figure 9-11e that all toughened specimens show ductile stress-deflection response (witnessed by a significant drop followed by a second peak with hardening and softening branch on the stress-deflection curve). This ductile stress-deflection response clearly indicates that the brittle cracking failure of cementitious mortar was significantly changed by the reinforcing octet lattice structures to ductile failure. The failure process of all toughened specimens is shown in Figure 9-13, as the symmetric boundary condition was used for simulation, the symmetrical mirrored results using the symmetrical boundary plane are also shown in the figure. Because CDPM was used as material model for

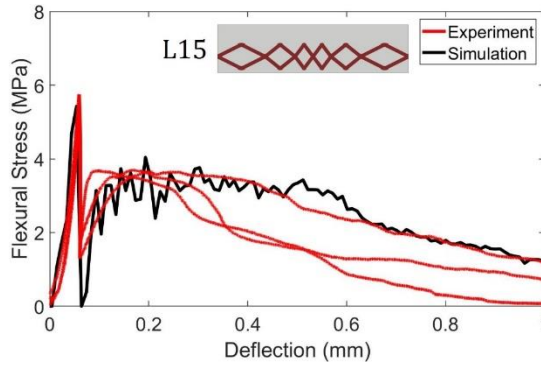
cementitious matrix, the model element damage is then indicated by plastic strain and the cracks are the regions with non-zero plastic strain. The entire failure process of the toughened cementitious mortar can be described by two stages. The first stage corresponds to the first peak on the stress-deflection curve which indicates the brittle cracking of cementitious matrix (deflection ranges from $d=0$ to $d=0.06$ mm). Similar to the plain mortar, when flexural load was applied, the highest tensile load generated at the bottom mid span of the toughened specimen. As soon as the tensile stress reached the tensile strength of the cementitious mortar (5.8MPa), a crack initiated at the bottom of the specimen and rapidly propagated to the top side. As shown in Figure 9-13, a main crack occurred at the mid span of each of the toughened specimen when the deflection reached 0.06 mm. It is shown in Figure 9-12 that both in experimental and simulation results the plain mortar specimens (REF) have the highest flexural cracking strength (6.33 MPa from experiment and 6.17MPa from simulation) while the toughened specimens have relatively lower flexural cracking strength. This is because the toughening phase has a lower elastic modulus than the cementitious matrix. Compared to the plain mortar, the neutral axis of the toughened composites is shifted closer to the top side of the specimen. As a result, under the same bending moment, a higher tensile stress will occur at the bottom side of the toughened composites. In addition, experimental specimens may contain defects such as entrapped air voids due to improper vibration, especially when complex lattice structures are used, the simulated flexural cracking strength is also relatively higher than experiment of some toughened specimens.



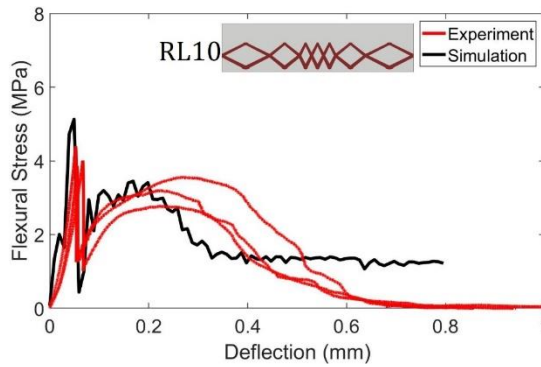
(a)



(b)



(c)



(d)

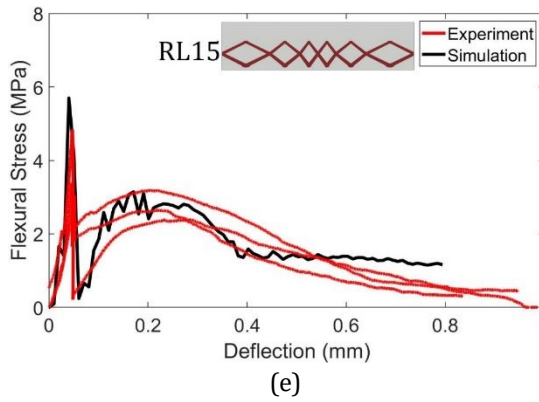


Figure 9-11 Flexural stress-deflection curves of four-point bending tests, a) reference, b) L10, c)L15 d)RL10, e)RL15

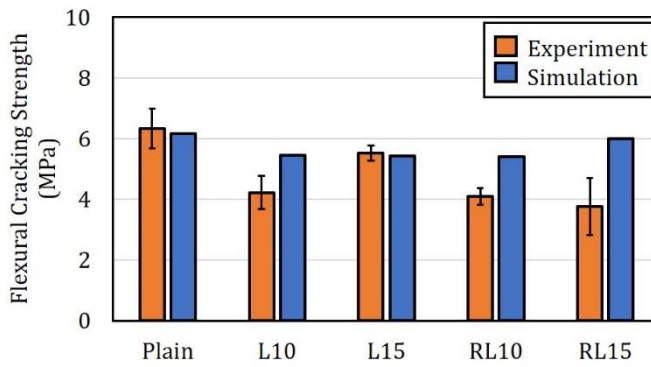
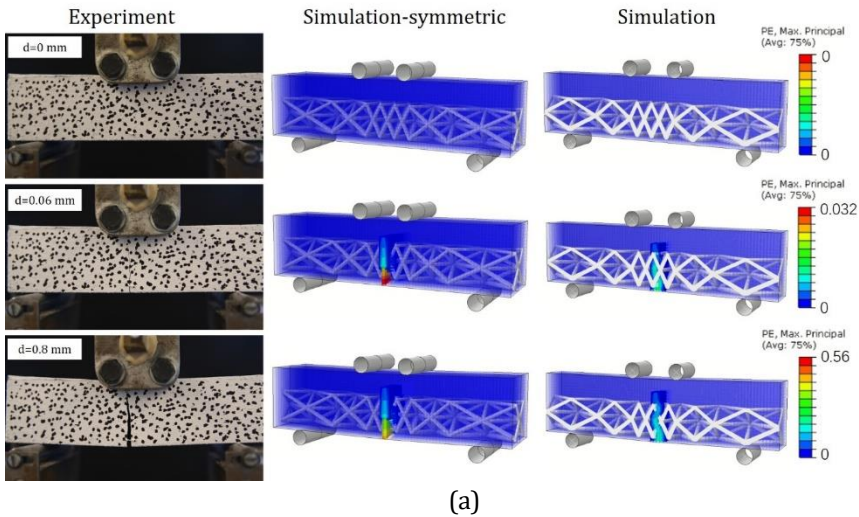
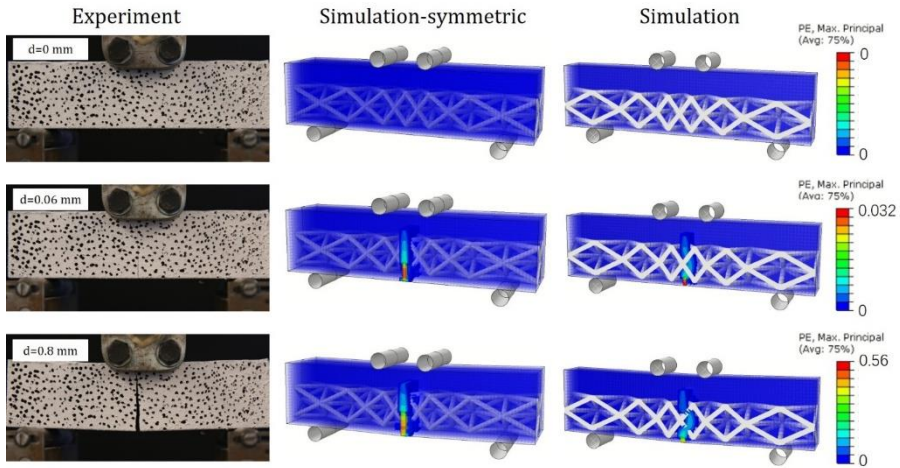


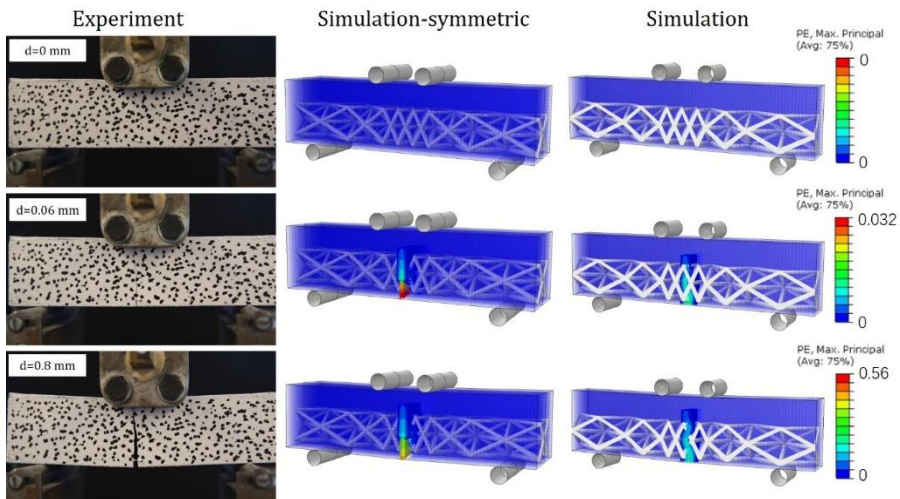
Figure 9-12 Flexural cracking strength of all tested specimens obtained from experiments and simulations



(a)



(b)



(c)

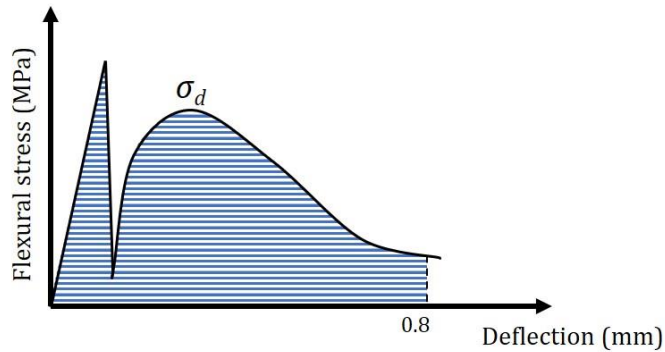


Figure 9-14 A typical stress-deflection curve of toughened cementitious composites, ductile failure stress (σ_d) and the total work of rupture (hatched area) is indicated

Because plain mortar (REF) showed brittle cracking failure without ductility, the ductile failure strength of REF specimens equals to zero according to previous definitions. Comparatively, as the toughened specimens exhibit ductile failure behavior, it can be seen from Figure 9-15 that they have distinctly higher ductile failure strength. In addition, because of the ductile failure behavior of the toughened specimens, the total work needed to rupture is also considerably increased comparing to the REF specimens. As shown in Figure 9-17, the total work of the toughened specimens increased by 1200 % (L10), 1143 % (L15), 743 % (RL10) and 785 % (RL15), compared to the REF.

Among all toughened specimens, only considering the apparent values, L10 and L15 show better mechanical performances for their higher ductile failure strength and higher total work of rupture than RL10 and RL15. However, in terms of the same amount of toughening phase material, the normalized values would give a fairer comparison between the toughened specimens. Under pure flexural loading condition, the tensile stress is linearly distributed along the height of the specimen on the midspan cross section. Struts with larger radius are able to bear higher stress and may provide better resistance to crack growth. Therefore, arranging the lattice struts radii according to the tensile stress distribution might be an efficient method to reduce the usage of toughening material meanwhile obtain good fracture resistance for the composites. The functionally graded lattice struts of RL10 and RL15 were designed based on this consideration.

It is clearly shown in Figure 9-15 to Figure 9-17 that, both from experimental and simulated results, RL10 and RL15 have considerably higher ductile failure strength, specific ductile failure strength and total work comparing to L10 and L15 when the values are normalized to the same amount of toughening phase. Compared to L10, RL10 showed an increase 50.59 % (52.40 % from simulation) of the ductile failure strength, 51.03% (35.60% from simulation) of the specific ductile failure strength and 13.34 % (34.56 % from simulation) of the total work meanwhile decreased 48.48 % of toughening phase material use. Comparing to L15, RL15 increased 57.18 % (62.02 % from simulation) of the ductile failure strength, 57.46% (46.73% from simulation) of the specific ductile failure strength and 50.03 % (42.30 % from simulation) of the total

work meanwhile decreased 47.48% of toughening phase material use. The ductile failure strength of the composites is mainly determined by the position and the total cross-sectional area of the lattice struts on the crack surface. On one hand, because L10, RL10, L15 and RL15 have the same octet structure the position of the struts on the crack surface are the same. On the other hand, although considering the entire lattice structure, L15 and RL15 have higher volumetric ratio, on the cross section of the crack surface the total cross-sectional area of the lattice struts of L10 and RL10 is higher than L15 and RL15. So, L10 and RL10 have even higher ductile failure strength than L15 and RL15. A summary of ductile failure strength and the total work of all tested specimens is given in Table 9-8.

According to previous analyses and discussions, from the qualitative point of view, the toughened composites have shown ductile failure behavior. Quantitatively, the results of ductile failure parameter values also indicate a distinct increase in ductility of toughened cementitious composites. More importantly, the ductile failure parameters also show that the functional grading is very efficient in enhancing the flexural ductility of the cementitious materials while reducing the toughening phase material use. In order to profoundly understand the failure mechanism as well as provide guidance in tailoring mechanical properties of the lattice structure toughened cementitious composites, an in-depth analysis on the fracture behavior is provided in the next section.

Table 9-8 Ductility parameters of the tested specimens

No.	Ductile failure strength /Simulation [MPa]	Normalized ductile failure strength /Simulation [MPa]	Specific ductile failure strength /Simulation [MPa/cm ³]	Total work /Simulation [J]	Normalized total work /Simulation [J/cm ³]
Plain	-	-	-	0.07(0.02)/0.07	0.07(0.02)/0.07
L10	3.69(0.31)/4.70	3.69(0.31)/4.70	0.14(0.01)/0.18	0.91(0.22)/1.00	35.19(8.51)/38.68
L15	3.67(0.02)/4.47	3.31(0.02)/4.03	0.13(0.00)/0.16	0.87(0.17)/1.08	30.34(5.93)/37.67
RL10	3.18(0.39)/4.02	5.56(0.68)/6.37	0.21(0.03)/0.25	0.59(0.09)/0.77	39.87(6.08)/52.04
RL15	2.74(0.41)/3.11	5.20(0.78)/5.92	0.20(0.03)/0.23	0.62(0.11)/0.73	45.52(8.07)/53.60

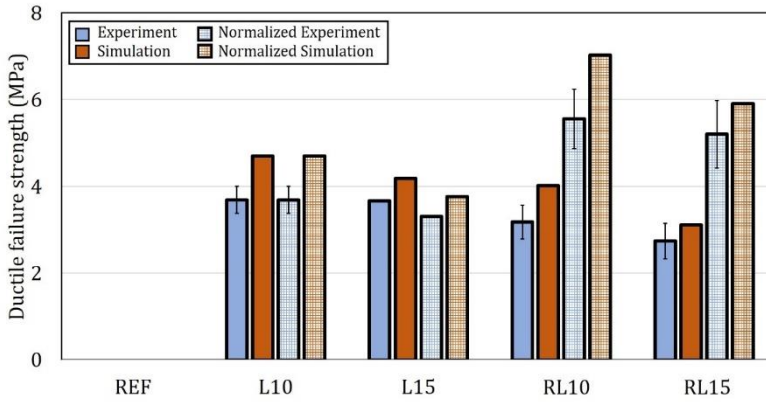


Figure 9-15 Ductile failure strength and its normalized value, standard deviation is indicated for experiment results

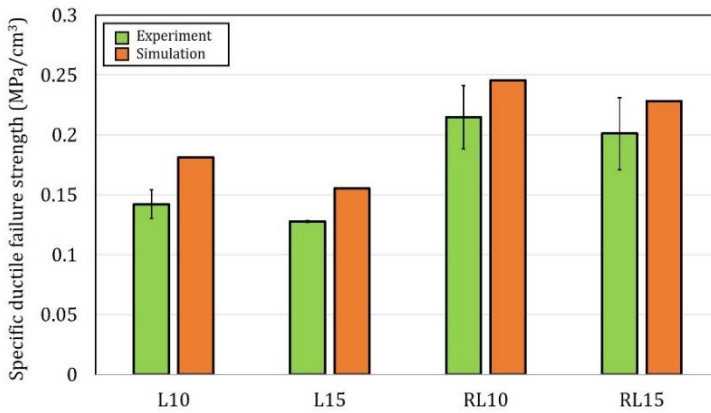


Figure 9-16 Specific ductile failure strength increased by per volume of toughening phase

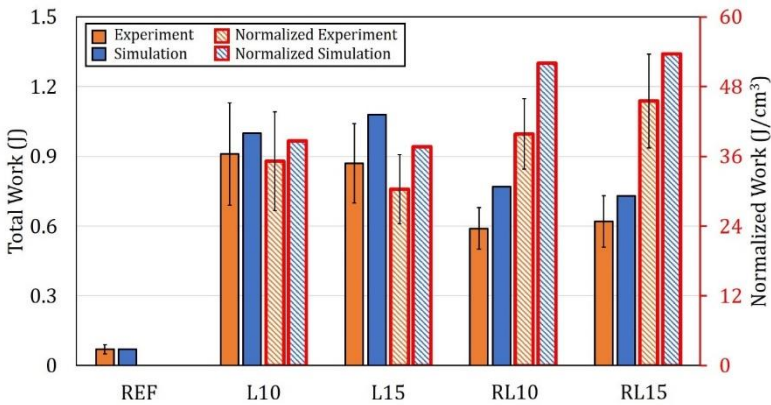


Figure 9-17 Total work (left y axis) and normalized total work (right y axis) of all tested specimens, standard deviation is indicated for experiment results

9.4.2 Fracture behavior

Taking RL15 as an example, the fracture behavior of the cementitious composites toughened by functionally graded structure is discussed in detail in this section. It was possible to study the fracture behavior after the first main crack appeared in the cementitious matrix as long as crack opening can be measured. By digital image correlation (DIC), crack mouth opening displacement (CMOD) was obtained during the tests and the fracture behavior of the toughened specimens is analyzed based on these data.

The experimentally obtained and simulated flexural load-CMOD curves of RL15 are shown in Figure 9-18. Both from experiments and simulations, obvious hardening can be observed as the crack opening increases. Under four-point bending, a pure bending zone forms in the middle of the specimen. As a result, Mode I fracture condition was obtained and the fracture process of the toughened specimen is similar to that of fiber reinforced cementitious material with pseudo strain hardening behavior; namely, the crack is bridged by the toughening phase between the generated crack surfaces. Because the struts constituting the lattice structure were connected within the cementitious matrix, pulling out of a single strut was not possible until it was stretched and completely broken. In addition, because the strength of the toughening phase (ABS) is significantly higher than the matrix tensile strength, the crack bridging stress could only be provided by the elastic stretching of the lattice struts exposed across the generated crack surface until the strut broken. Unlike the fiber reinforced cementitious materials, sliding between the toughening phase and the matrix interface is less likely to happen as the octet ABS structure was anchored in the cementitious matrix. Therefore, crack bridging force provided by detaching and sliding was not considered in this study. The maximum crack bridging strength is then determined by the strength of the toughening phase material. As can be seen from the simulated black curve in Figure 9-18, as CMOD increases the hardening branch reaches the flexural crack bridging strength at point "A". Correspondingly, the tensile stress in the lattice strut increased up to its tensile strength (25MPa, see Figure 9-19). The point "A" indicates the onset of the toughening phase failure and the maximum fiber bridging ability for a crack-open-hardening behavior. After point "A", the toughening phase started to fail, and, as a result, a softening branch can be observed from the load-CMOD curves. It can be seen from Figure 9-19 that, from point "B" to point "C", the lattice structure gradually cracked. Under ideal conditions, the tensile stress should be linearly distributed on the lattice strut from top to the bottom. However, due the heterogeneity of the cementitious matrix and the lattice structure, in reality after cracking a shear stress also exists inside the lattice struts so that the principle tensile stress distribution is not completely linear along the height direction.

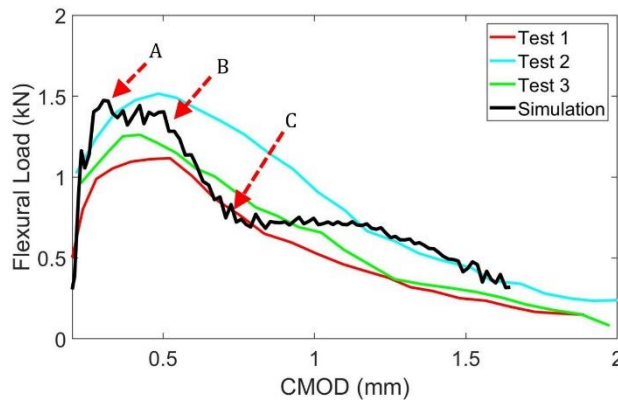


Figure 9-18 Flexural load-CMOD curves of RL15, CMOD is measured by DIC

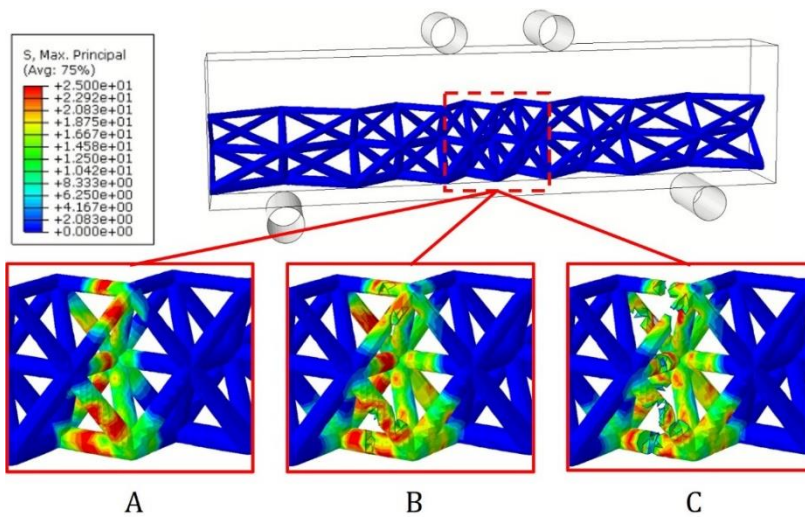


Figure 9-19 Simulated failure process of the toughening lattice structure corresponding to stress-CMOD curves

Stress distribution inside the lattice struts exposed by the crack surface can also be analytically calculated adopting the transformed area method (see Figure 9-20). As mentioned previously, it is assumed that elastic stretching of the exposed lattice struts provides the crack bridging force. Then, bending of the cracked cross section can be described by a transformed cross section combining the cross section of uncracked cementitious matrix A_m and the equivalent cross section A_i of the crack bridging lattice struts. A_i can be calculated by eq. (9-1).

$$A_i = \frac{E_r}{E_m} S_i \quad (9-1)$$

where S_i is the cross-sectional area of the lattice struts at a same height on the cross section; A_i is the equivalent cross-sectional area of the crack bridging lattice struts at a

same height; E_m and E_r are the elastic modulus of cementitious matrix and toughening phase, respectively.

The neutral axis coordinates y_t of the transformed cross section can be obtained by eq. (9-2) and the moment of inertia of the equivalent cross section I_t can be obtained by eq. (9-3).

$$y_t = \frac{A_m \frac{1}{2} h_m + \sum_1^i d_i A_i}{A_m + \sum_1^i A_i} \quad (9-2)$$

$$I_t = \frac{A_m h_m^2}{12} + A_m \left(\frac{h_m}{2} \right)^2 + \sum_1^i \left(\frac{A_i h_i^2}{12} + A_i (d_i - h_m)^2 \right) \quad (9-3)$$

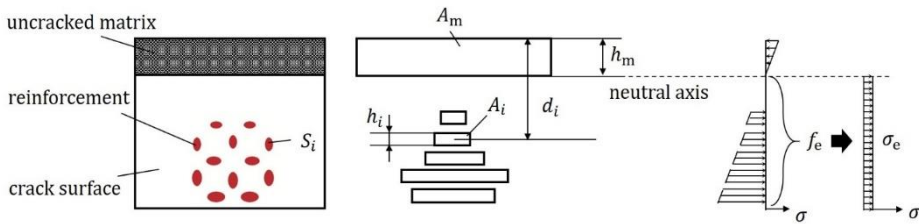


Figure 9-20 Schematics of transformed cross section and the stress distribution

where y_m and y_i are the centroid coordinates of the uncracked matrix cross section and equivalent cross sections; A_m is the area of the uncracked matrix cross section; h_m is the height of the uncracked matrix section; h_i is the height of the equivalent cross sections, respectively. Using the neutral axis as the reference, then $y_t = 0$ and h_m can be obtained.

After h_m is obtained, the moment of inertia I_t of the transformed cross section can be calculated by eq. (9-3) and the equivalent strain of this transformed cross section ε can be calculated by eq. (9-4).

$$\varepsilon = \frac{My}{I_t E_m} \quad (9-4)$$

Then the stress within the lattice struts at the cracked cross section can be obtained using the data from flexural load-CMOD curve (Figure 9-18). As the stress distribution varies along the height direction, the crack bridging stress σ of this cracked cross section needs to be calculated using the total force transferred within the lattice struts.

$$\sigma = \frac{\sum_1^i \sigma_i A_i}{A - A_m} \quad (9-5)$$

Here, A is the specimen cross section.

It is mentioned in the previous section that a hardening branch can be observed on the load-CMOD curves. Within all tested specimens the ductile failure strength is at least 2.74MPa, this is already higher than the “fiber slipping strength” (around 2.5MPa) defined in Chapter 5, namely the crack bridging ability of the composites developed in this chapter is already potentially sufficient for creating auxetic cementitious

composites. However, in terms of the strain hardening behavior observed in Chapter 8, the peak load of this hardening branch is still lower than the cracking load of the cementitious matrix and the multiple cracking behavior typical of strain hardening cementitious composites (SHCC) was not observed in any of the tested specimens. This indicates that, in the tested specimens, steady state cracking was not achieved and the generated cracks still followed Griffith-type cracking behavior. Similar to SHCC, the energy release of cracking on the lattice toughened cementitious composites can be determined by the J integral approach, as described in [6]. In order to obtain steady state cracking, the crack bridging complementary energy J (eq.9-6) needs to exceed the crack tip energy release rate J_{tip} . Under uniaxial tension condition:

$$J = \sigma_0 \delta_0 - \int_0^{\delta_0} \sigma \delta d\delta \quad (9-6)$$

As the crack tip is very small compared to the specimen size in length and height, then under plain stress conditions it holds:

$$J_{tip} = \frac{K_I^2}{E_m} \quad (9-7)$$

Where, σ_0 is the crack bridging strength and δ_0 is the corresponding crack opening displacement. The crack bridging complementary energy is indicated by the hatched area (see Figure 9-21). K_I and E_m are the fracture toughness and elastic modulus, respectively; K_I of plain cementitious mortar is normally $0.2 \sim 0.3 \text{ MPa}\sqrt{\text{m}}$.

However, under flexural loading conditions, the flat crack surface cannot be achieved. Because the tensile stress on a cross section is distributed linearly along the height, for a given bending moment the crack opening varies along the height direction of the specimen. Then, an equivalent crack opening should be found. Because the stress is linearly distributed along the height of the crack cross section, it is reasonable to assume that the crack opening is also linearly distributed (see Figure 9-22). In this sense, the equivalent crack opening of a cracked surface is half of the crack opening measured at the crack mouth then eq. (9-8) is written as:

$$J_b = \frac{1}{2} \sigma_0 \delta_0 - \frac{1}{2} \int_0^{\delta_0} \sigma \delta d\delta \quad (9-8)$$

Here, δ is the measured CMOD at the bottom of the cracked specimen; σ is the crack bridging stress which can be obtained by eq. (9-5). using the experimental and numerical simulated flexural load-CMOD data. The calculated complementary energy J_b results are shown in Figure 9-23.

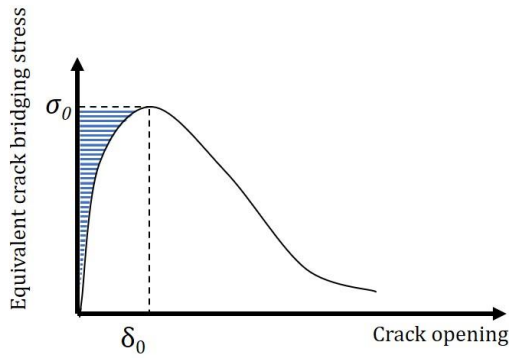


Figure 9-21 Schematics of crack bridging stress-crack opening curve, the shaded area indicates the crack bridging complementary energy [6, 7]

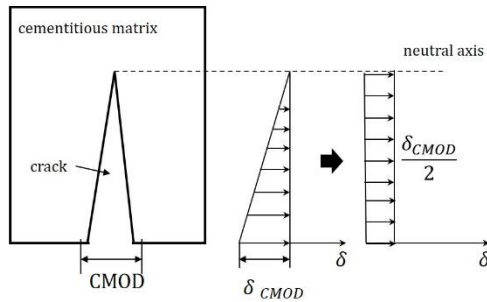


Figure 9-22 Equivalent crack opening under flexural load

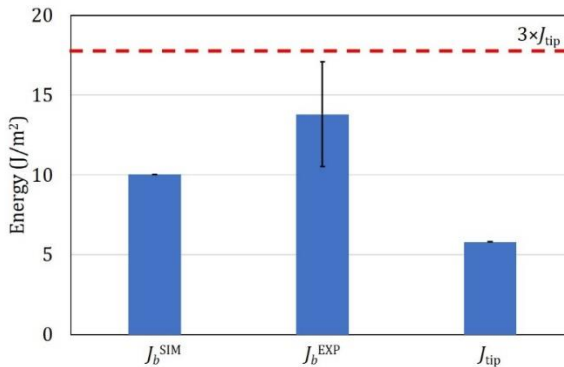


Figure 9-23 Comparison of crack bridging complementary energy of RL15 and the required energy at the crack tip (standard deviation is indicated for experimental results); dashed line indicates the minimum required complementary energy for strain hardening

Due to the heterogeneity of the cementitious composites, in order to achieve the so-called multiple cracking behavior, a quite large margin is required for the complementary energy J_b . It has been proved by [8] that for some fiber reinforced composites, J_b needs to be at least three times higher than J_{tip} to obtain a saturated multiple cracking behavior. Similarly, in this study such energy requirement is also adopted. As can be seen from Figure 9-23, the complementary energy of RL15 obtained from experiment J_b^{EXP} (13.80 J/m²) and simulation J_b^{SIM} (10.02 J/m²) are lower than the required energy $3 \times J_{tip}$ (17.4 J/m², marked by red dash line in Figure 9-23). As a result, although after the first cracking a hardening branch can be found on the stress-strain curve, the typical multiple cracking behavior of SHCCs could not be obtained by RL15 both from experiments and simulation observations.

Different methods can be used to increase the complementary energy, such as increasing the toughening phase strength and toughening phase ratio. In order to verify the multiple cracking criteria defined by the complementary energy J_b , additional numerical simulations were performed. In these simulations, the strength of the toughening phase f_r was assumed to be 30 MPa, 35 MPa and 40 MPa respectively, while maintaining the elastic modulus as 1590 MPa. Then the calculated complementary J_b will be 14.43 J/m², 19.63 J/m² and 25.65 J/m², respectively. In this sense, only when f_r is not less than 35 MPa, the J_b satisfies the requirement $3 \times J_{tip}$ (17.4 J/m²). As shown in Figure 9-24, when the toughening phase material strength f_r is 25 MPa (i.e., the ABS material used in this study) and 30 MPa, the lattice structure breaks at the deflection $d=1$ mm and eventually only one crack was obtained. Comparatively, when toughening phase material strength f_r is increased up to 35 MPa and 40 MPa, the complementary energy J_b is higher than $3 \times J_{tip}$, then the lattice structure does not completely break at $d=1$ mm and multiple cracks do occur (indicated by red arrows in Figure 9-24). In addition, because the energy requirement is satisfied in these two cases, the crack development is closer to the so-called steady state cracking with finer crack openings.

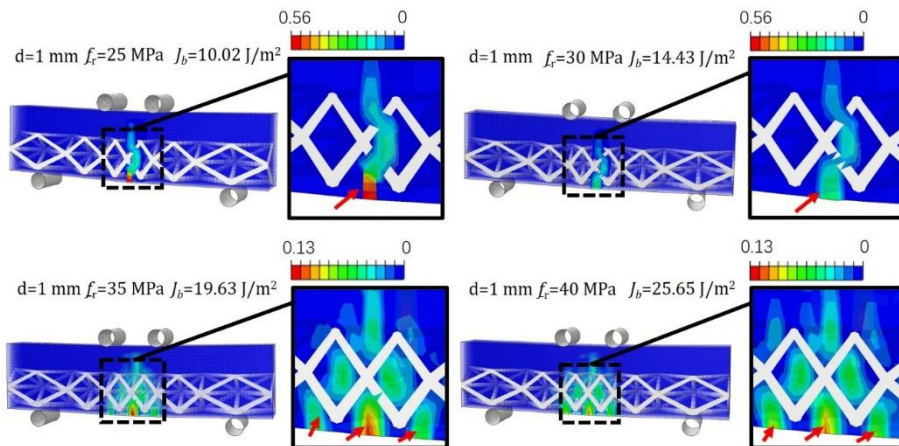


Figure 9-24 Cracking of specimens toughened by materials with different strength, cracks are indicated by red arrow

In this chapter, the modification of lattice structures has two aspects. One aspect is on the structural scale: modifying the structural parameters of the lattice. The effective stiffness and strength of the lattice structure can be enhanced by modifying the structural parameters such as the lattice density or the radius of the lattice struts. But here these structural parameters influence the cracking behavior of the cementitious composites in a different way. As shown in this section, after the first main crack appeared, the cracking behavior was influenced by the lattice struts that are bridging the crack. Other parts of the lattice structure have a limited influence because they are anchored in the cementitious matrix and the E-modulus of the ABS material is much lower than the cementitious matrix. By using the “transformed area method”, the influence of the designable parameters (lattice density and lattice struts radius) was quantitatively evaluated according to the proposed method in this section using eq. (9-2) to eq. (9-8). In this sense, the lattice structures can be designed and adjusted accordingly in order to obtain better cracking bridging. From the obtained results, arranging larger struts closer to the tension side gives the composites higher ductility but lower ultimate cracking strength.

Besides adjusting the structural parameters, another aspect is on the material scale: modifying the properties of the polymeric toughening phase material. For a given structural design, according to the analytical results in this section, the E-modulus of the polymeric material (and not the stiffness of the lattice structure) plays a critical role as it determines the total transformed cross-sectional area of the crack bridging lattice struts. Higher material E-modulus gives larger equivalent cross-sectional area and thus the lattice struts are able to bridge higher tensile stress. As a result, the ductility of the composites will be better. Compared to the E-modulus of steel (around 200 GPa) or fibers [9, 10] (around 40 GPa) which are usually used as reinforcement for cementitious materials, the E-modulus of the printed ABS (around 1.5 GPa) is significantly lower. It is difficult to obtain such high E-moduli for such printed polymeric material. Alternatively, according to the simulation results shown in Figure 9-24, increasing the strength of the printed ABS material by 40% would potentially give the cementitious composites multiple cracking behavior and potential increase in ductility. In this sense, comparing to the E-modulus, the strength of the printed ABS may be easier to improve to satisfy the numerical prediction. According to many previous researches, there are several approaches to enhance the strength of 3D printed polymeric materials. For example, modifying the printing parameters [4, 11, 12] and post processing [13, 14] can result in obviously improved strength of the printed material.

9.5 CONCLUSIONS

In this chapter, functionally graded polymeric lattice with three-dimensional octet structures is used as toughening phase to create cementitious composites with enhanced fracture resistance: four types of octet lattice structures are designed according to the bending moment and the tensile stress distribution of flexural loaded cementitious specimens. The designed lattice structures are 3D printed using

polymeric material ABS. Combining experimental, numerical and analytical approaches, the flexural properties and fracture behavior of the toughened cementitious composites are investigated. Based on the obtained results, several conclusions are drawn as follows:

- The fracture resistance of the cementitious composites was significantly increased compared to the plain cementitious material in terms of ductile failure strength and total work of rupture which indicates that the developed cementitious composites are competent for creating auxetic cementitious materials.
- The functional grading method proved to be very efficient in modifying flexural performance of the toughened cementitious composites. The functionally-graded toughening lattice structures use significantly less material while having even higher normalized ductility. In our study, an optimal case (RL15) is reducing 47.48% of toughening phase material meanwhile increasing 57.18 % of normalized ductile failure strength, 57.46 % of specific ductile failure strength and 50.03% of normalized total work of rupture.
- According to the analytical results, the crack bridging complementary energy J_b of the toughened cementitious composites used in this study is lower than the required energy J_{tip} for multiple cracking. As a result, although a hardening branch can be found in the stress-deflection curve of the cementitious composites, multiple cracking and strain hardening behavior are not achieved.
- According to the analytical model and numerical simulation results, the calculated complementary energy for the lattice structure toughened cementitious composites to achieve multiple cracking and strain hardening behavior doesn't satisfy the $3 \times J_{tip}$ requirement to create SHCCs. Informed from the simulation results, by increasing the strength of the toughening phase material from 25MPa to above 35MPa the energy requirement could be potentially satisfied.

REFERENCES

- [1] H.C. Tankasala, V.S. Deshpande, N.A. Fleck, Crack-Tip Fields and Toughness of Two-Dimensional Elastoplastic Lattices, *Journal of Applied Mechanics* 82(9) (2015).
- [2] N.A. Fleck, V.S. Deshpande, M.F. Ashby, Micro-architected materials: past, present and future, *Proceedings of the Royal Society A: Mathematical, Physical and Engineering Sciences* 466(2121) (2010) 2495-2516.
- [3] T. Li, Y. Chen, L. Wang, Enhanced fracture toughness in architected interpenetrating phase composites by 3D printing, *Composites Science and Technology* 167 (2018) 251-259.
- [4] Y. Xu, H. Zhang, B. Šavija, S. Chaves Figueiredo, E. Schlangen, Deformation and fracture of 3D printed disordered lattice materials: Experiments and modeling, *Materials & Design* 162 (2019) 143-153.
- [5] Y. Xu, B. Šavija, Development of strain hardening cementitious composite (SHCC) reinforced with 3D printed polymeric reinforcement: Mechanical properties, *Composites Part B: Engineering* 174 (2019) 107011.
- [6] V.C. Li, From micromechanics to structural engineering-the design of cementitious composites for civil engineering applications, (1993).
- [7] V.C. Li, On engineered cementitious composites (ECC), (2003).
- [8] T. Kanda, V. Li, Multiple Cracking Sequence and Saturation in Fiber Reinforced Cementitious Composites, (1998).
- [9] S. Cheng, J. Ji, M. Meng, Interfacial response of fibre-to-matrix in textile reinforced concrete between two cracks: Analytical solution, *Composite Structures* 245 (2020) 112380.
- [10] L. Nahum, A. Peled, E. Gal, The flexural performance of structural concrete beams reinforced with carbon textile fabrics, *Composite Structures* 239 (2020) 111917.
- [11] A.D. Valino, J.R.C. Dizon, A.H. Espera, Q. Chen, J. Messman, R.C. Advincula, Advances in 3D printing of thermoplastic polymer composites and nanocomposites, *Progress in Polymer Science* 98 (2019) 101162.
- [12] Y. Ming, S. Zhang, W. Han, B. Wang, Y. Duan, H. Xiao, Investigation on process parameters of 3D printed continuous carbon fiber-reinforced thermosetting epoxy composites, *Additive Manufacturing* 33 (2020) 101184.
- [13] S. Bhandari, R.A. Lopez-Anido, D.J. Gardner, Enhancing the interlayer tensile strength of 3D printed short carbon fiber reinforced PETG and PLA composites via annealing, *Additive Manufacturing* 30 (2019) 100922.
- [14] E.R. Fitzharris, I. Watt, D.W. Rosen, M.L. Shofner, Interlayer bonding improvement of material extrusion parts with polyphenylene sulfide using the Taguchi method, *Additive Manufacturing* 24 (2018) 287-297.

10

AUXETIC BEHAVIOR OF CEMENTITIOUS COMPOSITES WITH THREE-DIMENSIONAL CELLULAR STRUCTURE

In previous chapters, it was found that auxetic cementitious cellular composites (ACCCs) with two-dimensional planar patterns possess unique mechanical behavior under uniaxial compression: negative Poisson's ratio (NPR) which ensures the ACCCs excellent deformability. In this chapter, the approach developed in previous chapters was extended by creating auxetic cementitious composites with a 3D spatial cellular structure. Experimental results show that the 3D-ACCCs possess enhanced mechanical properties compared to the 2D-ACCCs.

10.1 INTRODUCTION

Previously, it has been found that in order to trigger the auxetic behavior in cementitious cellular composites, two prerequisites are necessary: a cracking initiation mechanism which was achieved by architecting the cellular structure and crack bridging ability achieved by reinforcing the constituent material with fibers. The auxetic behavior was obtained by the ACCCs with a two-dimensional cellular structure, which was introduced in Chapter 5 to Chapter 7. This approach is assumed to be also applicable by cementitious composites with three-dimensional cellular structures. Therefore, in this chapter, a 3D cellular structure was first designed by extrapolating the 2D elliptical pattern to 3D space for providing the crack initiation mechanism. Meanwhile, as Chapter 8 and Chapter 9 indicated that ABS reinforced cementitious composites have improved crack resistance, 3D printed ABS structures were also used here to create constituent material with crack bridging ability. Combining the 3D cellular structure and the ABS reinforced cementitious material, 3D-ACCCs were created. Under uniaxial compression, mechanical properties of the 3D-ACCCs were investigated and compared to the 2D-ACCCs and conventional foam concrete in terms of strength, deformability and energy absorption capacity.

10.2 METHODS AND MATERIALS

10.2.1 Design of the cellular structure

As clarified in previous chapters, in order to achieve the auxetic behavior, the cellular structure needs to be able to introduce distributed stress concentration such that cracking occurs at desired locations. For the ACCCs developed in Chapter 8, 2D patterns were used and the third dimension was the thickness of the specimen. The designing procedures of the 2D cellular structure is shown in Figure 10-1 by the following steps:

- A 3D domain which represents continuum material occupying a certain volume of space was created first (see Figure 10-1a).
- Elliptical cylinders were generated in the domain (see Figure 10-1b) such that they are orthogonally arranged along one direction of the domain and the elliptic cross-section parallel to one surface of the domain.
- The domain is geometrically subtracted by the elliptic cylinders transforming the continuum domain to a cellular structure (see Figure 10-1c).

Similarly, the 3D cellular structure was designed based on the approach developed for the 2D structure. By extrapolating the orthogonally arranged elliptic cylinders from one direction to three perpendicular directions (Figure 10-2b) of the Cartesian coordinates, the domain had elliptical pattern parallel to all three pairs of opposite surfaces. Afterwards, the domain was geometrically subtracted by all elliptical cylinders remaining cellular structures with 2D pattern facing three perpendicular directions (Figure 10-2c). Then, these cellular structures were placed concentrically (Figure 10-2d)

and the intersection of them is the generated cellular structure with a 3D pattern (Figure 10-2e).

For simplicity, one single unit of the 3D cellular structure (see Figure 10-3) was used for studying the mechanical behavior. As the 3D cellular structure is designed, compressive load can be applied from three perpendicular directions in space and the 3D-ACCCs may exhibit anisotropic behavior. Therefore, for simplification, the compressive load is only applied in the z direction (shown in Figure 10-3). As a result, from two other perpendicular directions (xoz and yoz shown in Figure 10-3) the deformation pattern of the 3D-ACCCs under compressive load is visible from experiment. Within this chapter, the Poisson's ratio was measured on the xoz direction. Besides the potential intrinsic anisotropy of the cellular structure, printing directions of the ABS material may also introduce anisotropic mechanical properties. For simplification, the anisotropic behavior of the 3D-ACCCs was not regarded as the main focus of this chapter and was not investigated. The effect of anisotropy should be further studied in the future.

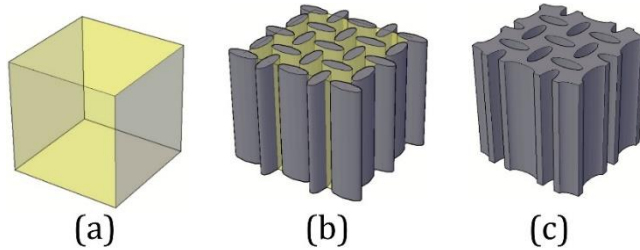


Figure 10-1 Schematics of designing process of ACCCs with 2D pattern

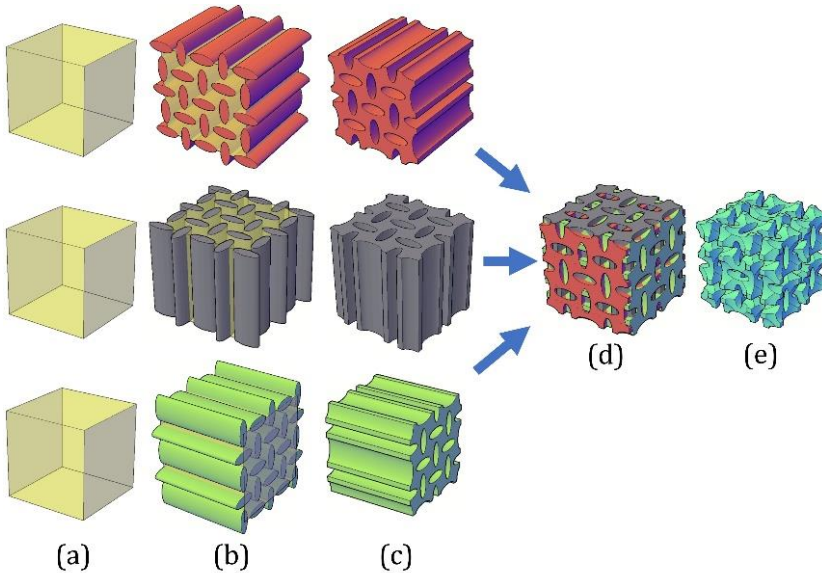


Figure 10-2 Schematics of designing process of cellular structure for 3D-ACCCs

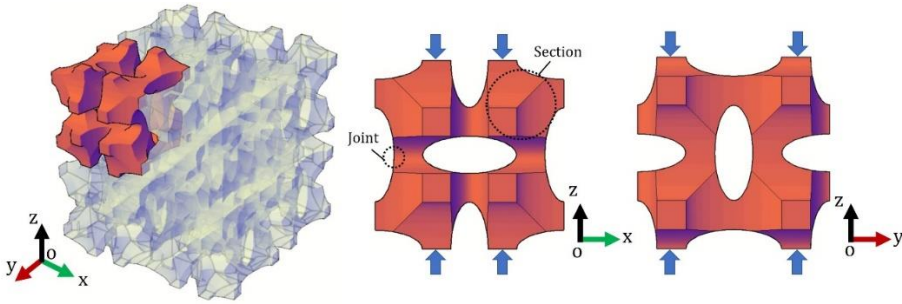


Figure 10-3 A single unit (red part) of the generated 3D cellular structure

As clarified in previous chapters, in order to achieve auxetic behavior, a stress concentration mechanism to trigger auxetic behavior and high fracture resistance of the constituent material are required. The stress concentration was already introduced by the 3D cellular structure, a detailed analysis is given later. As demonstrated in Chapter 8 and Chapter 9, 3D printed acrylonitrile butadiene styrene (ABS) can be used to increase the fracture resistance of cementitious material. Therefore, for the constituent materials, two self-reinforced strategies were used.

- ABS was used to print a shell of the 3D cellular structure which was designed in Figure 10-2e. The shell (0.7 mm thickness) was used as a mold to cast the cementitious mixture, on one hand; on the other hand, the shell itself was also used to reinforce the cementitious material and increase fracture resistance.
- Apart from the shell mold, internal reinforcement structure with varying cross-sectional reinforcing ratio was also designed and combined with the ABS shell mold (Figure 10-4). All joints were designed to be reinforced by ABS rods. One reinforcement was generated at each joint by placing a cylindrical rod at the center of the joint. The cross-sectional ratio of the rod to the joint is defined as the reinforcing ratio. Specimens with three different reinforcing ratios were prepared 10%, 20% and 30%, respectively (shown in Figure 10-4).
- The Ultimaker 2+ used in previous chapters was also used in this chapter to print the designs. Note that the reinforcement structures were printed inside the ABS shell (Figure 10-5). Printing parameters are listed in Table 10-1, and a printed shell mold is shown Figure 10-6.

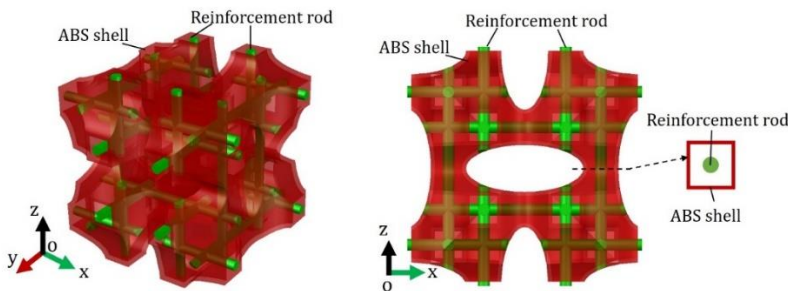


Figure 10-4 Schematics of ABS shell mold with reinforcement structures

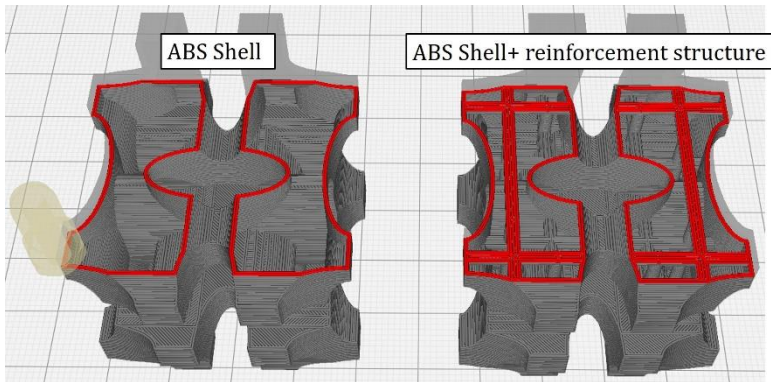


Figure 10-5 Printing process of the ABS molds

Table 10-1 Printing parameters

Parameters	Configuration
Nozzle diameter (mm)	0.6
Temperature (°C)	260
Layer height (mm)	0.15
Line width (mm)	0.35
Infill density (%)	100
Infill pattern	Lines
Printing speed (mm/s)	45

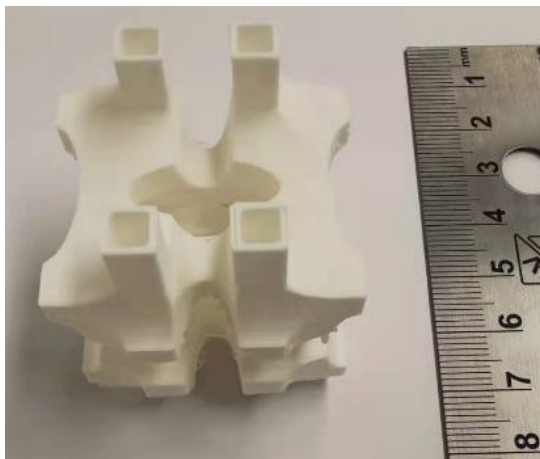


Figure 10-6 Printed ABS mold

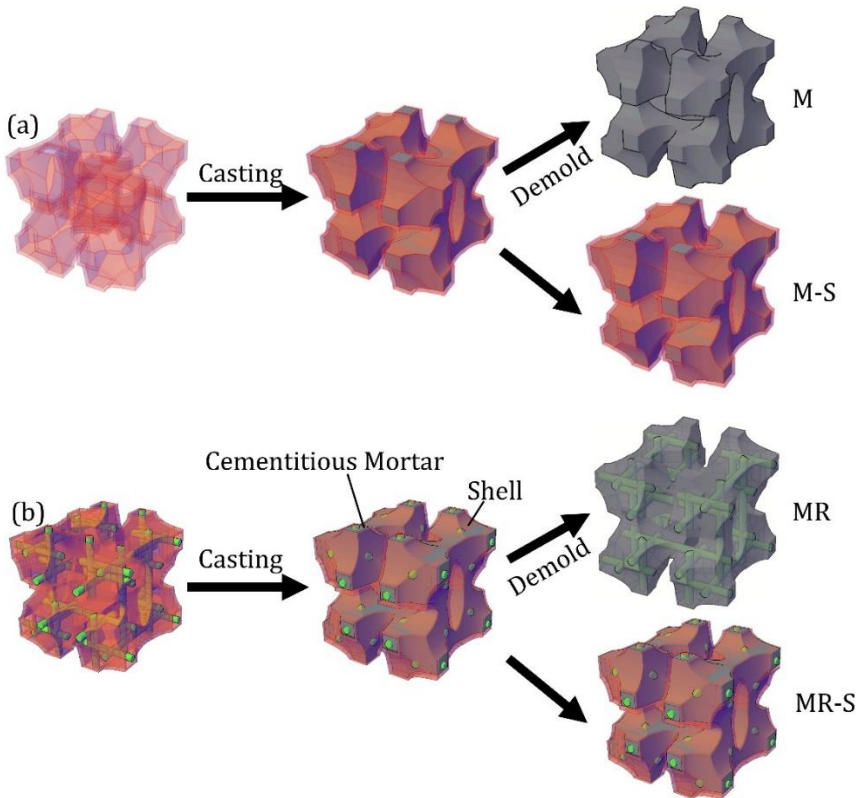


Figure 10-7 Schematics of a) ABS shell mold, b) shell mold with reinforcement and c) casted specimen

10.2.2 Mixing, casting and curing

As a three-dimensional structure with a complex geometry was used for the shell molds, high flowability was required for the cementitious mixture to ensure good casting quality of the specimens. Therefore, compared to the mixture used in Chapter 8 and Chapter 9 ($w/b=0.33$), the w/b ratio of the mixture used in this chapter was higher. The cementitious mixture proportion is listed in Table 8-1: a fine-grained mortar with water-to-binder ratio (w/b) of 0.40 was used to cast the 3D-ACCCs specimens.

Table 10-2 Mixture design of the matrix material (g/l)

CEM I 42.5 N	Fly ash	Sand (0.125~0.250 mm)	Superplasticizer (Glenium 51)	Water	w/b
458	542	458	2	396	0.40

The mixing procedures are the same as in Chapter 8. After mixing, the cementitious mixture was loaded into a syringe and the fresh mixture was intruded in

the printed 3D cellular structure followed by vibrating for 60s. In total, four series of specimens were prepared, as shown in Figure 10-7: Plain mortar (M), mortar with ABS shell (M-S), mortar with reinforcing structure (MR), and mortar with both reinforcing structure and ABS shell (MR-S). In order to study the influence of reinforcing structure on the MR specimens, three reinforcing ratios (10%, 20% and 30%) were used for the MR specimens and denoted as MR-P1, MR-P2 and MR-P3, respectively.

All specimens were wrapped in plastic film and kept under room temperature for 1 day, afterwards the specimens were cured in tap water until 7 days of age. One hour before testing, the M and MR specimens were obtained by removing the shell of the M-S and MR-S specimens. This was done by submerging the M-S and MR-S specimens in acetone for an hour to soften the ABS shell. Then, the shell was carefully removed by hand. As a result, plain mortar (M) specimens and mortar with reinforcement structure (MR) were obtained. A summary of all prepared specimens for testing is listed in Table 10-3. Three duplicates were prepared to be tested for all designs.

Table 10-3 Testing specimens

No.	Specimen Type
M	Plain Mortar
M-S	Mortar + Shell
MR-P1	Mortar + 10% Reinforcing ratio
MR-P2	Mortar + 20% Reinforcing ratio
MR-P3	Mortar + 30% Reinforcing ratio
MR-S	Mortar + 10% Reinforcing ratio + Shell

10.2.3 Mechanical tests

The experimental set-up is shown in Figure 10-8, two fixed steel loading plates were used to apply the external compressive load. Two plastic films were placed between the specimen and steel loading plates to reduce friction between the specimen and the steel plates. A uniaxial downwards displacement was applied by the upper steel plate at a quasi-static rate of 0.01mm/s. Load was recorded by the load cell, and displacement was recorded by the machine stroke during the tests. During the tests, a camera was placed in front of the specimens to take pictures. Afterwards, the Poisson's ratio was determined using these pictures.

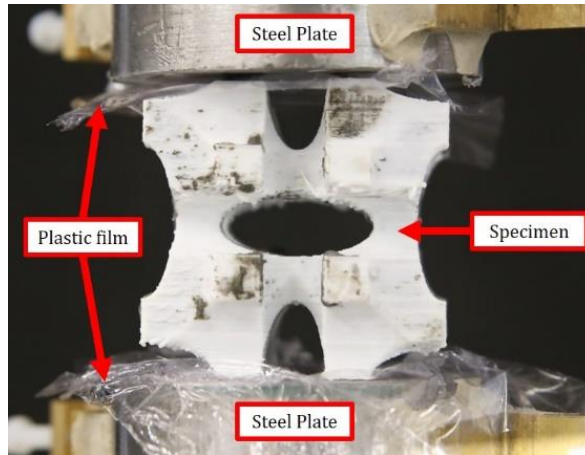


Figure 10-8 Experiment set-up for uniaxial compression

10.3 COMPRESSIVE BEHAVIOR OF THE 3D-ACCCs

10.3.1 Stress-strain response

The compressive deformation process of all tested specimens is shown in Figure 10-9 and the corresponding stress-strain curves are shown Figure 10-10. It can be found that, except the reference specimens (M), all other cementitious cellular composites show auxetic behavior: therefore, they are classified as 3D auxetic cementitious cellular composites (3D-ACCCs) which corresponds to the concept introduced in Chapter 5. Similar to the ACCCs with a 2D structure, the 3D-ACCCs also exhibit the typical three-stages stress-strain response.

Stage I corresponds to a strain range from 0% to 10% within which cracking initiates and propagates through the cellular structure. As soon as external load was applied, similar to the 2D-ACCCs tensile stress immediately occurs at the “joint” (see Figure 10-3) regions of the 3D cellular structure. For the M specimens, due to the brittle behavior of cementitious mortar, cracks initiated and propagated rapidly through the entire cellular structure leading to the failure of the specimen. In contrast, all other specimens with either ABS shell or reinforcement did not show rapid failure. Instead, after cracks initiated at the “joints” (see Figure 10-3) the ABS shell and the reinforcement provided enough crack resistance such that the generated local cracks could not propagate through the entire specimen. It is worth of noticing, owing to the high tensile strength of the ABS material compared to the cementitious matrix (approximately 25MPa), the peak strength of the specimens with ABS shell (MR-S and M-S) is obviously higher than the ones without shell (MR and M). Meanwhile, for the MR specimens, increasing reinforcing ratio substantially increased the cracking resistance, therefore the first peak of the MR-P2 and MR-P3 is obviously higher.

A typical behavior of the 3D-ACCCs within this stage is the auxetic behavior. As described in Figure 10-11, from 0% strain to 10% strain the Poisson’s ratio of the 3D-ACCCs is negative and decreases with respect to the strain. Correspondingly, the

elliptical cellular structure also generally disappeared due to the deformation of the cellular structure until the sections came into contact (see Figure 10-9).

Stage II indicates a compression damage process of the compacted cementitious composites constituent material. Within this stage the “section” (see Figure 10-3) of the 3D cellular structure started to contact. Correspondingly, although the Poisson’s ratio is still negative, the value of the Poisson’s ratio already started to increase with respect to the strain. The compression process of the 3D-ACCCs within this stage resembles the compressive behavior of conventional concrete blocks which typically have a compressive peak load indicating the compressive strength of the material. Owing to the ABS shell, the second peak strength of the MR-S and M-S is obviously higher than the specimens without the shell (MR and M). Even with the increased reinforcing ratio, the second peak of the MR is still considerably lower.

Stage III is a compacting process of the damaged remains under compressive load. Due to the remains being highly compacted, the stress was able to sharply increase as the compressive strain increased. A similar phenomenon was found in the 2D-ACCCs and was supposed to exist in conventional concrete as mentioned in a thought experiment by van Mier [1].

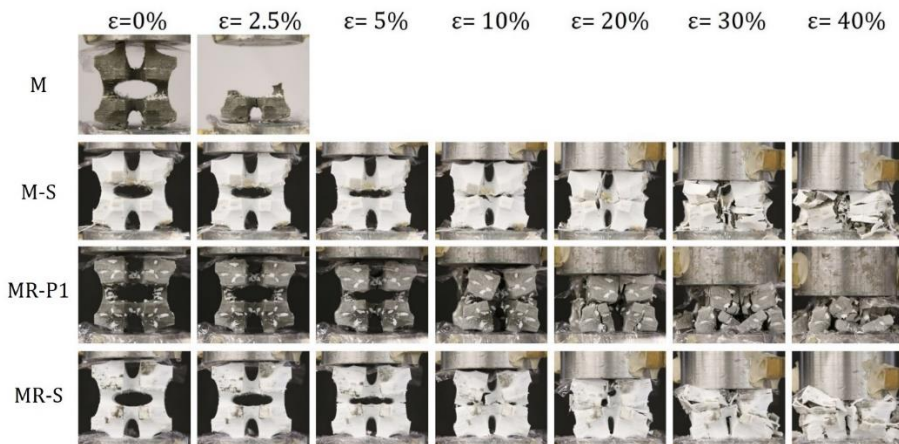


Figure 10-9 Compression process of the cementitious composites with 3D cellular structure

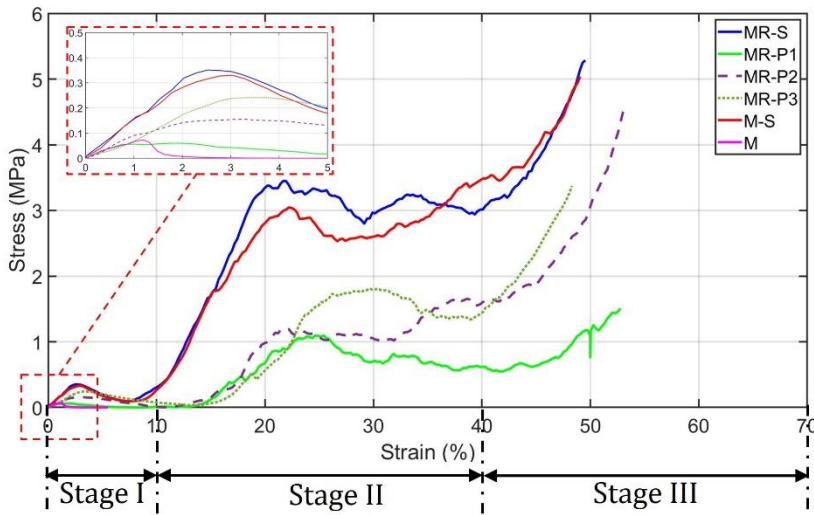


Figure 10-10 Stress-strain curves of cementitious composites with 3D cellular structure

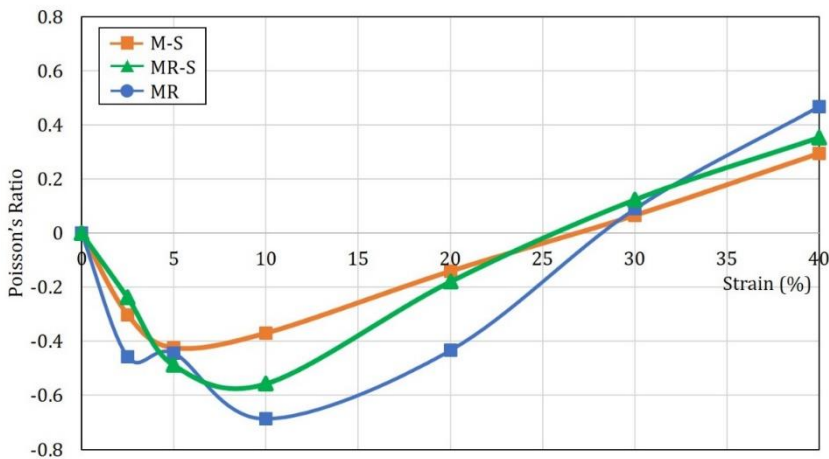


Figure 10-11 Poisson's ratio of the 3D-ACCCs

10.3.2 Compressive strength

The compressive strength was first defined as the highest compressive stress during Stage I and Stage II on the stress-strain curves of the ACCCs. Stage III was not considered as it is only a compacting process of damaged material. However, in some specific applications, for instance protection structures against earthquakes, this stage can provide considerably high energy absorption.

As a cellular material, low unit weight is an important feature of the ACCCs. Within the entire thesis the studied ACCCs (including the 2D-ACCCs and 3D-ACCCs) have considerably lower density than bulk cementitious constituent materials

(approximately 1850 kg/m³ for the mix we used). In this aspect, the ACCCs are similar to a widely used lightweight civil engineering material: foam concrete. Regarding the compressive strength, the ACCCs are comparable to the foam concrete with a density below 1200 kg/m³, see Figure 10-12. Among the developed ACCCs, P50 (2D) has the highest compressive strength of 3.7 MPa. Two types of the 3D-ACCCs with ABS shell also show similar compressive strength: M-S has 3.2 MPa and MR-S has 3.5 MPa, comparatively the MR has a rather low compressive strength of 1.1 MPa. As the density of 3D-ACCCs is lower than the 2D-ACCCs, the M-S and MR-S would have better efficiency in compressive strength with respect to the same density. It is shown in Figure 10-13 that the M-S and MR-S have 31% and 39% higher specific compressive strength comparing to the 2D-ACCCs(P50), respectively.

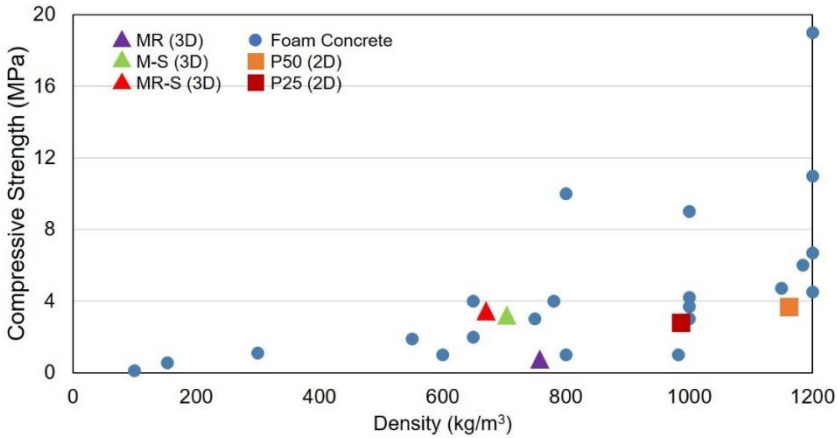


Figure 10-12 Compressive strength of the 2D-ACCCs and 3D-ACCCs comparing to foam concrete with respect to density; more details of P25 and P50 can be found in Chapter 5 and Chapter 6, data of foam concrete is adopted from [2, 3]

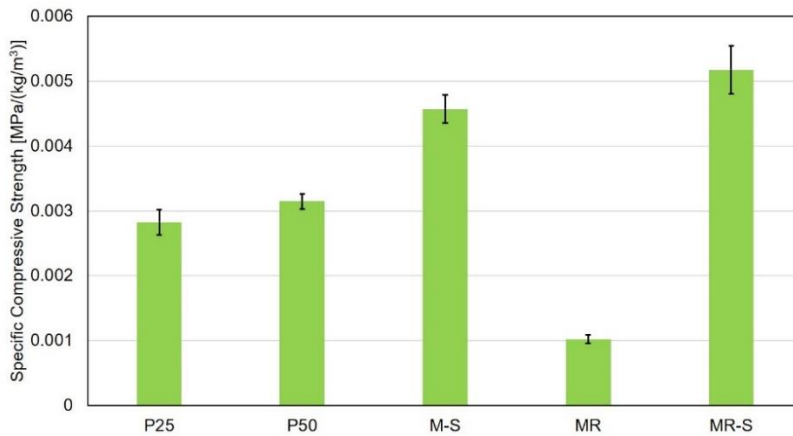


Figure 10-13 Specific compressive strength of the ACCCs, standard deviation is given; more details of P25 and P50 can be found in Chapter 5 and Chapter 6

10.3.3 Deformability and energy absorption capacity

Compared to conventional cementitious materials, one of the most promising characteristics of the ACCCs is their high deformability. The compressive deformability is defined as the strain (by percentage) at which the compressive strength occurs, namely the strain at the second peak for the ACCCs. As shown in Figure 10-14, the deformability all ACCCs (P25, P50, M-S, MR and MR-S) is distinctively higher than foam concrete and other cellular composites (M and P0) without auxetic behavior. Particularly, the deformability of 3D-ACCCs is also higher than that of the 2D-ACCCs. The large compressibility of the ACCCs may ensure excellent energy dissipation capacity. This is shown in Figure 10-15, defined as the area under load-displacement curves divided by volume of the specimen; due to the compressed displacement variability in different existing studies [4-9], the energy dissipation values of foam concrete reported in different researches have rather large deviation. Compared to conventional foam concrete, all ACCCs have higher energy absorption capacity per volume of the composite. More importantly, the ABS shell shows great potential for improving the energy absorption of the 3D-ACCCs. The energy absorption capacity of MR (1.22 J/cm^3) resembles that of the 2D-ACCCs (1.22 J/cm^3 for P50 and 1.16 J/cm^3 for P25). In contrast, when ABS shell was used, the energy absorption capacity of MR-S (8.13 J/cm^3) and M-S (7.38 J/cm^3) specimens was significantly improved: approximately 600% to 700% higher than 2D-ACCCs and at least 900% higher than conventional foam concrete.

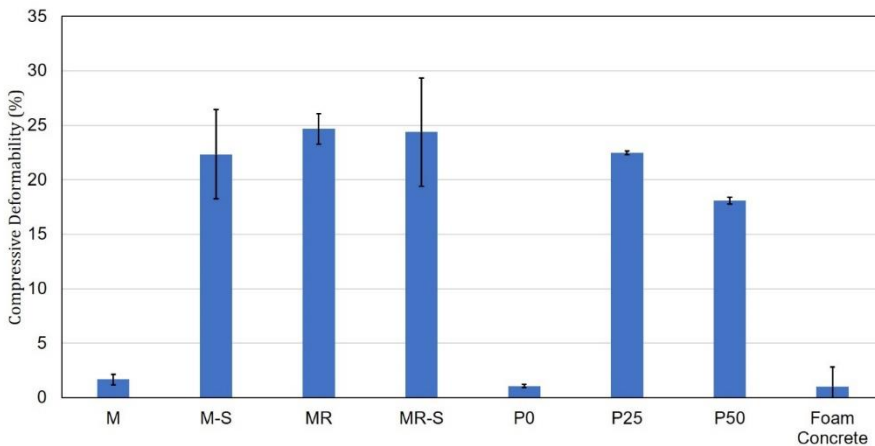


Figure 10-14 Compressibility of the cementitious cellular composites comparing to foam concrete, standard deviation is given; as the data of foam concrete was adopted from various references [4-9] large deviation is witnessed; more details of P0, P25 and P50 can be found in Chapter 5 and Chapter 6

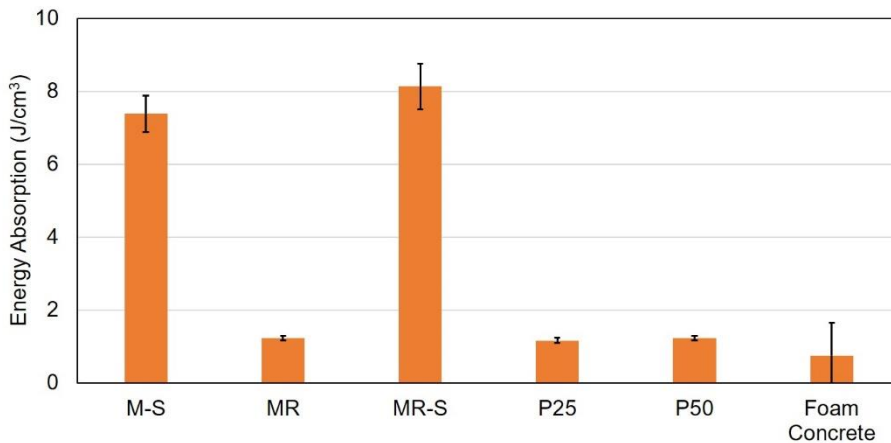


Figure 10-15 Energy absorption capability of the ACCCs comparing to foam concrete, standard deviation is given; as the data of foam concrete was adopted from various references [4-9] large deviation is witnessed; more details of P0, P25 and P50 can be found in Chapter 5 and Chapter 6

10.4 CONCLUSIONS

In this chapter, the approach proposed in previous chapters to develop auxetic cementitious cellular composites (ACCCs) is extended to 3D. Combining architecting three-dimensional cellular structure and tailoring the constituent material, 3D-ACCCs were developed. Uniaxial compressive tests were performed on the 3D-ACCCs. The deformation process and the stress-strain response of the 3D-ACCCs was evaluated. In addition, the compressive strength, deformability and energy absorption capacity were compared with 2D-ACCCs (developed in previous chapters) and conventional foam concrete. Based on the obtained experimental results, several conclusions can be drawn:

- By extrapolating the 2D elliptical planar cellular structure to the 3D space, a 3D cellular structure was created such that under compressive load tensile stress concentrated at desired regions which was key to induce crack initiation and achieve auxetic behavior.
- Similar to the 2D-ACCCs, high cracking resistance is necessary for the 3D-ACCCs to achieve auxetic behavior. Both the ABS shell and the reinforcing structure have the ability to provide cracking resistance for the 3D-ACCCs to achieve auxetic behavior.
- The 3D-ACCCs show a typical three-stage compressive behavior of the auxetic materials similar to the 2D-ACCCs. This ensures the 3D-ACCCs outstanding deformability. The highest deformability value obtained by the M-S (3D) reaches approximately 24.7% strain in contrast to approximately 1% for conventional foam concrete.
- In terms of specific compressive strength and energy absorption capacity, the ABS shell has considerably enhanced the performance of the 3D-ACCCs. The specific

strength of the M-S and MR-S are 31% and 39% higher than the 2D-ACCCs (P50). Meanwhile, the energy absorption capacity of the M-S and MR-S specimens are 600% to 700% higher than the 2D-ACCCs and at least 900% higher than conventional foam concrete.

REFERENCES

- [1] J.G. Van Mier, Fracture processes of concrete, CRC press 1997.
- [2] L. Chica, A. Alzate, Cellular concrete review: New trends for application in construction, *Construction and Building Materials* 200 (2019) 637-647.
- [3] Y.H.M. Amran, N. Farzadnia, A.A. Abang Ali, Properties and applications of foamed concrete; a review, *Construction and Building Materials* 101 (2015) 990-1005.
- [4] B. Wang, Y. Chen, H. Fan, F. Jin, Investigation of low-velocity impact behaviors of foamed concrete material, *Composites Part B: Engineering* 162 (2019) 491-499.
- [5] W. Nian, K.V.L. Subramaniam, Y. Andreopoulos, Experimental investigation on blast response of cellular concrete, *International Journal of Impact Engineering* 96 (2016) 105-115.
- [6] T.T. Nguyen, H.H. Bui, T.D. Ngo, G.D. Nguyen, Experimental and numerical investigation of influence of air-voids on the compressive behaviour of foamed concrete, *Materials & Design* 130 (2017) 103-119.
- [7] B. Su, Z. Zhou, Z. Li, Z. Wang, X. Shu, Experimental investigation on the mechanical behavior of foamed concrete under uniaxial and triaxial loading, *Construction and Building Materials* 209 (2019) 41-51.
- [8] T.T. Nguyen, H.H. Bui, T.D. Ngo, G.D. Nguyen, M.U. Kreher, F. Darve, A micromechanical investigation for the effects of pore size and its distribution on geopolymer foam concrete under uniaxial compression, *Engineering Fracture Mechanics* 209 (2019) 228-244.
- [9] Y. Yang, Q. Zhou, Y. Deng, The reinforcement attributes of multi-scale hybrid fiber throughout the uniaxial compression of ultra-low-weight foamed cement-based composites, *Construction and Building Materials* 242 (2020) 118184.

11

DISCUSSIONS, CONCLUSIONS AND OUTLOOK

In this final chapter, discussions and conclusions are given based on the main content and findings of the study. Afterwards, an outlook of future promising successive research directions is indicated.

11.1 DISCUSSIONS AND CONCLUSIONS

This thesis presents studies of a novel type of cementitious material: architected cementitious cellular material. Specifically, mechanical aspects are comprehensively investigated and discussed. In contrast to conventional cementitious materials which are designed by mixture proportioning, a new approach is proposed to manufacture cementitious materials: combining architected cellular structures with tailored cementitious mixtures. A unique auxetic behavior is achieved by cementitious materials developed by this new approach. Through subsequent investigations, solid knowledge on the mechanical properties of architected cementitious cellular materials is constructed. A general summary of the main findings and conclusions is drawn as follows:

- In order to combine tunable 2D planar cellular structure with cementitious mixtures, a method has been developed using digital fabrication techniques. Using the method, various types of cellular structures can be easily architected in combination with tailored cementitious mixture.
- Study on the cementitious lattices shows that the fracture behavior of cementitious cellular materials is highly dependent on the cellular structure. The crack pattern of the cementitious lattices follows the configuration of the lattice element orientation, and can thus be tuned by architecting the cellular structure.
- Unprecedented auxetic behavior, namely negative Poisson's ratio, can be achieved by cementitious materials. This, in principle, is done by architecting the fracture process of the cementitious materials. By adopting an elliptical cellular structure, the location of crack initiation is designed, and subsequent crack propagation is controlled by tailoring the crack-bridging ability of the constituent material using fiber incorporated cementitious mixture.
- Cracking-initiated section rotation is identified as the mechanism of the developed auxetic cementitious cellular composites (ACCCs) to exhibit auxetic behavior. Owing to this unique deformation behavior, the ACCCs possess excellent mechanical properties especially resiliency under cyclic loading: a range of 2.5% reversible strain under compressive cyclic loading was achieved. To the best of the authors' knowledge, this is extremely difficult and has never been achieved by any other types of cementitious materials.
- Apart from using conventional fibers, the crack-bridging ability of cementitious constituent materials can be ensured by using 3D printed polymeric structures as reinforcement. The reinforced cementitious composites exhibited enhanced crack-bridging ability, and even strain hardening behavior up to 1.5% of strain capacity under uniaxial tension.
- Using cementitious composites reinforced by 3D printed polymeric structures as the constituent material, ACCCs with three-dimensional cellular structures were developed, which validates the discovered mechanism for cementitious materials to achieve auxetic behavior. The developed 3D-ACCCs exhibits 31%~39% of enhanced specific compressive strength and 600%~700% higher energy

absorption capacity comparing to the ACCCs with a planar cellular structure, 900% energy absorption higher than conventional foam concrete.

11.2 RECOMMENDATIONS FOR FUTURE STUDY

The developed ACCCs have already shown excellent deformability and resiliency, which is achieved by architecting the constituent material and the cellular structure. While, for future studies, the properties of the developed ACCCs may be further improved from two different aspects: modifying the constituent material as well as the cellular structure. In terms of the constituent material, the focus in this thesis was mainly on the reinforcing or toughening phase design, while the cementitious matrix wasn't optimized. It should be noted, however, that the behavior of the cementitious constituent material also depends on the matrix properties[1]. It is possible that even higher ductility of the constituent materials could be obtained with lower w/b ratio. In terms of the cellular structure, by parametric studies, the elliptical structure might be optimized. Apart from the elliptical structure used in this thesis, other types of structures, for instance the re-entrant structures[2] may be also used to develop ACCCs. This is worth of further studying as well.

Comparing to other type of cementitious materials, the tunable cellular structure, high deformability, and resiliency under cyclic loading of the ACCCs are rather distinct. These features make ACCCs rather promising for energy harvesting purposes. In order to create an energy harvester, a piezoelectric material, for example piezoelectric polyvinylidene fluoride (PVDF) film, is usually mounted or attached on a substrate. As a type of construction material, using the ACCCs as the substrate for piezo-electric materials to harvest unused energy from infrastructures is rather promising. In this sense, several research directions are recommended.

11.2.1 Vibration-based energy harvester

Infrastructures exposed to ambient vibrations are widespread, such as roads exposed to vehicle loadings, railways exposed to train movements, or pavement exposed to footsteps. Under these conditions, a vibration-based energy harvester (VEH) may be utilized.

Two features of the VEH give the ACCCs potential to be used as substrate for piezoelectric energy harvesting materials.

- Usually, when a piezoelectric energy harvester is subject to ambient stress, it stretches in one direction (for instance along y axis, see Figure 11-1) to generate energy. In direct contrast, using the ACCCs as substrates, it also expands in longitudinal direction when stretched in transversal direction (see Figure 11-1) owing to the unique auxetic deformation behavior of the ACCCs. Some studies used auxetic metal as substrate for piezoelectric materials to create VEH [3, 4]. The results indicate that the electric power output is obviously higher comparing the conventional solid substrate.

- The power output of the VEH is highly dependent on the resonant frequency; namely, the environmental vibration frequency has to match the material natural frequency to provide optimal energy output. As a cellular material, ACCCs have a natural frequency range which can be tuned by architecting the cellular structure[5]. Therefore, ACCCs might provide a wide bandwidth for the VEH energy harvesting. The tuning process of the cellular structure could be performed using a data driven process: using numerical simulations (similar to Chapter 6), a large amount of data could be generated and therefore, the cellular structure could be optimized to increase the energy harvesting efficiency.

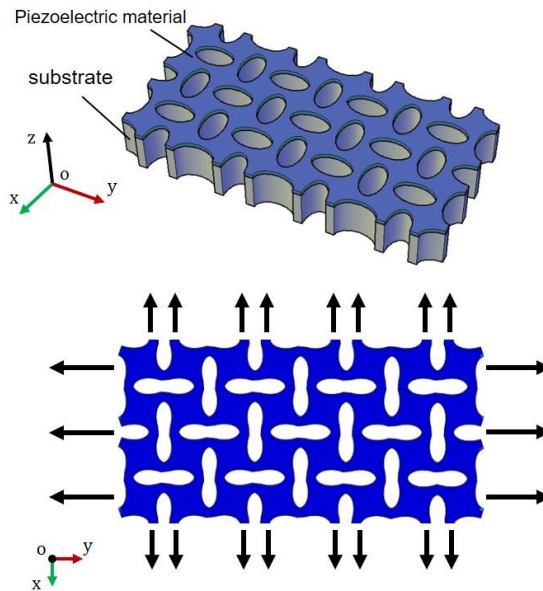


Figure 11-1 Schematics of using ACCCs as substrate for piezoelectric material

11.2.2 Strain-energy harvester

The large deformability/resiliency also makes the ACCCs very promising for harvesting strain energy. There are also many occasions in civil engineering exposed or potentially exposed to large deformations, for example, mass dampers in tall buildings and breakwaters exposed to sea waves. Under these conditions, the harvester would be exposed to large environmental deformations which could be utilized by the high deformability of the ACCCs. Meanwhile, owing to the large deformation, the energy output would not rely on the resonant condition of the harvester, which significantly decreases the difficulty of application of energy harvesters.

REFERENCES

- [1] T. Kanda, V.C. Li, New micromechanics design theory for pseudostrain hardening cementitious composite, *Journal of engineering mechanics* 125(4) (1999) 373-381.
- [2] H.L. Tan, Z.C. He, K.X. Li, E. Li, A.G. Cheng, B. Xu, In-plane crashworthiness of re-entrant hierarchical honeycombs with negative Poisson's ratio, *Composite Structures* 229 (2019) 111415.
- [3] W.J.G. Ferguson, Y. Kuang, K.E. Evans, C.W. Smith, M. Zhu, Auxetic structure for increased power output of strain vibration energy harvester, *Sensors and Actuators A: Physical* 282 (2018) 90-96.
- [4] Q. Li, Y. Kuang, M. Zhu, Auxetic piezoelectric energy harvesters for increased electric power output, *AIP Advances* 7(1) (2017) 015104.
- [5] N. Chandrasekharan, L.L. Thompson, Increased power to weight ratio of piezoelectric energy harvesters through integration of cellular honeycomb structures, *Smart Materials and Structures* 25(4) (2016) 045019.

SUMMARY

In recent years, the rapid development of digital fabrication technology has substantially boosted the research of architected cellular materials. Among them, the auxetic materials are a distinct type for their unusual deformation behavior: negative Poisson's ratio. When loaded longitudinally in compression, in contrast to conventional materials, the auxetic materials shrinks transversely, and vice versa. This featured deformation behavior gives the auxetic materials enhanced mechanical properties, especially high deformability and energy absorption ability. In many other fields, for instance metals and polymers, auxetic materials have already become a hot research topic. Numerous studies focusing on design, preparation, optimization, and application of auxetic materials have emerged. However, for cementitious materials, the auxetic behavior has never attracted attention and, to the author's knowledge, auxetic cementitious cellular materials have never reported in literature. Therefore, this study mainly focuses on the development of architected cementitious cellular materials with auxetic behavior. In order to accomplish the research objective, this PhD research was conducted in three stages:

- At first, in order to gain preliminary understanding of the mechanical behaviors of architected cementitious cellular materials, simple triangular lattices were investigated. Inspired by the conventional investment casting method widely used for metallurgy, an indirect 3D printing method was developed to prepare cementitious lattice specimens. Using this method, various types of cellular structures can be combined with designed cementitious mixture. According to experimental and numerical studies, it was found that although the cementitious materials are rather brittle, the fracture properties, especially cracking mode was still able to be architected by varying the cellular structure. This result has indicated the possibility of creating auxetic cementitious materials through tailoring the cracking process of cementitious materials.
- Then, based on the developed method in the previous stage, an elliptical shape cellular structure was used to tailor the cracking initiation of cementitious cellular material. By configuring the elliptical cellular structure, local tensile stress concentration was introduced at desired regions. Because cementitious materials have low tensile strength, cracks were ensured to initiate at these regions. In addition to architecting the cellular structure, cementitious mixture was also tailored to possess crack-bridging ability. This was accomplished by using fibers as toughening phase for the cementitious mixture. By constructing the architected cellular structure with the toughened cementitious mixture, auxetic cementitious cellular composites (ACCCs) were created for the first time. According to

experimental and numerical results, “cracking-initiated section rotation” was discovered as the auxetic mechanism of the ACCCs. Large compressive deformability (up to 22.5% of strain) is one characteristic of the created ACCCs. Apart from this, an unprecedented resiliency with an amplitude of 1.25% of strain has been achieved by the ACCCs.

- At last, the discovered auxetic mechanism of the ACCCs was validated by creating auxetic cementitious cellular composites with a three-dimensional cellular structure (3D-ACCCs). According to the previously discovered auxetic mechanism, a cellular structure was first generated by extrapolating the afore mentioned 2D planar pattern to be a 3D spatial structure. Meanwhile, in order to improve the crack bridging ability, 3D printed polymeric structures were used as reinforcement of the cementitious constituent material. It was found that the reinforced cementitious composites exhibited obvious enhanced crack bridging ability, even strain hardening behavior. Combining the designed 3D cellular structure with the polymer reinforced cementitious composites, 3D-ACCCs were successfully created. As such, the auxetic mechanism is validated. The created 3D-ACCCs exhibit higher deformability and significantly improved energy absorption ability than the ACCCs with planar pattern and conventional foam concrete.

Based on the findings of this PhD study, the ACCCs show excellent mechanical properties. This gives the ACCCs great potential to be used for civil engineering practices. Especially, the ACCCs possess high deformability and large resiliency that conventional cementitious materials are lacking. The ACCCs would be promising to be used as substrate for piezoelectric materials to create energy harvester. This is recommended to be implemented in future studies.

SAMENVATTING

In de afgelopen jaren heeft de snelle ontwikkeling van digitale fabricagetechnologie het onderzoek naar het ontwerpen cellulaire materialen aanzienlijk gestimuleerd. Onder hen zijn de auxetische materialen een apart type vanwege hun ongebruikelijke vervormingsgedrag: de negatieve Poisson-verhouding. Wanneer ze in de lengterichting worden belast op druk, krimpen de auxetische materialen, in tegenstelling tot conventionele materialen, in dwarsrichting en vice versa. Dit kenmerkende vervormingsgedrag geeft de auxetische materialen verbeterde mechanische eigenschappen, in het bijzonder een hoge vervormbaarheid en energieabsorptievermogen. Op veel andere gebieden, bijvoorbeeld metalen en polymeren, zijn auxetische materialen al een populair onderzoeksonderwerp geworden. Talloze studies gericht op ontwerp, voorbereiding, optimalisatie en toepassing van auxetische materialen zijn populair. Voor cementachtige materialen heeft het auxetische gedrag echter nooit aandacht getrokken en, voor zover de auteur weet, zijn auxetische cementachtige cellulaire materialen nooit in de literatuur vermeld. Daarom richt deze studie zich voornamelijk op de ontwikkeling van architectonische cementgebonden cellulaire materialen met auxetisch gedrag. Om de onderzoeksdoelstelling te bereiken, werd dit promotieonderzoek uitgevoerd in drie fasen:

- In eerste instantie werden eenvoudige driehoekige roosters onderzocht om een voorlopig begrip te krijgen van het mechanische gedrag van geconstrueerde cementachtige cellulaire materialen. Geïnspireerd door de conventionele investeringsgietmethode die veel wordt gebruikt voor de metallurgie, werd een indirecte 3D-printmethode ontwikkeld om cementachtige roostermonsters te maken. Met deze methode kunnen verschillende soorten celstructuren worden gecombineerd met een ontworpen cementmengsel. Volgens experimentele en numerieke studies werd gevonden dat, hoewel de cementachtige materialen nogal bros zijn, de breukeigenschappen, met name de scheurwijze, nog steeds konden worden ontworpen door de celstructuur te variëren. Dit resultaat heeft de mogelijkheid getoond om auxetische cementachtige materialen te creëren door het scheurproces van cementachtige materialen op maat te maken.
- Vervolgens werd, op basis van de in de vorige fase ontwikkelde methode, een elliptische celstructuur gebruikt om de scheurinitiatie van cementachtig celmateriaal op maat te maken. Door de elliptische cellulaire structuur te configureren, werd lokale trekspanningsconcentratie geïntroduceerd in gewenste zones. Omdat cementachtige materialen een lage treksterkte hebben, werd ervoor gezorgd dat er scheuren ontstonden in deze gebieden. Naast het ontwerpen van de

cellulaire structuur, werd een cementmengsel ook op maat gemaakt om scheuroverbruggend vermogen te bezitten. Dit werd bereikt door vezels te gebruiken als component voor de taaheid voor het cementachtige mengsel. Door de architectonische celstructuur te construeren met het taaie cementachtige mengsel, werden voor het eerst auxetische cementachtige cellulaire composieten (ACCC's) gemaakt. Volgens experimentele en numerieke resultaten werd "door scheuren geïnitieerde sectierotatie" ontdekt als het auxetische mechanisme van de ACCC's. Grote vervormbaarheid onder druk (tot 22,5% van de rek) is een kenmerk van de gecreëerde ACCC's. Afgezien hiervan is door de ACCC's een ongekende veerkracht bereikt met een amplitude van 1,25% van de rek.

- Eindelijk werd het ontdekte auxetische mechanisme van de ACCC's gevalideerd door auxetische cementachtige cellulaire composieten te maken met een driedimensionale cellulaire structuur (3D-ACCC's). Volgens het eerder ontdekte auxetische mechanisme werd eerst een cellulaire structuur gegenereerd door het bovengenoemde 2D-planaire patroon te extrapoleren naar een 3D-ruimtelijke structuur. Ondertussen werden, om het scheuroverbruggende vermogen te verbeteren, 3D-geprinte polymere structuren gebruikt als versterking van het cementachtige materiaal. Er werd gevonden dat de versterkte cementachtige composieten een duidelijk verbeterd scheuroverbruggend vermogen vertoonden, en zelfs spanningsverhardend gedrag werd bereikt. Door de ontworpen 3D-celstructuur te combineren met polymeer versterkte cementachtige composieten, werden 3D-ACCC's met succes gecreëerd. Als zodanig is het auxetische mechanisme gevalideerd. De gecreëerde 3D-ACCC's vertonen een hogere vervormbaarheid en een aanzienlijk verbeterd energieabsorptievermogen dan de ACCC's met een vlak patroon en ook dan conventioneel schuimbeton.

Op basis van de bevindingen van dit promotieonderzoek vertonen de ACCC's uitstekende mechanische eigenschappen. Dit geeft de ACCC's een groot potentieel om te worden gebruikt voor civieltechnische toepassingen. Vooral de ACCC's hebben een hoge vervormbaarheid en grote veerkracht die conventionele cementachtige materialen missen. ZDe ACCC's kunnen veelbelovend zijn om te worden gebruikt als substraat voor piëzo-elektrische materialen om energieoogstmachines te creëren. Het wordt aanbevolen om dit in toekomstige studies verder te onderzoeken.

LIST OF PUBLICATIONS

JOURNAL PUBLICATIONS

1. **Y. Xu**, H. Zhang, B. Šavija, S. Chaves Figueiredo, E. Schlangen, Deformation and fracture of 3D printed disordered lattice materials: Experiments and modeling, *Materials & Design* 162 (2019) 143-153.
2. **Y. Xu**, B. Šavija, Development of strain hardening cementitious composite (SHCC) reinforced with 3D printed polymeric reinforcement: Mechanical properties, *Composites Part B: Engineering* 174 (2019) 107011.
3. **Y. Xu**, H. Zhang, E. Schlangen, M. Luković, B. Šavija, Cementitious cellular composites with auxetic behavior, *Cement and Concrete Composites* 111 (2020) 103624.
4. **Y. Xu**, E. Schlangen, M. Luković, B. Šavija, Tunable mechanical behavior of auxetic cementitious cellular composites (CCCs): Experiments and simulations, *Construction and Building Materials* 266 (2021) 121388.
5. **Y. Xu**, H. Zhang, Y. Gan, B. Šavija, Cementitious composites reinforced with 3D printed functionally graded polymeric lattice structures: experiments and modelling, *Additive Manufacturing* (2021) 101887.
6. **Y. Xu**, B. Šavija, E. Schlangen, Multiscale experimental and numerical study on the deformation and fracture behavior of cementitious lattice materials, *Engineering fracture mechanics*, **(under review)**.
7. H. Zhang, B. Šavija, **Y. Xu**, E. Schlangen, Size effect on splitting strength of hardened cement paste: Experimental and numerical study, *Cement and Concrete Composites* 94 (2018) 264-276. **(correspondence)**
8. H. Zhang, **Y. Xu**, Y. Gan, Z. Chang, E. Schlangen, B. Šavija, Combined experimental and numerical study of uniaxial compression failure of hardened cement paste at micrometre length scale, *Cement and Concrete Research* 126 (2019) 105925. **(correspondence)**
9. H. Zhang, **Y. Xu**, Y. Gan, E. Schlangen, B. Šavija, Experimentally validated meso-scale fracture modelling of mortar using output from micromechanical models, *Cement and Concrete Composites* 110 (2020) 103567. **(correspondence)**
10. H. Zhang, **Y. Xu**, Y. Gan, Z. Chang, E. Schlangen, B. Šavija, Microstructure informed micromechanical modelling of hydrated cement paste: Techniques and challenges, *Construction and Building Materials* 251 (2020) 118983. **(correspondence)**

11. Z. Wan, **Y. Xu**, Y. Zhang, S. He, B. Šavija, Mechanical Properties and healing efficiency of 3D-printed ABS vascular based self-healing cementitious composite: Experiments and modelling, *Engineering Fracture Mechanics*. **(correspondence, under review)**
12. Z. Wu, **Y. Xu**, B. Šavija, Mechanical properties of lightweight cementitious cellular composites incorporating micro-encapsulated phase change material produced by indirect 3D printing, *materials*. **(correspondence, under review)**
13. Z. Chang, **Y. Xu**, Y. Chen, Y. Gan, E. Schlangen, B. Šavija, A discrete lattice model for assessment of buildability performance of 3D-printed concrete, *Computer-Aided Civil and Infrastructure Engineering* 36(5) (2021) 638-655.
14. Z. Wan, **Y. Xu**, B. Šavija, On the Use of Machine Learning Models for Prediction of Compressive Strength of Concrete: Influence of Dimensionality Reduction on the Model Performance, *Materials (Basel)* 14(4) (2021).
15. H. Zhang, Y. Gan, **Y. Xu**, S. Zhang, E. Schlangen, B. Šavija, Experimentally informed fracture modelling of interfacial transition zone at micro-scale, *Cement and Concrete Composites* 104 (2019) 103383.
16. Y. Gan, H. Zhang, **Y. Xu**, E. Schlangen, Kvan Breugel, Šavija, Experimental study of flexural fatigue behaviour of cement paste at the microscale, *International Journal of Fatigue* (2021) 106378.
17. S. C. Figueiredo, C. R. Rodríguez, Z. Y. Ahmed, D. H. Bos, **Y. Xu**, T. M. Salet, ... & F. P. Bos. An approach to develop printable strain hardening cementitious composites. *Materials & Design*, 169(2019): 107651.
18. S. C. Figueiredo, C. R. Rodríguez, Z. Y. Ahmed, D. H. Bos, **Y. Xu**, T. M. Salet, ... & F. P. Bos. Mechanical behavior of printed strain hardening cementitious composites. *Materials*, 13(10)(2020), 2253.

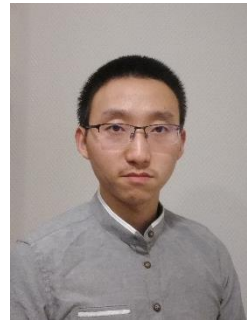
CONFERENCE PROCEEDINGS

1. **Y. Xu**, B. Šavija, E. Schlangen, Compression behaviors of cementitious cellular composites with negative Poisson's Ratio, FramCos, France, 2019.
2. **Y. Xu**, E. Schlangen, B. Šavija, Creating strain hardening cementitious composites (SHCCS) through use of additively manufactured polymeric meshes as reinforcement, FramCos, France, 2019.
3. **Y. Xu**, E. Schlangen, B. Šavija, Auxetic behavior of cementitious cellular composites under uniaxial compression and cyclic Loading, RILEM International Conference on Concrete and Digital Fabrication. Springer, Cham, 2020.
4. V. Huijgen, **Y. Xu**, E. Schlangen, B. Šavija, Flexural response of cementitious mortar bars reinforced by 3D printed polymeric mesh. 4th International Conference on ServiceLife Design for Infrastructures, RILEM, Delft, 2018.

5. L. Mercuri, C. R. Rodriguez, **Y. Xu**, S. C. Figueiredo, R. Mors, E. Rossi, ... & E. Schlangen, On the role of soft inclusions on the fracture behaviour of cement paste., FramCos, France, 2019.

CURRICULUM VITAE

Yading Xu



Sep.18th 1990 **Born in Sichuan, China**

Education

- | | |
|------------------------|---|
| Sep. 2009 - July. 2013 | B.Sc. student
Materials Science and Engineering
Tongji University, Shanghai, China |
| Sep. 2014 - July. 2017 | M.Sc. student
Materials Science and Engineering
China Building Materials Academy, Beijing, China |
| Sep. 2017 - Present | Ph.D. candidate
Civil Engineering and Geosciences
Delft University of Technology, Delft, Netherland |

